

CHEMICAL AND PHYSICAL CHARACTERIZATION OF HYBRID  
ORGANIC-INORGANIC LOW-DIMENSIONAL COORDINATION POLYMERS

By

JONATHAN DAVID WOODWARD

A DISSERTATION PRESENTED TO THE GRADUATE SCHOOL  
OF THE UNIVERSITY OF FLORIDA IN PARTIAL FULFILLMENT  
OF THE REQUIREMENTS FOR THE DEGREE OF  
DOCTOR OF PHILOSOPHY

UNIVERSITY OF FLORIDA

2003

To My Parents and Grandparents

## ACKNOWLEDGMENTS

I would very much like to thank my research advisor, Dr. Daniel Talham, for his support, guidance, encouragement, novel ideas, and advice during my time in his research group at the University of Florida. Despite some difficult times early on, Dan was willing to work with me. He encouraged me to continue my efforts and press on so that I could complete my degree. From Dan I have learned how to approach a research problem from an objective standpoint, how to interpret data, and, most importantly, how to present results in an acceptable manner.

I would also very much like to thank Dr. Rènal Backov, a postdoctoral fellow in our group for the past 2 years, for his help, support, and encouragement. Rènal was involved in many aspects of my graduate work and this dissertation would not be possible without his efforts. I would like to thank Dr. Khalil Abboud for his work in solving numerous crystal structures and for teaching me all about crystallography. I would also like to thank Dr. C. Russell Bowers, and his graduate student, Bhavin Adhyaru, for the use of the NMR equipment in the host-guest investigations. I would like to thank Bhavin in particular for the rather large amount of time spent in completing NMR experiments as well as writing and editing. I would like to thank Dr. Mark Meisel and his group members (Dr. Hitoshi Ohnuki, Dr. Brian Watson, A. Nicole Morgan, Ju-Hyun Park, and Diktys Stratakis) for performing bulk magnetic measurements on many of my samples over the past 5 years. I would like to acknowledge Dr. John Reynolds, Dr. Gus Palenik, Dr. Mark Meisel, and Dr. David Richardson for being part of my Ph.D. committee.

I would like to thank the past and present members of the Talham research group (Dr. Brian Ward, Dr. Gail Fanucci, Jeff Culp, Eduardo Perez-Cordero, Chen Liu, David Zipse, and Sarah Lane) for their support during my time here. I would also like to thank Brian for help in getting me started in my research; Gail for teaching me how to operate the lab machinery, including the computers; and Eduardo for teaching me some advanced math in order to model magnetic data. I would also like to especially thank Jeff for putting up with me during the time spent writing my thesis and his help with numerous things for the past five years.

I want to also give special thanks to my parents, Ann and Dennis Woodward and my grandmother, Virginia Prescott, for the support and encouragement throughout my entire life whenever I needed it. Without them, I certainly would have not made it this far.

## TABLE OF CONTENTS

	<u>page</u>
ACKNOWLEDGMENTS .....	iii
ABSTRACT.....	ix
CHAPTER	
1 INTRODUCTION .....	1
Low-Dimensional Materials .....	2
Introduction to Molecular Magnetism .....	3
Diamagnetism and Paramagnetism.....	3
Basic Relationships.....	4
Non-Interacting Spin Systems and the Curie Law.....	6
Interacting Spin Systems and the Curie-Weiss Law.....	7
Magnetic Exchange.....	9
Anisotropy.....	11
Dimers.....	16
Chains .....	20
Ladders.....	24
Self-Assembly of Supramolecular Architectures.....	27
Strategies for Building Supramolecular Architectures .....	27
Factors Affecting the Structure of Supramolecular Architectures.....	31
Porous Network Supramolecular Architectures.....	33
Scope of the Dissertation .....	38
2 STRUCTURAL, THERMAL, AND MAGNETIC PROPERTIES INVESTIGATION OF THREE TRANSITION METAL-4,4'-BIPYRIDINE COORDINATION POLYMERS: [Ni(4,4'-bipy) <sub>3</sub> (H <sub>2</sub> O) <sub>2</sub> ](ClO <sub>4</sub> ) <sub>2</sub> ·1.4(4,4'-bipy)·3(H <sub>2</sub> O), [Co(4,4'-bipy) <sub>3</sub> (H <sub>2</sub> O) <sub>2</sub> ](ClO <sub>4</sub> ) <sub>2</sub> ·1.4(4,4'-bipy)·3(H <sub>2</sub> O), and [Cu(4,4'-bipy) <sub>3</sub> (DMSO) <sub>2</sub> ](ClO <sub>4</sub> ) <sub>2</sub> ·2(4,4'-bipy) .....	39
Introduction.....	39
Experimental Section.....	41
Materials .....	41
Synthesis of [Ni(4,4'-bipy) <sub>3</sub> (H <sub>2</sub> O) <sub>2</sub> ](ClO <sub>4</sub> ) <sub>2</sub> ·1.4(4,4'-bipy)·3(H <sub>2</sub> O) .....	42
Synthesis of [Co(4,4'-bipy) <sub>3</sub> (H <sub>2</sub> O) <sub>2</sub> ](ClO <sub>4</sub> ) <sub>2</sub> ·1.4(4,4'-bipy)·3(H <sub>2</sub> O) .....	42
Synthesis of [Cu(4,4'-bipy) <sub>3</sub> (DMSO) <sub>2</sub> ](ClO <sub>4</sub> ) <sub>2</sub> ·2(4,4'-bipy).....	42
X-Ray Structure Determination .....	43

Thermal Analysis .....	44
Magnetic Measurements .....	45
Results and Discussion .....	46
Compound Synthesis .....	46
Description of the Structures .....	47
Structure of $[\text{Ni}(4,4'\text{-bipy})_3(\text{H}_2\text{O})_2](\text{ClO}_4)_2 \cdot 1.4(4,4'\text{-bipy}) \cdot 3(\text{H}_2\text{O})$ .....	47
Structure of $[\text{Co}(4,4'\text{-bipy})_3(\text{H}_2\text{O})_2](\text{ClO}_4)_2 \cdot 1.4(4,4'\text{-bipy}) \cdot 3(\text{H}_2\text{O})$ .....	53
Structure of $[\text{Cu}(4,4'\text{-bipy})_3(\text{DMSO})_2](\text{ClO}_4)_2 \cdot 2(4,4'\text{-bipy})$ .....	59
Thermal Properties .....	63
Magnetic Properties .....	72
Magnetic properties of $[\text{Ni}(4,4'\text{-bipy})_3(\text{H}_2\text{O})_2](\text{ClO}_4)_2 \cdot 1.4(4,4'\text{-bipy}) \cdot 3(\text{H}_2\text{O})$ ....	72
Magnetic properties of $[\text{Co}(4,4'\text{-bipy})_3(\text{H}_2\text{O})_2](\text{ClO}_4)_2 \cdot 1.4(4,4'\text{-bipy}) \cdot 3(\text{H}_2\text{O})$ ....	77
Magnetic properties of $[\text{Cu}(4,4'\text{-bipy})_3(\text{DMSO})_2](\text{ClO}_4)_2 \cdot 2(4,4'\text{-bipy})$ .....	79
Conclusions .....	82
3 A $^{31}\text{P}$ MAS NMR INVESTIGATION OF THE HOST-GUEST PROPERTIES OF TWO POROUS NETWORK SOLIDS, $[\text{Ni}(4,4'\text{-bipy})_3(\text{H}_2\text{O})_2](\text{ClO}_4)_2 \cdot 1.4(4,4'\text{-bipy}) \cdot 3(\text{H}_2\text{O})$ and $[\text{Co}(4,4'\text{-bipy})_3(\text{H}_2\text{O})_2](\text{ClO}_4)_2 \cdot 1.4(4,4'\text{-bipy}) \cdot 3(\text{H}_2\text{O})$ .....	83
Introduction .....	83
NMR Spectroscopy .....	84
Experimental Section .....	90
Materials .....	90
Sample Preparation .....	90
Gas Chromatography Analysis .....	91
NMR Spectroscopy .....	92
Powder X-Ray Diffraction .....	92
Results and Discussion .....	92
Sample Preparation .....	92
Guest Loss from Network Solids .....	93
Guest Exchange Investigations of Compound 1 Involving TMPO .....	94
Gas chromatography results .....	94
NMR results .....	96
X-Ray results .....	101
Guest Exchange in Compound 1 Involving Variable Quantities of TMPO .....	106
Gas chromatography results .....	106
NMR results .....	107
X-Ray results .....	110
Guest Exchange Investigations of Compound 1 Involving TEPO and TPPO .....	113
Gas chromatography results .....	113
NMR results .....	115
X-Ray results .....	117
Guest Exchange in Compound 2 Involving TMPO, TEPO, and TPPO .....	120
Gas chromatography results .....	120
NMR results .....	120

X-Ray results .....	123
Conclusions.....	126
<b>4 STRUCTURAL AND MAGNETIC CHARACTERIZATION OF A SERIES OF AZIDO-BRIDGED COPPER(II) COORDINATION POLYMERS.....</b>	<b>127</b>
Introduction.....	127
Azide Bridging Modes.....	127
Superexchange Properties of Azide Bridges.....	129
Experimental Section.....	137
Materials .....	137
Synthesis of $[\text{Cu}_2(\text{PhPyPy})_2-\mu-(\text{N}_3)_2(\text{N}_3)_2]$ .....	137
Synthesis of $[\text{Cu}_2(\text{terpy})_2-\mu-(\text{N}_3)_4][\text{Cu}_2-\mu-(\text{N}_3)_2(\text{N}_3)_2]$ .....	137
Synthesis of $[\text{Cu}_2(\text{terpy})_2-\mu-(\text{N}_3)_2(\text{N}_3)_2][\text{Cu}_3-\mu-(\text{N}_3)_4(\text{N}_3)_2]$ .....	138
Physical Characterization.....	138
X-Ray Structure Determination .....	138
Magnetic Measurements .....	139
Results and Discussion .....	140
Description of the Structures .....	140
Structure of $[\text{Cu}_2(\text{PhPyPy})_2-\mu-(\text{N}_3)_2(\text{N}_3)_2]$ .....	141
Structure of $[\text{Cu}_2(\text{terpy})_2-\mu-(\text{N}_3)_4][\text{Cu}_2-\mu-(\text{N}_3)_2(\text{N}_3)_2]$ .....	144
Structure of $[\text{Cu}_2(\text{terpy})_2-\mu-(\text{N}_3)_2(\text{N}_3)_2][\text{Cu}_3-\mu-(\text{N}_3)_4(\text{N}_3)_2]$ .....	149
Electron Paramagnetic Resonance .....	158
Magnetic Properties of $[\text{Cu}_2(\text{PhPyPy})_2-\mu-(\text{N}_3)_2(\text{N}_3)_2]$ .....	159
Magnetic data.....	159
Magnetic model and fits.....	161
Interpretation of the magnetic data .....	167
Rationalizing the sign and magnitude of the coupling constants.....	168
Magnetic Properties of $[\text{Cu}_2(\text{terpy})_2-\mu-(\text{N}_3)_4][\text{Cu}_2-\mu-(\text{N}_3)_2(\text{N}_3)_2]$ .....	169
Magnetic data.....	169
Magnetic model and fits.....	171
Interpretation of the magnetic data .....	180
Rationalizing the sign and magnitude of the coupling constants.....	181
Magnetic Properties of $[\text{Cu}_2(\text{terpy})_2-\mu-(\text{N}_3)_2(\text{N}_3)_2][\text{Cu}_3-\mu-(\text{N}_3)_4(\text{N}_3)_2]$ .....	186
Magnetic data.....	186
Magnetic model and fits.....	190
Interpretation of the magnetic data .....	193
Rationalizing the sign and magnitude of the coupling constants.....	194
Conclusions.....	198
<b>5 CONCLUSIONS.....</b>	<b>199</b>

APPENDIX

A CRYSTAL STRUCTURES OF SELECTED LOW-DIMENSIONAL SOLIDS.....	202
B ATOMIC COORDINATES AND BOND ANGLES AND DISTANCES .....	223
LIST OF REFERENCES.....	254
BIOGRAPHICAL SKETCH.....	269

Abstract of Dissertation Presented to the Graduate School  
of the University of Florida in Partial Fulfillment of the  
Requirements for the Degree of Doctor of Philosophy

CHEMICAL AND PHYSICAL CHARACTERIZATION OF HYBRID  
ORGANIC-INORGANIC LOW-DIMENSIONAL COORDINATION POLYMERS

By

Jonathan David Woodward

May 2003

Chair: Daniel R. Talham  
Department: Chemistry

This dissertation presents experimental results from the synthesis and structural, chemical, and physical characterization of representative low-dimensional coordination polymers. The structural, thermal, and magnetic properties of a series of clathrated porous network solids,  $[\text{Ni}(4,4'\text{-bipy})_3(\text{H}_2\text{O})_2](\text{ClO}_4)_2 \cdot 1.4(4,4'\text{-bipy}) \cdot 3(\text{H}_2\text{O})$ , **1**,  $[\text{Co}(4,4'\text{-bipy})_3(\text{H}_2\text{O})_2](\text{ClO}_4)_2 \cdot 1.4(4,4'\text{-bipy}) \cdot 3(\text{H}_2\text{O})$ , **2**, and  $[\text{Cu}(4,4'\text{-bipy})_3(\text{DMSO})_2](\text{ClO}_4)_2 \cdot 2(4,4'\text{-bipy})$  **3**, are described first. These materials consist of chains of transition metal ions (Ni(II), Co(II), and Cu(II)) bridged by 4,4'-bipyridine spacer ligands. The chains pack to form two-dimensional, non-interpenetrated sheets with hydrophobic, rectangular cavities within the framework. The sheets, in turn, pack to form three-dimensional structures with oblique channels containing enclathrated guest molecules and counterions extending throughout the solid. These enclathrated guests molecules are easily lost, suggesting that the samples are

thermally unstable. The magnetic properties of **1**, **2**, and **3** are similar in the sense that only very weak exchange interactions are present between the metal centers.

The host-guest properties of **1** and **2** were investigated. Gas chromatography experiments determined that both hosts exchange clathrated bipy molecules with trialkylphosphine oxide probe molecules, TMPO, TEPO, and TPPO. While the uptake of TMPO by both **1** and **2** is essentially complete, steric constraints are believed to limit the uptake of TEPO and TPPO by the host. The trialkylphosphine oxides interact with acid sites within the host as determined by  $^{31}\text{P}$  MAS NMR spectroscopy. TMPO interacts with both coordinated water molecules (strong acid sites) and lattice waters (weak acid sites) in compound **1** and coordinates directly to the metal centers in compound **2**. However, TEPO and TPPO seem to attack only the weaker acid sites within the hosts. X-ray diffraction patterns show that the loss of bipy and uptake of the probe causes significant structural rearrangements in **1** and only mild structural changes in **2**. However, the nature of these guest-exchanged products is unknown. These experiments showed that solid-state NMR spectroscopy can be used to investigate host-guest interactions.

Finally, the structural and magnetic properties of three azido-bridged copper(II) ladder-like coordination polymers,  $[\text{Cu}_2(\text{PhPyPy})_2-\mu-(\text{N}_3)_2(\text{N}_3)_2]$ , **4**,  $[\text{Cu}_2(\text{terpy})_2-\mu-(\text{N}_3)_4\text{Cu}_2-\mu-(\text{N}_3)_2(\text{N}_3)_2]$ , **5**, and  $[\text{Cu}_2(\text{terpy})_2-\mu-(\text{N}_3)_2(\text{N}_3)_2\text{Cu}_3-\mu-(\text{N}_3)_4(\text{N}_3)_2]$ , **6**, are discussed. Compound **4** structurally resembles ladder-like chains of weakly interacting end-on azido bridged copper(II) dimers. Magnetically, compound **4** consists of antiferromagnetic chains of ferromagnetically coupled  $S = \frac{1}{2}$  dimers. Compound **5** consists of ladder-like copper(II)

coordination polymers with double and single end-on azido bridges. Magnetically, compound **5** consists of ladder-like stacks of weakly interacting tetramers with a dominant and unusual antiferromagnetic exchange mediated through end-on azido bridges. Compound **6** structurally resembles ladder-like chains of weakly interacting copper(II) pentamers featuring both single and double end-on azide bridges. Magnetically, compound **6** consists of antiferromagnetic stacks of pentamers with two paramagnetic  $S = \frac{1}{2}$  sites and ferromagnetically coupled trimers.

## CHAPTER 1 INTRODUCTION

The original goal of the graduate research pertaining to this thesis focused on the design, self-assembly, and physical characterization of molecular coordination polymer ladder systems. This project was only partially successful; several new ladder-like materials were isolated as a result of serendipity rather than rational design and did not incorporate the desired structural and physical properties. However, in addition to the ladder-like structures mentioned above, several new low-dimensional materials were obtained from the course of this graduate research. The work presented in this dissertation is concerned primarily with investigating the structural, chemical, and physical properties of selected examples of these low-dimensional materials.

This chapter briefly provides the background information necessary to the research detailed in the following chapters. A basic concepts of molecular magnetism as applied to low-dimensional materials is introduced first. Included are discussions concerning the magnetic properties of both paramagnetic and exchanged coupled systems, including discrete oligomers and extended chains and ladders, and the theories that model the magnetic behavior of such materials. A general introduction to the field of supramolecular chemistry is then provided. Discussed are general strategies for building supramolecular architectures, particularly via the self-assembly of simple molecular and ionic components, general structural types of the resulting assemblies commonly encountered, and practical applications of such materials.

## Low-Dimensional Materials

The study of low-dimensional materials has been a rapidly expanding area of solid-state chemistry. Low-dimensional materials have structural and physical properties that are anisotropic in one or two dimensions.<sup>1-3</sup> These materials are often referred to as “quasi” low-dimensional systems since, despite being part of a three-dimensional solid, characteristic structural and physical properties exist principally within one or two dimensions. One-dimensional chains and two-dimensional sheets (Figure 1-1) are the most commonly encountered types of low-dimensional materials. The key structural features of low-dimensional materials are strong electrostatic or covalent bonds along chains or within sheets with weak, Van der Waals interactions between the chains or sheets. As a result of this anisotropic bonding, electronic, magnetic, and transport properties exist along chains or within sheets, or are enhanced compared to higher dimensional analogs, but are small or negligible between the chains or sheets.<sup>4</sup>

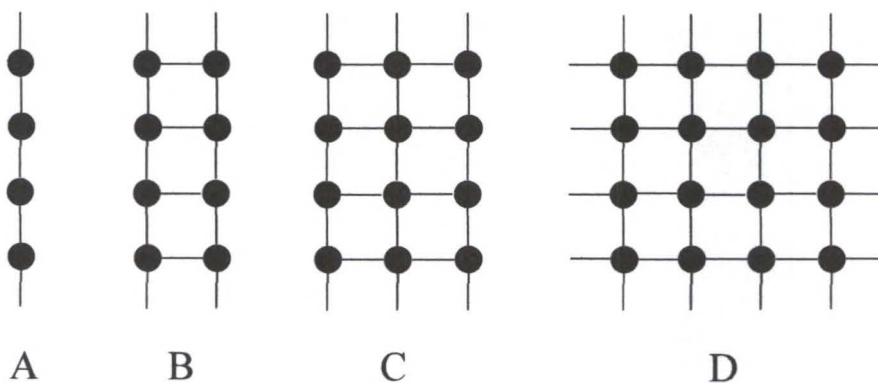


Figure 1-1. Examples of low-dimensional materials. A) One-dimensional chain. B) Two-leg ladder. C) Three-leg ladder. D) Two-dimensional sheet.

## Introduction to Molecular Magnetism

### Diamagnetism and Paramagnetism

When a material is subjected to an external, homogeneous field,  $H$ , a magnetization,  $M$ , is induced within the sample.<sup>5,6</sup> The quantities  $M$  and  $H$ , are related by

$$\chi = \frac{\partial M}{\partial H} \quad (1-1)$$

where  $\chi$  is the magnetic susceptibility. The susceptibility quantitatively measures the response of a material to an applied magnetic field. If the magnitude of the field is small, then to a good approximation, the magnetization is a linear function of the field, and the susceptibility can be expressed as

$$\chi = \frac{M}{H} . \quad (1-2)$$

The total susceptibility,  $\chi_T$ , is the sum of two components, a diamagnetic contribution,  $\chi_{dia}$ , and a paramagnetic term,  $\chi_{para}$

$$\chi_T = \chi_{para} + \chi_{dia} . \quad (1-3)$$

Diamagnetism is a property of all matter originating from the interaction of paired electrons with an applied magnetic field; since all materials have paired spins, all materials have diamagnetic contributions to the total susceptibility. When a diamagnetic material is placed within an external field, it is repelled since the sample produces a flux opposed to the applied field and moves toward regions of lower field strength.<sup>5</sup> Diamagnetic susceptibilities are typically small and negative (on the order of  $-10^{-6}$  emu mol<sup>-1</sup> to  $-10^{-4}$  emu mol<sup>-1</sup>) and are independent of field strength and temperature.<sup>5</sup>

Paramagnetism, on the other hand, is a property exhibited only by materials with unpaired electrons, such as transition metal complexes, rare earth compounds, and organic free radicals. When a paramagnetic material is placed within an external field, it is attracted to the field because of the interaction of the unpaired spins with the applied field and thus moves toward regions of higher field strength.<sup>5</sup> In general, low fields and high temperatures will tend to randomize the directions of these spins, resulting in small or zero net magnetic moments. Low temperatures and high fields, however, will align the spins with the field, resulting in a net moment. Paramagnetic susceptibilities are typically positive and much larger in magnitude than the corresponding diamagnetic susceptibilities, often in the order of  $10^4$  to  $10^2$  emu mol<sup>-1</sup> or more.<sup>5</sup> Diamagnetic susceptibilities can be estimated from Pascal's constants and subtracted from the total susceptibility (or ignored, if small compared to the paramagnetic contribution) to obtain the paramagnetic susceptibility.<sup>5,6</sup> Unlike diamagnetic susceptibilities, paramagnetic susceptibilities exhibit temperature dependence, often in very complex manners.

### Basic Relationships

In classical physics, the magnetization,  $M$ , of a sample results from a variation of its energy,  $E$ , in response to an applied magnetic field,  $B$ , through

$$M = -\frac{\partial E}{\partial B} \quad (1-4)$$

and

$$B = \mu H \quad (1-5)$$

where  $B$  is the magnetic induction field and  $\mu$  is the permeability.<sup>5,6</sup> When  $\mu > 1$ , the sample is paramagnetic and when  $\mu < 1$  the sample is diamagnetic. Similarly, in quantum

mechanics, a microscopic magnetization,  $\mu_n$ , of an energy level,  $E_n$ , in the presence of an external field is

$$\mu_n = -\frac{\partial E_n}{\partial B} \quad (1-6)$$

where  $n = 1, 2, 3$ , and so on. The macroscopic magnetization is then a weighted sum of all microscopic magnetizations in the sample, given by the Boltzmann distribution law

$$M = \frac{N_A \sum_n \left(-\frac{\partial E_n}{\partial B}\right) \exp\left(\frac{-E_n}{k_B T}\right)}{\sum_n \exp\left(\frac{-E_n}{k_B T}\right)} \quad (1-7)$$

where  $N_A$  is Avogadro's number and  $k_B$  is the Boltzmann constant and the denominator is the partition function,  $Z$ . The magnetic susceptibility is the variation of the magnetization with the external field

$$\chi = \mu_0 \left(\frac{\partial M}{\partial B}\right) \quad (1-8)$$

where  $\mu_0$  is the permeability of free space. At the limits of high temperature and low field, Equations 1-7 and 1-8 can be simplified to give new relations that are no longer functions of the derivatives  $\partial E_n/\partial B$ . Expanding the energy levels,  $E_n$ , in a power series of  $B$ , gives

$$E_n = E_n^{(0)} + E_n^{(1)} B + E_n^{(2)} B^2 + \dots \quad (1-9)$$

where  $E_n^{(i)}$  terms are the Zeeman coefficients.<sup>7a</sup> Retaining only linear terms, substituting back into Equation 1-8, and simplifying under the assumption that at zero field, the magnetization is zero, the susceptibility vs. temperature is

$$\chi = \frac{N \sum_n \left( \frac{E_n^{(1)2}}{k_B T} - 2E_n^{(2)} \right) \exp\left(\frac{-E_n^{(0)}}{k_B T}\right)}{\sum_n \exp\left(\frac{-E_n^{(0)}}{k_B T}\right)} \quad (1-10)$$

Equation 1-10 is the Van Vleck susceptibility.

### Non-Interacting Spin Systems and the Curie Law

The simplest type of paramagnetism is that of an ideal paramagnet, a system composed of non-interacting, randomly orientated spin centers (Figure 1-4A) 7b. In an ideal paramagnet, the magnetic susceptibility is inversely proportional to temperature. The Curie law is a simple relation that describes the variation of the susceptibility with absolute temperature for an ideal paramagnet and is given by

$$\chi = \frac{C}{T} \quad (1-11)$$

where  $C$  is the Curie constant given by

$$C = \frac{N_A g^2 \mu_B^2 S(S+1)}{3k_B} \quad (1-12)$$

and  $N_A$  is Avogadro's number,  $g$  is the  $g$ -Landé value,  $\mu_B$  is the Bohr Magneton, and  $S$  is the total spin of the system. A plot of the susceptibility versus temperature for a paramagnetic material that follows the Curie Law is a simple hyperbola. Other mathematical manipulations of the Curie law are useful as well. A plot of the inverse susceptibility versus temperature for a paramagnet is a straight line where the slope is the Curie constant and the  $x$ -intercept is zero

$$\chi^{-1} = \frac{T}{C} \quad (1-13)$$

while a plot of the product of susceptibility and temperature vs. temperature is a horizontal line

$$\chi T = C \quad (1-14)$$

Plots of the  $\chi$ ,  $\chi^{-1}$ , and  $\chi T$  vs.  $T$  for an arbitrary  $S = \frac{1}{2}$  material that obeys the Curie law, with  $g = 2.10$ , are shown in Figure 1-2.

### **Interacting Spin Systems and the Curie-Weiss Law**

In many paramagnetic materials, the unpaired electrons on the spin centers can interact with one another and the magnetic behavior is no longer ideal. The Curie-Weiss law, a semi-empirical modification to the Curie law, is a “first approximation” to model the magnetic behavior of materials with weak interactions between the spin centers, and is given by

$$\chi = \frac{C}{(T - \theta)} \quad (1-15)$$

In general, the interactions between the spins that cause these deviations are referred to as ferromagnetic and antiferromagnetic correlations. In the Curie-Weiss law, these interactions are described by  $\theta$ , the Weiss constant. When  $\theta > 0$ , the interactions are ferromagnetic, when  $\theta < 0$ , the interactions are antiferromagnetic, and when  $\theta = 0$ , the sample is paramagnetic. The Curie-Weiss law is valid for materials that undergo long-range order above the ordering temperature (i.e.  $T \gg T_c$ ). Plots of the  $\chi$ ,  $\chi^{-1}$ , and  $\chi T$  vs.  $T$  for antiferromagnetically ( $\theta = -15$  K) and ferromagnetically ( $\theta = 15$  K) coupled,  $S = \frac{1}{2}$  materials ( $g = 2.10$ ) that obey the Curie-Weiss law are shown in Figure 1-2. Note that when  $\theta > 0$ , the inverse susceptibility has a positive  $y$ -intercept and  $\chi T$  increases as  $T$  decreases. When  $\theta < 0$ , the  $y$ -intercept is negative and the  $\chi T$  product decreases when  $T$

decreases. The Curie-Weiss law is only a simple, general, empirical correction for describing deviations from ideal paramagnetism by accounting for the interactions of unpaired spins for magnetic materials especially when the structure is unknown. More

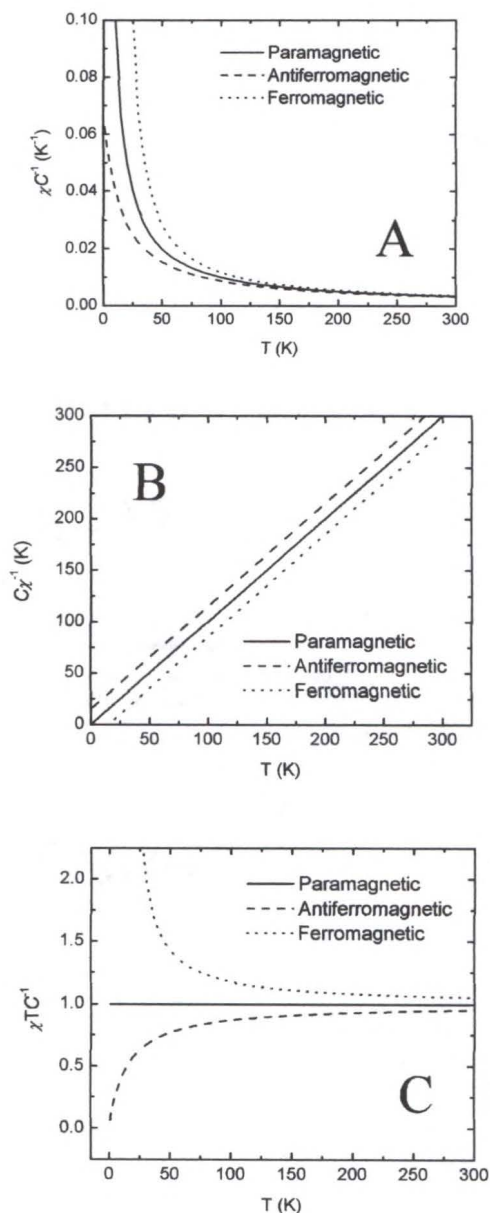


Figure 1-2. Common Curie (solid line) and Curie-Weiss (broken lines) law plots for an  $S = \frac{1}{2}$  magnetic material ( $g = 2.10$ ). A)  $\chi / C$  vs.  $T$ . B)  $C / \chi$  vs.  $T$ . C)  $\chi T / C$  vs.  $T$ . The dotted lines represent ferromagnetic coupling ( $\theta = 15$  K) and the dashed lines represent antiferromagnetic coupling ( $\theta = -15$  K). The susceptibility is normalized by division by the Curie constant,  $C$ .

complex magnetic systems, such as dimers and chains, require more complicated models to describe magnetic behavior.

### **Magnetic Exchange**

Magnetic exchange interactions are quantum effects that describe the interactions among unpaired spins in magnetic materials. Exchange interactions originate from a combination of the Pauli exclusion principle and electronic repulsions.<sup>8</sup> Two principal types of exchange can be distinguished: direct exchange and indirect exchange.<sup>9</sup> Direct exchange interactions result from the through-space overlap of spin orbitals, as in direct metal to metal bonding (Figure 1-3). These interactions are typically weak since electronic repulsive forces are large due to the close proximity of the unpaired electrons to one another.<sup>10</sup> For indirect exchange, the unpaired spins are coupled via nonmagnetic intermediaries, such as bridging diamagnetic atoms or molecules or itinerant electrons of conducting solids. The first case is referred to as a superexchange interaction (Figure 1-3) and the second case is referred to as RKKY exchange. Superexchange interactions are electronic (and not magnetic) interactions and are usually much larger in magnitude than the corresponding direct exchange, because intermediary groups increase the distance between metal centers, thus reducing electronic repulsions.<sup>10</sup> Pairwise exchange interactions can be expressed mathematically by a spin-Hamiltonian equation:

$$\hat{H} = -2 \sum_{i>j} J_{ij} \hat{S}_i \cdot \hat{S}_j \quad (1-16)$$

where the sum is taken over all nearest neighbor interactions between spins,  $\mathbf{S}_i$  and  $\mathbf{S}_j$ , with the magnitude of those interactions given by  $J$ , the coupling constant.<sup>5</sup> If  $J > 0$  and the unpaired electrons interact such that the spins align in a parallel fashion, the exchange

is referred to as ferromagnetic and the magnetic ground state is triplet (Figure 1-4B)<sup>7b</sup>. If  $J < 0$ , the unpaired spins align in an antiparallel manner, the exchange is referred to as antiferromagnetic and the magnetic ground state is singlet (Figure 1-4C)<sup>7b</sup>. The sign and magnitude of the coupling constant can depend on many factors, such as the number of unpaired electrons exchanged, structural parameters of the magnetic entity, orbital overlap of the spin centers and nonmagnetic intermediary, and electronic properties of the intermediary.

Other arrangements of unpaired spins within a system are also possible. Ferrimagnetism occurs in systems incorporating two alternating effective spins (Figure 1-4d)<sup>7b</sup>. For example, in a chain containing alternating  $S = \frac{1}{2}$  and  $S = 1$  spin centers, the unpaired electrons align antiparallel. However, because the effective spin values are different, the moments do not cancel each other out completely, resulting in a net magnetization.<sup>9</sup> In a canted antiferromagnetic system (Figure 1-4e)<sup>7b</sup>, the magnetic moment vectors of nearest neighbors are tilted. A small, but finite, magnetization results because the moments are not fully antiparallel and cancel each other out.<sup>9</sup>

A distinction should be made between magnetic exchange and magnetic ordering. Magnetic exchange describes short-range correlations (the local interactions between unpaired electrons). On the other hand, in a transition to long-range magnetic order, the unpaired spins over a relatively large domain in a magnetic material will spontaneously align in the absence of an externally applied field at some critical temperature.<sup>9</sup> Alignment of the spins can be parallel or antiparallel corresponding to ferromagnetic or antiferromagnetic ordering, respectively. The critical temperature for ferromagnetic ordering is the Curie temperature,  $T_C$ , and for antiferromagnetic ordering, the Neel

temperature,  $T_N$ .<sup>5,11</sup> The size of this domain is the magnetic correlation length,  $\xi$ , the distance over which unpaired spins are ordered; the divergence of  $\xi$  at a critical temperature is necessary for long-range ordering to occur in a magnetic material.<sup>2,11</sup> In an ordered ferromagnetic state, the unpaired spins align in a parallel manner and a net magnetization results (Figure 1-5). In an antiferromagnetically ordered state, the unpaired spins align in an antiparallel fashion and no net magnetization results (Figure 1-5).

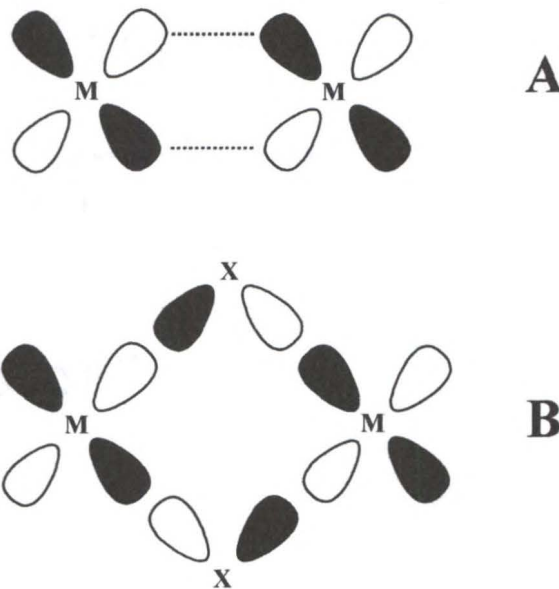


Figure 1-3. Magnetic exchange pathways. A) The transition metal (M) magnetic orbitals involved in through-space, or direct exchange. B) A superexchange pathway, mediated by a nonmagnetic ligand (X).

### Anisotropy

Before providing a brief discussion of anisotropy, the concepts of lattice and spin dimensionality must be described (Figure 1-6). Lattice dimensionality ( $d$ ) refers to the

geometrical distribution of the spins in space.<sup>9a</sup> When  $d = 0$ , the system consists of discrete, zero-dimensional (0-D) oligomers or clusters. When  $d = 1$ , the system consists

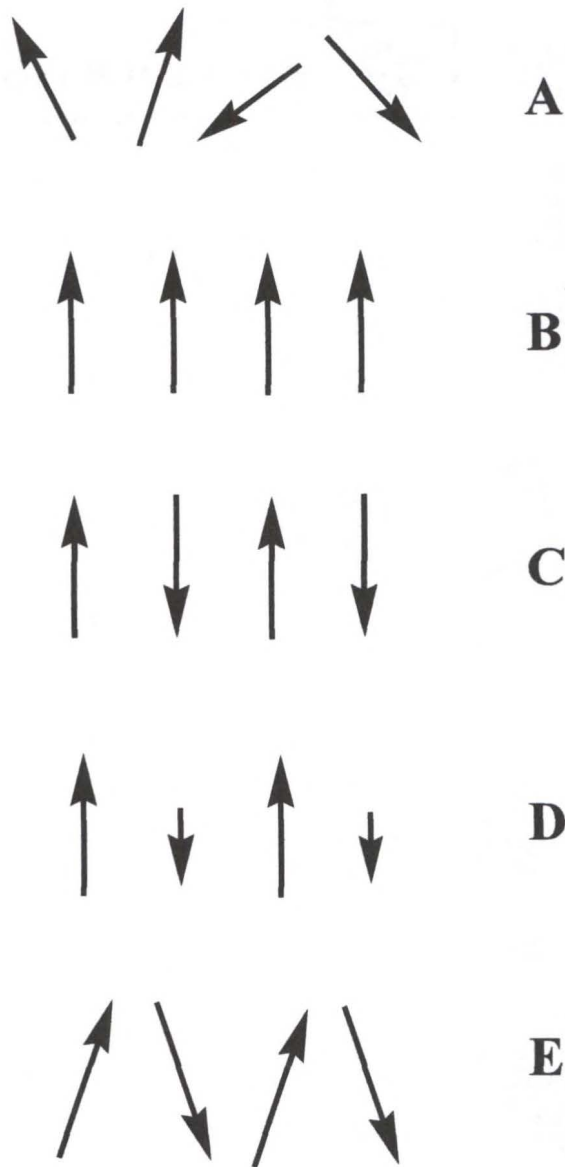


Figure 1-4. The spin angular momentum vectors representing various interactions between unpaired electrons. A) Paramagnetic. B) Ferromagnetic. C) Antiferromagnetic. D) Ferrimagnetic. E) Canted antiferromagnetic. Adapted from reference 7b.

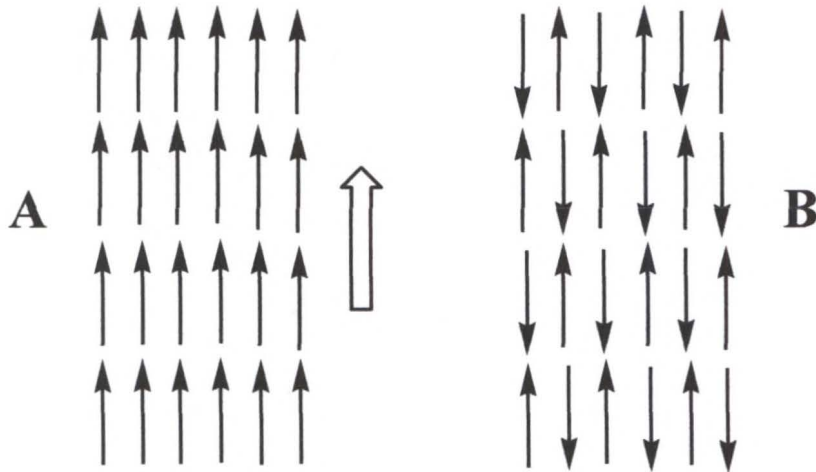


Figure 1-5. The spin angular momentum vectors in ordered magnetic states. A) Ferromagnetic ordering. B) Antiferromagnetic ordering. Note the ordered ferromagnetic state will have a net magnetic moment in the direction indicated by the hollow arrow while the ordered antiferromagnetic state will possess no resultant moment.

of one-dimensional (1-D) infinite chains and when  $d = 2$ , the system consists of infinite, two-dimensional (2-D) sheets. The spin dimensionality,  $n$ , refers to the contributions by the vector components of the spin angular momentum. When  $n = 1$ , the spin has only one component,  $S_z$ , and the system is Ising. When  $n = 2$ , the spin has two components,  $S_x$  and  $S_y$ , and the system is Planar. When  $n = 3$ , the spin has three components,  $S_z$ ,  $S_x$ , and  $S_y$ , and the system is Heisenberg.<sup>2,9</sup>

The concepts of spin and lattice dimensionality are especially important in determining whether a magnetic material can undergo long-range order.<sup>2,12-14</sup> The magnetic ordering phenomenon can be understood by considering that the transition from short-range to long-range order in these systems is accompanied by a crossover in the effective lattice dimensionality or the effective spin dimensionality of the system.<sup>9</sup> For example, although no long-range order for a 2-D Heisenberg system is predicted,<sup>15</sup> there

are numerous examples of such systems that in fact undergo such a transition.<sup>2</sup> This discrepancy can be explained through a crossover in the lattice dimensionality. The ordering occurs as a transition from a two-dimensional to three-dimensional lattice because, at the critical temperature, the interplanar couplings become important.<sup>9</sup>

Magnetic exchange interactions are often not isotropic in all three lattice and/or spin dimensions. For highly anisotropic magnetic materials, the predicted magnetic behavior will no longer be Heisenberg, but may resemble (for example) Ising and Planar behavior instead.<sup>9</sup> A more general spin-Hamiltonian equation that accounts for exchange anisotropy is

$$\hat{H} = -\sum_{i>j} (J_x \hat{S}_{ix} \cdot \hat{S}_{jx} + J_y \hat{S}_{iy} \cdot \hat{S}_{jy} + J_z \hat{S}_{iz} \cdot \hat{S}_{jz}) \quad (1-17)$$

When  $J_x = J_y = J_z$ , equation represents the isotropic Heisenberg model. If the components of  $J$  are different, then the exchange is anisotropic. For example, when the exchange is principally characterized by in-plane components,  $J_x = J_y$ , and  $J_z = 0$ , the Hamiltonian is referred to as the XY model, but if  $J_x \neq J_y \neq J_z$ , equation is referred to as the XYZ model.<sup>2,16</sup> Table 1-1<sup>9a,9b</sup> summarizes a few spin-Hamiltonian models for various cases of differing spin anisotropy and spin dimensionality.<sup>9</sup> Note the subtle distinction between the Z model and the Ising model.<sup>9</sup> For the Z model,  $n = 3$  and  $J_x = J_y = 0$  but  $S_x \neq 0$  and  $S_y \neq 0$  meaning that, although no exchange interaction occurs between nearest neighbor spins in the  $x$ - and  $y$ -directions, only in the  $z$ -direction, the total spin angular momentum still has  $x$ ,  $y$ , and  $z$  components. In contrast, the Ising model,  $n = 1$  and  $J_x = J_y = 0$  and  $S_x = S_y = 0$  meaning that, there is no exchange interaction in the  $x$ - and  $y$ -

directions, only in the z-direction, and the spin angular momentum only has a z component.

Table 1-1. Summary of Some Spin-Hamiltonian Models for Various Cases of Spin Anisotropy and Spin Dimensionality

Spin-Dimensionality	Interaction	Model
$n = 3$	$J_x = J_y = J_z$	Heisenberg
$S_x^2 = S_y^2 = S_z^2$	$J_x = J_y ; J_z = 0$	XY
	$J_x = J_y = 0 ; J_z$	Z
$n = 2$	$J_x = J_y$	Planar
$S_x^2 = S_y^2$	$J_x = 0 ; J_y$	Planar Ising
$n = 1$	$J_z$	Ising
$S_z^2$		

Adapted from references 9a and 9b.

Anisotropy in the exchange interaction often result from zero-field splitting or spin-orbit coupling effects.<sup>6</sup> In each of these cases, the anisotropy is represented by additional terms in the Hamiltonian such as

$$\hat{H}_{ZFS} = D \left[ \hat{S}_z^2 - \frac{S(S+1)}{3} \right] + E(\hat{S}_x^2 - \hat{S}_y^2) \quad (1-18)$$

$$\hat{H}_{SO} = \sum_i \lambda_i \hat{L}_i \cdot \hat{S} \quad (1-19)$$

Equation 1-18 represents the effect of zero-field splitting, where  $D$  is the axial or single-ion anisotropy factor and  $E$  is the rhombic or in-plane anisotropic component.

Equation 1-19 is the spin-orbit coupling Hamiltonian where  $\lambda_i$  is the spin-orbit coupling parameter and  $L$  and  $S$  are the orbital and spin angular momentum operators,

respectively. Spin-orbit coupling arises from the coupling of a  $^{2S+1}\Gamma$  ground state with an excited state from the same magnetic center.<sup>6</sup> The excited states are well separated in energy from the ground state and are not appreciably populated at room temperature.

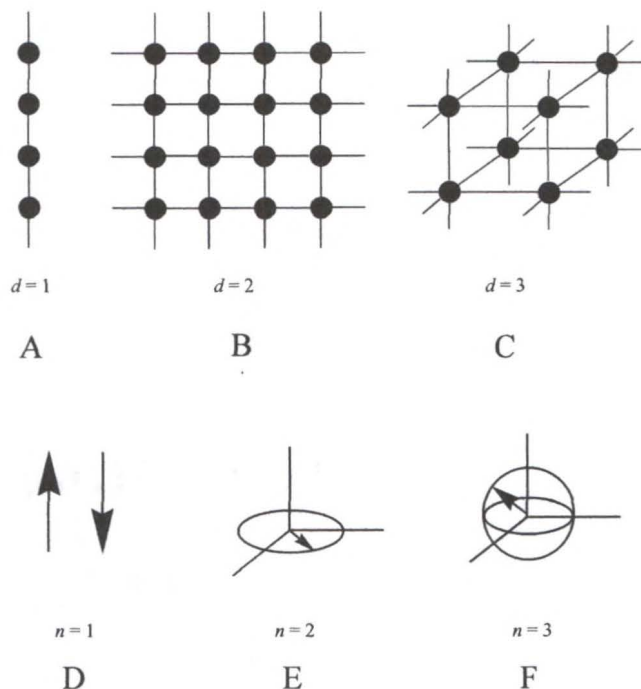


Figure 1-6. Lattice dimensionality and spin dimensionality. A) A one-dimensional chain has  $d=1$ . B) A two-dimensional sheet has  $d=2$ . C) A three-dimensional lattice has  $d=3$ . D) An Ising system has  $n=1$ . E) A Planar system has  $n=2$ . F) Heisenberg system has  $n=3$ .

Spin-orbit coupling can lead to  $g$ -factor anisotropy or zero-field splitting effects. Zero-field splitting describes the splitting of the Zeeman components in the absence of an external field due to the coupling of an  $S > \frac{1}{2}$  ground state with excited states.<sup>6</sup> Magnetic anisotropy can arise from other sources as well, such as higher-order exchange interactions, orbital angular momentum contributions, and low-symmetry ligand fields or magnetic dipolar fields that couple the moments to certain directions of a crystal.<sup>9</sup> However, the assignment of the origins of the anisotropy in the magnetic interactions is often difficult.

### Dimers

A dimer, denoted by a lattice dimensionality of  $d=0$ , represents the simplest type of interacting magnetic system. In a dimer, two spin centers can interact directly through

space or indirectly via intermediary superexchange ligands. Only the second case is considered here. In general, no long range ordering is possible for dimers and other  $d = 0$  oligomers and clusters (unless a crossover in lattice dimensionality occurs) and thus the magnetic interactions are only short-range correlations between the spin centers.

Figure 1-7 shows the structure of an  $S = \frac{1}{2}$  dimer, a dinuclear copper(II) moiety bridged by two diamagnetic ligands (X) capable of mediating a superexchange interaction between the two spin centers. Ancillary ligands (L) fill the remaining coordination sites on the metal ions.

If the unpaired electrons interact with one another, then individual spin quantum numbers for each metal center,  $S_A = S_B = \frac{1}{2}$ , are no longer valid.<sup>6</sup> The spin states of the

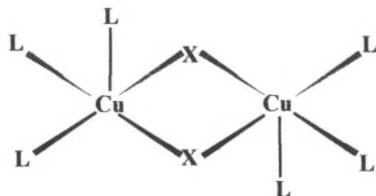


Figure 1-7. A square pyramidal copper(II) dinuclear complex where the metal centers are bridged by two diamagnetic ligands, X, and the remaining coordination sites are filled by ancillary ligands, L.

dimer are now  $S = 0$  and  $S = 1$ . In general, the energies of these spin states are not equal, but separated by an energy gap,  $J$ , defined as

$$J = E(S = 0) - E(S = 1). \quad (1-20)$$

The Hamiltonian for the isotropic exchange of a magnetic dimer is

$$\hat{H} = -2J\hat{\mathbf{S}}_A \cdot \hat{\mathbf{S}}_B + \mu_B \vec{\mathbf{B}} \cdot (g_A \hat{\mathbf{S}}_A + g_B \hat{\mathbf{S}}_B) \quad (1-21)$$

where  $\mathbf{S}_A$  and  $\mathbf{S}_B$  are the spin angular momentum operators representing the unpaired electrons on each metal center and  $J$  is called the isotropic exchange parameter that quantitatively accounts for the energy of the superexchange interaction. The second term is the Zeeman perturbation. Figure 1-8 shows the relation between the energy levels of the magnetic spin states as a function of applied field.<sup>6</sup> At zero field, the spin-Hamiltonian splits the two degenerate  $S = 1/2$  states into the  $S = 0$  and  $S = 1$  states. In the presence of a magnetic field, the Zeeman term further splits the energy level of the triplet removing all degeneracy but does not affect the singlet state. When  $J < 0$ , the  $S = 0$  singlet state is the magnetic ground state and the exchange is antiferromagnetic. In this case, the spins are coupled in an antiparallel fashion resulting in no net magnetic moment. When  $J > 0$ , the  $S = 1$  triplet state is the ground state and the exchange is ferromagnetic. In this case, the spins are coupled in a parallel fashion resulting in a net magnetic moment. The magnitude of the coupling constant is related to the difference in energy, or energy gap, between the ground and first excited state. From both the spin and Zeeman Hamiltonians, the resulting four energy levels for an  $S = 1/2$  dimer as a function of external field are  $E_1 = 0$ ,  $E_2 = J$ ,  $E_3 = J + \mu_B g B$ , and  $E_4 = J - \mu_B g B$ . The temperature dependence of the magnetic susceptibility, describing the changes in population of these magnetic energy levels, is given by

$$\chi_{Dimer} = \frac{2N_R N_A \mu_B^2 g^2}{3k_B T} \frac{\exp \frac{2J}{k_B T}}{1 + 3 \exp \frac{2J}{k_B T}} \quad (1-22)$$

A simulation of the  $\chi$  vs.  $T$  from Equation 1-22 for an  $S = 1/2$  dimer with  $g = 2.2$ ,  $J k_B^{-1} = -50$  K, and  $+50$  K is shown in Figure 1-9. Note that, when the exchange is antiferromagnetic, a maximum in the susceptibility is observed.

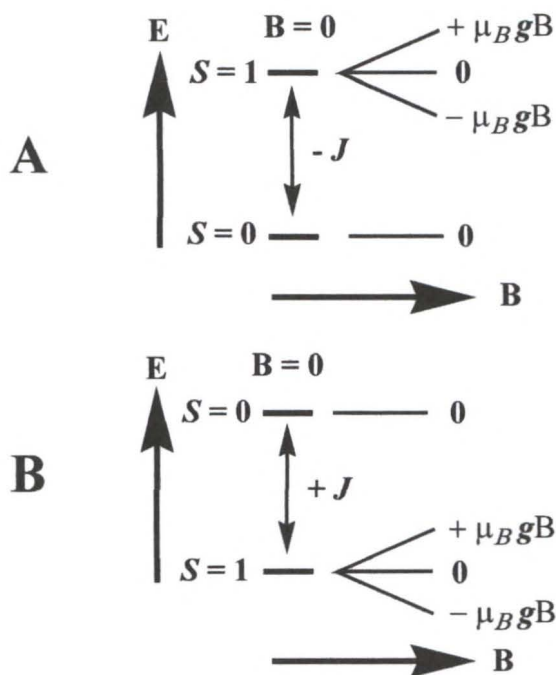


Figure 1-8. The splitting of the magnetic energy levels in an  $S = 1/2$  dimer. The zero-field spin states of the dimer correspond to the  $S = 0$  (singlet) and  $S = 1$  (triplet) states. An externally applied field splits only the triplet state. A) In an antiferromagnetically coupled dimer, the ground state is singlet. B) In a ferromagnetically coupled system the ground state is triplet. The coupling constant,  $J$ , is the energy gap between the ground state and the nearest excited state.

Dimers are among the most extensively studied magnetic systems.<sup>6</sup> In particular,  $\mu$ -dioxo bridged copper(II) dimers and  $\mu$ -diazido copper(II) dimers have received considerable attention.<sup>7,17-21</sup> The systems are convenient for the testing of theoretical models of magnetic systems. They also provide an understanding of how structural and electronic parameters affect the resulting magnetic properties. Finally, an understanding of the magnetostructural correlations for these simple systems provides a basis for continuing research efforts directed toward the design of novel magnetic materials with specifically tailored magnetic properties.

## Chains

Magnetic chain compounds are one-dimensional systems with a lattice dimensionality of  $d = 1$ . Uniformly spaced magnetically interacting spin centers represent the simplest class of chains. Since the spin centers are equivalent along the chain, the nearest neighbor exchange interactions between the spin centers are also equivalent. Examples of uniform chains include  $[\text{Cu}(\text{ox})] \cdot \frac{1}{3}\text{H}_2\text{O}$  (ox = oxalate),  $(\text{C}_6\text{H}_{11})\text{CuCl}_3$ ,<sup>22,23</sup> and  $[\text{Ni}(\text{en})_2(\text{NO}_2)](\text{ClO}_4)$  (en = ethylenediamine).<sup>24</sup> Figure 1-10 schematically represents an  $S = \frac{1}{2}$  uniform chain of Cu(II) ions.

The spin Hamiltonian representing the isotropic nearest neighbor superexchange between the metal centers over  $n$  sites is

$$\hat{H} = -J \sum_{i=1}^{n-1} \hat{\mathbf{S}}_{A_i} \cdot \hat{\mathbf{S}}_{A_{i+1}} \quad (1-23)$$

When  $n$  is infinite, no analytical solution can be calculated in order to determine the energies of the magnetic spin states and the susceptibility. However, the energies and susceptibility can be calculated exactly for small chains of finite number of metal centers. Then, by extrapolating these results to the case of an infinite chain, numerical solutions for the energies of the magnetic states and susceptibility can be approximated.<sup>25,26</sup> The temperature dependence of the magnetic susceptibility for an  $S = \frac{1}{2}$  uniform chain, extrapolated from a ring of  $n = 11$  spin centers, is

$$\chi = \frac{N_A g^2 \mu_B^2}{k_B T} \frac{0.25 + 0.074975x + 0.075235x^2}{1.0 + 0.9931x + 0.172135x^2 + 0.757825x^3} \quad (1-24)$$

where

$$x = \frac{|J|}{k_B T} \quad (1-25)$$

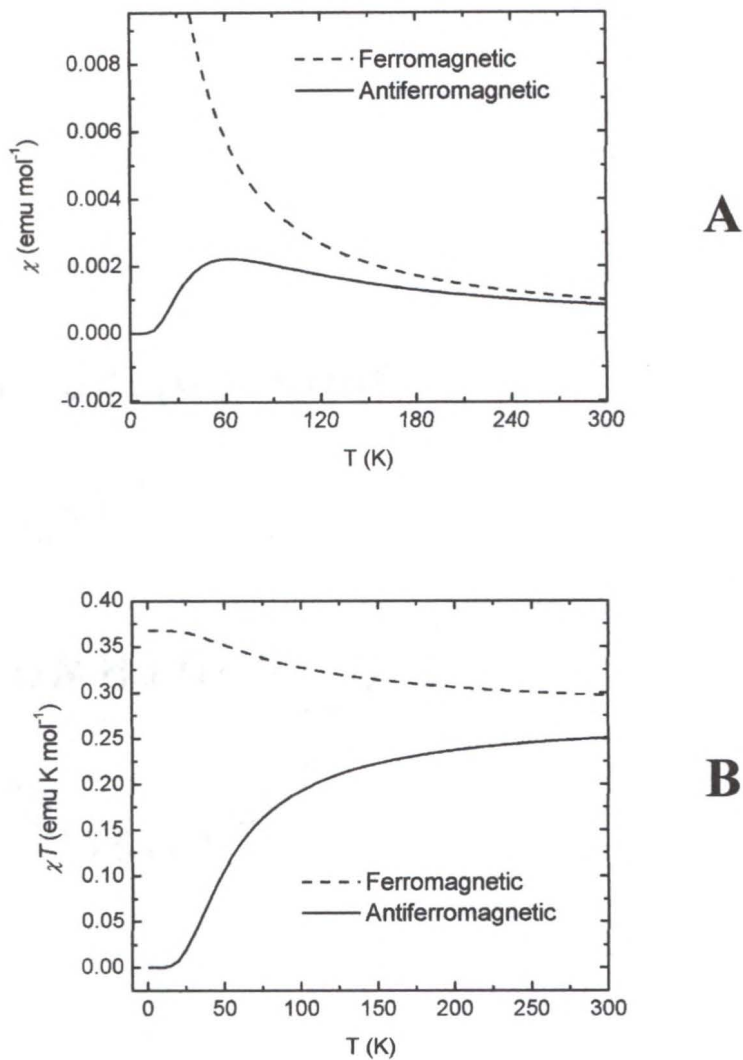


Figure 1-9. Temperature dependent magnetic susceptibility plots for an  $S = \frac{1}{2}$  dinuclear complex ( $g = 2.10$ ) modeled after Equation 1-22. A)  $\chi$  vs.  $T$ . B)  $\chi^{-1}$  vs.  $T$ . The dotted lines represent ferromagnetically coupled dimers ( $J k_B^{-1} = 50$  K) and the solid lines represent antiferromagnetically coupled dimers ( $J k_B^{-1} = -50$  K).



Figure 1-10. An exchange coupled, uniform  $S = \frac{1}{2}$  chain of Cu(II) ions.

Note that this equation is valid only for antiferromagnetic exchange along the chains ( $J < 0$ ) since, as  $T$  approaches 0, then  $\chi$  converges to 0 if  $n$  is small and finite. If  $n$  is infinite,  $\chi$  does not converge to 0 but to a finite value since the ground and excited states form a continuum of energy levels with no energy gap between ground state and next highest energy level.<sup>6</sup> When  $J > 0$ , then  $\chi$  diverges as  $T$  approaches 0. No corresponding analytical expression to describe the magnetic behavior of a ferromagnetically coupled uniform chain has been reported.<sup>6</sup>

A high temperature series expansion,<sup>27</sup> valid for both positive and negative  $J$  values, to describe the magnetic susceptibility for a  $S = 1/2$  uniform chain is given by

$$\chi = \frac{N_A g^2 \mu_B^2}{4k_B T} \left[ \frac{1.0 + 5.7980x + 16.9026x^2 + 29.3769x^3}{1.0 + 2.7980x + 7.0087x^2 + 8.6539x^3 + 4.5743x^4} \right]^{2/3} \quad (1-26)$$

where

$$x = \frac{J}{k_B T} \quad (1-27)$$

Regardless of the ferromagnetic or antiferromagnetic exchange interactions that are present along the chains, in principle, the isolated one-dimensional chains magnetically order only at  $T = 0$ . However, in real solids, chains are never completely isolated but experience interchain interactions, usually much weaker than the dominant intrachain exchange due to a crossover in lattice dimensionality. At low temperatures, these interchain interactions become important, the one-dimensional chains effectively behave as three-dimensional solids, and magnetic ordering occurs at finite temperatures.

A more complicated type of one-dimensional system is the alternating, or zig-zag, chain. In this system, there are two distinct types of spin centers and, as a result, there is

a regular alternation of the exchange interactions,  $J$  and  $J'$ , representing the nearest neighbor and next nearest neighbor couplings, respectively. Examples of alternating chains include  $\text{Cu}(\text{NO}_3)_2 \cdot 5/2\text{H}_2\text{O}$  <sup>28,29</sup> and  $(\text{ipa})\text{CuCl}_3$  (ipa = isopropylammonium) <sup>30,31</sup>. For instance, Figure 1-11 schematically represents an  $S = 1/2$  alternating chain of Cu(II) ions.

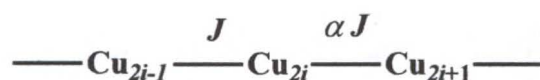


Figure 1-11. An exchange coupled, alternating  $S = 1/2$  chain of Cu(II) ions.

The spin-Hamiltonian representing for an alternating chain system is

$$\hat{H} = -J \sum_{i=1}^{n/2} [\hat{\mathbf{S}}_{A_{2i}} \cdot \hat{\mathbf{S}}_{A_{2i-1}} + \alpha \hat{\mathbf{S}}_{A_{2i}} \cdot \hat{\mathbf{S}}_{A_{2i+1}}] \quad (1-28)$$

where  $\alpha$  is the alternation parameter such that  $0 \leq \alpha \leq 1$  such that  $J' = \alpha J$ . Note that when  $\alpha = 0$ , the one-dimensional system behaves as isolated magnetic dimers, and when  $\alpha = 1$ , the system corresponds to a uniform chain. Again, when  $n$  is infinite, no analytical solution can be used to determine the energies of the magnetic spin states and the susceptibility for the alternating chain. However, analytical solutions can be obtained in a similar fashion for uniform chain.

The temperature dependence of the magnetic susceptibility for an  $S = 1/2$  alternating chain, extrapolated from a ring of  $n = 10$  spin centers, <sup>32</sup> is

$$\chi = \frac{N_A g^2 \mu_B^2}{k_B T} \frac{A + Bx + Cx^2}{1 + Dx + Ex^2 + Fx^3} \quad (1-29)$$

where

$$x = \frac{|J|}{k_B T} \quad (1-30)$$

The coefficients A – F are functions of  $\alpha$  and are provided elsewhere.<sup>6</sup> This equation is valid only when both exchange interactions are antiferromagnetic  $J \leq 0$  and both exchange parameters are within an order of magnitude of one another. In contrast to uniform chains, when  $J < 0$  and  $0 \leq \alpha < 1$ , then  $\chi$  converges to 0 as  $T$  approaches zero since an energy gap between the ground and excited magnetic states is present.<sup>6</sup>

### Ladders

Ladders, low-dimensional quantum systems that fall in between one-dimensional chains and two-dimensional sheets, consist of a finite number of magnetically coupled chains of spins (Figure 1-1).<sup>33,34</sup> In principle, one might expect that a smooth crossover in physical properties from chains to sheets would result if one assembled chains to progressively form ladders of increasing width but this is not generally true.<sup>33</sup>

The spin-Hamiltonian that, in general, represents ladder-like magnetic systems is

$$\hat{H} = -J_{\parallel} \sum_{a=1,2} \sum_{i=1}^n \hat{\mathbf{S}}_{i,a} \cdot \hat{\mathbf{S}}_{i+1,a} - J_{\perp} \sum_{i=1}^n \hat{\mathbf{S}}_{i,1} \cdot \hat{\mathbf{S}}_{i,2} \quad (1-31)$$

where  $\mathbf{S}_{i,a}$  represents the spin operator at site  $i$  ( $i = 1, 2, \dots, n$ ) on the leg  $a$  ( $a = 1, 2, \dots$ ) of the ladder with  $n$  rungs.<sup>33</sup> The terms  $J_{\perp}$  and  $J_{\parallel}$  denote the intra- and interrung exchange couplings, respectively. In “ideal” ladders, the magnitude of the coupling along the legs is comparable to the magnitude of the coupling along the rungs,  $J_{\perp} / J_{\parallel} \sim 1$ . When  $J_{\perp} / J_{\parallel}$  tend to zero, the exchange between the rungs is small compared to the exchange along the legs and the ladder behaves as a system of isolated chains. Conversely, when  $J_{\perp} / J_{\parallel}$  tend to infinity, the exchange along the legs is small compared

to the exchange along the rungs and the ladder behaves as a system of isolated dimers. Ideal spin ladders should also be well isolated from one another since appreciable interladder coupling ( $J'$ ) can cause transitions from the spin liquid ground state to a magnetically ordered state.<sup>33</sup>

The magnetic properties of ladders with an even number of legs are drastically different from those with an odd number of legs.<sup>35</sup> Ladders with an even number of legs (Figure 1-1), such as the inorganic cuprate  $\text{SrCu}_2\text{O}_3$ , are characterized by short-range spin correlations along the legs, a spin-liquid ground state.<sup>33,35,36</sup> Even-leg ladders consist of spin-singlet pairs with a spin-spin correlation length along the legs that show an exponential decay produced by the presence of a finite spin gap and tends to 0 as  $T$  approaches 0. In contrast, a ladder with an odd number of legs, such as  $\text{Sr}_2\text{Cu}_3\text{O}_5$ , exhibits power-law decay of spin-spin correlations that tend to finite values as  $T$  approaches 0 that are magnetically ordered due to the presence of gapless spinless excitations.<sup>33,35,36</sup>

Ladders with an even number of legs are characterized by a spin gap.<sup>33,35</sup> A spin gap is a finite energy gap between a nonmagnetic ground state and the first excited triplet state (Figure 1-12a). No continuum of excited states exists directly above the ground state. If the rungs of an antiferromagnetic ladder interact weakly with one another, *i.e.*,  $J_{\perp} / J_{\parallel}$ , the ground state has a total  $S = 0$  since the spins on each rung are in a singlet state.<sup>33</sup> To promote the ladder to the lowest excited state with a total  $S = 1$ , one of the pairs of spin singlets of the rungs must be promoted to an  $S = 1$  triplet. A quantum of energy, called the spin gap energy,  $\Delta E_{sg}$ , is required to excite one of the rung singlets into a triplet state. A frustrated spin state results since the spins are now aligned parallel

along one direction but anti-parallel along the other direction (Figure 1-12b).

Examination of the magnetization of a ladder compound as a function of changing external applied field can identify a spin gap. An abrupt increase in magnetization at a particular magnetic field indicates the presence of the energy gap (Figure 1-12c).

There has recently been a growing interest in the preparation and study of ladder-like molecular and solid-state materials. In the field of supramolecular chemistry, ladders represent one of many familiar structural topologies that are possible from the self-assembly of simple molecular or ionic nodes and spacers, such as metal ions or complexes and multifunctional bridging ligands, respectively, under certain stoichiometric ratios and reaction conditions.<sup>37</sup> Furthermore, molecular and solid-state ladders, as a consequence of their structure, often possess open or enclathrated cavities and extended channels that exhibit unique inclusion and catalytic phenomena.<sup>37</sup> In the field of low-dimensional materials, ladders represent a structural intermediate between one-dimensional chains and two-dimensional sheets.<sup>33</sup> Ladders represent ideal systems to investigate the gradual change in physical properties as the dimensionality increases from 1D chains, to quasi 1D / 2D systems, to 2D sheets. Furthermore, copper oxide ladders are part of the structure of many solid-state materials such as  $(\text{Sr}, \text{Ca})\text{Cu}_2\text{O}_3$  that, upon doping with holes, often exhibit superconductivity at liquid nitrogen temperatures or higher.<sup>35,38</sup> These copper oxide ladders are antiferromagnetic and it is believed that the superconductivity originates and is sustained within this portion of the structure. In order to better understand the origin and mechanism of high-temperature superconductivity, it is desirable to synthesize model low-dimensional compounds that adopt a ladder-like structure similar to those found in the cuprates.

## Self-Assembly of Supramolecular Architectures

The recent research efforts devoted to the rational design and crystal engineering of supramolecular solid-state materials were initially spawned by a concerted interest toward developing methods for predicting the crystal structures of organic compounds.<sup>39</sup> However, ongoing work in this field has continued due to the prospect of developing new materials with interesting structures and diverse, exploitable properties. One particular area in supramolecular chemistry has focused on synthesizing hybrid organic / inorganic materials through the self-assembly of simple, molecular or ionic building blocks. Compared to purely organic or inorganic analogous systems, these materials often possess improved thermal, chemical, and mechanical stability and exhibit unique or enhanced physical properties.<sup>40</sup> Hybrid organic / inorganic materials are potentially useful in a wide variety of applications including low temperature catalysis,<sup>41-43</sup> inclusion phenomena,<sup>37,44,45</sup> magnetism,<sup>40,46-49</sup> electrical conductivity,<sup>50-52</sup> photochemistry,<sup>53</sup> and second-order nonlinear optical behavior.<sup>54-57</sup>

### Strategies for Building Supramolecular Architectures

Under certain conditions, solution-phase molecular and ionic building blocks can self-assemble into discreet clusters or oligomers or extended one-, two-, and three-dimensional solids sustained through various types of chemical interactions such as coordinate covalent bonding,<sup>43,58</sup> electrostatic attractions,<sup>59,60</sup> hydrogen bonds,<sup>61-65</sup> and  $\pi$ -stacking.<sup>66-68</sup> In general, the overall molecular and solid-state structure is controlled by a combination of the binding constraints, geometrical preferences, and relative stoichiometric quantities of these building blocks. Therefore, much research has been devoted to the development of general strategies to better predict, design, and

control the structure of supramolecular architectures with the above guidelines in mind. By far the simplest and most common strategy applied is the node and spacer method. The node defines the overall geometry of the structure while multifunctional or multitopic spacer ligands are tethered to and propagate the geometrical preferences of node throughout the solid.<sup>69,70</sup> These simple, modular components are chosen as starting materials because their inherent bonding and geometrical propensities allow some degree of control and predictability over the structure of products.<sup>39</sup> Furthermore, by the careful selection or design of these building blocks, the physical properties of the solids can be “tuned” or “tweaked” to meet specific needs.<sup>39</sup>

A number of different approaches derived from the node and spacer strategy can be applied toward the design of supramolecular materials based on the nature of the building blocks or the chemical interactions responsible for sustaining the structure. The most common approach is the generation of hybrid organic / inorganic networks that are simple extensions of a specific transition metal or metal complex (metal center chelated by one or more poly-hapto ligands) geometry.<sup>39</sup> The metal coordination environment functions as the node and the spacer ligands are typically bridging ligands. In most cases, the molecular and solid-state structure of the assembly is sustained through coordinate covalent bonding and thus the structure is often referred to as a coordination polymer.

A variety of one-, two-, and three-dimensional coordination solids with novel topologies have been obtained using rigid, multifunctional spacer ligands such as pyrazine,<sup>71,72</sup> 4,4'-bipyridine,<sup>44,73-79</sup> 4,4'-azobis(pyridine),<sup>80</sup> bis(4-pyridyl)benzene,<sup>81</sup> bis-(4-pyridyl)-ethylene,<sup>81</sup> 2,4,6-tris(4-pyridyl)-1,3,5-triazine,<sup>82-85</sup> 1,3,5-tris(4-ethynylbenzotrile)benzene,<sup>86</sup> and 1,3,5-benzenetricarboxylic acid<sup>45,87</sup>

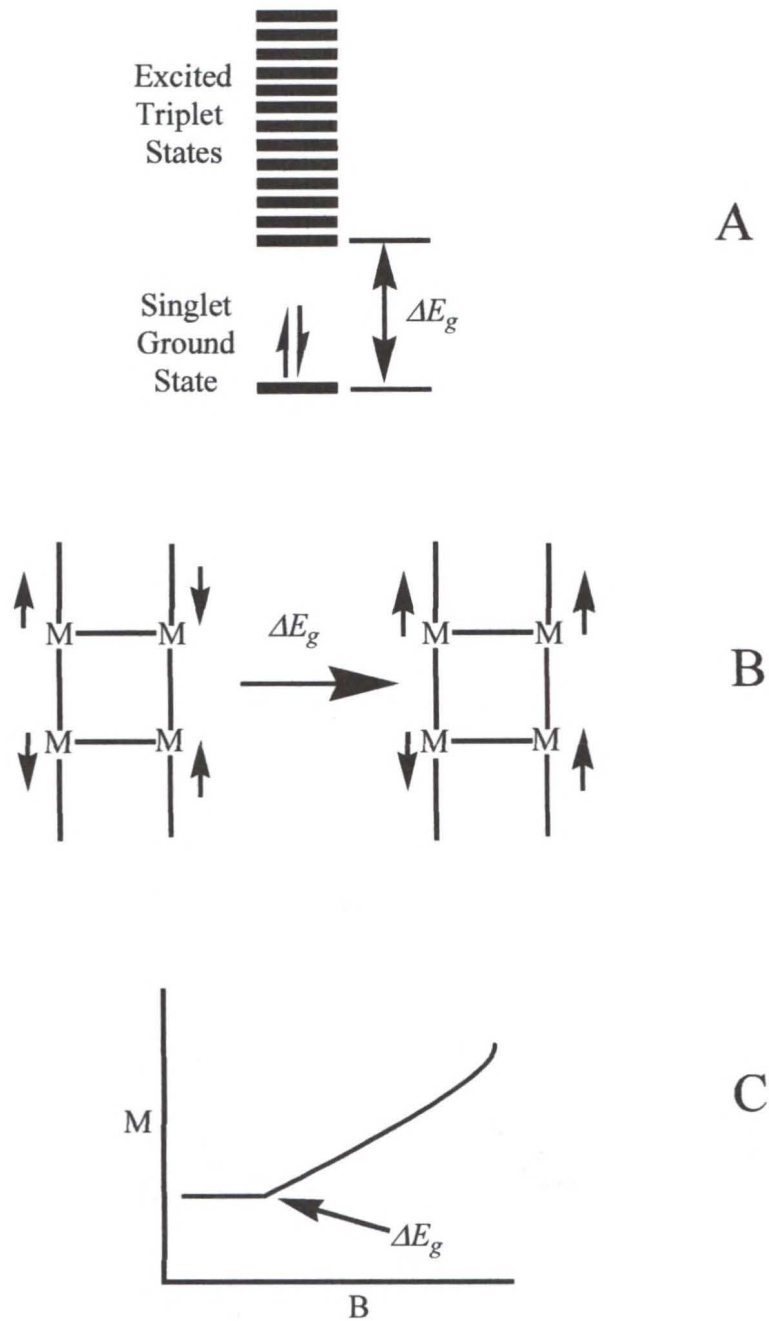


Figure 1-12. Spin Gap. A) The energy gap,  $\Delta E_g$ , between the singlet ground state and excited magnetic spin states in a two-leg ladder. B) The excitation of one of the strongly coupled rungs into a triplet state results in a frustrated spin state. C) The spin gap can often be identified by an abrupt increase of the field dependent magnetization.

with transition metal cations such as  $\text{Cu}^+$ ,  $\text{Cu}^{2+}$ ,  $\text{Ag}^+$ ,  $\text{Zn}^{2+}$ ,  $\text{Cd}^{2+}$ ,  $\text{Mn}^{2+}$ ,  $\text{Co}^{2+}$ ,  $\text{Fe}^{3+}$ , and  $\text{Ni}^{2+}$ . Predictable and structurally well-defined products are often produced from the self-assembly of rigid spacers with metal cations. In fact, rigid spacers are particularly ideal for designing and synthesizing porous network solids capable of clathrating small molecules. On the other hand flexible spacer ligands have not been extensively exploited except in a few cases.<sup>44,81,88</sup> Flexible spacers may allow the synthesis of hybrid organic / inorganic solids with structural features not found in those materials with rigid linking groups.<sup>89,90</sup> Unfortunately the incorporation of a higher degree of flexibility into the building blocks reduces the amount of predefined geometrical information from the reactant components and a multitude of different structures can arise from identical metal-ligand combinations or minor experimental variations.<sup>91</sup>

Hydrogen bonding interactions between nodes and spacers offer an alternative, but equally powerful, approach to the control of solid-state structures. Molecular components with complementary hydrogen-binding sites are well known and can be readily incorporated into building blocks to produce extended polymeric architectures sustained by interactions either directly between nodes or mediated by spacer ligands<sup>61</sup> Because these interactions are directional and their formation is often reversible, hydrogen bonded molecular assemblies are ideal for the design of structurally flexible networks with and adjustable size pores.<sup>61,62</sup> Obviously, networks can be also assembled by the concurrent action of both coordinate covalent and hydrogen bonds as well, though species like these are relatively less common.<sup>92</sup>

An alternative approach to the metal node and ligand spacer method involves the exploitation of exodentate multitopic ligands that act as both the nodes and spacers in the

network architecture. This method is exemplified by the construction of supramolecular architectures from solely organic molecules and has generated a number of architectures mimicking the structures of known inorganic minerals.<sup>70,84,86,93</sup> However, this method is also less predictable in terms of rationally developing functional topologies.<sup>70</sup>

### **Factors Affecting the Structure of Supramolecular Architectures**

A number of different factors can profoundly affect the molecular and solid-state structure of self-assembled coordination polymers, such as the stoichiometric ratios of the node and spacer, the different oxidation states and coordination preferences of the metal ion nodes, the structural and bonding propensities of spacer ligands, and the reaction solvents. The metal:ligand stoichiometry is one of the most important factors determining the dimensionality and limiting the possible topological architectures that can occur in a coordination solid. Consider the possible types of structural motifs, or supramolecular isomers,<sup>94</sup> that result from the combination of various spacer ligands with metallic moieties. A 1:1 ratio limits the architectures to either one-dimensional linear or zig-zag chains.<sup>64,69,89,95-102</sup> A 1:2 ratio can produce two-dimensional grids with rectangular cavities if the node is planar or octahedral<sup>40,44,74,75,92,95,103-105</sup> or three-dimensional diamondoid structures if the metal center is in a tetrahedral or S<sub>4</sub> environment.<sup>79,106-108</sup> A metal:ligand ratio of 1:1.5 can produce any of six very different architectures including the molecular ladder,<sup>70,88,94,109</sup> brick wall,<sup>74,88</sup> Lincoln log,<sup>73,110</sup> tongue and groove or bilayer,<sup>70,76,111</sup> herringbone,<sup>112</sup> or three-dimensional frame<sup>113</sup> if the metal moieties adopt only square planar or octahedral geometries. Additionally a trigonal metal center can generate two-dimensional hexagonal or honeycomb nets with a three-fold symmetric tritopic spacer such as 1,3,5-

trisubstituted benzenes in a 1:1.5 metal:ligand ratio.<sup>86,106</sup> The molecular railroad has been the only topology observed for a 1:2.5 stoichiometry but, unlike the ladder, the spacers are present as both bridges and terminal ancillary ligands.<sup>114,115</sup> Three-dimensional rectangular and interpenetrated grids, are possible with metal:ligand stoichiometries of 1:3 or smaller.<sup>116-119</sup> However, given the ubiquity of octahedral coordination environments, it is somewhat surprising that simple three-dimensional octahedral polymers remain largely unexplored.<sup>117</sup> Figure 1-13 schematically depicts selected supramolecular architectures built from the self-assembly of nodes (metal ions) with spacers (multifunctional bridging ligands).

Many of these topologies, such as the two-dimensional sheets, incorporate cavities and channels as part of the molecular and solid-state structure. In a few cases, the pores are open<sup>40</sup> but the void space is usually filled either by clathrated guests or interpenetration of neighboring lattices. This packing diversity between interpenetrated and noninterpenetrated porous solids can be identified as another form of supramolecular isomerism.<sup>115</sup>

The oxidation state and the coordination preferences of transition metals are also critical in determining the final molecular and solid-state structure. For example,  $\text{Cu}^{2+}$  normally prefers an axially distorted octahedral geometry and is known to form two-dimensional square networks with pyrazine or substituted pyrazine ligands<sup>71,120-122</sup> and interpenetrated two-dimensional networks with 4,4'-bipyridine.<sup>43</sup> However, trigonal and tetrahedral  $\text{Cu}^+$  cations can form two- and three-dimensional networks when bridged by bipy, pyrazine, or substituted pyrazine ligands.<sup>107,120,123,124</sup>  $\text{Ag}^+$  is observed in an

even wider range of coordination environments including linear,<sup>41,110</sup> trigonal,<sup>41</sup> tetrahedral,<sup>41,108,125</sup> square-planar,<sup>126</sup> square pyramidal,<sup>126</sup> and octahedral<sup>126</sup> when bound to pyrazine or bipy.

The presence of coordinated or lattice solvent molecules can dramatically affect to final structure. For instance, in  $[\text{Zn}(4,4'\text{-bipy})_2(\text{H}_2\text{O})_2]\text{SiF}_6$ ,<sup>74</sup> the coordination of solvent water molecules produces an interpenetrated sheet-like structure while a porous solid,  $[\text{Zn}(4,4'\text{-bipy})_2(\text{H}_2\text{O})_2]\text{SiF}_6 \cdot x\text{DMF}$ ,<sup>117</sup> is isolated under nonaqueous conditions. A similar solid-state structural difference is observed between the double-layered structure of the solvent inclusion compound  $[\text{Ag}(\text{pyrazine})_2][\text{Ag}(\text{pyz})_5](\text{PF}_6)_3 \cdot 2\text{S}$  (S =  $\text{CH}_2\text{Cl}_2$ ,  $\text{CHCl}_3$ , and  $\text{CCl}_4$ )<sup>126</sup> and the single-layered structure of the solvent-free compound  $[\text{Ag}(\text{pyz})_2](\text{PF}_6)$ .<sup>125</sup> Counterions can also influence the final structure. In the previous example, by replacing the  $\text{PF}_6^-$  counterions with  $\text{SbF}_6^-$ , the characteristic double-layer structure of Ag-pyrazine- $\text{PF}_6$  changes to the three-dimensional noninterpenetrating cubic framework  $\text{Ag}(\text{pyz})_3(\text{SbF}_6)$ <sup>126</sup> while substituting with  $\text{BF}_4^-$  ions changes the layered sheet-like structure of  $[\text{Ag}(\text{pyz})_2](\text{PF}_6)$ <sup>125</sup> to the interpenetrated three-dimensional structure  $[\text{Ag}_2(\text{pyz})_3](\text{BF}_4)_2$ .<sup>41</sup>

### **Porous Network Supramolecular Architectures**

The design and construction of hybrid organic / inorganic porous network solids is a particularly important and emerging area of supramolecular chemistry providing new generations of functional materials.<sup>42,60,127,128</sup> The great importance of porous solids in inclusion phenomena, such as adsorption / desorption, ion exchange, size and shape-selective molecular sieving, and catalysis, is due to their ability to reversibly clathrate or

trap species within their cavities and extended channels.<sup>129</sup> These pores possess a variety of sizes and shapes not observed in analogous inorganic porous solids such as zeolites and molecular sieves.<sup>87</sup> Furthermore, by a careful selection and design of the chemical components, the size and clathration properties of these pores can be designed and fine-tuned to meet specific needs while maintaining the overall structural and functional features of naturally occurring analogs.<sup>44</sup>

Like zeolites, most hybrid organic / inorganic coordination polymers bind guests within pores, cavities, and channels that are part of their lattice framework. In fact, a number of such coordination networks have been found to exhibit many other desirable zeolitic properties as well, such as stability and porosity of the framework,<sup>130</sup> guest exchange,<sup>131,132</sup> and selective catalytic activity.<sup>44</sup> Recent examples porous solids include the diamondoid, honeycomb, rectangular grid, ladder, brick wall, and octahedral frameworks constructed from tetrahedral, trigonal, and octahedral metal templates (Zn(II), Cd(II), Ag(I), and Cu(I)) and various multitopic spacer ligands.<sup>44,73,133-135</sup>

The reversible absorption and desorption of guests without the collapse of cavities or channels, while well known in materials such as zeolites, is a much less common phenomenon in molecular porous solids.<sup>136-138</sup> Upon loss of their guests, clathrated hosts irreversibly lose crystallinity,<sup>93</sup> undergo phase changes,<sup>139</sup> or alter their morphology without the simultaneous replacement of substitutes.<sup>139,140</sup> Few examples exist where cavities that have been collapsed due to crystal packing forces from guest loss are restored upon guest binding, however, it has recently been shown that some coordination or hydrogen-bonded networks can rapidly exchange inclusions or

counterions while maintaining crystal integrity.<sup>42,44,86,141,142</sup> Furthermore, the construction and access of large pores in either coordination polymers or hydrogen-bonded assemblies is often mitigated or precluded by self-inclusion or lattice interpenetration particularly if the void created by the open pores occupies more than 50 % of the crystal by volume.<sup>43,107,109,143</sup> Interpenetrated structures are of limited usefulness in inclusion chemistry but have significant potential in terms of other enhanced bulk properties, such as improved chemical, mechanical, and thermal stability.<sup>37,109</sup>

In order to design and construct functional porous solids with useful inclusion capabilities, a number of requirements should be met while accounting for the problems detailed above. The host framework should be rigid and robust, containing large, accessible cavities or channels capable of reversible guest binding in a stoichiometric manner.<sup>142</sup> Furthermore, the structural integrity of the pores should be maintained in the absence of clathrates.<sup>138,142</sup> The term “capable”, in this context, implies that the van der Waals surfaces and electrostatic potential surfaces of the host pores and guest should also be complementary.<sup>37,39</sup> The robustness of a channel or cavity is the ability to allow reversible release and adsorption of guest without the collapse of the host structure.<sup>144</sup>

In order to address these requirements, one approach focuses on the utilization of chemical interactions in two or three dimensions to maintain the integrity of the host structure after removal of the clathrated guests.<sup>134</sup> Porous three-dimensional networks sustained by strong coordinate covalent bonding often retain the vacant cavities and channels even after removal of the guest molecules without structural changes, such as

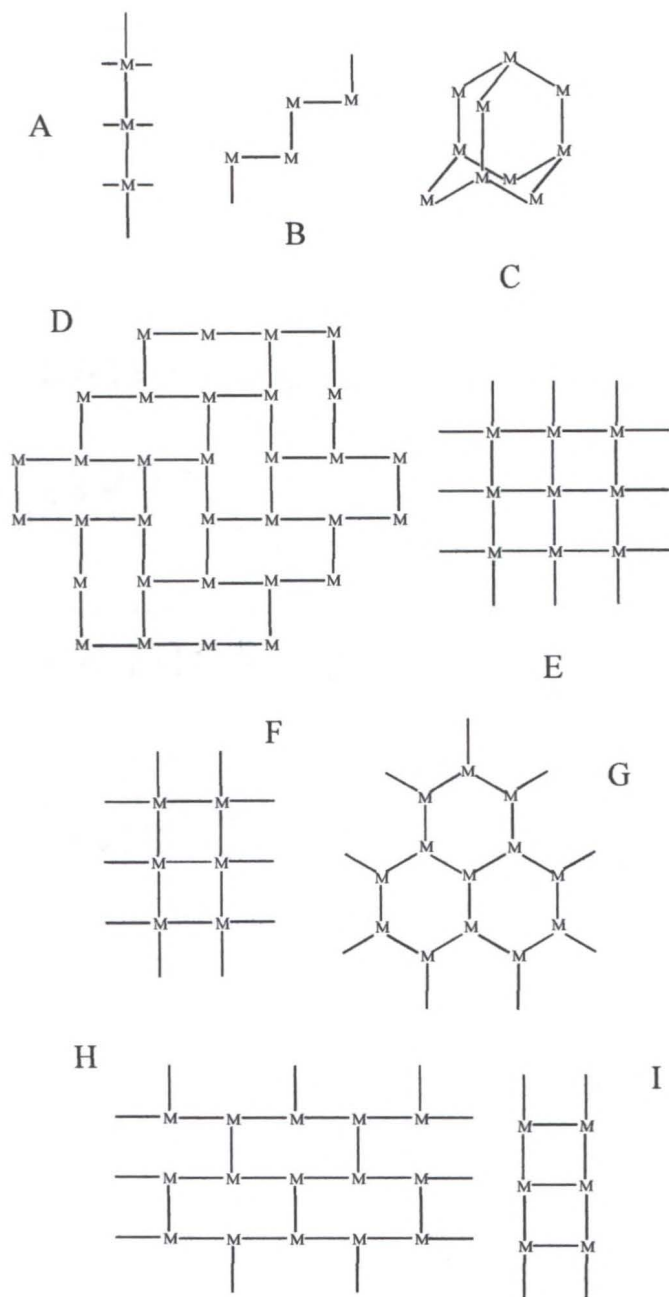


Figure 1-13. Examples of supramolecular architectures from the self-assembly of metal ions, M, with spacer ligands (lines). A) Linear chains. B) Zig-zag chains. C) Diamondoid. D) Herringbone sheet. E) Square grid sheet. F) Railroad. G) Honeycomb. H) Brick wall sheet. I) Ladder.

lattice interpenetration, at ambient temperature.<sup>70,76,145,146</sup> On the other hand, flexible pores sustained by weaker hydrogen bonding interactions may change in size in response to the uptake or loss of guests to ensure that void space is efficiently occupied thus avoiding self-inclusion.<sup>62</sup>

Another approach involves the use of interpenetration to produce porous solids with robust cavities and channels.<sup>77,144</sup> This method may, at first, seem self-defeating since the interpenetration of neighboring lattice frameworks often completely fills void space thus preventing the formation of extended cavities and channels.<sup>42,69,73,84,107,108,110</sup> In fact, most strategies aimed at synthesizing porous solids have been directed toward the inhibition of interpenetrated networks. However, if the spacer is of sufficient length the self-inclusion may only reduce the size of, but not completely fill, the pores, leaving small voids for small-molecule inclusion.<sup>144</sup> The lattice interpenetration can therefore afford rigid, three-dimensional networks with the desired robust, albeit smaller, channels.

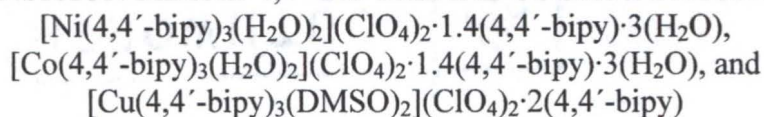
Despite the large amount of research and work effort devoted toward the synthetic aspect of solid-state supramolecular chemistry in terms of producing functional materials and elucidating methods for the rational design and fabrication of such materials, studies of the chemical reactivity of these materials has been lacking.<sup>147</sup> In fact most of the studies have been limited to inclusion properties of clathrated porous solids, such as the absorption-desorption processes and guest exchange of guest molecules.<sup>45,87,142,144,147</sup> This imbalance of synthetic work compared to chemical reactivity studies of supramolecular materials is largely due to the fact that, unlike the well characterized chemical reactivity properties of molecular and ionic species which

are generally soluble in one or more common solvents, most coordination polymers are insoluble in most common organic and inorganic solvents thus rendering any reactivity studies difficult at the very least.<sup>147</sup>

### **Scope of the Dissertation**

The work presented in this dissertation, Chapters 2, 3, and 4, focuses on, in general, investigating the structural and physical properties of representative solid-state materials obtained throughout the course of this graduate research. In Chapter 2, the structural, thermal, and magnetic properties of a series of clathrated porous network solids are described in detail. Chapter 3 describes the host-guest properties of these porous solids determined through gas chromatography, solid-state NMR spectroscopy, and X-ray diffraction. Chapter 4 details the structural and magnetic properties of a series of ladder-like azido bridged Cu(II) coordination polymers. Finally, the structures of selected coordination polymers that did not quite fit within the context of the themes of the chapters are presented in Appendix A.

CHAPTER 2  
STRUCTURAL, THERMAL, AND MAGNETIC PROPERTIES INVESTIGATION OF  
THREE TRANSITION METAL-4,4'-BIPYRIDINE COORDINATION POLYMERS:



### Introduction

The rational design and synthesis of functional organic/inorganic network solids has recently been the focus of intense research in materials chemistry. Much of the interest in this field is driven by the wide variety of potential applications such materials can afford, including host-guest chemistry,<sup>44</sup> ion exchange,<sup>37</sup> molecular sieving,<sup>37,44,45</sup> catalysis,<sup>41-44</sup> non-linear optics,<sup>54-57</sup> electrical conductivity,<sup>50-52</sup> and magnetism.<sup>40,46-49</sup> Often such materials are designed and built from simple, modular components such as a metal ions and organic spacer ligands. The spacers are typically multifunctional ligands capable of coordinating to the metal ions and propagating structural information dictated by the coordination requirements and geometry of the metal sites throughout a solid.<sup>69</sup> The assembly of these components through intermolecular forces *e.g.* donor-acceptor interactions,<sup>148,149</sup> hydrogen bonds,<sup>61,63,64</sup> and  $\pi$ -stacking<sup>66</sup> can produce solids whose molecular and crystal structure can be profoundly affected by a number of factors, most notably the metal:spacer stoichiometry. For example, transition metal ions combined with linear organic spacers can assemble to form structures resembling linear<sup>64,69,95,96,100,101</sup> or zigzag chains,<sup>69,78,99</sup>

molecular ladders,<sup>70,88,94,109</sup> two-dimensional grids,<sup>40,44,47,40,69,74,92,100,104,105,150,151</sup> railroads,<sup>114,115</sup> or three-dimensional networks,<sup>152,153</sup> if the metal:spacer stoichiometry is 1:1, 1:1.5, 1:2, 1:2.5, or 1:3, respectively.

One commonly employed spacer is the bifunctional heterocyclic molecule 4,4'-bipyridine and a number of coordination polymers with different network architectures in the solid state have been reported incorporating this ligand.<sup>40,44,69,70,101,105,109,114,151</sup> Examples of one-dimensional chains include  $[\text{Co}(\text{SO}_4)(\text{H}_2\text{O})_3(4,4'\text{-bipy})]\cdot 2(\text{H}_2\text{O})$ ,<sup>96</sup>  $[\text{Ni}(\text{Et-XA})_2(4,4'\text{-bipy})]\cdot 0.5(\text{EtOH})\cdot (\text{CHCl}_3)$  (Et-XA = ethylcarbonadithiolate),<sup>98</sup>  $[\text{Co}(\text{NCS})_2(\text{H}_2\text{O})_2(4,4'\text{-bipy})]\cdot (4,4'\text{-bipy})$ ,<sup>95</sup> and  $[\text{Mn}(\text{hfac})_2(4,4'\text{-bipy})]$  (hfac = hexafluoroacetylacetonato),<sup>97</sup> while  $[\text{Ni}(4,4'\text{-bipy})_{2.5}(\text{H}_2\text{O})_2](\text{ClO}_4)_2\cdot 1.5(4,4'\text{-bipy})\cdot 2(\text{H}_2\text{O})$ <sup>114</sup> and  $[\text{Co}(4,4'\text{-bipy})_{1.5}(\text{NO}_3)_2]\cdot \text{Guest}$  (Guest = MeCN or  $\text{CHCl}_3$ )<sup>109</sup> form railroad and ladder-like structures, respectively. Examples of two-dimensional grids or sheets include  $[\text{Cd}(4,4'\text{-bipy})_2(\text{NO}_3)_2]\cdot 2(\text{C}_4\text{H}_6\text{Br}_2)$ ,<sup>44</sup>  $[\text{Cu}(4,4'\text{-bipy})(\text{H}_2\text{O})_2(\text{FBF}_3)_2]\cdot (4,4'\text{-bipy})$ ,<sup>92</sup>  $[\text{Co}(\text{NCS})_2(4,4'\text{-bipy})_2]\cdot 2(\text{CH}_3\text{CH}_2)_2\text{O}$ ,<sup>95</sup>  $[\text{M}(4,4'\text{-bipy})(\text{ox})]$  (M = Fe(II), Co(II), Ni(II), and Zn(II) and ox = oxalato),<sup>40</sup> and  $[\text{M}(4,4'\text{-bipy})_2(\text{H}_2\text{O})_2](\text{ClO}_4)_2\cdot \text{Guest}$  (M = Cu, Zn, and Cd and guest = enclathrated guest molecule).<sup>133</sup>

### Chapter Summary

This chapter reports the crystal structures, thermal behavior, and magnetic properties of a series of three linear chain compounds containing the 4,4'-bipyridine spacer that organize in the solid state to form new non-interpenetrated network solids.

The compounds  $[\text{Ni}(4,4'\text{-bipy})_3(\text{H}_2\text{O})_2](\text{ClO}_4)_2 \cdot 1.4(4,4'\text{-bipy}) \cdot 3(\text{H}_2\text{O})$  **1**,  $[\text{Co}(4,4'\text{-bipy})_3(\text{H}_2\text{O})_2](\text{ClO}_4)_2 \cdot 1.4(4,4'\text{-bipy}) \cdot 3(\text{H}_2\text{O})$  **2**, and  $[\text{Cu}(4,4'\text{-bipy})_3(\text{DMSO})_2](\text{ClO}_4)_2 \cdot 2(4,4'\text{-bipy})$  **3**, were each prepared by the direct combination of three moles of 4,4'-bipyridine with one mole of their respective metal ion. Compounds **1** and **2** are isostructural and were crystallized under inert atmosphere, hydrothermal conditions. The related structure **3** was isolated under ambient laboratory conditions from dimethyl sulfoxide. All three materials share a common structural motif with one-dimensional, covalently linked chains interacting via hydrogen bonding and  $\pi$ -stacking forces to form layered sheets with characteristic hydrophobic, rectangular cavities. These sheets are packed in a manner that aligns the cavities to form oblique channels occupied by enclathrated guest molecules and counterions that extend throughout the solid. The thermal instability of these coordination polymers is associated with the relatively low temperatures at which the guest molecules are lost. Temperature and field dependent magnetization measurements revealed weak magnetic coupling between the paramagnetic metal centers as 4,4'-bipy is a poor mediator of superexchange interactions.<sup>97,98,154</sup>

## Experimental Section

### Materials

Copper(II) perchlorate hexahydrate (98 %), cobalt(II) perchlorate hexahydrate (98 %), nickel(II) perchlorate hexahydrate (98 %), 4,4'-bipyridine (98 %), and sodium azide were purchased from Aldrich (Milwaukee, WI). Dimethyl Sulfoxide (99.9 %) was purchased from Fisher Scientific (Pittsburgh, PA). Ethanol (100 %) was purchased from Aaper Chemical (Shelbyville, KY). All reagents were used without further purification.

### Synthesis of $[\text{Ni}(4,4'\text{-bipy})_3(\text{H}_2\text{O})_2](\text{ClO}_4)_2 \cdot 1.4(4,4'\text{-bipy}) \cdot 3(\text{H}_2\text{O})$

A solution was prepared by dissolving 731 mg of  $\text{Ni}(\text{ClO}_4)_2 \cdot 6 \text{H}_2\text{O}$  ( $2.0 \times 10^{-3}$  mol) in 10 mL of water contained within a Teflon canister. Addition of 934 mg of 4,4'-bipyridine ( $6.0 \times 10^{-3}$  mol) and 2 mL of ethanol to this solution resulted in a blue-green colored suspension. This canister was sealed within a homemade, stainless steel hydrothermal vessel, purged with argon gas, and heated to 150 °C for 5 days. The container was subsequently cooled to room temperature over a period of 24 hours without any specific control over the rate of cooling. The resulting blue-green crystals, obtained in 88 % yield (based on initial quantity of bipy), were washed with water before further characterization. The crystals become opaque within a few hours upon removal from the solvent. Elemental analysis calculated for  $\text{NiC}_{45}\text{H}_{46}\text{N}_9\text{O}_{13}\text{Cl}_2$ : C, 51.44 %; H, 4.42 %; N, 12.00 %. Found: C, 50.88 %; H, 4.47 %; N, 12.14 %.

### Synthesis of $[\text{Co}(4,4'\text{-bipy})_3(\text{H}_2\text{O})_2](\text{ClO}_4)_2 \cdot 1.4(4,4'\text{-bipy}) \cdot 3(\text{H}_2\text{O})$

Using the same procedure described for **1**, 731 mg of  $\text{Co}(\text{ClO}_4)_2 \cdot 6 \text{H}_2\text{O}$  ( $2.0 \times 10^{-3}$  mol) was reacted with 934 mg of 4,4'-bipyridine ( $6.0 \times 10^{-3}$  mol) in 10 mL of water with 2 mL of ethanol at 150 °C for 3 days. The resulting orange crystals, obtained in 92 % yield (based on initial quantity of bipy), were washed with water before further characterization. The crystals become opaque within a few hours upon removal from the solvent. Elemental analysis calculated for  $\text{CoC}_{45}\text{H}_{46}\text{N}_9\text{O}_{13}\text{Cl}_2$ : C, 51.43 %; H, 4.42 %; N, 11.99 %. Found: C, 50.87 %; H, 4.47 %; N, 12.14 %.

### Synthesis of $[\text{Cu}(4,4'\text{-bipy})_3(\text{DMSO})_2](\text{ClO}_4)_2 \cdot 2(4,4'\text{-bipy})$

A solution containing 741 mg of  $\text{Cu}(\text{ClO}_4)_2 \cdot 6 \text{H}_2\text{O}$  ( $2.0 \times 10^{-3}$  mol) dissolved in 10 mL of DMSO was combined with a solution containing 934 mg of 4,4'-bipyridine ( $6.0 \times 10^{-3}$  mol) dissolved in 10 mL of DMSO. The resulting dark blue colored mixture,

contained within an evaporating dish, initially produced small blue block-like crystals within two weeks of solvent evaporation. Within and additional four weeks, light blue colored hexagonal plates of **3** were isolated and washed with DMSO before further characterization.

### X-ray Structure Determination

A blue-green crystal of **1** (0.25 x 0.23 x 0.23 mm<sup>3</sup>), an orange crystal of **2** (0.51 x 0.36 x 0.17 mm<sup>3</sup>), and a blue crystal of **3** (0.24 x 0.21 x 0.12 mm<sup>3</sup>) were selected for X-ray analysis. Each crystal was mounted on a glass fiber under nitrogen gas. The same data collection procedure was used for each sample. Data were collected at 173 K on a Siemens SMART PLATFORM equipped with a CCD area detector and a graphite monochromator utilizing MoK $\alpha$  radiation ( $\lambda = 0.71073 \text{ \AA}$ ). Cell parameters were refined using up to 8192 reflections. A full sphere of data (1850 frames) was collected using the  $\omega$ -scan method (0.3° frame width). The first 50 frames were re-measured at the end of data collection to monitor instrument and crystal stability (maximum correction on I was < 1 %). Absorption corrections by integration were applied based on measured indexed crystal faces.

The structures were solved by the Direct Methods in *SHELXTL6*<sup>155</sup> and refined using full-matrix least squares. Structures **1** and **2** were solved and refined in space group *C2/c* while **3** was solved and refined in *Cc*, which afforded better results. The stoichiometry is the same in **1** and **2** ( $[\text{M}(4,4'\text{-bipy})_3(\text{H}_2\text{O})_2](\text{ClO}_4)_2 \cdot 1.4(4,4'\text{-bipy}) \cdot 3(\text{H}_2\text{O})$  where M = Ni or Co) but different from **3** ( $[\text{Cu}(4,4'\text{-bipy})_3(\text{DMSO})_2](\text{ClO}_4)_2 \cdot 2(4,4'\text{-bipy})$ ). The non-H atoms were treated anisotropically, whereas the hydrogen atoms were calculated in ideal positions by riding on their

respective carbon atoms. The H atoms from the coordinated water molecules were found and refined. The uncoordinated 4,4'-bipyridine molecules and perchlorate anions are disordered in each structure. In **1** and **2**, two half-bipy guest moieties are each disordered about a center of inversion. The perchlorate anions are disordered in four parts but the oxygen atoms on only two major components were found in Difference Fourier maps and refined anisotropically. Only the Cl atoms of the minor disordered parts were found and refined. In **3**, a single guest 4,4'-bipy has one pyridyl ring disordered. The S atom of one coordinated DMSO molecule is disordered as well. The site occupation factors of the disordered parts were dependently refined to 0.88(1) for the major part and consequently 0.12(1) for the minor part; S' was refined with an isotropic thermal parameter. For both perchlorate anions, disorder was found each in two positions and their site occupation factors were dependently refined to 0.69(1) and 0.31(1) for one anion, and 0.50(1) for each part of the second disordered anions. A total of 428 and 427 parameters were refined employing  $F^2$  in the final cycle using 4328 and 4393 reflections with  $I > 2\sigma(I)$  to yield  $R_1$  of 7.72 % and 7.79 % and  $wR_2$  of 21.58 % and 22.38 % for **1** and **2**, respectively. A total of 755 parameters were refined employing  $F^2$  in the final cycle using 10055 reflections with  $I > 2\sigma(I)$  to yield  $R_1$  and  $wR_2$  of 5.62 % and 12.61 %, respectively, for **3**.

### Thermal Analysis

Thermogravimetric analyses (TGA) of the title compounds were performed on a computer-controlled Hi Res TGA 2950 thermogravimetric analyzer. Powdered samples of **1** (4.5740 mg), **2** (3.7460 mg), and **3** (6.3730 mg) were loaded into alumina pans and heated with a ramp rate of 10 °C/min from room temperature to 600 °C. Thermal

desorption mass spectrometry measurements were recorded on a MAT 95 utilizing electron ionization techniques. Crystalline samples, contained within capillary tubes, were evacuated, loaded into direct insertion probes, and heated with a ramp rate of 10 °C / min from 30 °C to 400 °C.

### **Magnetic Measurements**

Bulk magnetization measurements were obtained from a standard Quantum Design MPMS SQUID magnetometer. The samples consisted of randomly oriented single crystals with a total mass of 32.3 mg for **1**, 19.4 mg for **2**, and 51.0 mg for **3**. A gel cap and plastic straw were used as the sample holder during the measurements.

Magnetization versus temperature measurements were run from 2 K to 300 K. The sample was zero-field cooled to 2 K before a measuring field of 1000 G was applied and the data set was then taken while warming the sample from the lowest temperature.

Magnetization versus field measurements were performed at 2 K from 0 to 50 kG. The background signals arising from the gel cap and straw were measured independently and subtracted from the results. The diamagnetic contribution of each sample, estimated from Pascal's constants ( $\chi_D = -446 \times 10^{-6} \text{ emu mol}^{-1}$  for **1** and **2** and  $\chi_D = -516 \times 10^{-6} \text{ emu mol}^{-1}$  for **3**) was also subtracted from the results.<sup>5,6</sup>

ESR spectra were recorded with a Bruker ER 200D spectrometer modified with a digital signal channel and digital field controller. Data were collected using a U. S. EPR SPEC300 data acquisition program and converted to ASCII format using a U. S. EPR EPRDAP data analysis program.

## Results and Discussion

### Compound Synthesis

The network coordination polymers **1**, **2**, and **3** were synthesized by the direct combination of one mole of  $M(\text{ClO}_4)_2 \cdot 6\text{H}_2\text{O}$  ( $M = \text{Ni(II)}$ ,  $\text{Co(II)}$ , or  $\text{Cu(II)}$ ) with three moles of 4,4'-bipyridine in solution. Note that the products contain more than three equivalents of bipy, some present as enclathrated guest molecules in addition to the coordinated ligands.

Since the bipy ligand is relatively insoluble in water, the reaction conditions afforded by the hydrothermal technique are essential for the crystallization of **1** and **2** where the metal-bipy suspension is dissolved by the high temperature ( $150^\circ\text{C}$ ) and pressure conditions within the vessel. In order to prevent the formation of unwanted side products, such as high oxidation state metal oxides particularly with cobalt, the reaction mixture was heated for no longer than 5 days, purged with argon gas, and treated with small quantities of ethanol (acting as a mild reducing agent). The products are sensitive to loss of solvent and become opaque within a few hours upon exposure to air. For **1** and **2**, small changes in the metal-bipy stoichiometry (for example, by using 2.5 or 3.5 moles of bipy per mole of  $\text{Ni(II)}$  or  $\text{Co(II)}$ ) always produced the same products.

Single crystals of **3** were obtained under normal laboratory conditions by crystallization from DMSO. Similar attempts employing hydrothermal synthesis resulted in the formation of impure powders. Crystalline products of **3** were obtained only several weeks due to the slow rate of evaporation of DMSO. Unlike **1** or **2**, crystals of **3** do not appear to be sensitive to loss of solvent. Furthermore, a secondary product crystallizes from solution in addition to **3**. During the first two to three weeks of crystallization, small blue blocks first appear followed by the crystallization of blue hexagonal plates of

**3** after an additional month or more. These blue blocks were determined to be an extended three-dimensional Cu(II)-4,4'-bipyridine network of the molecular formula  $[\text{Cu}_2(4,4'\text{-bipy})_5(\text{DMSO})_3(\text{ClO}_4)](\text{ClO}_4)_3 \cdot 3(\text{DMSO}) \cdot (\text{H}_2\text{O})$  with hydrophobic, rectangular, enclathrated channels that extend throughout the solid.<sup>156</sup> Reducing the concentration of bipy (2.5 moles of bipy per mole of copper), favors the formation of the three-dimensional network while at higher concentrations (3.0 moles and 3.5 moles of bipy per mole of copper), relatively equal quantities of **3** and the 3-D network crystallize from solution.

### Description of the Structures

Crystallographic and structural refinement data for **1**, **2**, and **3** are listed in Table 2-1. Selected bond angles and distances for **1**, **2**, and **3** are given in Tables 2-2, 2-3, and 2-4, respectively. Tables of atomic coordinates and thermal displacement parameters are provided in Appendix B.

#### Structure of $[\text{Ni}(4,4'\text{-bipy})_3(\text{H}_2\text{O})_2](\text{ClO}_4)_2 \cdot 1.4(4,4'\text{-bipy}) \cdot 3(\text{H}_2\text{O})$

The structure of **1** consists of one-dimensional cationic  $[\text{Ni}(4,4'\text{-bipy})_3(\text{H}_2\text{O})_2]^{2+}$  chains that pack to form layered sheets in the solid. The local coordination environment surrounding a typical Ni(II) ion is shown in Figure 2-1. The metal is six-coordinate and the coordination sphere consists of four pyridyl nitrogen donors, one from each of four 4,4'-bipyridine ligands and two oxygen atoms from two aqua ligands. The  $\text{NiN}_4\text{O}_2$  unit locally adopts an axially compressed octahedral geometry. The four nitrogen atoms define the equatorial plane and the oxygen atoms occupy the axial sites. Both Ni—O bond distances are equal (2.06 Å) but shorter than the Ni—N bonds. Furthermore, both of the Ni—N bonds from the terminal bipy ligands are equal (Ni—N21, and Ni—N21A =

Table 2-1. Summary of Crystallographic Data for **1**, **2**, and **3**

Empirical Formula	C <sub>44</sub> H <sub>46</sub> Cl <sub>2</sub> N <sub>9</sub> NiO <sub>13</sub>	C <sub>44</sub> H <sub>46</sub> Cl <sub>2</sub> N <sub>9</sub> CoO <sub>13</sub>	C <sub>50</sub> H <sub>52</sub> Cl <sub>2</sub> N <sub>10</sub> CuO <sub>10</sub> S <sub>2</sub>
Formula Weight	1038.51	1038.73	1199.62
Space Group	Monoclinic, C2/c	Monoclinic, C2/c	Monoclinic, Cc
<i>a</i> , Å	17.5696(8)	17.614(2)	19.0931(9)
<i>b</i> , Å	11.4101(5)	11.514(1)	11.1949(5)
<i>c</i> , Å	24.479(1)	24.604(2)	25.607(1)
$\alpha$ , deg	90	90	90
$\beta$ , deg	93.065(1)	92.448(2)	94.810(1)
$\gamma$ , deg	90	90	90
<i>V</i> , Å <sup>3</sup>	4900.4(4)	4985.6(9)	5454.0(4)
<i>Z</i>	4	4	4
<i>T</i> , K	173(2)	173(2)	173(2)
$\lambda$ (Mo K $\alpha$ ), Å	0.71073	0.71073	0.71073
$\rho_{\text{calc}}$ , g cm <sup>-3</sup>	1.408	1.384	1.461
$\mu$ , cm <sup>-1</sup>	5.76	5.21	6.44
R <sup>a</sup> (R <sub>w</sub> <sup>b</sup> )	0.0709 (0.2069)	0.0736 (0.2173)	0.0466 (0.1179)

$$^a R = \frac{\sum ||F_o| - |F_c||}{\sum |F_o|} \quad ^b R_w = \frac{\sum [(|F_o| - |F_c|)w^{1/2}]}{\sum [|F_o|w^{1/2}]}$$

Table 2-2. Selected Bond Lengths [Å] and Angles [°] for **1**<sup>a</sup>

Ni—O1	2.060	O1—Ni—O1A	179.82
Ni—O1A	2.060	N11—Ni—N11A	180.000
Ni—N11	2.127	N21—Ni—N21A	177.20
Ni—N11A	2.184	N11—Ni—N21	88.60
Ni—N21	2.115	N11—Ni—O1	89.91
Ni—N21A	2.115	N11A—Ni—N21	91.40
		N11A—Ni—O1	90.09
		N21—Ni—O1	92.44

<sup>a</sup> Symmetry transformations used to generate equivalent atoms: #1, -x, y, -z+3/2; #2, x, y+1, z; #3, x, y-1, z; #4, -x-1/2, -y+1/2, -z+2; #5, -x, -y+2, -z+2.

Table 2-3. Selected Bond Lengths [Å] and Angles [°] for **2**<sup>a</sup>

Co—O1	2.061	O1—Co—O1A	178.68
Co—O1A	2.061	N11—Co—N11A	180.000
Co—N11	2.180	N21—Co—N21A	176.37
Co—N11A	2.232	N11—Co—N21	88.19
Co—N21	2.168	N11—Co—O1	90.66
Co—N21A	2.168	N11A—Co—N21	91.81
		N11A—Co—O1	89.34
		N21—Co—O1	92.17

Table 2-4. Selected Bond Lengths [Å] and Angles [°] for  $3^a$ 

Cu—O1	2.396	N1—Cu—N1'	178.39
Cu—O2	2.376	N2—Cu—N3	179.25
Cu—N1	2.049	O1—Cu—O2	178.17
Cu—N2	2.025	N1—Cu—N2	91.09
Cu—N3	2.033	N1—Cu—N3	89.03
Cu—N1'	2.060	N1'—Cu—N2	90.51
S(1)—O1	1.507	N1'—Cu—N3	89.36
S(2)—O2	1.488	N1—Cu—O1	90.69
S(2')—O2	1.347	N2—Cu—O1	91.49
		N3—Cu—O1	87.78
		N1'—Cu—O1	89.13
		N1—Cu—O2	90.01
		N2—Cu—O2	86.81
		N3—Cu—O2	93.93
		N1'—Cu—O2	90.21
		S1—O(1)—Cu	141.6
		S2—O(2)—Cu	145.9
		S2'—O(2)—Cu	154.1

2.12 Å) but one of the Ni—N bonds (Ni—N11A = 2.18 Å) from a bridging bipy is longer than the other such bond (Ni—N11, 2.13 Å).

According to the spectrochemical series, water is a weaker field ligand than bipy and thus Ni—O bond distances should be longer than Ni—N bonds. The aqua ligands are expected to be the sites of an axial elongation. However, from the structural data, the opposite effect is observed. Steric repulsion from the pyridyl rings coordinated to the metal centers could cause a rather significant lengthening of Ni—N bonds. Note also that the hydrogen atoms from the coordinated water molecules hydrogen bond to the terminal nitrogen atoms from monodentate bipy's on adjacent chains thus polarizing the H—O bonds to a greater extent. The oxygen atom effectively becomes more negatively charged, and as a consequence, is more attracted to the positively charged metal center resulting in a smaller than expected Ni—O bond distance.

Two of the bipy ligands, coordinated *trans* with respect to one another, bridge the Ni(II) ions to form infinite one-dimensional linear chains that extend along the crystallographic *c*-axis. A single chain is depicted in Figure 2-2. The Ni—Ni distance along a chain is  $a/2$  units (11.41 Å). For each bridging bipy ligand, the pyridyl rings are not coplanar but twisted along the central C—C bond at an angle of 29.7° with respect to each other. Ignoring the uncoordinated guests, the metal:bipy stoichiometry in **1** is 1:3 since the bipy ligands perpendicular to the chains are monocoordinate.

The Ni—bipy chains are juxtaposed in a side-by-side fashion to form two-dimensional sheets within the crystallographic *bc*-plane. A typical sheet is shown in Figure 2-3. Within each sheet, the chain spacing is  $b/2$  units. In addition to packing forces, the sheets are held together by a combination of hydrogen bonding interactions between the protons of the coordinated water molecules and the terminal nitrogen atoms from the monodentate bipy ligands on adjacent chains (N—H bond distance of 1.81 Å) and offset  $\pi$ -stacking between the monocoordinate bipy ligands on adjacent chains. The face-to-face distance between these overlapping bipy groups is  $\sim 3.7$  Å. Note that in order to maximize the favorable  $\pi$ -stacking interactions, no twisting of the pyridyl rings is observed along the central C—C bond for these monodentate bipy ligands. The characteristic packing motif of the Ni—bipy chains produces rectangular, hydrophobic cavities within the sheets. Each cavity is defined by four nickel ions at the corners and along the sides by the faces of the two bridging bipy's and the edges of the two pairs of  $\pi$ -stacked terminal bipy ligands. The dimensions of the cavities are  $b/2 \times c$  and, if the Van der Waals radii of the carbon atoms from the bipy's are approximated as 1.7 Å, the effective size of the cavities is approximately 9.7 Å x 10.7 Å.

As shown in Figures 2-4 and 2-5, the sheets pack to form a layered solid-state structure along the crystallographic *c*-axis. Although the sheets align in registry along the *b*-axis, they are offset by  $\frac{1}{2}$  step in both the *a*- and *c* directions. The characteristic packing results in an alignment of the hydrophobic cavities to form oblique channels extending along the [2 0 -2] direction, as shown in Figure 2-6. The void space within hydrophobic pores and between the sheets is not empty but occupied by clathrated guest molecules and counterions acting to prevent the interpenetration of adjacent sheets.

The pores within the framework host are not empty, but occupied by enclathrated guest molecules and counterions (Figures 2-3 to 2-6). These lattice guests are extensively disordered throughout the solid thus leading to the rather high final refinement value in the structural solution. Approximately 1.5 crystallographically inequivalent, uncoordinated bipy molecules, each disordered about centers of inversion, are present per asymmetric structural unit. Extensive hydrogen bonding interactions between the lattice waters and the coordinated waters, perchlorate ions, and bipy guests are present throughout the channels. The clathrated bipy molecules seem to form a secondary lattice of organic molecules interpenetrated within the porous network structure of **1**. Coordination polymers with both guest enclathrated and empty cavities and channels present throughout the solid are known. 40,44,47,69,70,95,109,114

Each rectangular cavity in **1** clathrates an uncoordinated 4,4'-bipy molecule stabilized by both weak hydrogen bonding and hydrophobic interactions. These guests are crystallographically centrosymmetric and disordered about a center of inversion. The guest is positioned approximately at the center of the cavity such that the edges of one pair of borders (the pair of  $\pi$ -stacked monocoordinate bipy ligands) is directed toward

the faces of the guest and the faces of the other pair of borders (the bipy bridges) is directed toward the edges of the guest with the edge-to-face distances of *ca.* 2.5 Å – 3.0 Å. Note that the pyridyl rings of this bipy molecule are coplanar. The interior hydrogen atoms from the bipy form both two- and three-center hydrogen bonds with one (2.39 Å) and two oxygen atoms (2.29 Å and 2.53 Å), respectively, from nearby perchlorate counterions.

Uncoordinated, disordered bipy guests are clathrated between the sheets of **1** and are stabilized by  $\pi$ -stacking and hydrogen bonding interactions as well. Each face directed toward the space between the sheets from the pair of monocoordinate bipy ligands that comprise part of the borders of the hydrophobic cavities interacts with a single such bipy guest. These guests stack in an offset parallel fashion with the pair of  $\pi$ -stacked monocoordinate bipy ligands that comprise part of the borders of the cavities with a face-to-face distance of *ca.* 3.3 Å, indicative of  $\pi$ -stacking interactions. Note that these bipy guests are oriented almost perpendicular with respect to the bipy's clathrated within the cavities. The terminal nitrogen atoms from these bipy's form hydrogen bonds (2.48 Å) with oxygen atom from nearby perchlorate counterions.

The lattice water molecules are positioned in the vicinity of the bridging bipy ligands and the perchlorate counterions are in close proximity to the bipy guests located between the sheets. One of the lattice water molecules simultaneously hydrogen bonds with a proton from the coordinated water molecule (H—O, 1.99 Å), the terminal nitrogen atom from the bipy molecules between the sheets (N—O, 2.64 – 2.82 Å), the oxygen atom of a nearby perchlorate counterion (O—O, 2.82 Å), and another nearby lattice water

molecule (O—O, 2.84 Å). This second lattice water molecule also hydrogen bonds with an oxygen atom from a neighboring perchlorate counterion (2.07 Å).

The structure of **1** bears close resemblance to a compound reported by Yaghi and coworkers,  $[\text{Ni}(4,4'\text{-bipy})_{2.5}(\text{H}_2\text{O})_2](\text{ClO}_4)_2 \cdot 1.5(4,4'\text{-bipy}) \cdot 2(\text{H}_2\text{O})$ .<sup>114</sup> Though this material is a covalent molecular railroad as opposed discrete 1-D chains, both structures incorporate both bridging and terminal bipy ligands as well as 4,4'-bipy enclathrated channels. The Ni—N(bridging) distances (2.13 Å – 2.19 Å) in **1** are comparable to those found in the railroad structure (2.11 Å) but are larger than those found in the *cis*-chain  $[\text{Ni}(4,4'\text{-bipy})(\text{Et-XA})_2] \cdot 0.5(\text{EtOH}) \cdot (\text{CHCl}_3)$  (2.07 Å – 2.09 Å, Et-XA = ethylcarbonadithiolate)<sup>98</sup> and the 2-D covalent grid  $[\text{Ni}(4,4'\text{-bipy})(\text{ox})]$  (2.09 Å, ox = oxalato).<sup>40</sup> The Ni—N(terminal) distances (2.115 Å) of **1** are also similar to those found in  $[\text{Ni}(4,4'\text{-bipy})_{2.5}(\text{H}_2\text{O})_2](\text{ClO}_4)_2 \cdot 1.5(4,4'\text{-bipy}) \cdot 2(\text{H}_2\text{O})$  (2.15 Å). Furthermore, Ni—O distances (2.06 Å) are also close to those in the Yaghi structure (2.08 Å) and in  $[\text{Ni}(4,4'\text{-bipy})(\text{ox})]$  (Ni—O(oxalato) bonds) (2.05 Å). All O—Ni—O, N(bridging)—Ni—N(bridging), and N(terminal)—Ni—N(terminal) angles are 180° and O—Ni—N and N(bridging)—Ni—N(terminal) angles are close to 90°.

#### **Structure of $[\text{Co}(4,4'\text{-bipy})_3(\text{H}_2\text{O})_2](\text{ClO}_4)_2 \cdot 1.4(4,4'\text{-bipy}) \cdot 3(\text{H}_2\text{O})$**

Other than substituting the metal center Co(II) for Ni(II) and small differences in characteristic bond angles and distances, the structure of **2** is virtually identical to **1** and thus no pictures or description is given. The structure of **2** resembles the *trans*-1-D chain compounds reported by Jacobson and coworkers,  $[\text{Co}(4,4'\text{-bipy})(\text{SO}_4)(\text{H}_2\text{O})_2] \cdot 2(\text{H}_2\text{O})$  and  $[\text{Co}(4,4'\text{-bipy})(\text{Cl})_2(\text{DMSO})_2]$  where the solvent molecules and counterions, not terminal bipy ligands, occupy the non-bridging coordination sites on the metal centers.<sup>96</sup>

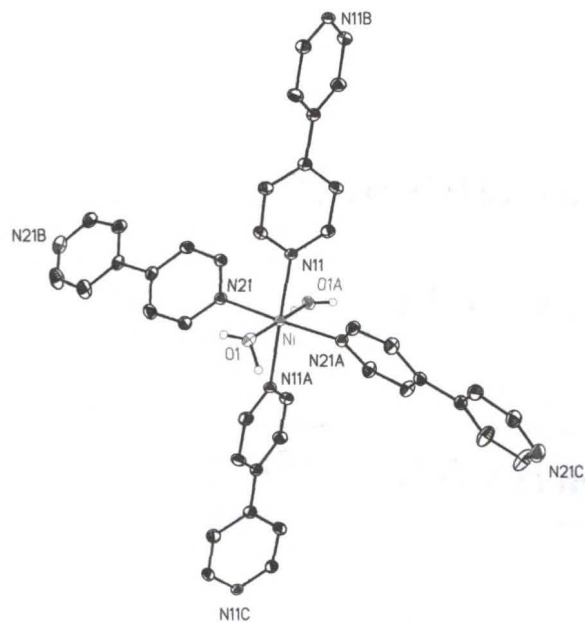


Figure 2-1. The local coordination environment of a typical Ni(II) metal center in compound **1**. All aromatic hydrogen atoms have been omitted for clarity. All non-hydrogen atoms are represented by thermal ellipsoids drawn to encompass 30 % of electron density.

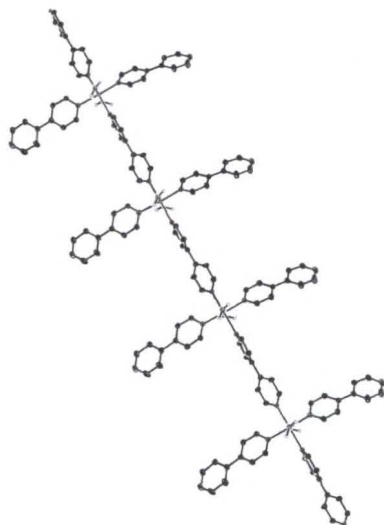


Figure 2-2. The structure of compound **1** along the crystallographic *c*-axis representing a linear, one-dimensional Ni-bipy chain. All aromatic hydrogen atoms have been omitted for clarity. All non-hydrogen atoms are represented by thermal ellipsoids drawn to encompass 30 % of electron density.

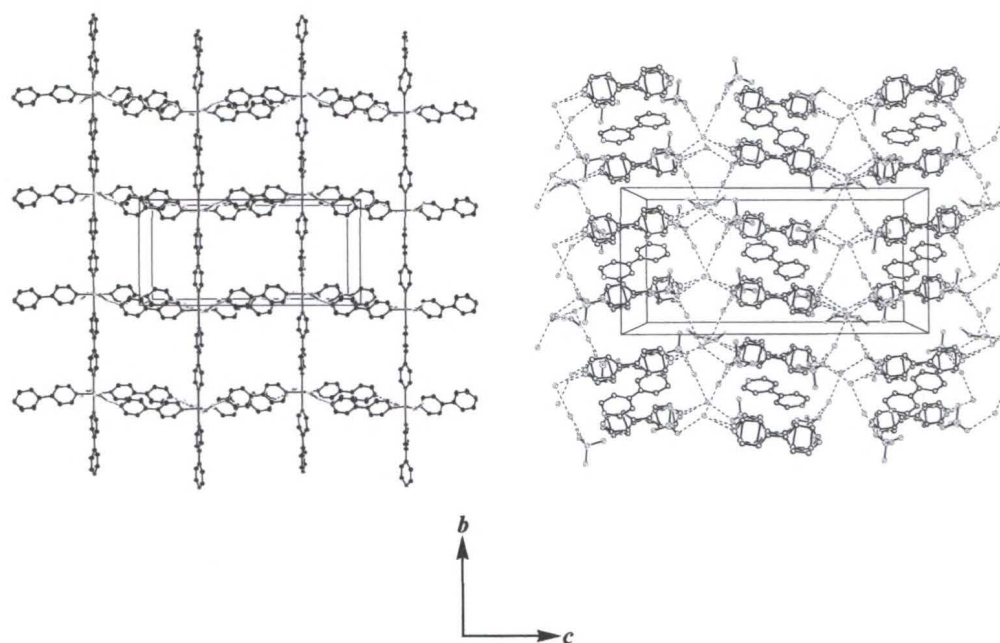


Figure 2-3. The structure of compound 1 within the crystallographic  $bc$ -plane representing a two-dimensional sheet (left) with the accompanying guests and counterions (right). For clarity, the aromatic hydrogen atoms and guests in the left-hand figure have been omitted and the coordinated guests have been omitted in the right-hand figure.

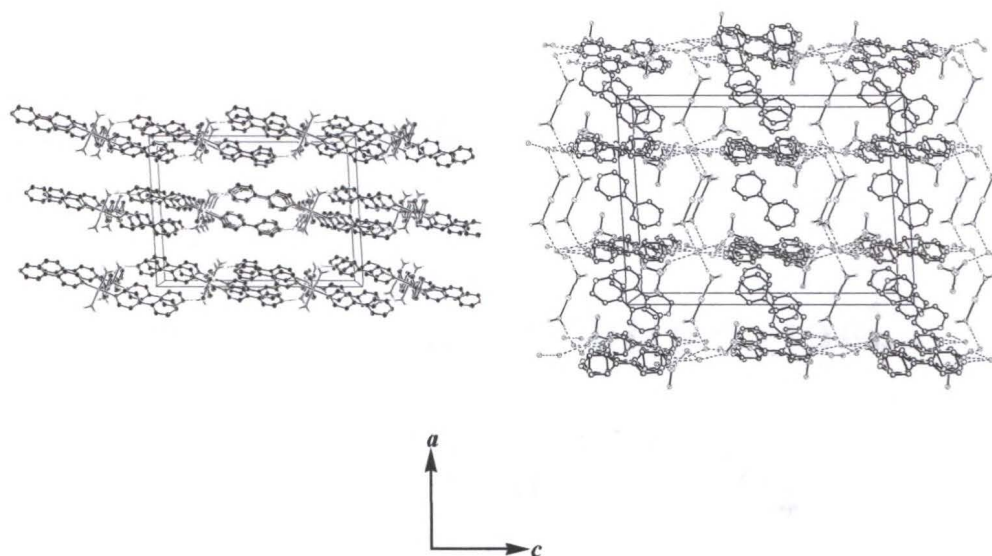


Figure 2-4. The structure of compound **1** within the crystallographic *ac*-plane showing the layered two-dimensional sheets (left) with the accompanying guests and counterions (right). For clarity, the aromatic hydrogen atoms and guests in the left-hand figure have been omitted and the coordinated bipy ligands have been omitted in the right-hand figure.

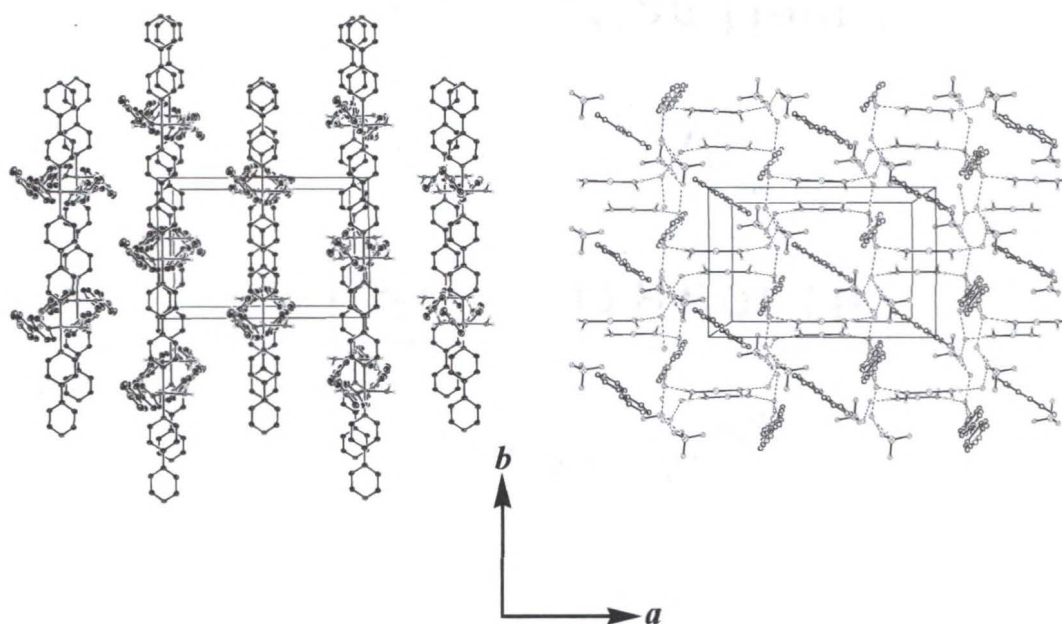


Figure 2-5. The structure of compound **1** within the crystallographic  $ab$ -plane showing the layered two-dimensional sheets (left) with the accompanying guests and counterions (right). For clarity, the aromatic hydrogen atoms and guests in the left-hand figure have been omitted and the coordinated bipy ligands have been omitted in the right-hand figure.

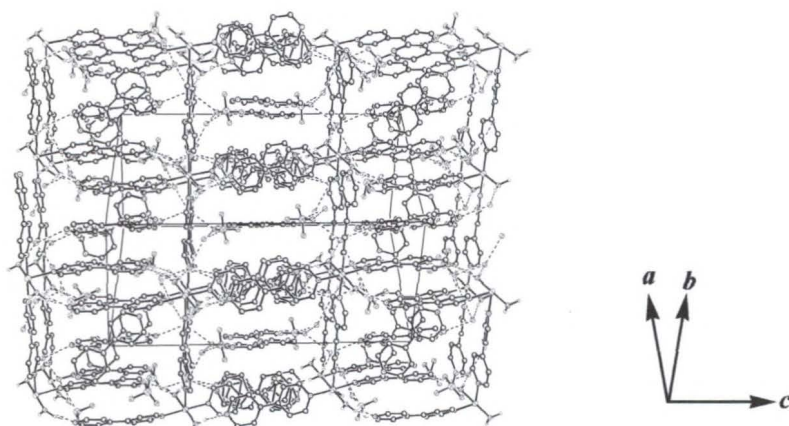


Figure 2-6. The hydrophobic channels in compound **1** that extend along the  $[2\ 0\ -2]$  direction with the accompanying guests and counterions. For clarity, the aromatic hydrogen atoms have been omitted.

The Co—N(bridging) distances (2.18 – 2.23 Å) in **2** are comparable to those in the chains [Co(SO<sub>4</sub>)(H<sub>2</sub>O)<sub>3</sub>(4,4'-bipy)]·2(H<sub>2</sub>O) (~ 2.17 Å)<sup>96</sup> as well as in the 2-D covalent grid [Co(4,4'-bipy)(ox)] (2.15 Å, ox = oxalato).<sup>40</sup> All Co—N distances in **2** are larger than the corresponding Ni—N distances in **1**. The Co—O distances in **2** (2.06 Å) are also comparable with those in [Co(4,4'-bipy)(SO<sub>4</sub>)(H<sub>2</sub>O)<sub>2</sub>]·2(H<sub>2</sub>O) (2.08 Å) and [Co(4,4'-bipy)(ox)] (2.08 Å).

### Structure of [Cu(4,4'-bipy)<sub>3</sub>(DMSO)<sub>2</sub>](ClO<sub>4</sub>)<sub>2</sub>·2(4,4'-bipy)

The structure of **3** consists of one-dimensional cationic [Cu(4,4'-bipy)<sub>3</sub>(DMSO)<sub>2</sub>]<sup>2+</sup> chains that pack to form layered sheets in the solid. Although **3** is structurally related to **1** and **2**, some important differences are present. The local coordination environment surrounding a typical Cu(II) ion is shown in Figure 2-7. The metal is six-coordinate and the coordination sphere consists of four pyridyl nitrogen donors, one from each of four 4,4'-bipyridine ligands and two oxygen atoms from ligated DMSO molecules. One DMSO ligand per metal center is disordered about the sulfur atom. The CuN<sub>4</sub>O<sub>2</sub> unit locally adopts an axially elongated octahedral geometry. The four nitrogen atoms define the equatorial plane and the oxygen atoms occupy the axial sites. Both Cu—O bond distances are equal (2.40 Å) and longer than the Cu—N bonds. Furthermore, the Cu—N bonds from the terminal bipy ligands (2.02 – 2.03 Å) are shorter than the Cu—N bonds from the bridging bipy ligands (2.05 – 2.06 Å).

Two of the bipy ligands, coordinated *trans* with respect to one another, bridge the Cu(II) ions to form infinite one-dimensional linear chains that extend along the crystallographic *c*-axis. A single chain is depicted in Figure 2-8. The Cu—Cu distance along a chain is approximately *a*/2 units (11.2 Å). For each bridging bipy ligand, the

pyridyl rings are not coplanar but twisted along the central C—C bond at an angle of  $61.4^\circ$  with respect to each other, considerably larger than the similar such dihedral angles observed in **1** and **2**. Ignoring the uncoordinated guests, the metal:bipy stoichiometry in **1** is 1:3 since the bipy ligands perpendicular to the chains are monocoordinate.

The Cu—bipy chains are juxtaposed in a side-by-side fashion to form quasi-two-dimensional sheets within the crystallographic *bc*-plane. A typical sheet is shown in Figure 2-9. Within each sheet, the chain spacing is approximately  $b/2$  units. Weak N—H contacts ( $2.6 \text{ \AA}$ ) between the terminal nitrogen atoms from the bipy ligands with the nearby hydrogen atoms from the bridging bipy ligands on adjacent chains and S—H contacts ( $2.9 \text{ \AA}$ ) between the hydrogen atoms near the terminal nitrogen atoms from the monocoordinate bipy ligands with the neighboring sulfur atoms from DMSO ligands on adjacent chains are present. Additionally, offset  $\pi$  stacking are observed between the monocoordinate bipy ligands on adjacent chains. The face-to-face distance between these overlapping bipy groups is  $\sim 3.8 \text{ \AA}$ . The pyridyl rings on the monocoordinate bipy ligands are twisted  $11.9^\circ$  along the central C—C bond with respect to one another thus likely reducing the effectiveness of the stabilizing  $\pi$  interactions between the bipy pairs. The characteristic packing motif of the Cu—bipy chains produces rectangular, hydrophobic cavities within the sheets. Each cavity is defined by four copper ions at the corners and along the sides by the faces of the two bridging bipy's and the edges of the two pairs of  $\pi$ -stacked terminal bipy ligands. The dimensions of the cavities are  $b/2 \times c$  and, if the Van der Waals radii of the carbon atoms from the bipy's are approximated as  $1.7 \text{ \AA}$ , the effective size of the cavities is approximately  $9.5 \text{ \AA} \times 11.3 \text{ \AA}$ , slightly larger than the cavities present in **1** and **2**.

As shown in Figures 2-10 and 2-11, the sheets pack to form a layered solid-state structure along the crystallographic *c*-axis. Although the sheets align in registry along the *b*-axis, they are offset by  $\frac{1}{2}$  step in both *a* and *c*. The characteristic packing results in an alignment of the hydrophobic cavities to form oblique channels extending along the [2 0 -2] direction, as shown in Figure 2-12, just as in **1** and **2**. Note the hydrophobic interactions between the nearest neighbor methyl groups from DMSO ligands between the sheets.

The pores within the framework host are not empty, but occupied by enclathrated guest molecules and counterions as shown in Figures 2-9 to 2-12. The lattice guests are relatively less disordered in **3** compared to **1** and **2** thus resulting in a better structural refinement. Two crystallographically inequivalent, uncoordinated bipy molecules are present per asymmetric structural unit. Hydrogen bonding interactions between the perchlorate ions, bipy guests, and the host are observed but weaker and less prevalent than those similar interactions present in **1** and **2**. Again, the clathrated bipy molecules seem to form a secondary lattice of organic molecules interpenetrated within the porous network structure of **3**.

Each rectangular cavity of **3** clathrates an uncoordinated 4,4'-bipy molecule stabilized by hydrophobic interactions with the host framework. One pyridyl ring per guest is disordered about the central C—C bond. Unlike in **1** and **2**, the guest is not positioned at the center of the cavity. The edges of one pair of borders (the pair of  $\pi$ -stacked monocoordinate bipy ligands) is directed toward the faces of the guest and the faces of the other pair of borders (the bipy bridges) is directed toward the edges of the guest with the edge-to-face distances of *ca.* 2.9 Å – 3.8 Å. Note that the pyridyl rings of

this bipy molecule are slightly twisted  $12.6^\circ$  with respect to each other along the central C—C bond.

Uncoordinated, bipy guests are clathrated between the sheets of **3** and are stabilized by  $\pi$ -stacking and hydrogen bonding interactions as well. Unlike in **1** and **2**, these guests are not disordered. Each face directed toward the space between the sheets from the pair of monocoordinate bipy ligands that comprise part of the borders of the hydrophobic cavities interacts with a single such bipy guest. These guests stack in an offset parallel fashion with the pair of  $\pi$ -stacked monocoordinate bipy ligands that comprise part of the borders of the cavities with a face-to-face distance of *ca.* 3.7 Å, indicative of  $\pi$ -stacking interactions. Note that these bipy guests are oriented almost perpendicular with respect to the bipy's clathrated within the cavities. The terminal nitrogen atoms from these bipy's form weak N—H contacts (2.6 Å) with hydrogen atoms from nearby bridging bipy ligands that are part of the framework.

The perchlorate counterions are in close proximity to the bipy guests located between the sheets. The perchlorate oxygen atoms are observed to weakly interact with hydrogen atoms from the bridging bipy ligands (O—H contacts of 2.4 Å), both interior hydrogen atoms from the monocoordinate bipy ligands (O—H contacts of 2.4 – 2.6 Å), and the hydrogen atoms from DMSO ligands (O—H contacts of 2.5 Å).

Unlike in **1** or **2**, the Cu—O bonds are longer than the Cu—N bonds in **3**. The DMSO molecules are weaker field ligands compared to the bipy ligands and, in combination with the Jahn-Teller effect, the solvent molecules are located on the axially distorted coordination sites. The Cu—N(bridging) distances (2.03 – 2.06 Å) are comparable to those in the 1-D chains  $[\text{Cu}(4,4'\text{-bipy})(\text{SO}_4)(\text{H}_2\text{O})_3]\cdot 2(\text{H}_2\text{O})$  (2.05

Å)<sup>69</sup> but smaller than the corresponding distances (1.99 Å) in [Cu(4,4'-bipy)(FBF<sub>3</sub>)<sub>2</sub>(H<sub>2</sub>O)<sub>2</sub>](4,4'-bipy).<sup>92</sup> All Cu—N distances in **3** are smaller than the corresponding Ni—N and Co—N distances in **1** and **2**, respectively. The Cu—O distances (2.06 Å) are comparable with the those in [Cu(4,4'-bipy)(SO<sub>4</sub>)(H<sub>2</sub>O)<sub>3</sub>]<sub>2</sub>(H<sub>2</sub>O) (1.95 Å – 2.2 Å). All O—Cu—O, N(bridging)—Cu—N(bridging), and N(terminal)—Cu—N(terminal) angles are close to 180° but O—Cu—N and N(bridging)—Cu—N(terminal) angles deviate from 90°, more so than in **1** and **2**, where N(bridging) and N(terminal) denote the nitrogen atoms from bridging and terminal bipy ligands, respectively.

### Thermal Properties

Compounds **1** and **2** are unstable in air due to loss of enclathrated guest molecules. The compounds can be kept in humid environment or under solvent, but both compounds discolor and change texture if left in laboratory atmosphere within a few hours. Thermogravimetric analysis (TGA) and thermal desorption mass spectrometry show the stepwise loss of water followed by uncoordinated bipyridine. From Figure 2-13, mass loss between room temperature and 56 °C corresponds to three moles of water corresponding to guest water molecules in the chemical formula. Water continues to be released up to near 150 °C. Above 85 °C, bipyridine is lost continuously up to approximately 250 °C. The TGA plot of **2**, shown in Figure 2-14 undergoes similar, but somewhat more complex, guest molecule loss process. Note that the onset temperature for the guest loss in **1** is significantly lower (by approximately 30 °) compared to **2**.

In contrast to **1** and **2**, the copper compound **3** is stable in air at room temperature. Without solvent molecule guests, it does not experience the same decomposition process.

From Figure 2-15, the first mass decrease observed by TGA occurs above 100 °C and corresponds to loss of guest bipyridine molecules.

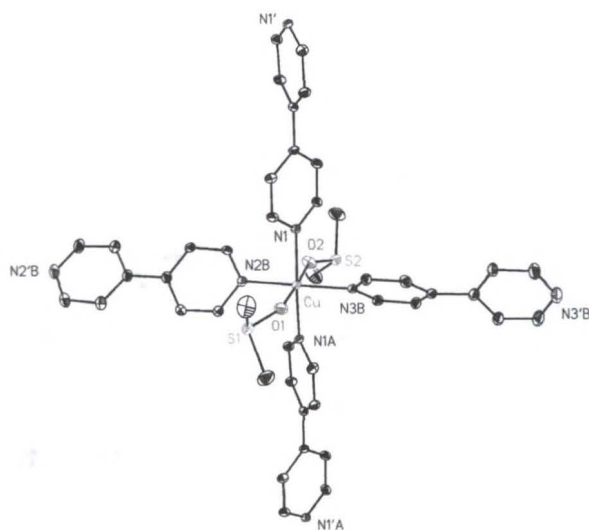


Figure 2-7. The local coordination environment of a typical Cu(II) metal center in compound 3. All hydrogen atoms have been omitted for clarity. All non-hydrogen atoms are represented by thermal ellipsoids drawn to encompass 30 % of electron density.

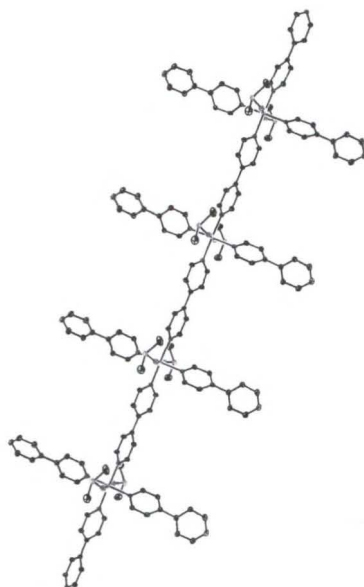


Figure 2-8. The structure of compound **3** along the crystallographic *c*-axis representing a linear, one-dimensional Cu-bipy chain. All hydrogen atoms have been omitted for clarity. All non-hydrogen atoms are represented by thermal ellipsoids drawn to encompass 30 % of electron density.

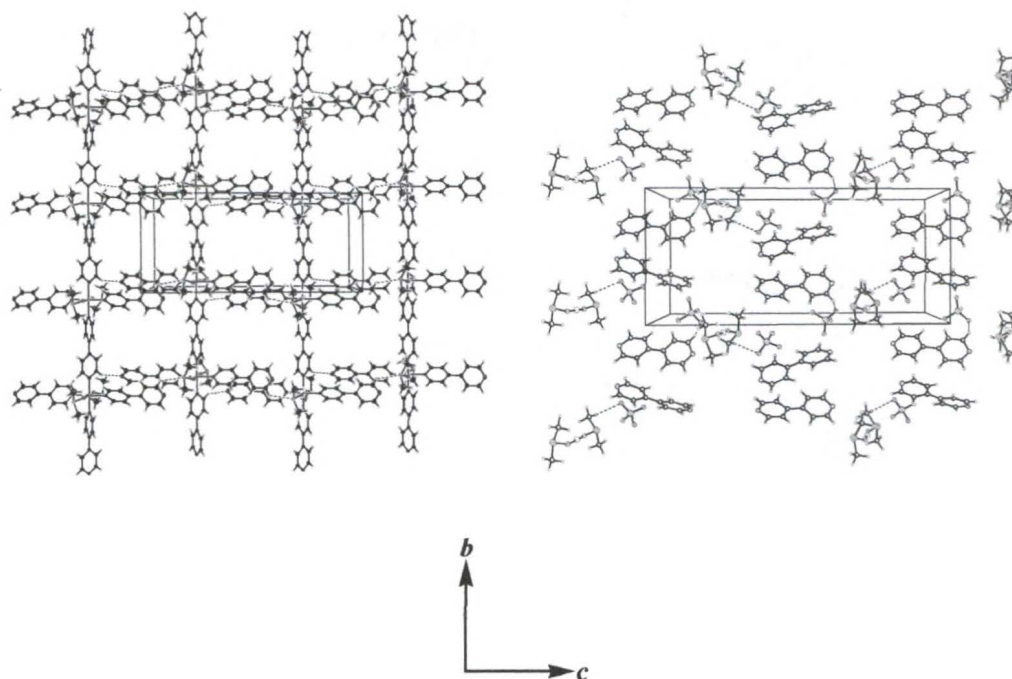


Figure 2-9. The structure of compound **3** within the crystallographic  $bc$ -plane representing a two-dimensional sheet (left) with the accompanying guests and counterions (right). For clarity, the guests have been omitted in the left-hand figure and the coordinated bipy ligands have been omitted in the right-hand figure.

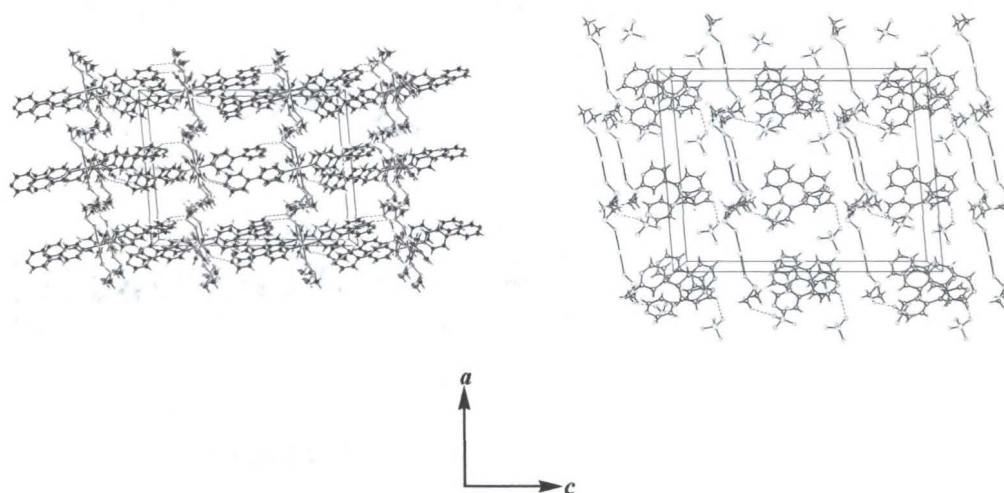


Figure 2-10. The structure of compound **3** within the crystallographic *ac*-plane showing the layered two-dimensional sheets (left) with the accompanying guests and counterions (right). For clarity, the guests have been omitted in the left-hand figure and the coordinated bipy ligands have been omitted in the right-hand figure.

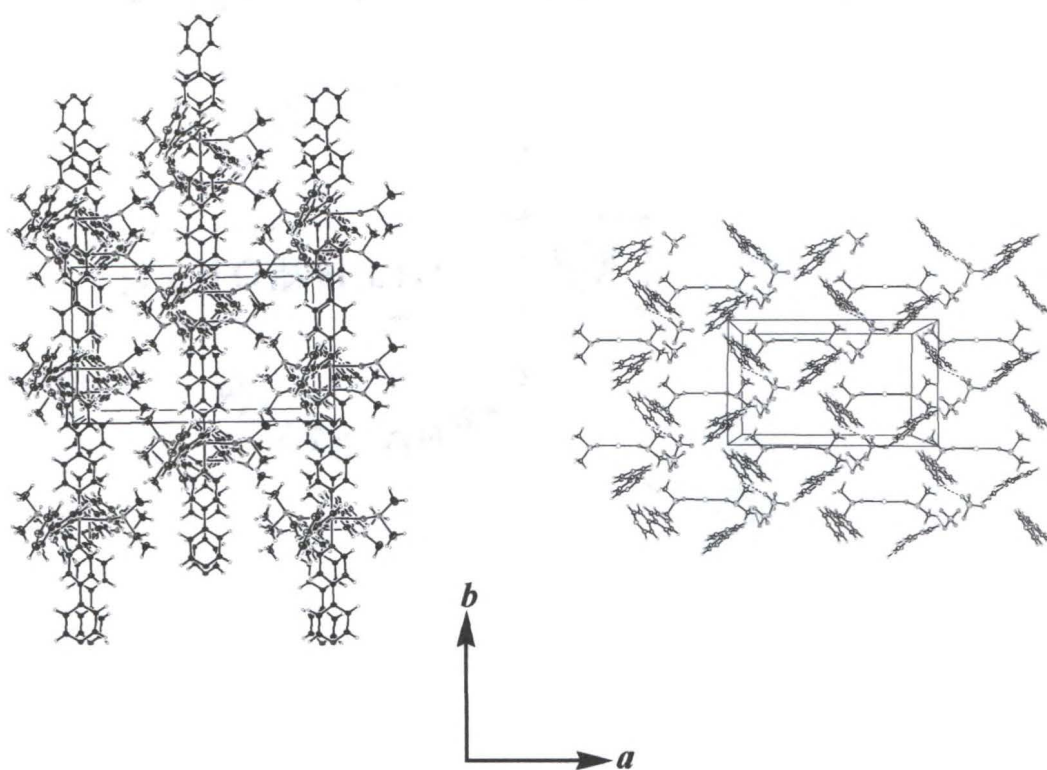


Figure 2-11. The structure of compound **3** within the crystallographic  $ab$ -plane showing the layered two-dimensional sheets (left) with the accompanying guests and counterions (right). For clarity, the guests have been omitted in the left-hand figure and the coordinated bipy ligands have been omitted in the right-hand figure.

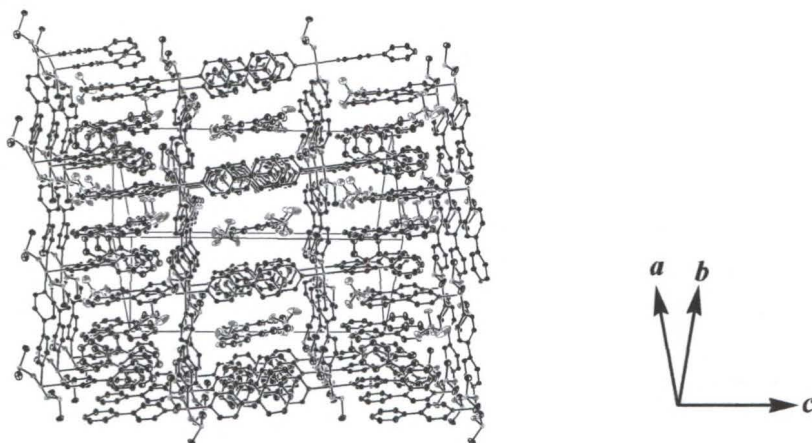


Figure 2-12. The hydrophobic channels within compound **3** that extend along the  $[2\ 0\ -2]$  direction with the accompanying guests and counterions. For clarity, the hydrogen atoms have been omitted.

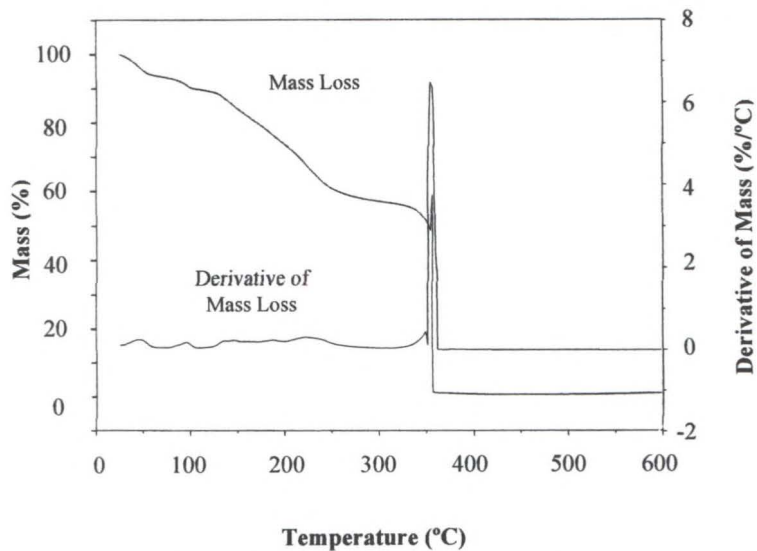


Figure 2-13. TGA thermogram of compound 1 depicting the observed mass loss and negative values of the first derivative ( $\% / ^\circ\text{C}$ ).

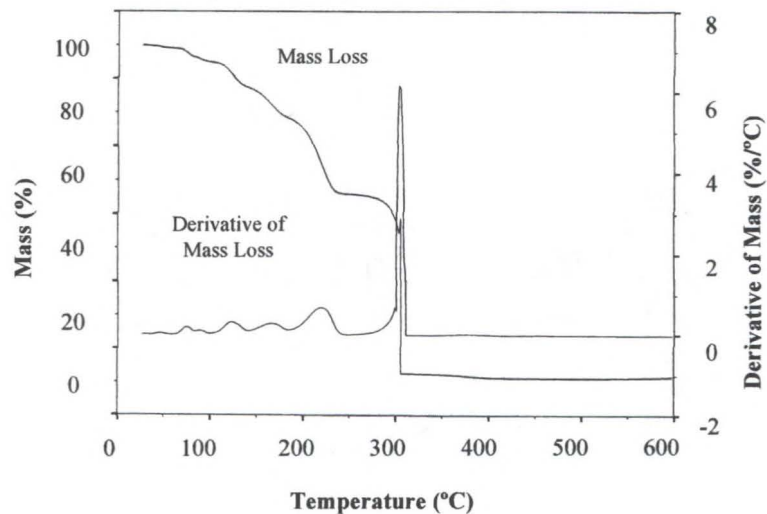


Figure 2-14. TGA thermogram of compound 2 depicting the observed mass loss and negative values of the first derivative ( $\% / ^\circ\text{C}$ ).

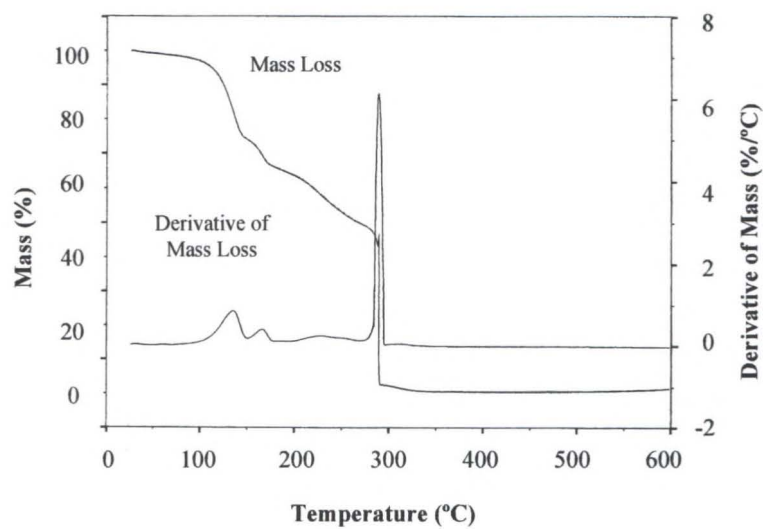


Figure 2-15. TGA thermogram of compound **3** depicting the observed mass loss and negative values of the first derivative (% / °C).

## Magnetic Properties

The molar magnetic susceptibility,  $\chi_M$ , and inverse molar susceptibility, at 1000 G over the temperature range of 2 K - 300 K for **1** and **3** are plotted in Figures 2-16 and 2-19, respectively. The molar magnetization,  $M_M$ , at 2 K over the field range of 0 – 50 kG for **1** and **3** are plotted in Figures 2-17 and 2-20, respectively. The molar magnetic susceptibility at 1000 G over the temperature range of 2 K-50 K for **2** is plotted in Figure 2-18.

### Magnetic Properties of $[\text{Ni}(\text{4,4}'\text{-bipy})_3(\text{H}_2\text{O})_2](\text{ClO}_4)_2 \cdot \text{1.4}(\text{4,4}'\text{-bipy}) \cdot \text{3}(\text{H}_2\text{O})$

The room temperature (*i.e.* 300 K) susceptibility ( $\chi_M = 4.2 \times 10^{-3} \text{ emu mol}^{-1}$ ) of **1** correlates well with the value expected for uncoupled,  $S = 1$  metal centers ( $\chi_M = 4.2 \times 10^{-3} \text{ emu mol}^{-1}$ ). Recall the structure of **1** consists of linear chains of 4,4'-bipyridine bridged Ni(II) ions. Since **1** is comprised of chains of Heisenberg  $S = 1$  spins that experience single-ion,  $D$ , and in-plane,  $E$ , anisotropies, an  $S = 1$ , one-dimensional chain model incorporating both zero-field splitting and exchange parameters is appropriate to fit the magnetic data. Only exchange interactions along the chains were considered; coupling between the chains was ignored since interchain bonding is noncovalent. The Heisenberg model is an appropriate starting point as octahedral Ni(II) complexes have nearly isotropic  $g$ -factors ( $g = 2.25$ ).<sup>5,157</sup> The Hamiltonian may be written as

$$\hat{H} = -J \sum_i \hat{\mathbf{S}}_i \cdot \hat{\mathbf{S}}_{i+1} + D \sum_i (\hat{S}_i^z)^2 + E \sum_i [(\hat{S}_i^x)^2 - (\hat{S}_i^y)^2] + g\mu_B B \cdot \sum_i \hat{\mathbf{S}}_i \quad (2-1)$$

where  $J$  is the exchange interaction,  $D$  is the single-ion anisotropy,  $E$  is the in-plane anisotropy, and  $B$  is the applied magnetic field.<sup>158</sup> From this Hamiltonian, the parallel,  $\chi_{\parallel}$ , and perpendicular,  $\chi_{\perp}$ , susceptibilities (neglecting the  $E$  parameter) are

$$\chi_{\parallel} = \chi_z = \frac{2N_A g_{\parallel}^2 \mu_B^2}{3k_B T} \left( 1 - \frac{D - 4zJ}{3k_B T} \right) \quad (2-2)$$

$$\chi_{\perp} = \chi_{x,y} = \frac{2N_A g_{\perp}^2 \mu_B^2}{3k_B T} \left( 1 - \frac{D + 8zJ}{6k_B T} \right) \quad (2-3)$$

and the susceptibility representing the average of contributions that are parallel and perpendicular to the chains, is

$$\chi_{ave} = \frac{1}{3}(\chi_{\parallel} + 2\chi_{\perp}) \quad (2-4)$$

since magnetic measurements were performed on randomly oriented samples.<sup>1</sup>

A theoretical treatment of the magnetization in the high field limit of the Hamiltonian given in Equation (2-1) has not yet been reported, however in the limit that  $J = 0$  and  $E = 0$ , expressions for the high field dependence of the magnetization do exist.<sup>1</sup> The expressions representing the magnetization perpendicular,  $M_{\perp}$ , and parallel,  $M_{\parallel}$ , to the chains (neglecting the  $E$  and  $J$  parameters) are

$$M_{\perp} = \frac{2N_A B_{\perp} g_{\perp}^2 \mu_B^2}{\sqrt{4g_{\perp}^2 \mu_B^2 B_{\perp}^2 + D^2}} \frac{-e^{-\frac{E_0}{kT}} + e^{-\frac{E_1}{kT}}}{e^{-\frac{D}{kT}} + e^{-\frac{E_0}{kT}} + e^{-\frac{E_1}{kT}}} \quad (2-5)$$

where

$$E_{0,1} = \pm \frac{\sqrt{4g_{\perp}^2 \mu_B^2 B_{\perp}^2 + D^2}}{2} + D \quad (2-6)$$

and

$$M_{\parallel} = \frac{N_A g_{\parallel} \mu_B \left\{ -e^{-\frac{E_2}{kT}} + e^{-\frac{E_3}{kT}} \right\}}{1 + e^{-\frac{E_2}{kT}} + e^{-\frac{E_3}{kT}}} \quad (2-7)$$

where

$$E_2 = g_{\parallel} \mu_B B_{\parallel} + D \text{ and } E_3 = -g_{\parallel} \mu_B B_{\parallel} + D \quad (2-8)$$

and the magnetization representing the average of contributions that are parallel and perpendicular to the chains, is

$$M_{ave} = \frac{1}{3} (M_{\parallel} + 2M_{\perp}) \quad (2-9)$$

for powdered samples.

The temperature dependence of the inverse susceptibility for **1** between 5 K and 50 K were fit by a simple Curie-Weiss law model and the results of the fit yield a Weiss temperature  $\theta = -2$  K, and from the Curie constant,  $g = 2.20$ . The temperature dependence of the low field susceptibility was fit using the expressions in Equations 2-2, 2-3, and 2-4, and the results of this analysis, when using  $g = 2.20$ , are given by the solid line in Figure 2-16, where  $J/k_B = -0.9$  K,  $D/k_B = 4.7$  K, and  $E = 0$ . The small, negative coupling constant suggests the presence of a weak antiferromagnetic exchange along the chains. Since these measurements were performed on randomly oriented samples, the sign of  $D$  cannot be unambiguously determined.<sup>6</sup> The  $D/|J|$  ratio of  $\sim 5$  suggests indicates that **1** is an example of a large  $D/|J|$  system with strong planar anisotropy.<sup>158-161</sup> Naturally, the fitting procedure would be significantly improved if the data extended to sufficiently low temperature so as to reveal the maximum of the susceptibility, observed at  $T = 2$  K.

The field dependence of the low temperature magnetization in Figure 2-17 was fit using the expressions in Equations 2-5 to 2-9. In the limit that  $J = 0$  and  $E = 0$ , the model provides a prediction that closely resembles the experimental data when  $g = 2.20$  and  $D/k_B \approx 7$  K. The analysis of the low field susceptibility indicates that  $D/|J| \approx 5$ , so the

approximation that  $J = 0$  is clearly not justified. Nevertheless, this analysis does provide an upper bound for the value of  $D$  and is consistent with the low field analysis. For the purpose of comparison, the  $S = 1$  Brillouin function, which is appropriate for zero exchange coupling effects, is plotted in Figure 10 as the dotted line. Once again, the data clearly suggest the presence of finite magnetic coupling in **1**.

The delocalized  $\pi$  system of 4,4'-bipyridine should allow the ligand to effectively mediate superexchange interactions when covalently bridging paramagnetic centers.<sup>5</sup> Furthermore, the coupling is expected to be antiferromagnetic as explained by a spin-polarization mechanism for the propagation of exchange interactions.<sup>154</sup> The magnitude of the coupling is small ( $J/k_B = -0.9$  K), but is consistent with the coupling constants measured for other similar bipy bridged complexes [Ni(Et-XA)<sub>2</sub>(4,4'-bipy-)]·0.5(EtOH)·(CHCl<sub>3</sub>) (Et-XA = ethylcarbonadithiolate),<sup>98</sup> [Mn(hfac)<sub>2</sub>(4,4'-bipy)] (hfac = hexafluoroacetylacetonato),<sup>97</sup> [Cu<sub>2</sub>(tren)<sub>2</sub>(4,4'-bipy)](BPH<sub>4</sub>)<sub>4</sub>,<sup>162</sup> [Cu<sub>2</sub>(dien)<sub>2</sub>(4,4'-bipy)(ClO<sub>4</sub>)<sub>2</sub>](ClO<sub>4</sub>)<sub>2</sub>,<sup>163</sup> and [Mn- $\mu$ -(4,4'-bipy)(4,4'-bipy)(NCS)<sub>2</sub>(H<sub>2</sub>O)<sub>2</sub>]<sub>n</sub>.<sup>164</sup> Since a typical  $sp^2-sp^2$  C—C single bond is 1.50 Å and a C=C double bond is 1.35 Å, the carbon—carbon bond between the pyridyl rings (1.49 Å) for each coordinated bipy ligand in **1** is principally of single bond character. The  $\pi$  orbital conjugation between these pyridyl rings is small and the rings twist along this central C—C single bond in order to minimize the steric repulsions felt by the interior hydrogen atoms.<sup>164</sup> This twisting disrupts the exchange along the  $\pi$ -orbital pathway and thus hindering the effectiveness of bipy to propagate a superexchange interaction between paramagnetic centers.

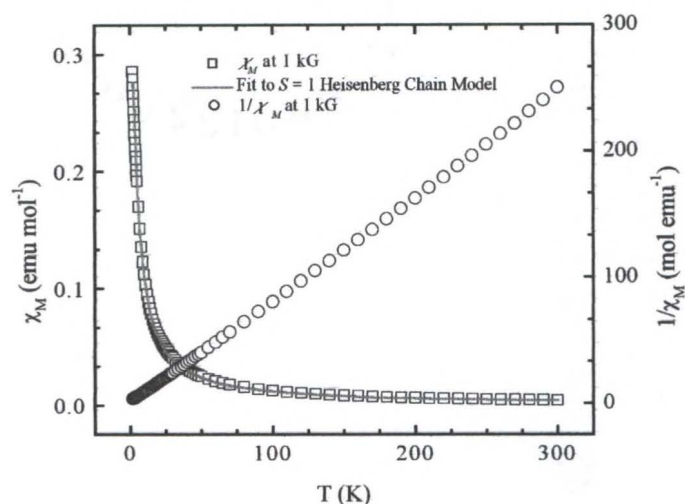


Figure 2-16. The molar magnetic susceptibility,  $\chi_M$ , and inverse susceptibility,  $1/\chi_M$ , at 1 kG from 2 K to 300 K for compound 1 are shown as open boxes and open circles, respectively. The data have been corrected for background signals arising from the sample container and diamagnetic contributions. The fit of  $\chi$  to the Heisenberg  $S = 1$  chain model from Equations 2-2, 2-3, and 2-4 is shown by the solid line.

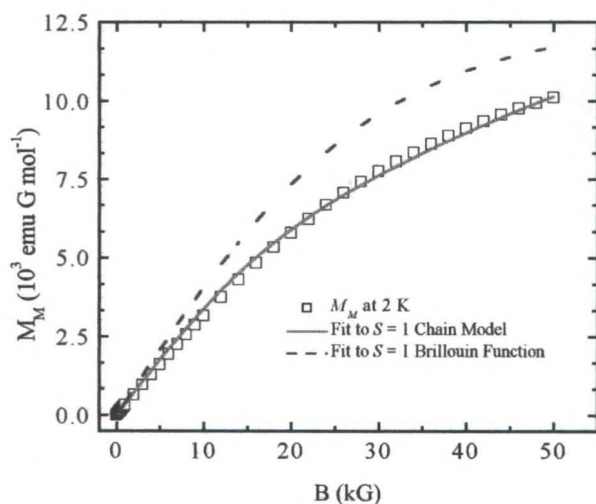


Figure 2-17. The molar magnetization ( $M_M$ ) at 2 K from 0 to 50 kG for compound 1 is shown as open boxes. The data have been corrected for background signals arising from the sample container. The fit of  $M$  to the  $S = 1$  chain model from Equations 2-5 to 2-9 and the  $S = 1$  Brillouin function is shown by the solid line and dotted line, respectively.

### Magnetic Properties of $[\text{Co}(\text{4,4}'\text{-bipy})_3(\text{H}_2\text{O})_2](\text{ClO}_4)_2 \cdot 1.4(\text{4,4}'\text{-bipy}) \cdot 3(\text{H}_2\text{O})$

A complete analysis of the magnetic data for **2** is more complicated compared to analogous Ni(II) and Cu(II) systems since, in Co(II) systems, spin-orbit coupling effects are important, a thermal dependence of the spin quantum number is observed (depopulation of  $S = 3/2$  state to  $S = 1/2$  state at low temperatures), and significant anisotropy in the  $g$ -factors is present.<sup>1,5,6</sup> The Co(II) ions of **2** form chains of Ising  $S = 1/2$  spins that assume an  $S = 1/2$  state at temperatures below 30 K. The  $S = 1/2$  Ising model is an appropriate starting point since octahedral Co(II) complexes have highly anisotropic  $g$ -factors.<sup>1,5,7</sup> Again, only exchange interactions along the chains were considered. The general Hamiltonian may be written as

$$\hat{H} = -2J \sum_{i \leq j} \alpha \hat{S}_i^z \cdot \hat{S}_j^z + \beta \hat{S}_i^x \cdot \hat{S}_j^x + \gamma \hat{S}_i^y \cdot \hat{S}_j^y + g\mu_B B \cdot \sum_i \hat{S}_i \quad (2-10)$$

where, in the Ising model,  $\alpha = 1$  and  $\beta = \gamma = 0$ , zero-field splitting terms have been neglected, and the remaining terms have the usual meaning. From this Hamiltonian, the parallel and perpendicular susceptibilities are

$$\chi_{\parallel} = \chi_z = \frac{N_A g_{\parallel}^2 \mu_B^2}{4k_B T} \exp\left(\frac{2|J|}{k_B T}\right) \quad (2-11)$$

$$\chi_{\perp} = \chi_{x,y} = \frac{N_A g_{\perp}^2 \mu_B^2}{8|J|} \left[ \tanh\left(\frac{|J|}{k_B T}\right) + \frac{|J|}{k_B T} \text{sech}^2\left(\frac{|J|}{k_B T}\right) \right] \quad (2-12)$$

and the susceptibility representing the average of contributions that are parallel,  $\chi_{\parallel}$ , and perpendicular,  $\chi_{\perp}$ , to the chains, is

$$\chi_{ave} = \frac{1}{3}(\chi_{\parallel} + 2\chi_{\perp}) \quad (2-13)$$

since magnetic measurements were performed on randomly oriented samples.<sup>1,7</sup>

Unlike Ni(II) systems, significant anisotropy with Co(II) spins is observed and a complete analysis of the magnetic behavior requires data from single crystals in different orientations with respect to their measuring magnetic field.<sup>1,5,6</sup> Since the reported experiments were performed on powder specimens, both perpendicular and parallel  $g$ -tensor components were unavailable. Thus, any meaningful fits to the low-temperature susceptibility data in the absence of known values of both  $J$  and  $g_{\parallel}$  and  $g_{\perp}$ -values are difficult. However, simulations of the low-temperature susceptibility from the Ising model from Equations 2-11, 2-12, and 2-13, shown in Figure 2-18, reproduced the data relatively well. The coupling constant was fixed at  $J = -0.4$  K, similar to the value obtained from fits to the susceptibility data of **1** (since **2** is isostructural to **1**). Three sets of  $g$ -values ( $g_{\parallel} = 8$  and  $g_{\perp} = 1.5$ ,  $g_{\parallel} = 6$  and  $g_{\perp} = 3.5$ , and  $g_{\parallel} = 4$  and  $g_{\perp} = 4.25$ ) were obtained for octahedral Co(II) ions from a universal curve reported by Carlin.<sup>5</sup> The fitting expression was also corrected for uncoupled,  $S = \frac{1}{2}$  impurities and fixed at a high limit of 10 %. The model incorporating all three sets of  $g$ -values reproduced the low-temperature susceptibility well, with the best results obtained for  $g_{\parallel} = 8$  and  $g_{\perp} = 1.5$ . Increasing or decreasing the magnitude of the coupling constant had resulted in poor simulations of the data. Thus, while it was not possible to unambiguously estimate the  $g$ -value components, the simulations provided a rough estimate of the sign and magnitude of the exchange parameter. Qualitatively speaking, the cobalt analog, **2**, also shows little evidence of magnetic exchange just as in **1** and **2**.

**Magnetic Properties of [Cu(4,4'-bipy)<sub>3</sub>(DMSO)<sub>2</sub>](ClO<sub>4</sub>)<sub>2</sub>·2(4,4'-bipy)**

For the case of the Cu(II) ions of **3**, the room temperature (*i.e.* 300 K) susceptibility ( $\chi_M = 1.2 \times 10^{-3} \text{ emu mol}^{-1}$ ) correlates well with the value expected for uncoupled,  $S = \frac{1}{2}$  metal centers ( $\chi_M = 1.3 \times 10^{-3} \text{ emu mol}^{-1}$ ). The temperature dependence of the molar magnetic susceptibility at 1 kG, shown in Figure 2-19, was fit well by the Curie law using a  $g$ -value of 2.06, as determined from room temperature ESR measurements. The field dependence of the molar magnetization up to 50 kG at 2 K, shown in Figure 2-20, was also fit well by the  $S = \frac{1}{2}$  Brillouin function, with a  $g$ -value of 2.06, which describes non-interacting magnetic spins.<sup>5,6</sup> Consequently, **3** behaves essentially as a chain of non-interacting,  $S = \frac{1}{2}$  metal centers that are uncoupled even at 2 K. The larger dihedral angles between the pyridyl rings on the bridging bipy ligands may disrupt the superexchange pathway to a greater extent than in **1** or **2** and could account for the lack of any observed exchange interaction.

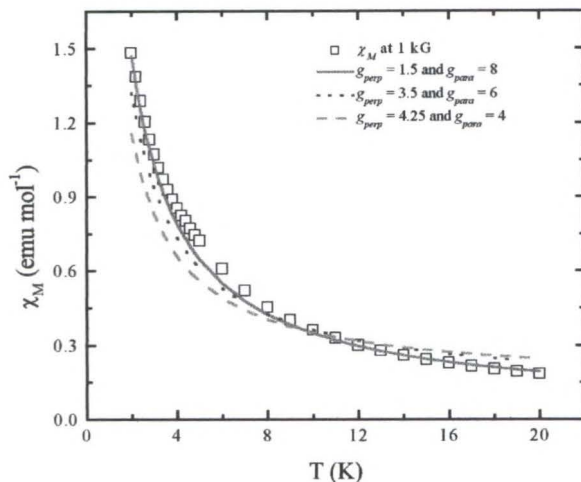


Figure 2-18. The molar magnetic susceptibility,  $\chi_M$ , at 1 kG from 2 K to 300 K for compound **2** is shown as open boxes. The data have been corrected for background signals arising from the sample container and diamagnetic contributions. The simulations of  $\chi$  to the  $S = \frac{1}{2}$  Ising model are from Equations 2-11, 2-12, and 2-13 where  $J$  is fixed at  $-0.4$  K while  $g_{\perp} = 1.5$  and  $g_{\parallel} = 8$  for the solid line,  $g_{\perp} = 3.5$  and  $g_{\parallel} = 6$  for the dotted line, and  $g_{\perp} = 4.25$  and  $g_{\parallel} = 4$  for the dashed line.

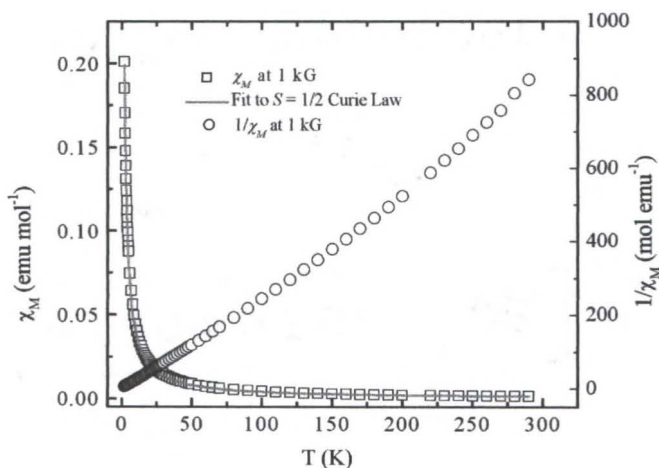


Figure 2-19. The molar magnetic susceptibility,  $\chi_M$ , and inverse susceptibility,  $1/\chi_M$ , at 1 kG from 2 K to 300 K for compound **3** are shown as open boxes and open circles, respectively. The data have been corrected for background signals arising from the sample container and diamagnetic contributions. The fit of  $\chi$  to the  $S = \frac{1}{2}$  Curie Law is shown by the solid line.

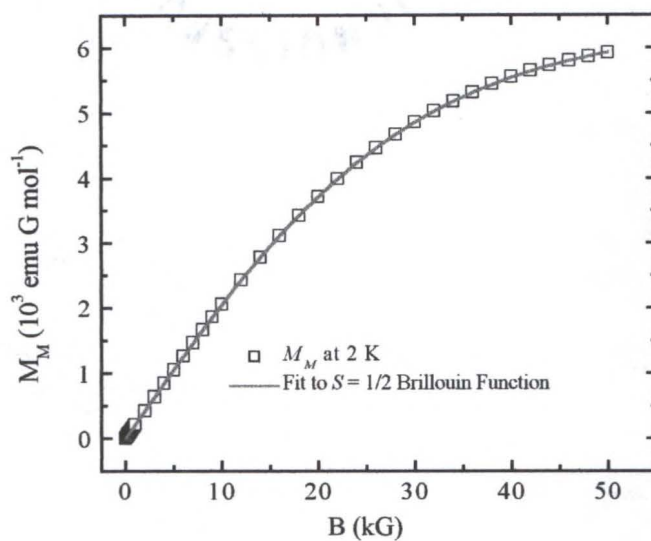


Figure 2-20. The molar magnetization ( $M_M$ ) at 2 K from 0 to 50 kG for compound **3** is shown as open boxes. The data have been corrected for background signals arising from the sample container. The fit of  $M$  to the  $S = 1/2$  Brillouin function is shown by the solid line.

## Conclusions

Three new hybrid organic-inorganic coordination polymers have been isolated and characterized. These materials consist of chains of transition metal ions (Ni(II), Co(II), and Cu(II)) bridged by 4,4'-bipyridine spacer ligands. The chains pack to form two-dimensional, non-interpenetrated sheets with hydrophobic, rectangular cavities present within the framework. The sheets, in turn, pack to form a three-dimensional structure with oblique channels containing enclathrated guest molecules and counterions extending throughout the solid. These enclathrated guests are easily lost suggesting that the samples are thermally unstable. In general terms, the magnetic properties of **1**, **2**, and **3** are similar in the sense that weak exchange interactions,  $J$ , are present between the metal centers.

Coordination polymers with hydrophobic cavities and channels extending throughout the solid-state structure have received much attention due to their ability to act as molecular sieves with size and shape specificity and catalytic substrates.<sup>37,44,45</sup> Compounds **1**, **2**, and **3** are clearly examples of network solids with cavities and channels that prefer to enclathrate hydrophobic guests (uncoordinated bipy molecules). The ability of these coordination polymer hosts to exchange guests is described in Chapter 3.

CHAPTER 3  
A  $^{31}\text{P}$  MAS NMR INVESTIGATION OF THE HOST-GUEST PROPERTIES OF TWO  
POROUS NETWORK SOLIDS,  
 $[\text{Ni}(4,4'\text{-bipy})_3(\text{H}_2\text{O})_2](\text{ClO}_4)_2 \cdot 1.4(4,4'\text{-bipy}) \cdot 3(\text{H}_2\text{O})$  and  
 $[\text{Co}(4,4'\text{-bipy})_3(\text{H}_2\text{O})_2](\text{ClO}_4)_2 \cdot 1.4(4,4'\text{-bipy}) \cdot 3(\text{H}_2\text{O})$

**Introduction**

The design and construction of hybrid organic-inorganic porous network solids through the self-assembly of simple, molecular and ionic components is an emerging area of supramolecular chemistry that can provide new generations of functional materials. The importance of porous solids in inclusion phenomena, *e.g.* adsorption / desorption, ion exchange, and size and shape-selective molecular sieving, as well as catalysis, is due, in part, to their ability to reversibly clathrate or trap species within their cavities and extended channels.<sup>129</sup> Like zeolites, many hybrid organic / inorganic solids clathrate guests within pores, cavities, and channels that are part of their lattice framework. These pores often possess a variety of sizes and shapes not observed in analogous inorganic porous solids such as zeolites and molecular sieves, thus potentially yielding novel and unique inclusion capabilities.<sup>87</sup> A number of porous coordination networks have been found to exhibit many other desirable zeolitic properties as well, such as stability and porosity of the framework, guest exchange, and selective catalytic activity.<sup>42,44,93,142</sup> By careful selection and design of the chemical components, the size and clathration properties of these pores can be fine-tuned to meet specific needs while maintaining the overall structural and functional features found in naturally occurring analogs.<sup>37</sup>

Despite the large amount of research devoted toward the synthetic aspect of solid-state supramolecular chemistry in terms of producing functional materials and elucidating methods for the rational design and fabrication of such materials, studies of the chemical reactivity of these materials has been lacking.<sup>147</sup> In fact most of these reactivity studies have been limited to the investigation of the inclusion properties of porous solids, such as the guest exchange and adsorption-desorption processes of small molecules.<sup>45,87,142,144,147</sup> The imbalance of synthetic work compared to reactivity studies of supramolecular materials is largely due to the fact that, unlike the well-characterized chemical reactivity properties of molecular and ionic species that are generally soluble in many common solvents, most coordination polymers are insoluble in most organic and inorganic solvents thus rendering any reactivity studies difficult.<sup>147</sup>

Yaghi, *et al.*, has reported selective guest binding and removal of alcohols and ketones from a three-dimensional porous Zn(II)-Benzenetricarboxylate network and aromatic molecules from a layered porous Co(II)-Benzenetricarboxylate network without collapsing the host.<sup>45,87</sup> Endo, *et al.* has described the reversible non-selective guest binding and removal of ketones, esters, hydrocarbons, and haloalkanes, as solids, liquids, and gases, within a zeolitic anthracene-bis(resorcinol) layered, hydrogen-bonded network.<sup>142</sup> Kondo, *et al.* has reported the adsorption and desorption properties of small gas molecules, *e.g.* methane, within microporous interpenetrated M-4,4'-azopyridine (M = Mn(II), Cd(II), and Co(II)) coordination networks without breaking apart the host.<sup>144</sup>

### **NMR Spectroscopy**

Magic angle spinning (MAS) NMR spectroscopy is a very useful technique for investigating chemical interactions within solid-state materials and can be applied toward

determining the presence of enclathrated guests within porous solids.<sup>165</sup> Additionally, pore sizes can be estimated as well as observing the dynamic behavior of the guests (*i.e.* chemical exchange), the nature of the binding sites (provided a coupling constant can be measured), and the relative strength of any specific chemisorption and physisorption interaction (*i.e.* acid-base, coordination, hydrogen bonding, and adsorption).<sup>165</sup>

One approach to studying the interactions of guest molecules within hosts involves the use of small probe molecules that can be inserted within the lattice of a solid.<sup>166</sup> Using probe molecules containing spin  $\frac{1}{2}$  nuclei (e.g.  $^1\text{H}$ ,  $^{13}\text{C}$ ,  $^{15}\text{N}$ ,  $^{19}\text{F}$ ,  $^{31}\text{P}$ , and  $^{129}\text{Xe}$ ) are useful because the corresponding NMR signals are not complicated by quadrupolar interactions.<sup>165</sup> In the past, several NMR probes, including 2- $^{13}\text{C}$  acetone,<sup>167-171</sup> 4- $^{13}\text{C}$  mesityl oxide,<sup>172-175</sup> and  $^{15}\text{N}$  pyridine,<sup>176-180</sup> have been used to specifically identify and quantify acidic sites in solid acids such as zeolites and amorphous silica-alumina. Unfortunately, the small magnetogyric ratios, low natural abundances, and relatively limited chemical shift ranges of  $^{15}\text{N}$  (0.4 % abundant) and  $^{13}\text{C}$  (1.1 % abundant) requires either extensive signal averaging or the use of isotopically enriched materials in order to obtain high resolution NMR spectra.<sup>166,181</sup> To avoid both of these problems, a more suitable probe molecule would incorporate a more sensitive NMR active nucleus such as phosphorus-31.<sup>182</sup> The large gyromagnetic ratio and near 100 % natural abundance of  $^{31}\text{P}$  results in a significant increase in NMR signal intensity compared to either  $^{13}\text{C}$  or  $^{15}\text{N}$  without the use of expensive enriched samples.<sup>181,183,184</sup> Furthermore, the large isotropic chemical shift range and full chemical shift anisotropy can provide useful information regarding the chemical

environments of the  $^{31}\text{P}$  nucleus.<sup>181,185,186</sup> Therefore, phosphorous-containing probe molecules are well suited for probing the nature and strength of host-guest interactions.

Recently,  $^{31}\text{P}$  MAS NMR spectroscopy has been applied specifically toward for the identification and quantification of Lewis and Brønsted sites on the surfaces and within solid acids.<sup>166,182,187-190</sup> In the past, trialkylphosphines (TAP), and in particular, trimethylphosphine (TMP), have been the probe molecules of choice for the characterization of solid acids by  $^{31}\text{P}$  MAS NMR spectroscopy.<sup>166,182,190-194</sup> The coordination of a TAP molecule to an acidic site results in a characteristic chemical shift that is strongly dependent on the Brønsted or Lewis nature of that site.<sup>186</sup> In fact,  $^{31}\text{P}$  NMR spectroscopy can not only distinguish between Brønsted-complexed TMP from Lewis-bound TMP but also resolve peaks due to varying local environments of the coordinated probe molecules.<sup>166,186</sup> The basicity of trimethylphosphine ( $\text{pK}_a = 5.3$  in water) results in the formation of a protonated base ( $\text{TMPH}^+$ ) upon coordination to any Brønsted site with a characteristic chemical shift of about  $-3$  ppm (referenced to 80 % *o*-phosphoric acid) that is largely invariant with the strength of the acid site.<sup>181,195</sup> Thus, TMP has been extensively used to determine the presence and quantity of Brønsted sites in solid acids. Lewis bound TMP exhibits a considerable upfield shift relative to the Brønsted site.<sup>181,186</sup> However, the similar chemical shift of Lewis bound and physisorbed TMP causes difficulty in using this probe to unambiguously determine the presence and population of Lewis sites in a solid.<sup>181,186</sup> Rapid chemical exchange dynamics between bound and free TMP molecules at room temperature can also lead to uncertainty in the identification and quantification of acid sites.<sup>181</sup> Furthermore, TMP is

a highly flammable and air-sensitive liquid at room temperature and preparing solid acid standards for quantitative measurements is difficult.<sup>181,185</sup>

Like trialkylphosphines, trialkylphosphine oxides (TAPO's) are also suitable basic probe molecules for studying interactions within solid acids as they are able to distinguish Brønsted sites from Lewis sites.<sup>166,181,183,186,188</sup> The intrinsic basicity of trialkylphosphine oxides is on the same order of magnitude as trimethylphosphine.<sup>186</sup> However, the removal of the phosphorous atom from the basic site leads to a wide range of chemical shifts that vary with the strength of the acid site.<sup>186</sup> Unlike the corresponding TAP's, TAPO's are solids at room temperature, not susceptible to oxidation, and can thus be introduced into a host through solution-state chemistry.<sup>181,182</sup> The most commonly used trialkylphosphine oxides are trimethylphosphine oxide (TMPO) and triethylphosphine oxide (TEPO).<sup>186</sup> The ability of these materials to measure acidity in both solution and in solids is known and TEPO, for example, has been used as a probe for determining solvent acidity.<sup>196</sup> Unfortunately, there are few published reports describing the use of trialkylphosphine oxides as probe molecules to study interactions with porous solids.<sup>181</sup>

The chemical shift of an NMR peak resulting from the interaction of a basic probe molecule with an acid site in a host is primarily due to local changes in the magnetic field around the NMR active nucleus originating from electronic changes in the probe molecule as a whole.<sup>186,197,198</sup> An acid-base interaction can be viewed as a transfer of electron density from the base to the acid site thus creating overlap between the LUMO, the electron deficient orbital on the acid ( $\phi_A$ ), and the HOMO ( $\phi_B$ ), one of the orbitals on

the base that contains a lone pair of electrons (Figure 3-1).<sup>165,186</sup> As the adduct bond strength increases, the electron density “flows” away from the basic oxygen atom. The net loss of electron density from the NMR active nucleus due to the formation of an acid/base adduct ( $\Phi_{AB}$ ) can be observed in the phosphorous-31 NMR.<sup>165,186</sup>

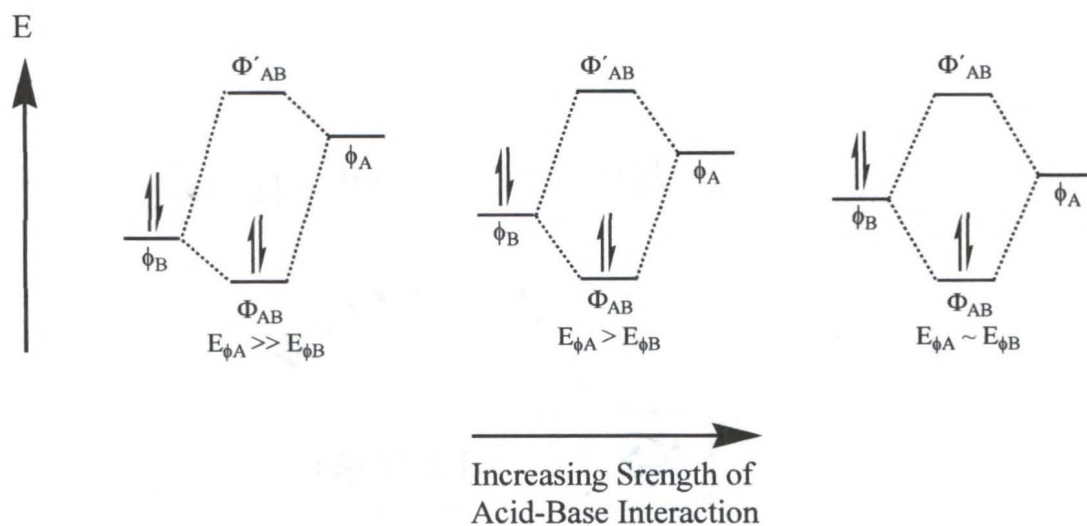


Figure 3-1. An acid-base reaction from a molecular orbital perspective. The electron deficient acid,  $\phi_A$ , reacts with the electron rich base,  $\phi_B$ , to form an adduct,  $\Phi_{AB}$ . As the strength of the acid-base interaction increases, the adduct progressively becomes more covalent in character. Adapted from reference 165.

If the basic probe molecule interacts with a Brønsted acid site, such as water, the resulting adduct bond is characterized by some degree of proton sharing between the acid and the base.<sup>186</sup> Consider the hydrogen bonding of the oxygen atom from a trialkylphosphine oxide with the proton of an acidic water molecule. Increasing the strength of the acid site transfers this shared proton to the base. The (water) O—H and (TAPO) P—O bond order both decrease while the O—H bond order increases in the resulting TAPO—H<sub>2</sub>O adduct. The phosphorous atom therefore becomes deshielded shifting the corresponding NMR signal downfield. The stronger acid-base interactions,

the greater the  $^{31}\text{P}$  resonance shifts downfield. However, once the proton is completely transferred to the base, no further downfield shift of the NMR signal will be observed. Instead, for any stronger acid sites, the same chemical shift will be seen in the spectrum.<sup>186</sup>

The coordination of a base to a Lewis acid, such as a metal ion, will also result in the formation of an adduct bond.<sup>186</sup> The strength of the acid site will therefore be directly related to the strength of the adduct bond. Again, consider the effect of coordination of a trialkylphosphine oxide probe molecule directly to a metal center. As the acid strength increases, the electron density gradually transfers from the oxygen atom to the metal ion to a greater extent. The P—O bond order decreases while the M—O bond order increases. The phosphorous atom becomes more deshielded and the corresponding NMR resonance progressively shifts downfield. At very high acid strengths no further change in the chemical shift is expected, unless oxygen atom transfer occurs.<sup>186</sup> In this case, acid site is oxidized thus reducing the trialkylphosphine oxide to the corresponding trialkylphosphine.

Recently, Rakiewicz *et al.* characterized the acid sites of amorphous silica-alumina, zeolites HY, dealuminated HY, and USY, and gamma-alumina with trimethylphosphine oxide.<sup>181</sup> The authors were able to identify and differentiate Lewis and Brønsted sites and then measure the population of those sites. The trend in assigning chemical shift ranges for Lewis or Brønsted bound phosphine oxides includes work by Lunsford and Baltusis.<sup>166,187,188,193</sup> Despite consistency in identifying and characterizing Brønsted sites, each author has assigned a different region to the chemical shifts for the Lewis bound probe.

## Chapter Summary

The purpose of this chapter is to investigate the host-guest properties of two porous network structures,  $[\text{Ni}(4,4'\text{-bipy})_3(\text{H}_2\text{O})_2](\text{ClO}_4)_2 \cdot 1.4(4,4'\text{-bipy}) \cdot 3(\text{H}_2\text{O})$ , **1**, and  $[\text{Co}(4,4'\text{-bipy})_3(\text{H}_2\text{O})_2](\text{ClO}_4)_2 \cdot 1.4(4,4'\text{-bipy}) \cdot 3(\text{H}_2\text{O})$ , **2**, introduced in Chapter 2. In particular, solid-state NMR spectroscopy is shown to be an effective probe of host-guest interactions. Specifically, this work focuses on exchanging pre-existing guests clathrated within the hosts with trialkylphosphine oxide probe molecules. Additionally,  $^{31}\text{P}$  MAS NMR spectroscopy is shown to be an effective tool for investigating host-guest interactions by observing the interactions of these probe molecules within the hosts. Finally, the structural changes within the host that result from the guest exchange is examined by powder X-ray diffraction.

## Experimental Section

### Materials

Trimethylphosphine oxide (100 %) was purchased from Alpha Aesar. Triethylphosphine oxide (98.0 %) and tri-*n*-propylphosphine oxide (99.9 %) were purchased from Strem Chemicals. Hexanes (99.9 %) and ethyl acetate (99.9 %) were purchased from Fisher Chemicals. Details regarding the preparation of crystalline samples of the network solids, **1** and **2**, are described in Chapter 2. All reagents were used without any further purification.

### Sample Preparation

A generalized procedure was employed for the guest exchange reactions involving the host network solids **1** and **2**. All reactions were performed under ambient laboratory conditions. A known amount of TMPO was dissolved in 50.0 mL of a 50 / 50 % vol. mixture of hexane and ethyl acetate, while TEPO and TPPO were dissolved in

50.0 mL of hexane. Crystalline samples of the network solids were ground into fine powders and suspended within the solution containing dissolved probe molecule. The standard initial loading concentration, referred to as the insertion ratio, used in the preparation of all samples was one mole of probe molecule per mole of host. This suspension was then stirred for approximately two hours. The resulting powder was collected by gravity filtration and a portion of the remaining solvent was saved for gas chromatography (GC) analysis. The powder was then suspended in pure solvent without any dissolved probe molecule and stirred for an additional hour. Again, the product was collected by gravity filtration and a portion of the remaining solution was saved for GC analysis. The powder was air dried before any further characterization. In addition, samples of **1** with variable initial loading concentrations of TMPO were also prepared by an analogous method. Insertion ratios varying from 0.01 moles to 2.0 moles of TMPO per mole of host were utilized.

### **Gas Chromatography Analysis**

All gas chromatography experiments were performed using a Hewlett Packard 5890 Series II equipped with a hydrogen flame ionization detector. Component concentrations from both the insertion and rinsing solutions described above were determined relative to an internal standard, cyclohexanone. A 0.5  $\mu\text{L}$  portion of the hexane solution was injected onto the column (25 m, 0.33  $\mu\text{m}$  film thickness, 0.20 mm ID HP-5 (Crosslinked 5 % PH ME Siloxane)). The column, initially at 80  $^{\circ}\text{C}$ , was immediately ramped to a temperature of 250  $^{\circ}\text{C}$  at a rate of 25  $^{\circ}\text{C} / \text{min}$  and held for 5 min.

## **NMR Spectroscopy**

All  $^{31}\text{P}$  NMR experiments were acquired on a Bruker Avance 400 MHz NMR Spectrometer operating at 161.976 MHz. A 4.0 mm triple resonance MAS probe was used for conventional work and a 2.5 mm double resonance MAS probe for fast-spinning experiments. A  $90^\circ_x$  pulse width of 4.0  $\mu\text{s}$  and a sweep width of 140 kHz were used in the acquisition of all spectra. An inversion recovery experiment on the host network solids containing the TAPO probe molecules showed that the spin-lattice relaxation times for the  $^{31}\text{P}$  sites were small (20-30 ms), hence a 100 ms recycle delay time was used. All resonances were referenced to 85 % *o*-phosphoric acid.

## **Powder X-Ray Diffraction**

All powder X-ray diffraction experiments were performed at the Major Analytical Instrumentation Center, University of Florida, using a Philips APD 3720 X-ray powder diffractometer with the  $\text{CuK}_\alpha$  line,  $\lambda = 1.54 \text{ \AA}$ , as the X-ray source. Finely powdered samples of both the network solids and the network solids containing the probe molecules were mounted onto glass slides with an amyl acetate / Collodion adhesive mixture. All samples were scanned at a rate of 0.2  $^\circ$  per minute from 4  $^\circ$  to 20  $^\circ$ .

## **Results and Discussion**

### **Sample Preparation**

Solution-phase guest exchange reactions were utilized in order to facilitate the uptake of the probes within the hosts. Crystalline samples of **1** and **2** were ground into fine powders in order to provide a maximum surface area for the probe molecules to enter the host. Non-coordinating, chemically inert solvents (hexane and ethyl acetate) were used as reaction media to ensure that only the probe molecules are taken into the host. Upon completion of the guest exchange reactions, the products were washed with solvent

to remove any TAPO's physisorbed onto the surfaces of the host. No additional loss of bipy and or probe was observed suggesting that the probes must be bound strongly to the host.

The insertion ratio is the molar quantity of trialkylphosphine oxide probe taken in per mole of host (or host metal ion). A standard insertion ratio of one mole of TAPO per mole of host, employed in most guest exchange reactions, was chosen to ensure that a sufficient quantity of the phosphorus-containing probes are taken within the host to be easily be detected by  $^{31}\text{P}$  NMR spectroscopy without extensive signal averaging. The addition of excess quantities of probe was avoided to minimize the structural rearrangements resulting from the guest exchange. In order to investigate the possibility of the trialkylphosphine oxide probe molecules populating different or multiple acid sites as well as monitor structural changes that occur as function of quantity of guests exchanged within the hosts, samples of **1** were prepared with variable insertion ratios of TMPO. The initial loadings cover the range of 0.01 moles to 2.0 moles of TMPO per mole of **1**.

#### **Guest Loss From the Network Solids**

For all guest exchange experiments, the uptake of the trialkylphosphine oxides by **1** and **2** is always accompanied by the loss of 4,4'-bipyridine. The displaced bipy molecules are presumably the clathrated guests, not the coordinated ligands. In order to determine the origin of the bipy loss, *i.e.*, from the TAPO or the solvent, blank reactions, those without the presence of the probes, were performed in parallel to the guest exchange reactions. As shown in Figures 3-3 and 3-15, negligible bipy loss was observed from the control experiments indicating that the probe molecules, not the solvent, displace the bipy from the hosts.

The X-ray powder diffraction patterns of **1** and **2** before and after the blank reactions (without the probe molecules) are shown in Figure 3-2. The Bragg peaks of the powder patterns do not shift, appear, or disappear to any appreciable extent. The solvent does not cause any bipy to be released from the host and no appreciable structural rearrangements occur within the porous solids. However, the solvent causes the hosts to become less crystalline however, as many peaks are broadened decrease in intensity due to a small loss of structural coherence, particularly in **2**.

### **Guest Exchange Investigations of Compound 1 Involving TMPO**

#### **Gas Chromatography Results**

The gas chromatography experiments monitoring the guest exchange of bipy with TMPO from **1** are summarized in column bar graph format in Figure 3-3. The insertion ratio corresponds to one mole of TMPO per mole of host. The TMPO uptake by **1** is essentially complete, *i.e.*, the host takes in essentially all of the initial available quantity of the probe. Furthermore, the displacement of a significant quantity of bipy accompanies the TMPO uptake suggesting that the probe is actually taken within the host as opposed to physisorbing or chemisorbing onto the surfaces of crystallites of **1**. A schematic of the exchange of bipy for TMPO within the layered, porous host **1** is summarized schematically in Figure 3-4.

The exchange of guests within **1** (and **2**) is essentially governed by two competing factors: the interactions between TMPO and the host versus the bipyridine and the host and steric and size constraints of the probes, guests, and pores. Since TMPO is potentially both a Brønsted and Lewis base, the principal driving force for its uptake may be the formation of strong acid-base and donor-acceptor adducts between the probes and the host, however other stabilizing interactions may lead to absorption of the probe as

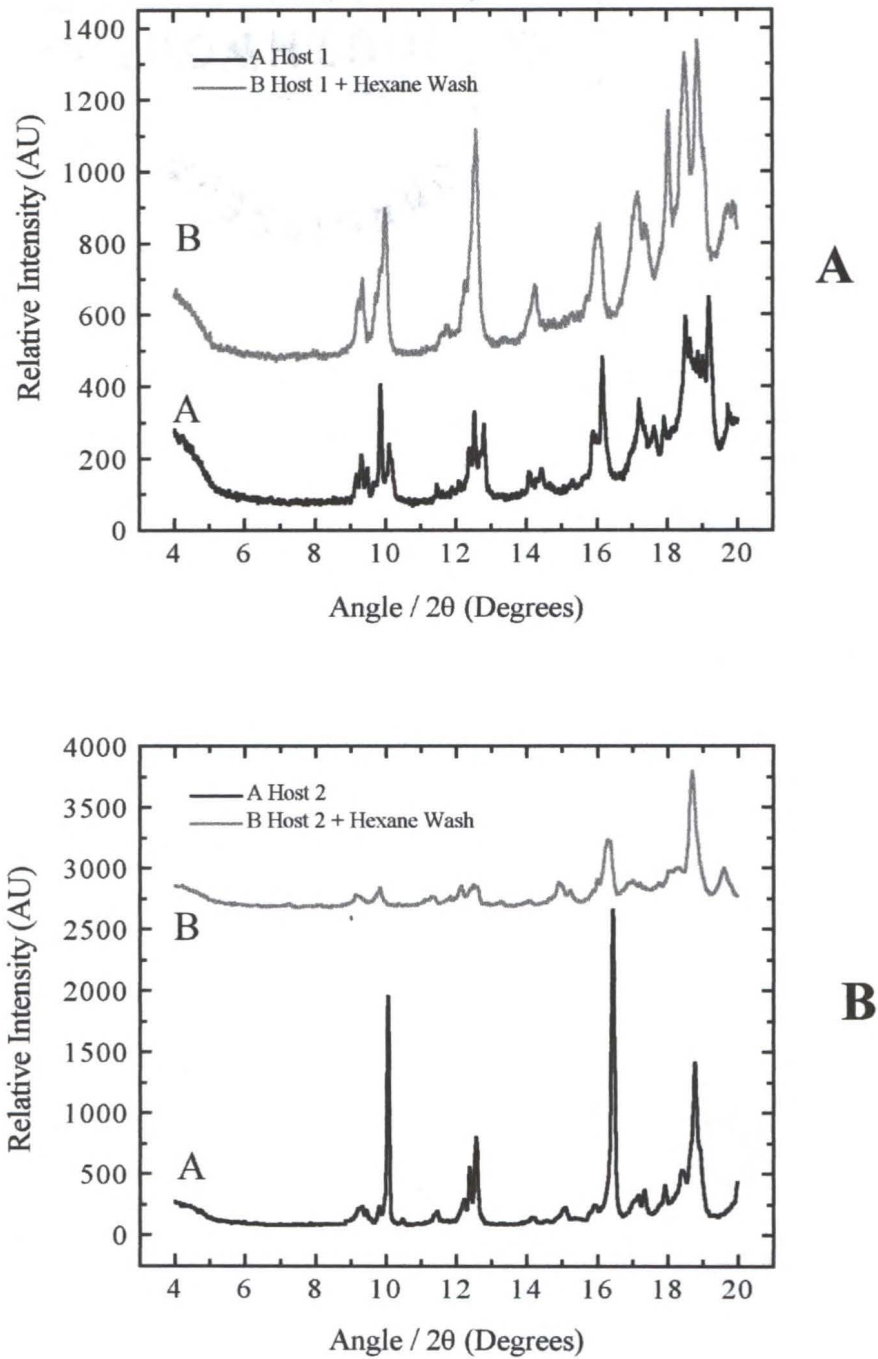


Figure 3-2. Powder X-ray diffraction patterns before (black) and after (red) washing with hexane. A) Compound 1. B) Compound 2.

well. From the crystal structure of **1**, these potential acid sites correspond to coordinated and lattice water molecules and metal ions. The size and steric bulk of TMPO (and especially TEPO and TPPO with the longer alkyl chains), the limited size and space present within the pores and between the sheets, and the presence of clathrated guests may act to hinder the probe uptake by the host. Since perchlorate counterions, lattice waters, and bipy molecules occupy much of the void space within the pores and between the sheets, evidently insufficient space is available within the host to accommodate both TMPO and the existing guests. As a result, the TMPO displaces the bipy guests. The interactions between the TMPO and the hosts must therefore be stronger and more favorable than the packing forces and host-guest interactions holding the bipy's within the host and the probes. Aiding and driving the guest exchange are the stabilizing solvation interactions between the hexane and the displaced hydrophobic bipy molecules.

### **NMR Results**

In order to investigate the interactions between the probe and the host after the guest exchange, experiments were performed to determine the  $^{31}\text{P}$  MAS NMR chemical shift range for TMPO upon successive dilution water since the phosphine oxide presumably interacts with water molecules present in **1**. The shaded regions in the NMR spectra represent this range.

The  $^{31}\text{P}$  NMR spectrum for crystalline TMPO is shown in Figure 3-5 A. One peak at 39.7 ppm is observed, corresponding to crystalline, non-interacting TMPO. Figure 3-5 B shows the static  $^{31}\text{P}$  NMR spectrum upon adding a small aliquot of water 41.2 ppm and 45.9 ppm. As shown in Figures 3-5 C and 3-5 D, the peak at 45.9 ppm progressively loses intensity while a new peak at 51.0 ppm appears and grows in intensity as the TMPO solution (containing approximately 79 % and 71 % probe by mass,

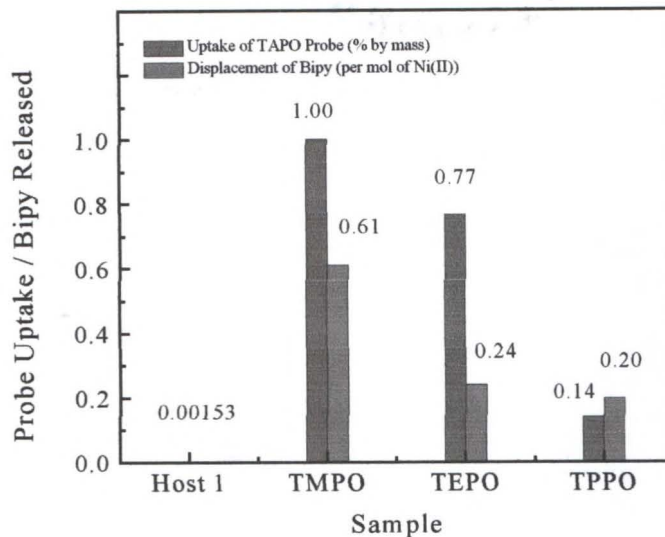


Figure 3-3. The gas chromatography results monitoring the guest exchange reactions in Host 1. The left-hand columns denote the fraction of probe taken in by the host and the right hand columns represent the relative quantity of clathrated bipy released.

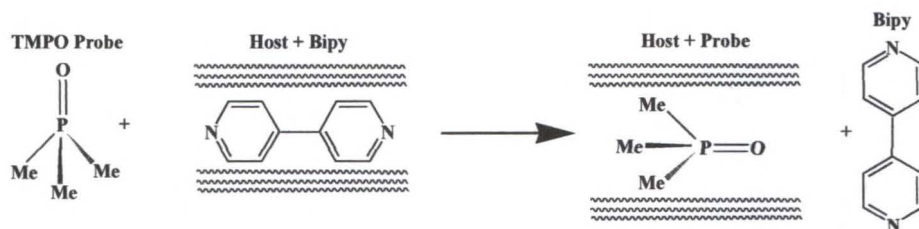


Figure 3-4. The guest exchange of 4,4'-Bipyridine with TMPO in Hosts 1.

respectively) is further diluted. In the high dilution limit (*ca* 100  $\mu\text{L}$  of water) corresponding to approximately 43 % TMPO by mass, all intermediate resonances at 45.9 ppm have disappeared and only a single peak at 51.0 ppm remains (Figure 3-5 E). The downfield shifting of the TMPO  $^{31}\text{P}$  resonance is consistent with that reported. 165,166,181,183,186,188

For aqueous solutions of TMPO, the peak with the highest chemical shift

represents the strongest possible acid-base interaction with free water and corresponds to the hydrated solute. The peaks that appear in the intermediate regions may, in fact, be comprised of two distinct resonances, one corresponding to the hydrated TMPO, and the other from crystalline TMPO. The chemical exchange at room temperature between these two species is fast on the NMR time-scale so the two peaks coalesce and a single resonance is observed. At higher TMPO concentrations, the corresponding NMR peaks are dominated by undissolved fraction and thus only partial downfield shifting is observed. As the TMPO is diluted with water, the hydrated TMPO peak begins to dominate and the average of the wet and dry peaks shift downfield. When there is no crystalline TMPO remaining and the entire sample is hydrated, no further downfield shifting is observed. The downfield shifting of the  $^{31}\text{P}$  resonances as a function of dilution of trialkylphosphine oxides with water can provide a means for assigning NMR peaks when TMPO is used to probe interactions with **1**. After the exchange of bipy with TMPO,  $^{31}\text{P}$  resonances appearing in this shaded region indicate that the TMPO is interacting with an acid site of strength similar to water. Peaks shifted downfield with respect to the former are then likely due to the probe interacting with stronger acid sites. Figure 3-6 schematically depicts some of the possible physisorption interactions, *e.g.* the probe adsorbing to the surface or between the layers, and chemisorption interactions, *e.g.*, hydrogen bonding to lattice waters or aqua ligands or direct coordination to the metal centers. Note that this scheme does not imply any specific orientation or position of the probe with respect to the host or metal centers.<sup>165</sup>

Figure 3-7 shows the  $^{31}\text{P}$  MAS NMR spectrum of **1** after the exchange of bipy with one mole of TMPO per mole of host. A spinning speed of 8.0 kHz effectively

separates the spinning sidebands, identified with asterisks, from the characteristic peaks corresponding to the various chemical environments of the  $^{31}\text{P}$  nucleus. Two broadened peaks are observed between the chemical shift range of 40.0 ppm and 80.0 ppm. The resonance at 49.6 ppm appears within the shaded region for TMPO interacting with water. The peak is therefore assigned to the probe molecules binding to acid sites of comparable strength to water. Based on the crystal structure of **1**, these weak acid sites may be uncoordinated lattice water molecules. The peak at 68.0 ppm corresponds to TMPO interacting with an acid site stronger than unbound water molecules since this peak is clearly shifted downfield with respect to the former resonance. From the crystal structure of **1**, the strong acid sites are most likely the coordinated water molecules. The assignment of these peaks is consistent with those of Baltusis and Rakiewicz in their NMR studies of solid acid zeolites and amorphous silica-alumina substrates with trialkylphosphine oxides.<sup>166,181,188</sup> Furthermore, the NMR spectrum in does not indicate the presence of surface bound, physisorbed TMPO to crystallites of **1**, expected at 39.7 ppm.<sup>166,181,188</sup>

Evidently the TMPO does not coordinate directly to the Ni(II) ions. Otherwise, significant broadening and shifting of the resonances would result, perhaps to the extent that the spectrum would not be observed at all.<sup>199</sup> This conclusion is further justified since the guest exchange reaction causes no observable change the color of **1**. The direct coordination of the TMPO to the metal centers necessarily involves the replacement of the aqua and /or bipy ligands. However, the GC experiments did not indicate the presence of displaced water. The limited size and space present within the pores and between the sheets likely hinders ligand replacement and thus rendering the metal ions

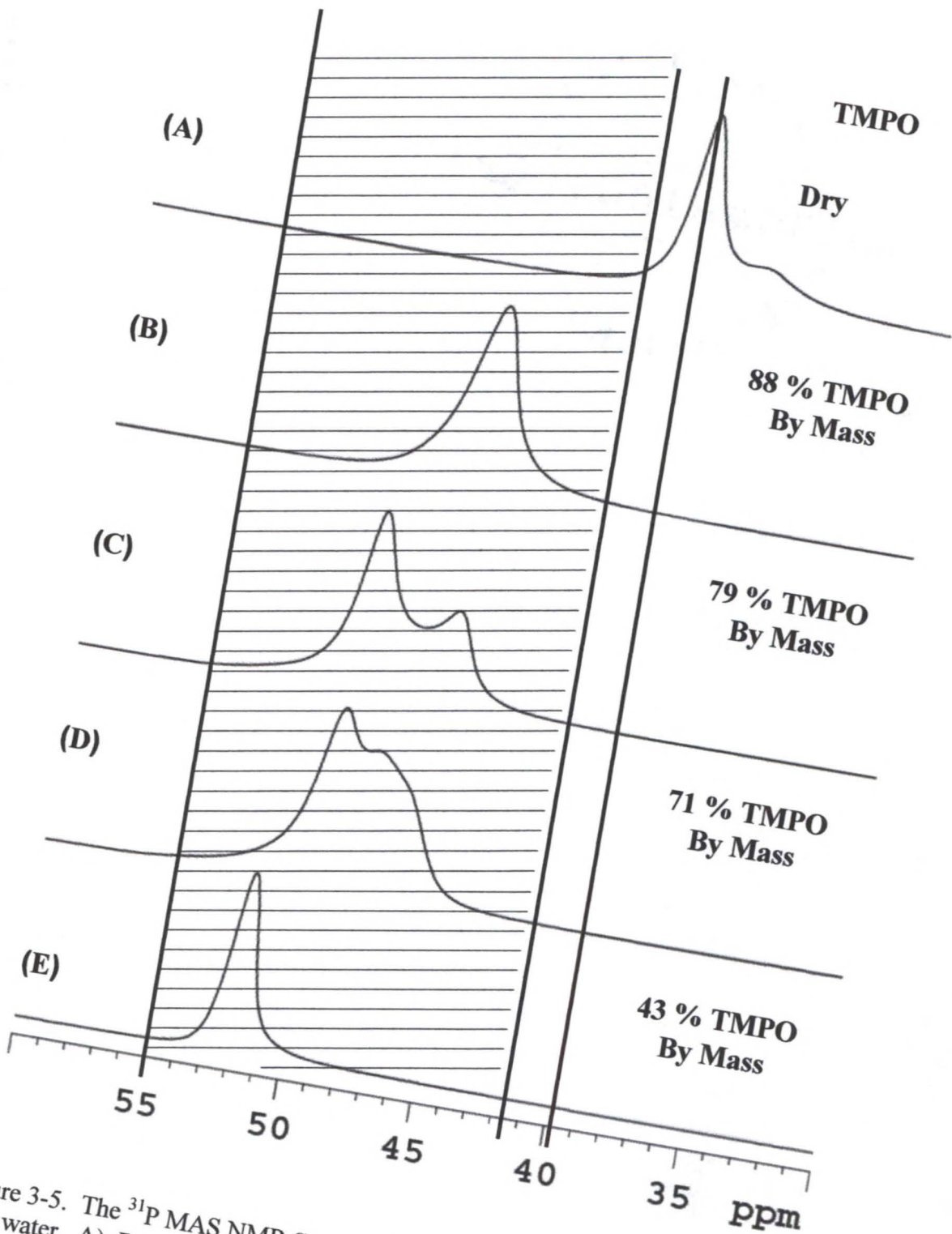


Figure 3-5. The  $^{31}\text{P}$  MAS NMR Spectra of TMPO as a result of dissolving and diluting with water. A) Dry TMPO. B) 88 % TMPO solution. C) 79 % TMPO solution. D) 71 % TMPO solution. E) 43 % TMPO solution.

less accessible acid sites compared to the water molecules for TMPO. In fact, the presence of relatively well-defined peaks suggests that the phosphorous nuclei are not in close proximity to the metal centers at all.

Based on the insertion ratio of one mole of TMPO per mole of host, the TMPO should preferentially bind to the strongest available acid sites, one or both of the aqua ligands. Then, in the NMR spectrum, only one or two peaks at approximately 70 ppm corresponding to these strong-acid interactions is expected. However, the NMR spectrum also shows evidence of the probe interacting with both weak acid sites (the lattice waters) along with the strong acid sites. Evidently, due to the above-mentioned size and steric constraints of the probe, clathrates, and pores, the TMPO is unable to access all of the strong acid sites and distribute themselves uniformly throughout the host. Consequently, the probe molecules interact with more accessible weaker acid sites, the lattice water molecules, as well.

### **X-Ray Results**

Figures 3-8 A and 3-8 B show the powder X-ray diffraction patterns of **1** before and after the exchange of bipy with one mole of TMPO per mole of host, respectively. The powder patterns are clearly different from one another indicating the guest exchange produces significant structural rearrangements within **1**. Recall that the characteristic porous network structure of **1** is sustained, in large part, by stabilizing interactions between the host and the guest bipy molecules. TMPO is topologically and chemically different than bipy and is not expected to fulfill the same role as a guest. As a result the structural changes occur in order to accommodate the presence of the TMPO as well as fill the void spaces left by the vacated bipy guests. The host also becomes less crystalline due to a decrease in the structural coherence as many Bragg peaks have broadened and

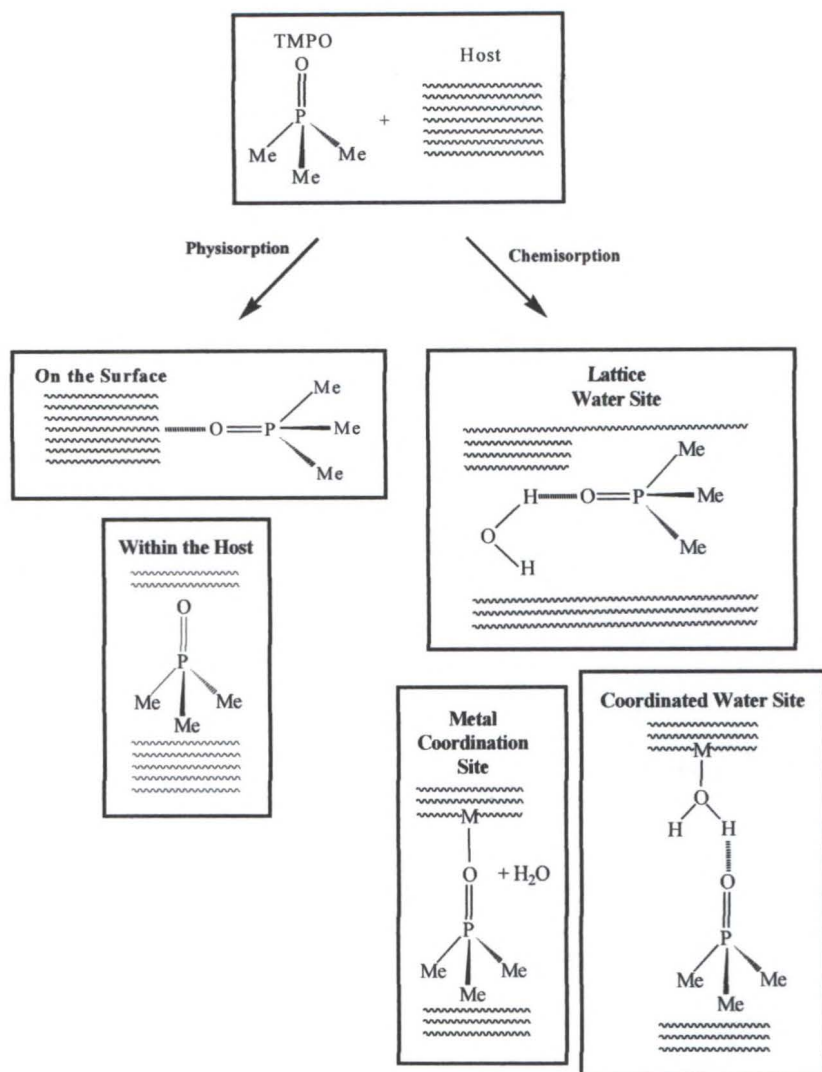


Figure 3-6. The possible interactions of TMPO with Hosts 1 and 2. Physorption interactions on the surface or within the host are shown on the left. Chemical interactions with the host, such as acid-base interactions with the acidic water molecules or direct coordination to the metal centers, are shown on the right.

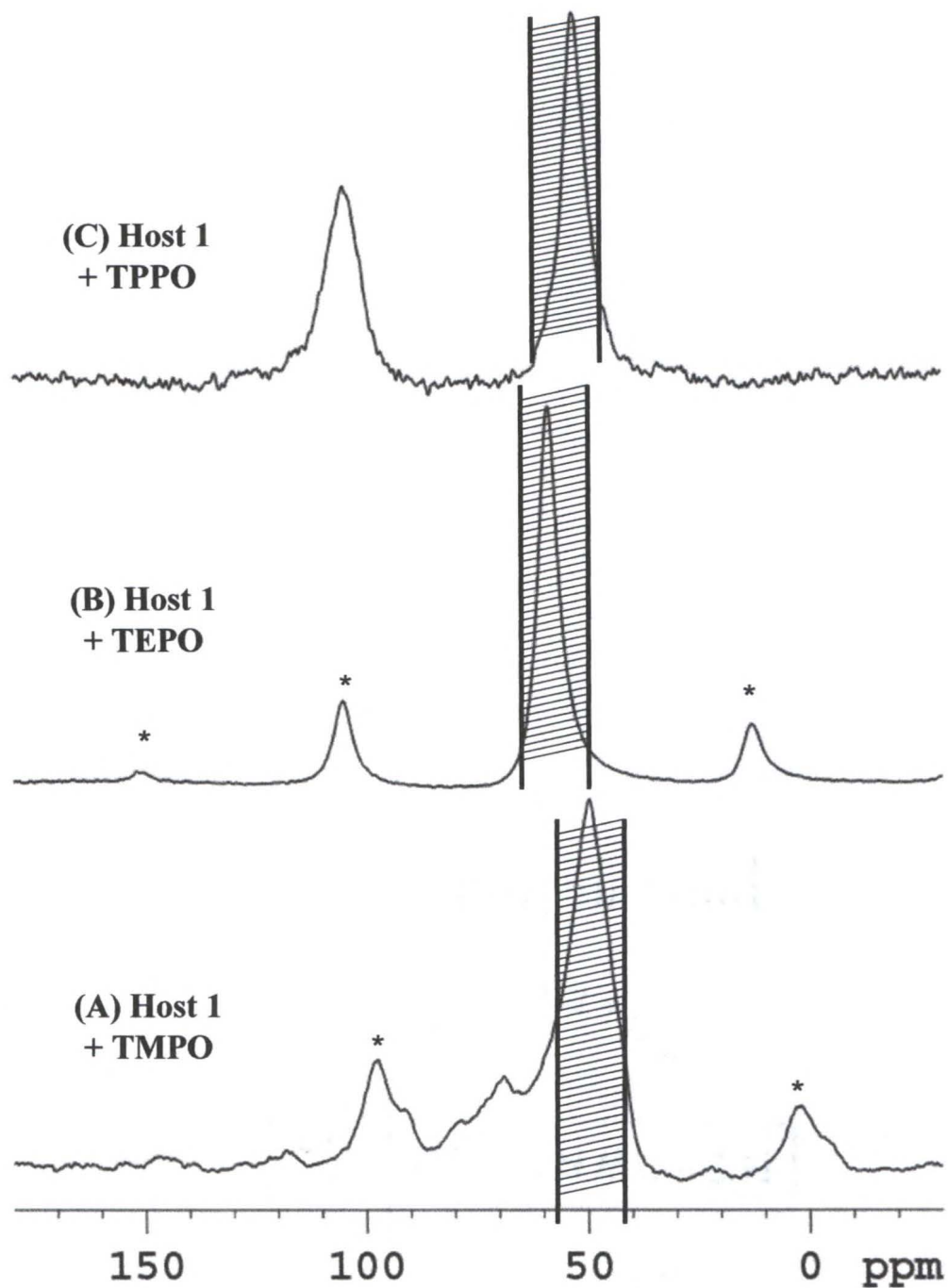


Figure 3-7. The  $^{31}\text{P}$  MAS NMR Spectra of Host 1 after the guest exchange of 4,4'-Bipyridine. A) Exchange with TMPO. B) Exchange with TEPO. C) Exchange with TPPO. The spinning sidebands are denoted by asterisks (\*).

lost intensity. Because of the relatively amorphous nature of the product, the nature of the structural changes cannot be readily determined. However, the characteristic porous network structure of **1** has not completely collapsed. If this were the case, observable color or solubility changes might occur and essentially no diffraction would be observed.

A few Bragg peaks present in the original host material remain in the TMPO sample but other reflections have either disappeared or moved as a result of the guest exchange. Note the non-correspondence of many Bragg peaks from the  $7^\circ$  to  $9^\circ$  and  $14^\circ$  to  $20^\circ$  regions. For example, the three broadened, low-intensity peaks at  $7.3^\circ$ ,  $7.8^\circ$ , and  $8.0^\circ$  observed after the guest exchange are not present in the original host structure. Additionally, the small, broadened peak at  $14.3^\circ$  and intense, unresolved peak at  $19.0^\circ$  both disappear after the guest exchange, being replaced by a group of coalesced peaks between  $14.5^\circ$  and  $15.5^\circ$  and two intense, unresolved reflections at  $19.5^\circ$  and  $20.0^\circ$ , respectively. However, a few Bragg peaks seem to be common to both samples. The two intense peaks at  $12.5^\circ$  and  $18.8^\circ$  as well as the two moderately intense reflections at  $16.0^\circ$  and  $18.3^\circ$  are preserved after the guest exchange, although somewhat broadened and less intense. The most striking feature is the movement or disappearance of the  $[2\ 0\ 0]$  reflection at  $10.0^\circ$ , corresponding to the interplanar spacing. In response to the bipy loss and probe uptake, the sheets should move and a corresponding change in position of the  $[2\ 0\ 0]$  peak is expected. Unfortunately, this peak cannot be readily identified the product because the ordered layering of sheets has been disrupted and randomized.

The X-ray diffraction results seem to suggest two possibilities concerning the nature of the guest-exchanged host. One possibility is that only the overall porous network structure of **1** essentially remains intact after the guest exchange but only the

layering of the sheets has become disrupted and randomized within the solid. As a result, a loss of crystallinity and some structural rearrangements occur within the host due to the non-uniform dispersal of the probe throughout the host causing significant structural disorder in the system. The other possibility is that the guest-exchanged product may be a mixture of two distinct materials. One fraction retains characteristics of the original host and the other portion corresponds to a new, unidentified material. Because the guest exchange does not occur uniformly throughout the host, likely due to the steric constraints described above, the probe molecules are not distributed homogeneously throughout the host and only some of the bipy guests are lost. Therefore, some portion of the original material is unaffected while the other fraction undergoes significant structural rearrangements. It is unknown to what extent the original host structure has been preserved in the affected fraction.

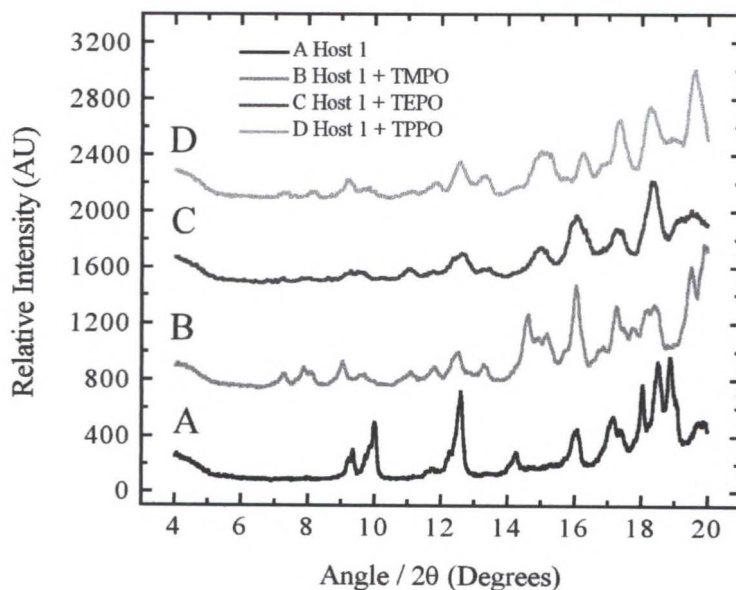


Figure 3-8. Powder X-ray diffraction patterns of Host 1 before and after the guest exchange of 4,4'-Bipyridine. A) No probe. B) Exchange with TMPO. C) Exchange with TEPO. D) Exchange with TPPO.

## Guest Exchange in Compound **1** Involving Variable TMPO Concentrations

### Gas Chromatography Results

In order to further examine the changes in population of the various acid sites by TMPO, samples were prepared by exchanging bipy with variable quantities of the probe from **1**. Specifically, insertion ratios ranging from 0.01 moles to 2.0 moles of TMPO per mole of host were employed. The gas chromatography experiments monitoring the guest exchange from **1** as a function of TMPO concentration are depicted in Figure 3-9.

Throughout the concentration range of 0.01 moles to 2.0 moles of TMPO per mole of host, the probe uptake by **1** is essentially complete and is accompanied by a displacement of bipy. From the plot in Figure 3-9, the TMPO uptake by the host is relatively linear. However, the quantity of bipy released initially increases but quickly begins to level out at a loading of 0.1 moles of probe per mole of host and then remains relatively constant. Then, at a concentration of 1.0 mole of probe per mole of host, the quantity of bipy released gradually increases again. Even at relatively low probe concentrations (0.1 moles of TMPO per mole of host and higher) evidently sufficient quantities of TMPO are present within the pores to hinder any further bipy loss. If these escape routes for bipy are blocked, then the entry paths for the probe should also be hindered preventing the probe from further penetrating the host. Since the strong acid sites deep within the host are now no longer accessible but all of the available TMPO is still taken within **1**, the probes must then be populating weaker, but more accessible, acid sites within the host. At high probe concentrations (1.0 mole per mole of host), the uptake of excess quantities of probe facilitates the displacement of more bipy.

At low probe loadings, significant quantities of bipy are released despite the small amounts of probe taken within the host. This result is surprising since the uptake of small

amounts of the probe is expected to displace correspondingly small amounts of bipy. Thus the interactions between **1** and the TMPO are much stronger and more favorable than the preexisting host-bipy interactions. At higher probe loadings, the opposite effect is observed; the amount of bipy lost relative to the TMPO taken in by the host is now small.

### NMR Results

Figures 3-10 and 3-11 depict the  $^{31}\text{P}$  MAS NMR spectra of **1** as a function of the TMPO loading. Figure 3-10 shows selected NMR spectra over the entire measured

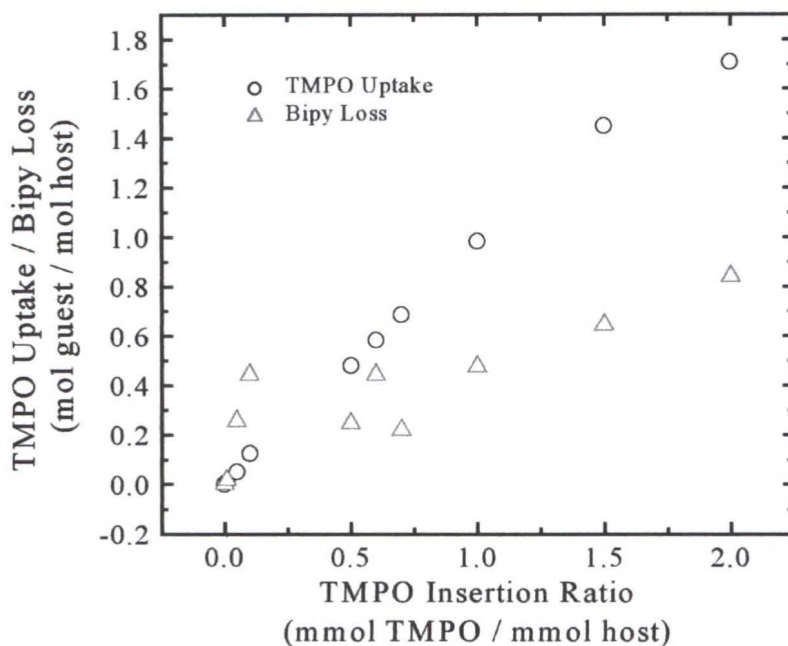


Figure 3-9. Exchange of 4,4'-Bipyridine with variable quantities of TMPO within Host **1**. The loss of 4,4'-Bipyridine is shown by the open triangles and the TMPO uptake is represented as the open circles.

loading range of 0.01 moles to 2.0 moles of probe per mole of host. Figure 3-11 focuses on a specific loading range of 0.05 moles to 1.0 mole of probe per mole of host to illustrate change in the spectra as the quantity of TMPO taken in by **1** increases

(discussed below).

At low TMPO loadings (0.01 moles to 0.1 moles per mole host), poor signal-to-noise ratio in the NMR spectra is observed due to the sparse presence of the probe (Figure 3-10). In each spectrum two peaks are observed, one at 49.6 ppm and another at 68.0 ppm corresponding to the interaction of TMPO with multiple types of acid sites. These spectra closely resemble the NMR spectrum in Figure X described above in both the presence and positions of the two peaks. As explained earlier, the peak at 49.6 ppm is assigned to the TMPO interaction with weak acid sites, presumably the unbound, lattice water molecules in **1**. The peak at 68.0 ppm corresponds to TMPO interacting with stronger acid sites, the aqua ligands. Note that the peaks in these spectra are of comparable intensity suggesting that, within this concentration regime, the population of both the weak and strong acid sites accessible by the probe is relatively equal.

The presence of two peaks within this low concentration regime is similar to the spectra observed at the higher loading of one mole of probe per mole of host. The TMPO, present in very limited quantities, was expected to preferentially bind to the strongest available acid sites and consequently produce only the single NMR peak at 68.0 ppm. However, even at the lowest TMPO loadings, the steric constraints prevent the probe from accessing all of the strongest acid sites and thus are not uniformly distributed throughout the host. As a result, in addition to binding to the stronger acid sites, the probe molecules interact with weaker, but more accessible, acid sites as well thus giving rise to the additional NMR peak at 49.6 ppm.

At intermediate TMPO loadings (0.5 moles to 1.0 moles per mole of host), the signal-to-noise ratio in the NMR spectra has improved significantly due to the greater

amount of probe present (Figure 3-11). As the concentration of TMPO increases from 0.5 moles to 0.6 moles per mole of host, a rather dramatic change occurs in the corresponding NMR spectra. The peak at 68.0 ppm, assigned to TMPO binding to the strong acid sites (aqua ligands) abruptly decreases in intensity (on an absolute intensity scale) while a similar, sudden increase in intensity is also observed from the peak at 49.6 ppm, corresponding to the probe interacting with the weak acid sites (the lattice water molecules). The change in intensity is related to a change in population of the various binding sites by TMPO in the host. The TMPO suddenly begins populating the weaker acid sites in favor of the stronger acid sites. This event could be due to structural rearrangements occurring as a result of the guest exchange. If the pores or sheets are opened in a manner that exposes the lattice water molecules, then these weaker acid sites may be more accessible to the TMPO thus accounting for the changes in population of the acid sites.

At the high TMPO loadings (1.0 moles – 2.0 moles per mole of host) the intensity of the peak at 49.6 ppm corresponding to TMPO binding to unbound acid sites (the lattice water molecules) levels off while the peak at 68.0 ppm corresponding to the probe interacting with stronger acid sites (the aqua ligands) progressively decreases in intensity (Figure 3-10). As more TMPO is taken within the host, a small shoulder at 42.2 ppm appears and is assigned to TMPO physisorbed to surfaces of **1**. Furthermore, two new peaks at 74.4 ppm and 79.4 ppm are observed as well, assigned to TMPO interacting with chemically inequivalent strong acid sites, again the aqua ligands. Recall from the crystal structure, the two protons on the water ligands are not equivalent since one hydrogen atom bonds to a nearby lattice water molecule and the other interacts with the terminal

nitrogen atom from a neighboring monocoordinate bipy ligand. As more TMPO is taken in, the more accessible unbound water sites become saturated. In response, the remaining available probes begin to physisorb to the surfaces of the host as well as populate stronger, albeit less accessible, acid sites.

### **X-ray Results**

The powder X-ray diffraction patterns of **1** before and after the exchange of bipy with variable quantities of TMPO are shown in Figure 3-12 (A – J). Comparing the diffraction patterns for each guest-exchanged product to the original material indicates that significant structural rearrangements have occurred within the host.

From the loading range of 0.01 moles to 0.6 moles of probe per mole of host, the diffraction patterns appear the same indicating that the guest exchange produces essentially the same material (Figures 3-12 B – 3-12 F). The products are amorphous because many of the diffraction peaks are broadened and have lost intensity. There is virtually no correspondence of the Bragg peaks from the guest-exchanged samples with the original material. In particular, the interplanar [2 0 0] reflection has disappeared and the layered structure of **1** has been disrupted. The structural rearrangements occur in response to fill the void spaces left by large quantity of bipy released from **1** compared to the small amount of TMPO taken in. Insufficient quantities of TMPO are available to fulfill the role as guest and occupy the void spaces left by the vacated bipy. Additionally, the non-uniform, random distribution of the TMPO produces structural disorder within the host leading to the broadened, low intensity reflections in the diffraction pattern.

A structural change occurs between the loadings of 0.6 moles and 0.7 moles of TMPO per mole of host (Figures 3-12 F and 3-12G). Although the structure of the product resembles that of the samples from the lower probe loadings, an increase in the

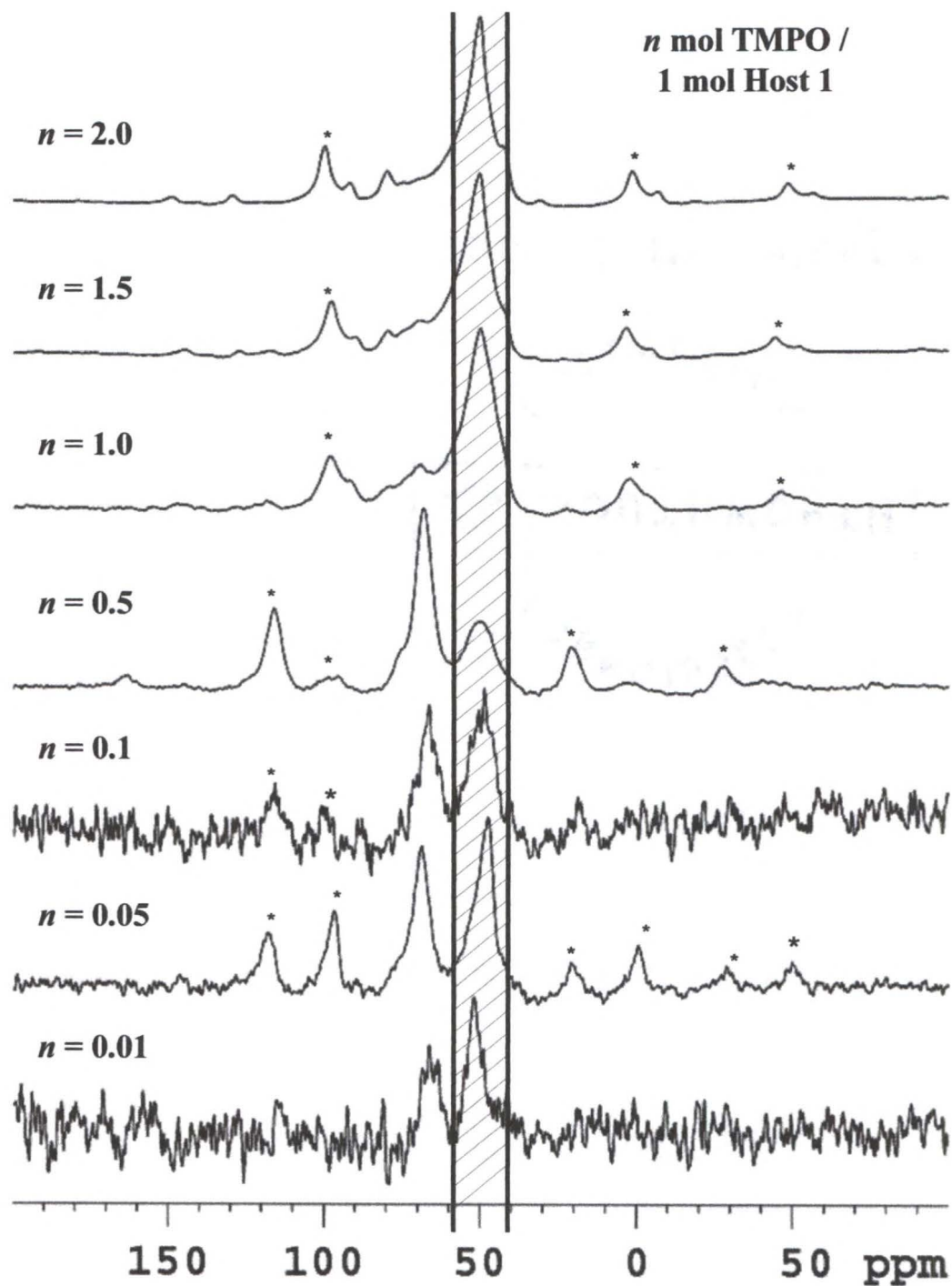


Figure 3-10. The  $^{31}\text{P}$  MAS NMR Spectra of Host 1 after the guest exchange of 4,4'-Bipyridine with variable quantities of TMPO. The spinning sidebands are denoted by asterisks (\*).

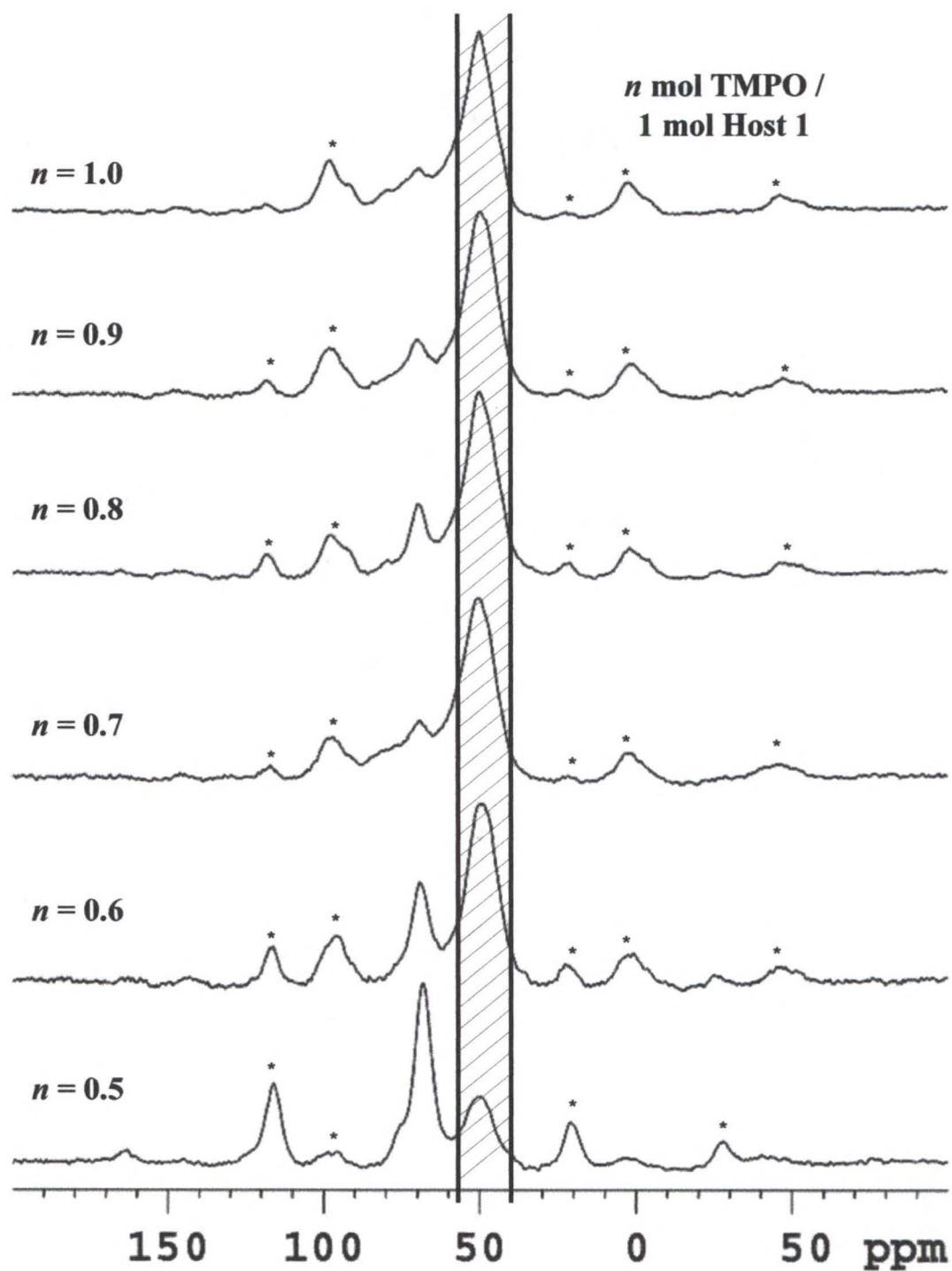


Figure 3-11. The  $^{31}\text{P}$  MAS NMR Spectra of Host 1 after the guest exchange of 4,4'-Bipyridine with variable quantities of TMPO, focusing between the concentration range of 0.5 moles to 1.0 moles of TMPO per mole of host. The spinning sidebands are denoted by asterisks (\*).

structural coherence is observed and the product is significantly more crystalline. The nature of this transformation is, however, uncertain. The host releases less bipy compared to the lower probe loadings and sufficient TMPO is available that it can more efficiently fill void spaces left by the displaced bipy and the structural rearrangements to fill the resulting void spaces thus reducing the severity of the structural rearrangements by the host. The increased crystallinity could also be due to a more homogeneous distribution of the TMPO throughout the host. Note that the increase in crystallinity of the sample occurs at the same concentration range that the change in population of the acid sites by the probe in the NMR spectra. The significance of this correlation is, however, unclear.

At the high TMPO loadings (1.0 moles to 2.0 moles per mole of host), no further structural rearrangements are observed and the product remains relatively crystalline (Figures 3-12 H – 3-12J). However, as the TMPO loading increases to 2.0 moles per mole of host, the guest-exchanged sample becomes amorphous again which is consistent with an increased quantity of bipy lost by **1**.

### **Guest Exchange Investigations of Compound 1 Involving TEPO and TPPO**

#### **Gas Chromatography Results**

The gas chromatography experiments monitoring the guest exchange of bipy with TEPO and TPPO within **1** are summarized in column bar graph format in Figure 3-3. Recall that **1** takes in essentially all of the initial available quantity of TMPO. In contrast, **1** takes in approximately 75 % of the available quantity of TEPO and only a small quantity (15 %) of TPPO. Despite the (slightly) greater predicted acidity of both TEPO and TPPO, the relatively long alkyl chains act to inhibit their uptake by the **1** and **2**. The TMPO “fits” within the pores and between the sheets better than TEPO and TPPO. Only

a small quantity of bipy is displaced by TEPO and TPPO suggesting that this probe may not be penetrating the host as well as TMPO but instead collects at or near the surfaces of crystallites of **1**.

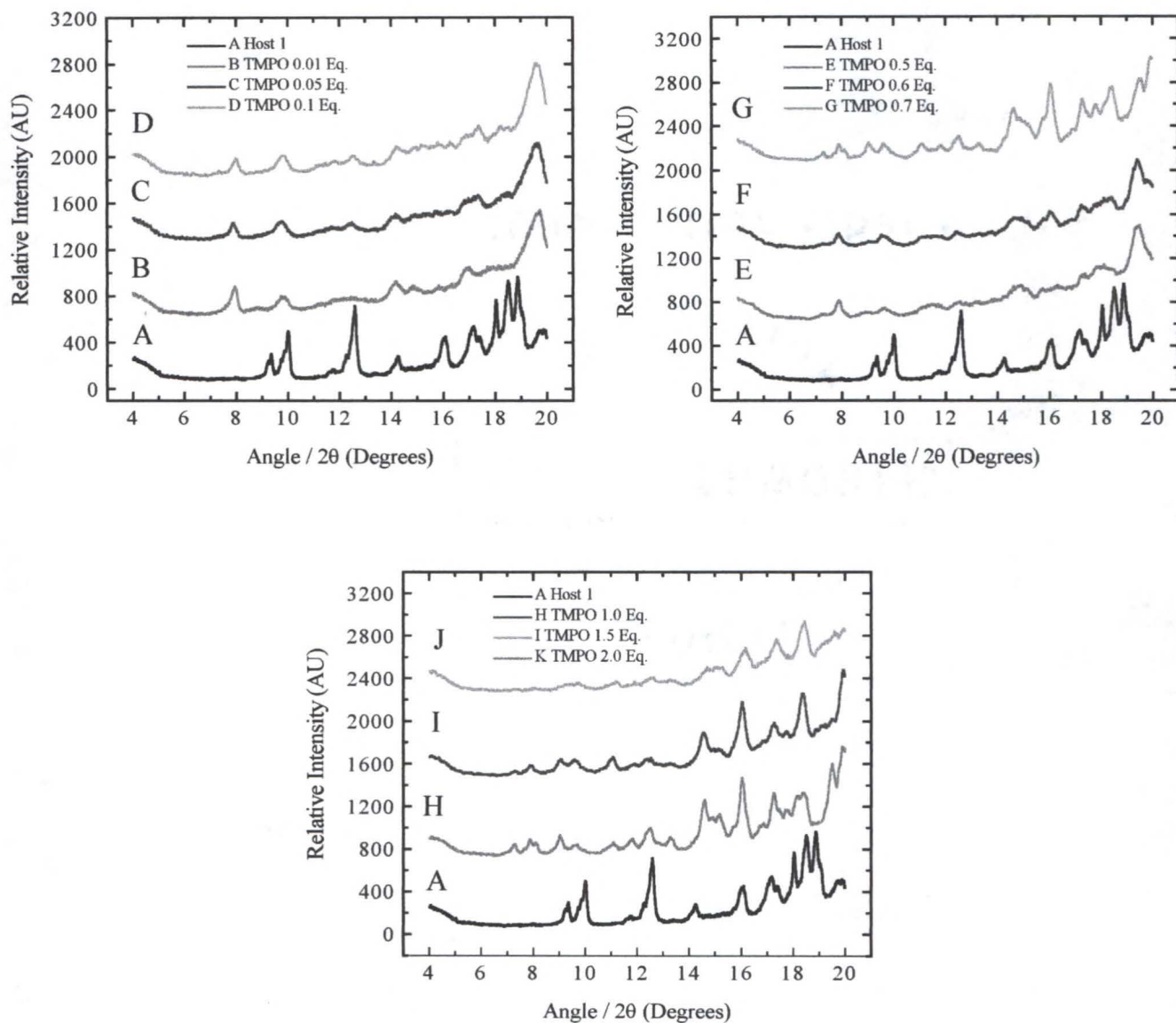


Figure 3-12. Powder X-ray diffraction patterns before and after the guest exchange of 4,4'-Bipyridine with variable quantities of TMPO per mole of Host **1**. The quantity of probe taken in corresponds to A) No TMPO. B) 0.01 moles of TMPO. C) 0.05 moles of TMPO. D) 0.1 moles of TMPO. E) 0.5 moles of TMPO. F) 0.6 moles of TMPO. G) 0.7 moles of TMPO. H) 1.0 mole of TMPO. I) 1.5 moles of TMPO. J) 2.0 moles of TMPO.

## NMR Results

The NMR spectra of crystalline and dilute aqueous samples of TEPO and TPPO, shown in Figures 3-13 and 3-14, respectively, exhibit a similar shifting of dry and wet peaks, as does TMPO.<sup>165,166,183,186,188</sup> Note the presence of peaks corresponding to both crystalline and hydrated TEPO, shown in Figure 3-13 A, due to the hygroscopic nature of TEPO and TPPO.

The NMR spectrum of **1** after the guest exchange of bipy with 0.75 moles of TEPO per mole of host is shown in Figure 3-7 B. The spectrum shows a single broad peak at 58.9 ppm. This peak is assigned to TEPO interacting uncoordinated lattice water molecules of **1** since this resonance appears in the shaded region corresponding to TEPO interacting with free water. The lack of any additional peaks downfield with respect to the 58.9 ppm resonance indicates that TEPO is not populating any stronger acid sites, such as coordinated water molecules. This result is not readily explained and is not consistent with the findings of Baltusis and Rakiewicz.<sup>166,181,188</sup> The TEPO is unable to access to stronger acid sites within the host possibly due to steric constraints. The probe therefore only interacts with lattice water molecules within the host or surface physisorbed water if the TEPO only collects at the surface. Furthermore, there is no evidence for direct coordination of TEPO to the metal centers due to the presence of relatively narrow, well-defined peaks in the NMR spectrum as well as the lack of any observable color change in the host resulting from the guest exchange. In fact, the relatively mild broadening of the peaks indicates that the magnetic interaction between the <sup>31</sup>P nucleus and the paramagnetic Ni(II) ions is weak suggesting that TEPO is not in close proximity to the metal centers.

The NMR spectrum of **1** after the guest exchange of bipy with 0.15 moles of TPPO per mole of host is shown in Figure 3-7 C. The initial quantity of the probe corresponds to 1 mole of TPPO per mole of host. The relatively low signal-to-noise ratio correlates with the GC measurements confirming that **1** takes in only a small quantity of TPPO. The NMR spectrum shows two broad peaks at 52.7 ppm and 105.3 ppm. Since the upfield peak appears in the shaded region corresponding to TPPO interacting with unbound water, this resonance is assigned to TPPO interacting with lattice water molecules present in **1**. This peak could be due to the interaction of TPPO with surface bound physisorbed water as well if the probe is not taken within the host. This interaction could also be due to TPPO interacting with surface physisorbed water as well. The downfield peak could be due to TPPO interacting with a coordinated water molecules at or near the surfaces of **1**, however, the assignment of this peak is not clear since a similar downfield peak was not observed with TEPO. If the probe is in close proximity to the metal ions, this resonance could also result from through-space interactions between the dipolar  $^{31}\text{P}$  nuclei and the paramagnetic Ni(II) ions and is expected to experience considerable upfield or downfield shifting depending on the orientation of the phosphorous nuclei with respect to the metal centers. Again, there is no conclusive evidence for direct coordination of TPPO to the metal centers. Therefore, the assignment of the downfield resonance at 105.3 ppm to a strong acid-base interaction between the probe and the host rather than a magnetic effect is more reasonable.

The resonances corresponding to both TEPO and TPPO interacting with unbound, lattice water (58.9 ppm and 52.7 ppm, respectively) and are shifted downfield compared to the corresponding TMPO peak (49.6 ppm). Since TEPO and TPPO are both stronger

bases than TMPO, the former probes interact more strongly with the unbound water sites resulting in the corresponding  $^{31}\text{P}$  NMR resonances to shift downfield to a greater extent. However, note that the TEPO resonance is significantly shifted downfield more than the TPPO peak, despite the greater expected basicity of TPPO. The reason for this discrepancy is unclear though.

### **X-Ray Results**

Figures 3-8 C and 3-8 D show the powder X-ray diffraction patterns for **1** after the exchange of bipy with 0.75 moles of TEPO and 0.15 moles of TPPO per mole of host, respectively. The powder patterns of the TEPO and TPPO samples are quite similar, indicating the guest exchange causes the same structural changes and produces essentially the same product. However, a comparison of the powder patterns, particularly the  $14^\circ$  to  $20^\circ$  range, shows that the guest-exchanged TMPO product is different from the TEPO and TPPO samples.

Comparing the powder patterns of the TEPO and TPPO samples with the corresponding pattern of the original host indicates that the guest exchange produces significant structural rearrangements as well as reducing the crystallinity of **1**. The extent of the structural changes is much greater than expected considering the relatively small quantity of bipy released compared to the TMPO material. Had TEPO and TPPO simply physisorbed or chemisorbed to the surfaces of crystallites of **1**, the corresponding powder diffraction patterns would more closely resemble that of the original host material. A few Bragg peaks present in the original host material remain in the TEPO and TPPO samples but other reflections have either disappeared or moved as a result of the guest exchange. Just as in the TMPO sample, the nature of the structural changes that occur in **1** as a result of the bipy loss and TEPO and TPPO insertion cannot be readily determined.

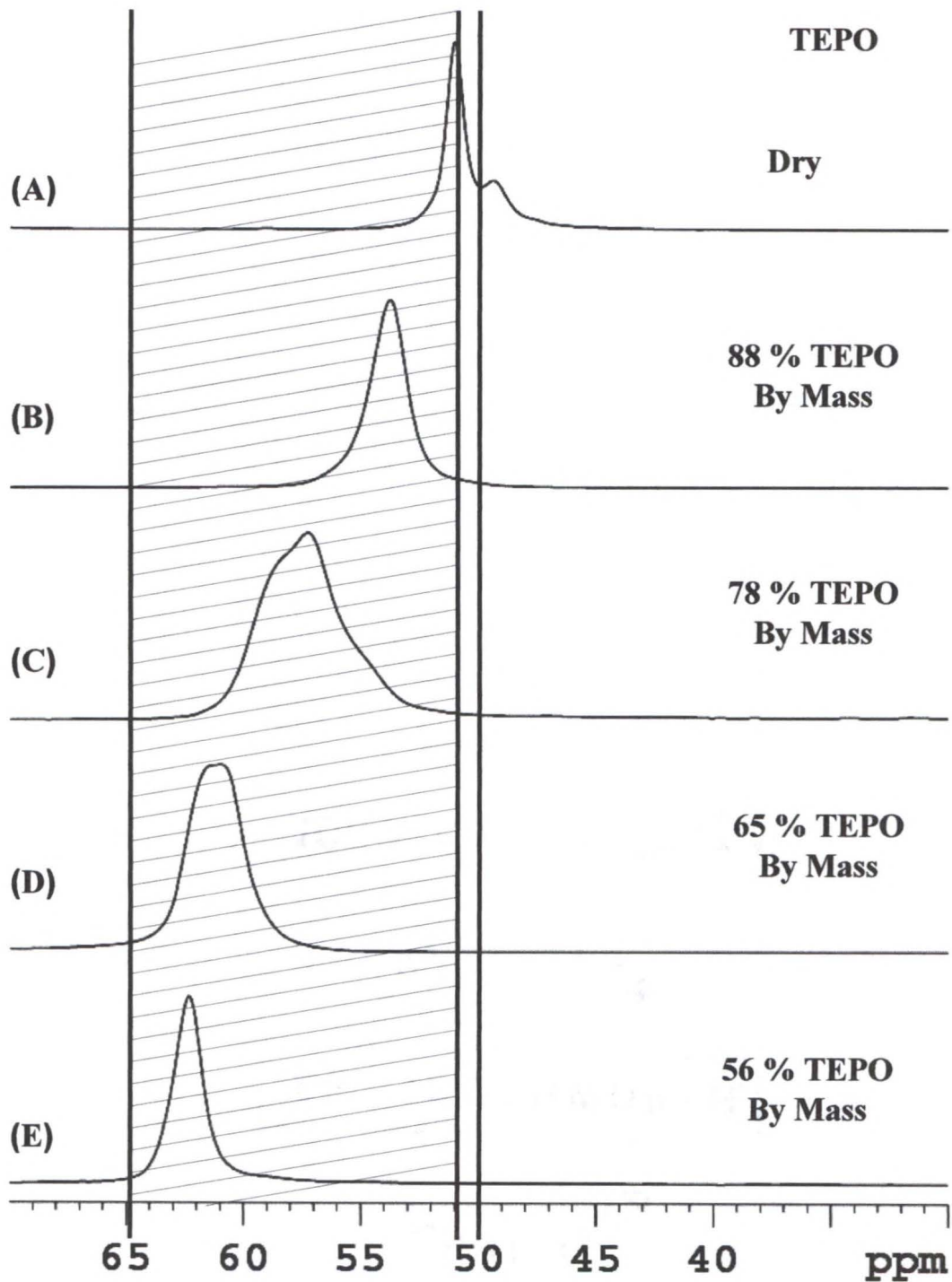


Figure 3-13. The  $^{31}\text{P}$  MAS NMR Spectra of TEPO as a result of dissolving and diluting with water. A) Dry TEPO. B) 88 % TEPO solution. C) 78 % TEPO solution. D) 65 % TEPO solution. E) 56 % TEPO solution.

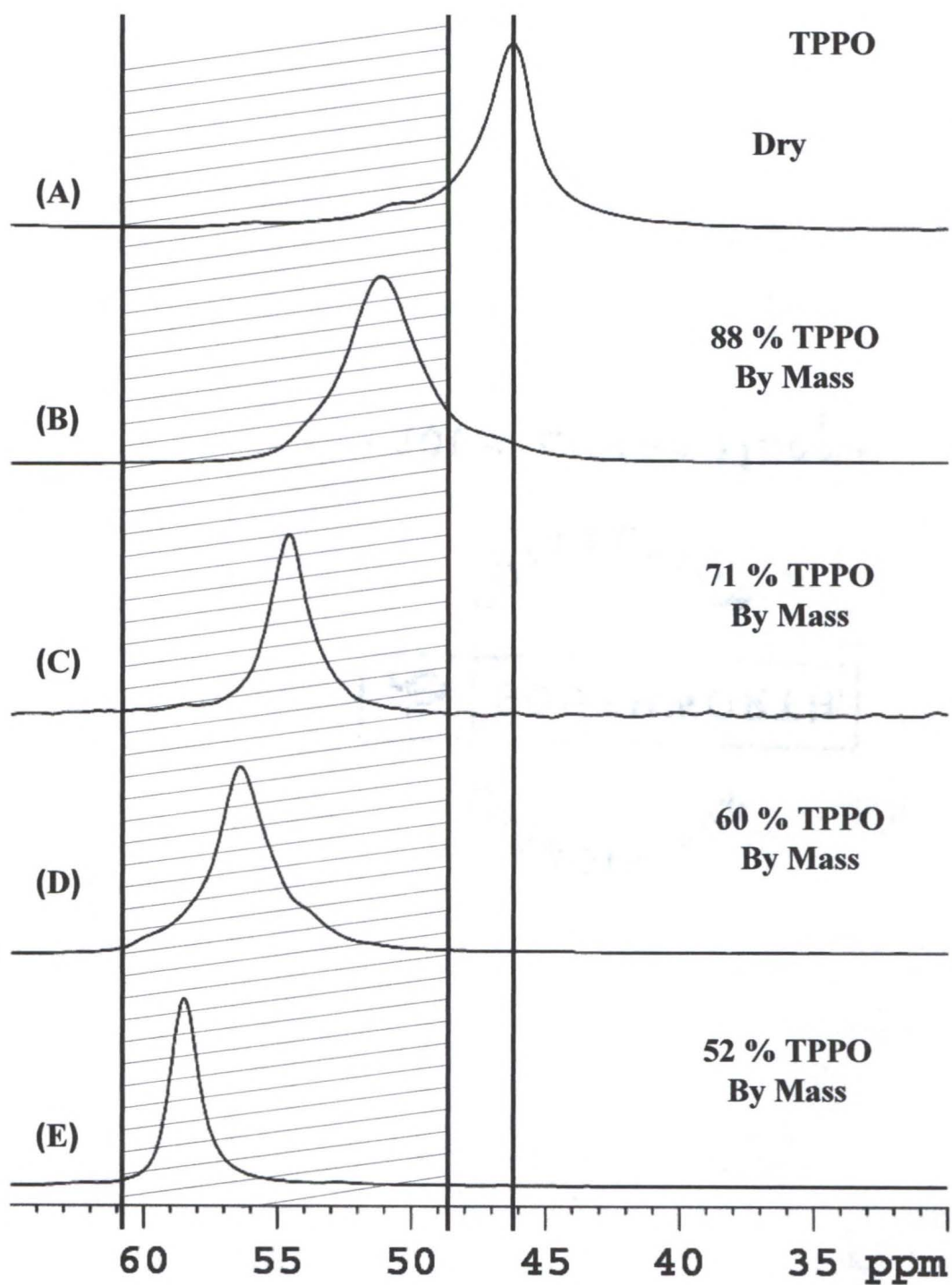


Figure 3-14. The  $^{31}\text{P}$  MAS NMR Spectra of TPPO as a result of dissolving and diluting with water. A) Dry TPPO. B) 88 % TPPO solution. C) 71 % TPPO solution. D) 60 % TPPO solution. E) 52 % TPPO solution.

## Host-Guest Exchange of Compound **2** Involving TMPO, TEPO, and TPPO

### Gas Chromatography Results

The gas chromatography experiments monitoring the guest exchange of bipy with TMPO, TEPO, and TPPO within **2** are summarized in column bar graph format in Figure 3-15. Just as in **1**, **2** takes in essentially all of the available quantity of TMPO but releases more bipy than **1**. Furthermore, significantly more TEPO and TPPO are taken within **2** than **1** and the accompanying bipy loss proceeds to a greater extent as well. In fact, the TEPO uptake by **2** is nearly complete. Cobalt(II) is more oxophilic and susceptible to oxidation than nickel(II) and this propensity is exhibited in the guest exchange reactions. Given the same initial available quantities of the TAPO's, the uptake of the oxygen containing probe molecules by **2** is much greater compared to **1**. Therefore, despite the steric and size constraints that apparently hinder the uptake of TEPO and TPPO by **1**, these obstacles are overcome in **2** due to the oxophilic nature of the host.

### NMR Results

The large quadrupole moment of the Co(II) nucleus along with the coupling of the dipolar interaction of the  $^{31}\text{P}$  nucleus from the trialkylphosphine oxides with the magnetic moment due to the unpaired electrons of the metal centers produces significant broadening and shifting of the characteristic resonances in **2**.<sup>199</sup> In order to unambiguously identify and resolve the peaks from spinning sidebands, high spinning speeds (>10 kHz) were required. Because of these magnetic interactions, the assignment of the  $^{31}\text{P}$  peaks in the NMR spectra are difficult because the positions of the resonances

are now determined not only by the chemical environment, but by the relative orientation of the phosphorous nucleus with respect to the Co(II) ions as well.<sup>199</sup>

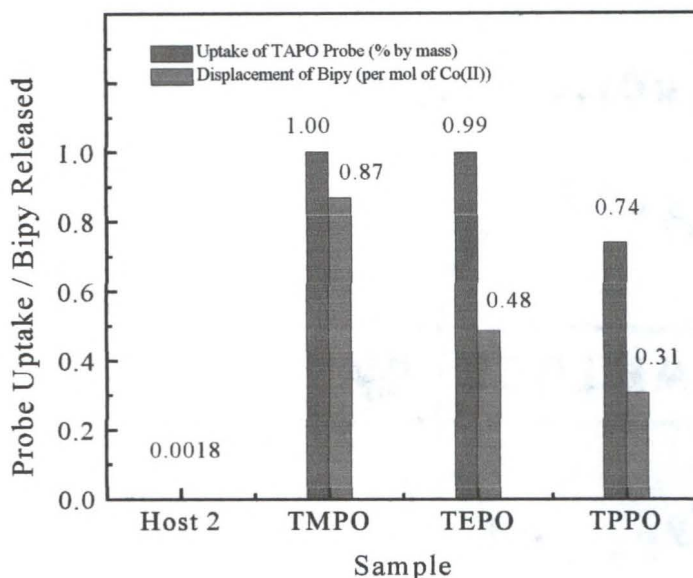


Figure 3-15. The gas chromatography results monitoring the guest exchange reactions in Host **2**. The left-hand columns denote the fraction of probe taken in by the host and the right hand columns represent the relative quantity of clathrated bipy released.

The NMR spectrum of **2** after the guest exchange of bipy with 1.0 mole of TMPO per mole of host is shown in Figure 3-16 A. A single broad resonance was identified at 26.9 ppm. This peak is shifted upfield considerably compared to resonances observed for both crystalline and wet TMPO as well as TMPO interacting with **1**. This peak is tentatively assigned to direct TMPO coordination to the Co(II) ions. However, it is unclear whether this resonance is a chemical shift effect due solely to the TMPO coordination, to the coupling of the dipolar moments of the <sup>31</sup>P nucleus with the magnetic moments from the metal centers, or a combination of both effects.<sup>199</sup> The uptake of TMPO by **2** results in an observable color change from orange to pink suggesting a slight change in the ligand field about the Co(II) ions although the geometry still remains

octahedral. Due to the highly oxophilic nature of the Co(II) ions, the TMPO may have replaced one or both of the aqua ligands coordinated to the metal centers although the GC measurements did not indicate the presence of water in solution. This replacement would account for the color change after the guest exchange. It should also be noted that no peaks corresponding to TMPO interacting with either coordinated lattice water molecules are observed in the NMR spectrum, even at high spinning speeds. Evidently, the TMPO prefers to coordinate directly to metal centers rather than interact with the water molecules. In contrast, TMPO interacts with the lattice waters and aqua ligands rather than the Ni(II) ions in **1**. The profound broadening of the peak is likely due to the close proximity to and strong interaction of the TMPO with the Co(II) nucleus.<sup>199</sup>

The NMR spectra of **2** after the guest exchange of bipy with 1.0 mole of TEPO and 0.75 moles of TPPO per mole of host are shown in Figures 3-16 B and 3-16 C, respectively. In the case of **2** with TEPO, two chemical shifts were observed at high spinning speeds, one at 62.4 ppm and another at 103.1 ppm. These peaks are assigned to the interaction of TEPO with unbound and coordinated water sites, respectively. In the case of **2** with TPPO, a relatively low signal-to-noise ratio spectrum was observed just as with TPPO in **1**. A single broad resonance is observed at 124.3 ppm attributed to probe interacting only with bound water. However, again these assignments are tentative because broadening and possible chemical shift effects between the dipole moment of <sup>31</sup>P and the unpaired electrons of Co(II) ions.<sup>199</sup> Since the peaks are observed at frequencies consistent with those observed with TEPO and TMPO in **1** where interactions corresponding to bound and unbound water (the shaded region) were observed, these peak assignments are not unreasonable. Unlike TMPO, the uptake of TEPO and TPPO

by **2** produces no observable color changes in the samples suggesting no appreciable change in the ligand field of the Co(II) ions. Steric constraints may prevent ligand replacement by TEPO and TPPO resulting in direct metal coordination. However, the same spectral broadening from the interactions between the  $^{31}\text{P}$  nuclei and the Co(II) ions is observed suggesting that the TEPO and TPPO are in close proximity to the metal centers.

### **X-Ray Diffraction Results**

Figures 3-17A and 3-17B show the powder X-ray diffraction patterns of **2** before and after the exchange of bipy with one mole of TMPO, respectively. Recall from above that washing the host with solvent caused **2** to become less crystalline. A similar loss of crystallinity is observed after the guest exchange reaction as well. Note that the powder pattern of the guest-exchanged product resembles the corresponding pattern of the original material rather closely. However, the reflections in the  $7^\circ$  to  $10^\circ$  range decrease in intensity, move, and disappear after the guest exchange, particularly the interplanar  $[2\ 0\ 0]$  peak at  $10^\circ$ , so the structure of the new product is not exactly the same as the original host. Some disorder within the host is apparent and the layered sheet structure becomes disrupted. Despite the larger quantity of bipy displaced and the (aqua) ligand replacement that occurs in the TMPO sample, the structural rearrangements are rather mild in contrast to the significant structural changes in analogous samples of **1**. Although TMPO is chemically and topologically different from bipy, evidently TMPO fulfills the same role of guest as does bipy because the structures before and after the guest exchange are quite similar. Unlike **1**, **2** is capable of exchanging bipy with TMPO without producing dramatic structural rearrangements within the host.

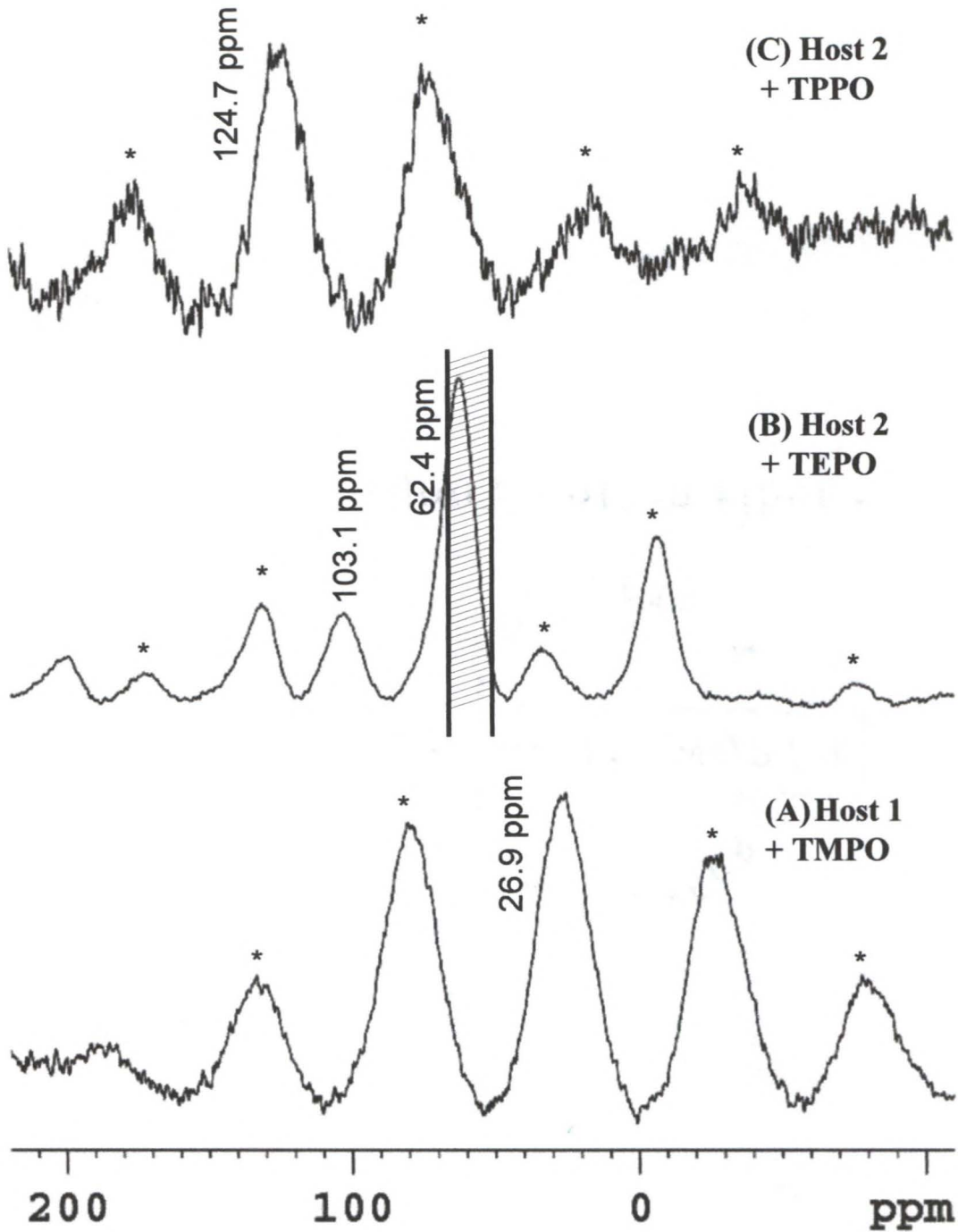


Figure 3-16. The  $^{31}\text{P}$  MAS NMR Spectra of Host 2 after the guest exchange of 4,4'-Bipyridine. A) Exchange with TMPO. B) Exchange with TEPO. C) Exchange with TPPO. The spinning sidebands are denoted by asterisks (\*).

Figures 3-17 C and 3-17 D show the powder X-ray diffraction patterns for **2** after the exchange of bipy with 1.0 moles of TEPO and 0.75 moles of TPPO per mole of host, respectively. The powder patterns of the TEPO and TPPO samples are quite similar, indicating the guest exchange causes the same structural changes and produces essentially the same product. The extent of the structural changes is consistent with the relatively large quantity of bipy released and probe taken in. A comparison of the powder patterns, particularly the 15 ° to 20 ° range, shows that the guest-exchanged has peaks common to both the original sample **2** and the analogous TEPO and TPPO samples of **1**. The exchange of bipy with TEPO and TPPO seem to cause similar structural rearrangements in both **1** and **2**. Again, the nature of these structural changes is not completely clear.

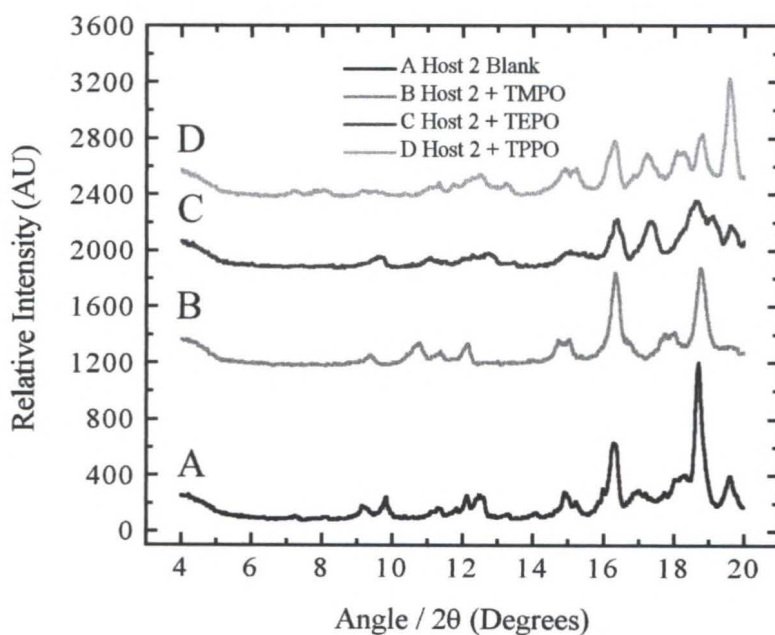


Figure 3-17. Powder X-ray diffraction patterns of Host **2** before and after the guest exchange of 4,4'-Bipyridine. A) No probe. B) Exchange with TMPO. C) Exchange with TEPO. D) Exchange with TPPO.

## Conclusions

This chapter describes the host-guest properties of two porous network structures,  $[\text{Ni}(4,4'\text{-bipy})_3(\text{H}_2\text{O})_2](\text{ClO}_4)_2 \cdot 1.4(4,4'\text{-bipy}) \cdot 3(\text{H}_2\text{O})$ , **1**, and  $[\text{Co}(4,4'\text{-bipy})_3(\text{H}_2\text{O})_2](\text{ClO}_4)_2 \cdot 1.4(4,4'\text{-bipy}) \cdot 3(\text{H}_2\text{O})$ , **2**. Gas chromatography experiments have determined that the both hosts exchange clathrated bipy molecules with trialkylphosphine oxide probe molecules, TMPO, TEPO, and TPPO. While the uptake of TMPO by both **1** and **2** is essentially complete, steric constraints are believed to limit the uptake of TEPO and TPPO by the host. The trialkylphosphine oxides interact with acid sites within the host as determined by  $^{31}\text{P}$  MAS NMR spectroscopy. TMPO interacts with both coordinated water molecules (strong acid sites) and weak acid site (lattice water) in **1** and coordinates directly to the metal centers in **2** but TEPO and TPPO seem to attack only the weaker acid sites within the hosts. X-ray diffraction patterns indicate the loss of bipy and uptake of probe causes significant structural rearrangements within the **1** but only mild structural changes are observed in **2** however the nature of these guest-exchanged products is unknown. These experiments have shown that solid-state NMR spectroscopy can be used to investigate host-guest interactions.

CHAPTER 4  
STRUCTURAL AND MAGNETIC PROPERTIES OF A SERIES OF AZIDO-  
BRIDGED COPPER(II) LADDER-LIKE COORDINATION POLYMERS

**Introduction**

The rational design and synthesis of polynuclear transition metal complexes with characteristic structural and physical properties has, in recent years, been an area of great interest in materials science and solid-state chemistry. These materials can be often built through the self-assembly of simple molecular or ionic components, *e.g.* transition metal ions or complexes with multifunctional bridging ligands, in solution. These bridging ligands act to propagate the structural and geometrical properties of the metal center, which can heavily influence the topology of the overall molecular or solid-state structure. These topologies include oligomers, one-dimensional chains, two-dimensional sheets, and three-dimensional networks. The overall structures can also be affected by reaction and crystallization conditions, most notably the metal:bridging ligand stoichiometry and as such, much effort has dedicated to elucidating and cataloging various synthetic strategies for building such molecular and extended solid-state materials. These materials often have useful bulk electronic, magnetic, and optical properties.

**Azide Bridging Modes**

Among the most common bridging ligands employed in the design of molecular and solid-state materials are halides and pseudohalides (thiocyanate, cyanate, and azide). The azide ( $N_3^-$ ) anion is a versatile ligand known to adopt a wide variety of coordination modes in transition metal complexes. Aside from coordinating in a monodentate

fashion<sup>200-203</sup>, ligating through only one nitrogen atom, this ligand can exhibit a variety of bridging modes as well. In general, two types of bridging modes are known for the azido ligand: the  $\mu$ -(1,1) or “end-on” mode<sup>204-209</sup> and  $\mu$ -(1,3) or “end-to-end” mode<sup>210-215</sup>, illustrated schematically in Figure 4-1. In the end-on mode, the bridge is established through a single nitrogen donor while in the end-to-end mode, both peripheral nitrogen atoms participate in the bridge. The bis(bidentate) bridging modes ( $\mu$ -(1,1) and  $\mu$ -(1,3)), where the metal centers are doubly bridged, are the most commonly encountered but single end-on<sup>216</sup> and end-to-end bridges<sup>217</sup>, although more scarce, are known as well. Numerous examples of discreet and extended transition metal structures sustained by azide-bridge are known, including oligomers (dimers, trimers, tetramers, etc.), clusters, chains, and sheets.<sup>218-225</sup> Of these materials, azido-bridged dimers of Cu(II) are by far the most common.<sup>206,226-229</sup>

Other bridging modes are possible, such as the  $\mu$ -(1,1,1)<sup>230</sup>, where a single nitrogen donor bridges three metal centers, and the  $\mu$ -(1,1,3)<sup>231-235</sup>, a combination of the end-on and end-to-end bridge. Furthermore, the simultaneous presence of two or more different azide coordination modes within the same structure is possible.<sup>236</sup> For example, complexes with the combination of both terminal and end-to-end bridged azido ligands are rare<sup>237</sup> but structures with both terminal and end-on bridged azido groups are more common<sup>238-241</sup> and samples with both end-on and end-to-end azido groups present are very rare.<sup>226,242-245</sup>

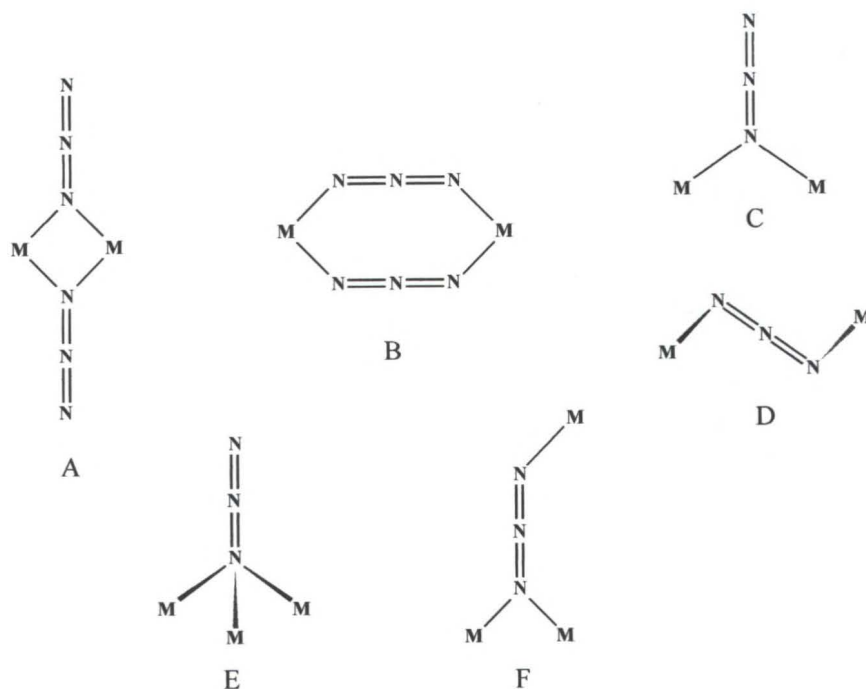


Figure 4-1. Schematic depicting the various bridging modes adopted by the azide ligand. A) the  $\mu$ -(1,1) or double end-on bridge. B) The  $\mu$ -(1,3) or double end-to-end bridge. C) The  $\mu$ -(1,1) or single end-on bridge. D) The  $\mu$ -(1,3) or single end-to-end bridge. E) The  $\mu$ -(1,1,1) bridge. F) The  $\mu$ -(1,1,3) bridge.

### Superexchange Properties of Azide Bridges

The azide ion is a well-known mediator of superexchange interactions between metal centers with unpaired spins. A diverse array of magnetic properties is possible due to the various types of bridging modes exhibited by the azide ion.<sup>6</sup> The end-on bridging mode typically mediates ferromagnetic exchange interactions between the metal centers.<sup>6,17,237,246-249</sup> In many cases, the exchange is so strong, that the energy gap between the spin triplet ground state and the spin singlet excited state is so large that the excited  $S = 0$  state is, at best, only weakly populated at high temperature.<sup>250,251</sup> In contrast, the end-to-end bridging mode typically mediates antiferromagnetic exchange interactions.<sup>6,17,222,237,246,252,253</sup> In some cases, the singlet state is stabilized with

respect to the excited triplet state to the extent that the corresponding compounds appear diamagnetic at room temperature.<sup>214,254</sup>

In symmetric end-to-end azide bridges where the three nitrogen atoms are contained within the plane of the metal centers, the exchange is typically strongly antiferromagnetic.<sup>6,205</sup> For example, if the end-to-end azide ligands coordinate to the equatorial sites of two Cu(II) ions, the metal centers are strongly antiferromagnetically coupled. This is due to the significant unpaired spin density associated with the  $d_{x^2-y^2}$  orbitals for both octahedral and square pyramidal coordinated Cu(II) ions. The appreciable delocalization of the electron density to the bridging azide ligand coordinated to both equatorial Cu(II) ions renders this type of bridge an efficient mediator of superexchange interactions.

In complexes with asymmetric azide bridges (with both long and short Cu—N bonds), and non-coplanar azide bridges (all three atoms of the  $N_3^-$  ion are not contained within the plane of the metal centers), the exchange between the spin centers is typically weak.<sup>6,205,255</sup> Obviously, poor orbital overlap and hence weak exchange results from long Cu—N bonds. In Cu(II) complexes, non-coplanar bridges often result from the azide ion coordinating to the axial sites on one metal center and the equatorial sites on the other ion. If the Cu(II) ions are octahedral or square pyramidal, the exchange is negligibly small while the coupling is weakly antiferromagnetic in trigonal bipyramidal geometries.<sup>205,255</sup> The unpaired spins in octahedral and square pyramidal Cu(II) ions principally reside in the  $d_{x^2-y^2}$  atomic orbitals and low unpaired electron density is associated with the  $d_z^2$  orbital. There is a good delocalization of the electron density to the bridging azide ligand coordinated to the equatorial Cu(II) ions but the delocalization

to the azide bridge coordinated to the axial Cu(II) ions is poor since the  $d_z^2$  orbital is occupied by paired spins. Therefore, the magnitude of the exchange is weak. The antiferromagnetic coupling is greater between the axial-equatorial coordination sites in the trigonal bipyramidal geometry of Cu(II) ions due to the increased unpaired spin density associated with the  $d_z^2$  orbitals due to admixture from  $d_x^2-y^2$  orbitals.<sup>205,255</sup>

It is known that both the magnitude and sign of superexchange interactions mediated by end-on azide bridges are strongly dependent on characteristic structural-bonding parameters of the magnetic M—N<sub>3</sub>—M unit, including M—N bond distance, the M—N—M bridging angle, and the planarity of the M—N<sub>3</sub>—M moiety.<sup>6,250,251</sup> Under most circumstances, an end-on azide bridge mediates a ferromagnetic exchange between the metal centers. In order to rationalize this behavior, numerous theoretical approaches have been developed to determine the relative energies between the magnetic orbitals, the frontier molecular orbitals involved in the superexchange processes.<sup>6,205,250,251</sup> In fact, the relative energies of these magnetic orbitals heavily influence both the sign and magnitude of the exchange. For example, in  $\mu$ -1,1-diazido copper(II) complexes, the sign and magnitude of the exchange interaction is highly dependent on the Cu—N—Cu bridging angle.<sup>6,251</sup> If the bridging angle is small (100° - 105°), the net exchange is ferromagnetic and the magnitude of the exchange increases as the bridging angle closes.<sup>21,205,238,256</sup> However, if the bridging angle is large (> 108.5°), the net exchange is typically antiferromagnetic.<sup>238,256</sup>

Consider the magnetic orbitals of a doubly end-on azido bridged copper(II) dimer (Figure 4-2).<sup>6,17,236,246,270</sup> The magnetic orbitals,  $\Phi_S'$  and  $\Phi_{AS}'$ , of the dimer are the in-phase (symmetric) and out-of-phase (asymmetric) combinations of the metal  $d$ -type

atomic orbitals that contain the unpaired electrons and the symmetry adapted  $\sigma$ -type HOMO's (highest occupied molecular orbitals) from the principally  $p$ -type azide atomic orbitals. The "symmetric" and "asymmetric" character refers to the symmetry of the orbitals with respect to a mirror plane perpendicular to the molecular plane. Note that the magnetic orbitals are principally of antibonding character.

The energy variation of the  $\Phi_S'$  and  $\Phi_{AS}'$  orbitals when the M—N—M bridging angle varies is essentially governed by the metal  $d$ -orbital / ligand  $p$ -orbital antibonding overlaps (Figure 4-2).<sup>6,17,246</sup> For bridging angles close to  $90^\circ$ , the overlaps of the  $\chi_S$  and  $\chi_{AS}$   $d$ -orbitals with  $\phi_S'$  and  $\phi_{AS}'$   $\sigma$ -orbitals are equal and negative and thus the two magnetic orbitals are degenerate; strict orthogonality of the orbitals is observed. Actually, the angle is slightly higher than  $90^\circ$  due to admixture from ligand  $s$  orbitals close in energy to the  $p$  orbitals. Therefore, at low bridging angles, since the magnetic orbitals are degenerate, a triplet ground state is stabilized, and the ferromagnetic contribution to the total exchange dominates. As the bridging angle increases, the energy of  $\Phi_S'$  becomes less negative due to the decrease in antibonding character. Conversely, the energy of  $\Phi_{AS}'$  becomes more negative due to the increase in antibonding character. Therefore the energy difference between the magnetic orbitals increases thus stabilizing the singlet magnetic ground state. At bridging angles greater than  $108.5^\circ$ , the energy difference between the magnetic orbitals is large enough that the antiferromagnetic contribution to the total exchange dominates. At the particular angle of  $108.5^\circ$ , the angle of accidental orthogonality, the singlet and triplet states are accidentally degenerate and no net exchange interaction observed since the ferromagnetic and antiferromagnetic contributions exactly compensate for one another. The same molecular orbital approach

has been used to rationalize the signs of coupling constants for other structural and electronic perturbations as well, such as in-plane distortions of the magnetically important Cu—(N<sub>3</sub>)<sub>2</sub>—Cu moiety, the effects of ancillary ligands, and changing the electronegativity of the bridge.<sup>6</sup>

Another approach to rationalizing the signs of the coupling constants between the end-to-end and end-on azide bridges is the spin polarization mechanism (Figure 4-3).<sup>205,257</sup> The role of the low-energy, doubly occupied ligand orbitals is considered in the spin polarization approach. Each  $\pi_g$  orbital of the azide ion describes two paired electrons localized at the two terminal nitrogen atoms. At each instant, one of the two electrons is “spin up”, or has an  $\alpha$  spin, and the other is “spin down”, or has a  $\beta$  spin. For end-on azide ligands bridging octahedral and square pyramidal Cu(II) ions, a  $\pi_g$  electron on the bridging nitrogen atom is partially delocalized toward the two metal  $d_{x^2-y^2}$  orbitals. The polarization of the unpaired spins on the metal centers produces a parallel alignment thus giving rise to ferromagnetic coupling. In contrast, for the end-to-end case, an  $\alpha$  spin electron is partially delocalized toward one of the metal centers and the  $\beta$  spin is partially delocalized toward the other metal center. The polarization of the unpaired electrons on the metal centers results in an antiparallel alignment thus giving rise to the antiferromagnetic coupling.

### Chapter Summary

The purpose of this chapter is to investigate the structural and magnetic properties of three azido-bridged copper(II) ladder-like coordination polymers, [Cu<sub>2</sub>(PhPyPy)<sub>2</sub>- $\mu$ -(N<sub>3</sub>)<sub>2</sub>(N<sub>3</sub>)<sub>2</sub>], **4**, [Cu<sub>2</sub>(terpy)<sub>2</sub>- $\mu$ -(N<sub>3</sub>)<sub>4</sub>Cu<sub>2</sub>- $\mu$ -(N<sub>3</sub>)<sub>2</sub>(N<sub>3</sub>)<sub>2</sub>], **5**, and [Cu<sub>2</sub>(terpy)<sub>2</sub>- $\mu$ -(N<sub>3</sub>)<sub>2</sub>(N<sub>3</sub>)<sub>2</sub>Cu<sub>3</sub>- $\mu$ -(N<sub>3</sub>)<sub>4</sub>(N<sub>3</sub>)<sub>2</sub>], **6**. The first part of the chapter examines in detail both the

molecular and solid-state structure of the title compounds. The second part of the chapter describes the magnetic properties of the title compounds. Bulk magnetization and susceptibility data as well as the appropriate theoretical models needed to describe the magnetic behavior are discussed. Furthermore, the magnetic exchange interactions, mediated by the various azide ligands bridging the Cu(II) metal centers, are examined and rationalized on the basis of characteristic structural-bonding parameters.

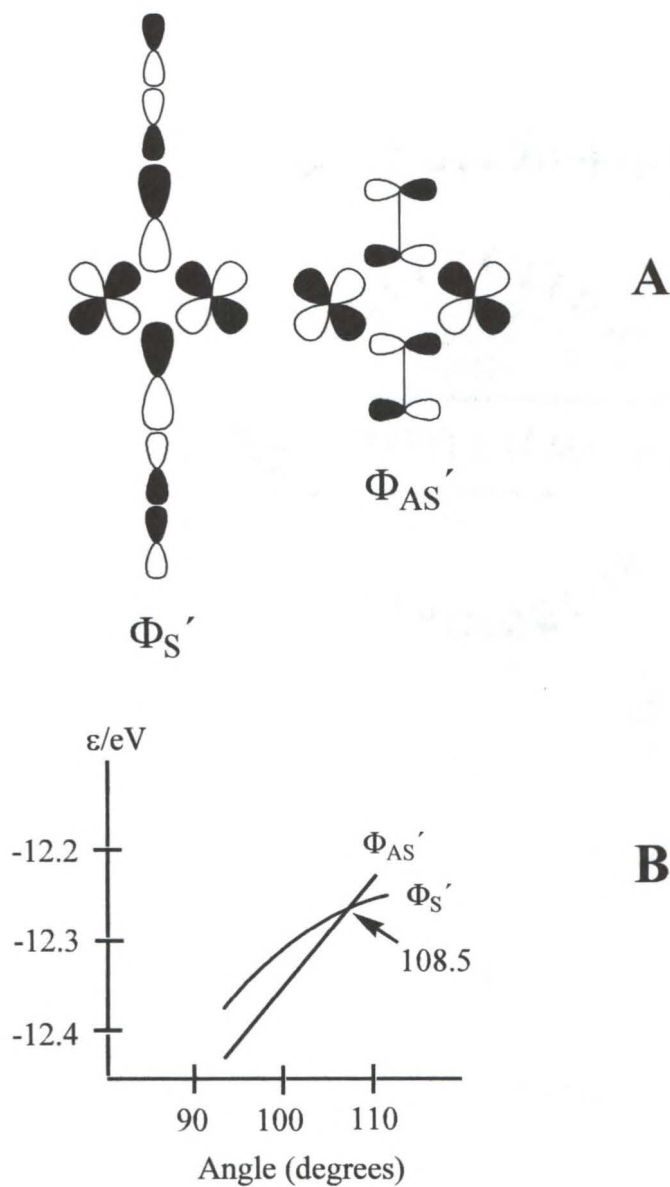


Figure 4-2. Correlating the sign of exchange interactions with the metal-azide bridging angle. A) Magnetic orbitals for planar  $\mu$ -1,1-diazaido copper(II) dimers. B) Graph depicting the energy variation of the  $\Phi_{AS'}$  and  $\Phi_{S'}$  magnetic orbitals vs. the bridging angle in planar  $\mu$ -1,1-diazaido copper(II) dimers (bottom) obtained from extended Hückel calculations. Adapted from references 236 and 270.

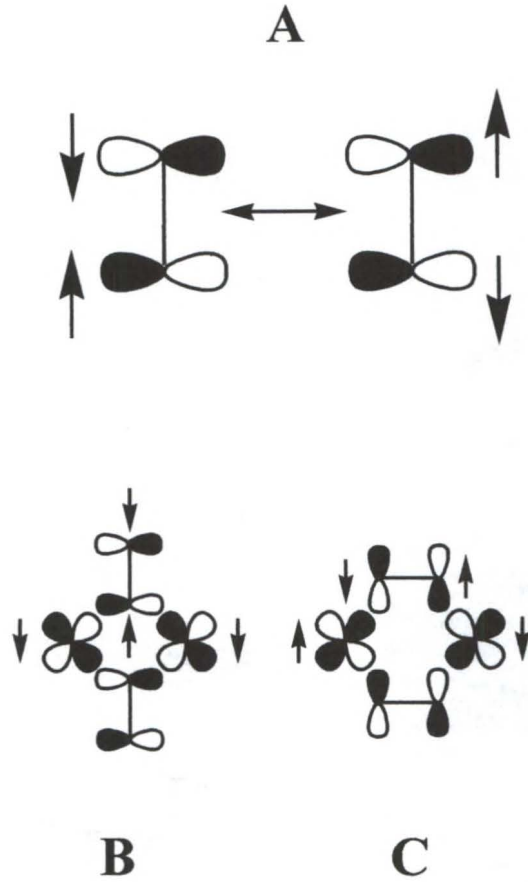


Figure 4-3. Schematic depicting the spin polarization mechanism A) The  $\pi_g$  orbital of an azide ion. B) The unpaired spins on the metal centers are polarized in a parallel fashion in the end-on bridging mode, leading to ferromagnetic exchange interactions. C) The spins are polarized in an antiparallel manner in the end-to-end bridging mode leading to the antiferromagnetic coupling (bottom right). Adapted from references 205 and 257.

## Experimental Section

### Materials

Copper(II) perchlorate hexahydrate (98 %), 2,2':6,2''-terpyridine (98 %), 4-(3-phenylpropyl)pyridine (97 %) and sodium azide (99 %) were purchased from Aldrich Chemical Co. Dimethyl Sulfoxide (99.9 %) was purchased from Fisher Scientific (Pittsburgh, PA). All reagents were used without further purification. Throughout this chapter, DMSO refers to dimethyl sulfoxide, terpy refers to 2,2':6,2''terpyridine, and PhPrPy refers to 4-(3-phenylpropyl)pyridine. Unless stated otherwise, all reactions and crystallizations were performed under ambient laboratory conditions.

### Synthesis of $[\text{Cu}_2(\text{PhPyPy})_2-\mu-(\text{N}_3)_2(\text{N}_3)_2]$

A solution containing 105 mg of Phprpy (0.532 mmol) dissolved in 20 mL of DMSO was added, drop wise, to a solution containing 800 mg of  $\text{Cu}(\text{ClO}_4)_2 \cdot 6\text{H}_2\text{O}$  (2.16 mmol) dissolved in 20 mL of DMSO resulting in a blue colored solution. A solution containing 344 mg of  $\text{NaN}_3$  (5.29 mmol) dissolved 20 mL of DMSO was added, drop wise, to the above copper-terpy solution producing a dark green colored solution. After approximately one week, dark green-black needles of **4** crystallized from solution, werecollected by vacuum filtration, and washed with ethanol (yield 61 % based on PhPrPy being the limiting reagent). Analysis calculated for  $\text{Cu}_2\text{C}_{14}\text{H}_{15}\text{N}_{14}$ : C, 48.75 %; H, 4.39 %; N, 28.44 %. Found: C, 47.92 %; H, 4.29 %; N, 28.26 %.

### Synthesis of $[\text{Cu}_2(\text{terpy})_2-\mu-(\text{N}_3)_4\text{Cu}_2-\mu-(\text{N}_3)_2(\text{N}_3)_2]$

A solution containing 80 mg of terpy (0.343 mmol) dissolved in 10 mL of DMSO was added, drop wise, to a solution containing 800 mg of  $\text{Cu}(\text{ClO}_4)_2 \cdot 6\text{H}_2\text{O}$  (2.16 mmol) dissolved in 10 mL of DMSO resulting in a blue colored solution. A solution containing

501 mg of  $\text{NaN}_3$  (7.71 mmol) dissolved 20 mL of DMSO was added, drop wise, to the above copper-terpy solution producing a dark green colored solution. After approximately one week, dark green-black needles of **5** crystallized from solution, were collected by vacuum filtration, and washed with ethanol (yield 64 % based on terpy being the limiting reagent). Analysis calculated for  $\text{Cu}_4\text{C}_{30}\text{H}_{22}\text{N}_{30}$ : C, 34.09 %; H, 2.10 %; N, 39.76 %. Found: C, 34.00 %; H, 1.99 %; N, 39.46 %.

#### **Synthesis of $[\text{Cu}_2(\text{terpy})_2-\mu-(\text{N}_3)_2(\text{N}_3)_2\text{Cu}_3-\mu-(\text{N}_3)_4(\text{N}_3)_2]$**

A solution containing 80 mg of terpy (0.343 mmol) dissolved in 10 mL of DMSO was added, drop wise, to a solution containing 800 mg of  $\text{Cu}(\text{ClO}_4)_2 \cdot 6\text{H}_2\text{O}$  (2.16 mmol) dissolved in 10 mL of DMSO resulting in a blue colored solution. A solution containing 344 mg of  $\text{NaN}_3$  (5.29 mmol) dissolved 20 mL of DMSO was added, drop wise, to the above copper-terpy solution producing a dark green colored solution. After approximately one week, dark green-black needles of **6** crystallized from solution, were collected by vacuum filtration, and washed with ethanol (yield 58 % based on terpy being the limiting reagent). Analysis calculated for  $\text{Cu}_5\text{C}_{30}\text{H}_{22}\text{N}_{36}$ : C, 29.91 %; H, 1.84 %; N, 41.89 %. Found: C, 30.03 %; H, 1.71 %; N, 41.64 %.

#### **Physical Characterization**

Elemental analyses were performed by the University of Florida Spectroscopic Services Laboratory.

#### **X-ray Structure Determination**

Black needles of **4** ( $0.45 \times 0.12 \times 0.04 \text{ mm}^3$ ), **5** ( $0.46 \times 0.10 \times 0.03 \text{ mm}^3$ ), and **6** ( $0.17 \times 0.07 \times 0.02 \text{ mm}^3$ ) were selected for X-ray analysis. Each crystal was mounted on a glass fiber under nitrogen gas. The same data collection was used for each sample. Data were collected at 173 K on a Siemens SMART PLATFORM equipped with a CCD

area detector and a graphite monochromator utilizing MoK $\alpha$  radiation ( $\lambda = 0.71073 \text{ \AA}$ ). Cell parameters were refined using 7838 reflections. A hemisphere of data (1381 frames) was collected using the  $\omega$ -scan method (0.3 ° frame width). The first 50 frames were re-measured at the end of data collection to monitor instrument and crystal stability (maximum correction of I was < 1 %). Absorption corrections by integration were applied based on measured indexed crystal faces.

All structures were solved by the Direct Methods in *SHELLXTL6* and refined using full-matrix squares.<sup>155</sup> The non-H atoms were treated anisotropically, whereas the hydrogen atoms were calculated in ideal positions by riding on their respective carbon atoms. For **4**, the asymmetric unit consists of a half-dimer. Part of the pyridine moiety and part of the propyl fragment,  $-\text{C}_6(\text{H}_2)\text{C}_7(\text{H}_2)-$ , are both disordered; N1 of the pyridyl group is not disordered. The disorder was refined in two parts. Their site occupation factors were dependently refined to 0.56(1) for the major part and consequently 0.44(1) for the minor part. A total of 264 parameters were refined using  $F^2$  in the final cycle using 3477 reflections with  $I > 2\sigma(I)$  to yield  $R_1 = 3.18 \%$  and  $wR_2 = 6.99 \%$ . For **5**, the asymmetric unit consists of a half-tetramer. A total of 289 parameters were refined using  $F^2$  in the final cycle using 4330 reflections with  $I > 2\sigma(I)$  to yield  $R_1 = 3.86 \%$  and  $wR_2 = 9.69 \%$ . For **6**, the asymmetric unit consists of a half-pentamer. A total of 323 parameters were refined using  $F^2$  in the final cycle using 4771 reflections with  $I > 2\sigma(I)$  to yield  $R_1 = 4.39 \%$  and  $wR_2 = 8.37 \%$ .

### **Magnetic Measurements**

Bulk magnetization measurements, performed in Professor Mark Meisel's laboratory in the Department of Physics, University of Florida, were obtained from a

standard Quantum Design MPMS SQUID magnetometer. The samples consisted of randomly oriented single crystals with a total mass of 40.8 mg for **4**, 96.3 mg for **5**, and 57.7 mg for **6**. A polyethylene canister and plastic straw were used as the sample holder during the measurements. Magnetization versus temperature measurements were run from 2 K to 300 K. The sample was zero-field cooled to 2 K before a measuring field of 100 G was applied and the data set was then taken while warming the sample from the lowest temperature. Magnetization versus field measurements were performed at 2 K over the range of 0 to 50 kG. The background signals arising from the canister and straw were measured independently and subtracted from the results. The diamagnetic contribution from each sample, estimated from Pascal's constants ( $\chi_D = -345.52 \times 10^{-6}$  emu mol<sup>-1</sup> for **4**,  $\chi_D = -452.08 \times 10^{-6}$  emu mol<sup>-1</sup> for **5**, and  $\chi_D = -491.10 \times 10^{-6}$  emu mol<sup>-1</sup> for **6**) was also subtracted from the results.<sup>5,6</sup>

ESR spectra were recorded in a Bruker ER 200D spectrometer modified with a digital signal channel and digital field controller on polycrystalline samples contained within evacuated quartz sample tubes. Data were collected using a U. S. EPR SPEC300 data acquisition program and converted to ASCII format using a U. S. EPR EPRDAP data analysis program. The temperature was controlled by and Oxford Instruments ITC 503 temperature-controller and an ESR 900 continuous flow liquid helium cryostat.

## Results and Discussion

### Description of the Structures

Crystallographic and structural refinement data for **4**, **5**, and **6** are listed in Table 4-1. Tables of atomic coordinates and thermal displacement parameters and bond angles and distances for **4**, **5**, and **6** are provided in the Appendix B.

**Table 4-1.** Summary of Crystallographic Data for Compounds **4**, **5**, and **6**.

Sample	<b>4</b>	<b>5</b>	<b>6</b>
Empirical Formula	C <sub>28</sub> H <sub>30</sub> Cu <sub>2</sub> N <sub>14</sub>	C <sub>15</sub> H <sub>11</sub> Cu <sub>2</sub> N <sub>15</sub>	C <sub>15</sub> H <sub>11</sub> Cu <sub>2.5</sub> N <sub>18</sub>
Formula Weight	689.74	528.47	602.27
Space Group	Monoclinic, P2(1)/n	Monoclinic, P2(1)/n	Triclinic, P-1
<i>a</i> , Å	5.2066(2)	14.4872(8)	6.6035(6)
<i>b</i> , Å	10.7847(4)	7.1430(4)	12.660(1)
<i>c</i> , Å	27.069(1)	18.454(1)	13.110(1)
$\alpha$ , deg	90	90	88.682(2)
$\beta$ , deg	91.620(1)	95.719(1)	76.278(2)
$\gamma$ , deg	90	90	82.819(2)
<i>V</i> , Å <sup>3</sup>	1519.4(1)	1900.2(2)	1056.4(1)
<i>Z</i>	2	4	2
<i>T</i> , K	173(2)	173(2)	173(2)
$\lambda$ (Mo K $\alpha$ ), Å	0.71073	0.71073	0.71073
$\rho_{\text{calc}}$ , g cm <sup>-3</sup>	1.508	1.847	1.893
$\mu$ , mm <sup>-1</sup>	1.445	2.280	2.552
<i>R</i> <sub>1</sub> <sup>a</sup> ( <i>wR</i> <sub>2</sub> <sup>b</sup> )	0.0318 (0.0699)	0.0386 (0.0969)	0.0439 (0.0837)

$$^a R_1 = \sum (||F_0| - |F_c||) / \sum |F_0| \quad ^b wR_2 = [\sum [w(F_0^2 - F_c^2)^2] / \sum [w(F_0^2)^2]]^{1/2}$$

$$S = [\sum [w(F_0^2 - F_c^2)^2] / (n - p)]^{1/2}$$

$$w = 1/[\sigma^2(F_0^2) + (0.0370 * p)^2 + 0.31 * p], p = [\max(F_0^2, 0) + 2 * F_c^2] / 3$$

### Structure of [Cu<sub>2</sub>(PhPyPy)<sub>2</sub>- $\mu$ -(N<sub>3</sub>)<sub>2</sub>(N<sub>3</sub>)<sub>2</sub>]

The structure of **4** consists of neutral, chain-like stacks of [Cu<sub>2</sub>(PhPrPy)<sub>2</sub>- $\mu$ -(1,1-N<sub>3</sub>)<sub>2</sub>(N<sub>3</sub>)<sub>2</sub>] dinuclear units. The centrosymmetric dimers, shown in Figure 4-4 are comprised Cu(II) ions bridged by two end-on azido ligands. The Cu—Cu distance is 3.10 Å while the Cu—N—Cu bridging angle is 101.9°. The Cu(N<sub>3</sub>)<sub>2</sub>Cu units are planar; no folding of the CuN<sub>2</sub> planes about an in-plane axis joining the two bridging atoms (N2 and N2A) is observed. The local coordination environment of each metal center is distorted octahedral. The equatorial plane is defined by four nitrogen atoms, two from the intradimer end-on azide bridges (N2 and N2A), one from the monocoordinate azide ligand (N5), and one from the pyridyl donor (N1) of the organic ligand 4-(3-phenylpropyl)pyridine. All equatorial Cu—N bond distances (1.97 Å to 1.99 Å) are similar. The bridging azide ligands are nearly linear (178.5°) while the terminal azide

groups are slightly bent ( $176.4^\circ$ ) at the central nitrogen atom. The axial coordination results from weak Cu—N contacts with the monocoordinate azide ligands on adjacent dimers within a chain; each metal center interacts with the terminal and ligated nitrogen atoms from two different azide ions. The Cu—N bond to the terminal nitrogen atom ( $2.62 \text{ \AA}$ ) is much shorter than the Cu—N bond to the ligated nitrogen atom ( $3.14 \text{ \AA}$ ) on the monocoordinate azide ligand on adjacent dimers. As a result of Jahn-Teller distortions, the axial Cu—N bonds are considerably longer than the equatorial bonds. The coordinated PhPrPy molecules are disordered in two parts about the 1,3-propyl fragments. Due to packing forces and bonding constraints of the propyl fragments, the phenyl groups of the organic ligands are not coplanar with the pyridyl moieties but twisted upwards (or downwards)  $113.1^\circ$  with respect to one another. These pyridyl moieties are themselves not coplanar with the  $\text{Cu}(\text{N}_3)_2\text{Cu}$  moieties but twisted  $69.5^\circ$  out of the plane of the dimers.

The dinuclear units stack atop one another to form chains that extend along the crystallographic *a*-axis. A single chain of **4** is shown in Figure 4-4. Within each chain, adjacent dimers are related by a single translation along the crystallographic *a*-axis and  $\frac{1}{4}$  translation along the *b*-axis, but stack in registry along the *c*-axis. The interdimer bonding consists of both double asymmetric end-to-end and end-on azide bridges. The terminal nitrogen atoms from the monocoordinate azide ligands weakly interact with the metal centers on adjacent dimers to form the asymmetric end-to-end bridges with long Cu—N contacts of  $2.62 \text{ \AA}$ . The CuA—N5—N6 and CuB—N7—N6 (CuB on an adjacent dimer) bridging angles are  $126.4^\circ$  and  $105.8^\circ$ , respectively while the dihedral angle between the two planes defined by CuB—N5—N6—N7 and N5—N6—N7—CuA

is  $94.3^\circ$ . The ligated nitrogen atoms from the same monodentate azide ligands also weakly interact with the metal centers on adjacent dimers within a chain thus producing the asymmetric end-on bridges with the long Cu—N contacts of  $3.14 \text{ \AA}$ . The CuA—N5—CuAB (CuAB is a copper ion on an adjacent dimer) bridging angle is  $90.6^\circ$ . Note that **4** can be viewed as an alternating chain because of the regular alternation of the intradimer end-on azide bridging with the interdimer asymmetric end-on and end-to-end azide bridges. However, since the interdimer interactions are significantly weaker than the intradimer bonding, **4** is better described as stacks of weakly interacting dimers.

Although both the phenyl and pyridyl rings from the organic ligands within each chain are stack in an offset parallel fashion,  $\pi$  interactions are negligible due to the large distance ( $\sim 5 \text{ \AA}$ ) between the molecules. Twin N—H contacts from the weak interactions between the terminal nitrogen atoms from the monocoordinate azide ligands and the pyridyl hydrogen atoms of the organic ligands are observed both within ( $2.44 \text{ \AA}$ ) and between ( $2.59 \text{ \AA}$ ) the ladder-like chains.

The packing diagrams of **4** are shown in Figure 4-5. Note that the packing of the chains in the crystallographic *bc*-plane resembles a herringbone motif. Adjacent chains are related by a single translation along the crystallographic *b*-axis, but  $\frac{1}{2}$  translation along the *c*-axis. The chains pack in registry along the *b*-axis. Along the *c*-axis, the chains are arranged in a zig-zag fashion and positioned approximately  $75^\circ$  with respect to one another. Since the phenyl rings between the chains are not oriented in a face-to-face coplanar fashion, no  $\pi$ -stacking interactions between the organic fragments are present. Instead,  $\pi$ -facial hydrogen bonding ( $\sim 3 \text{ \AA}$ ) is observed between hydrogen atoms of the propyl fragments and the faces of the phenyl rings on adjacent chains.

Structure 4 bears close resemblance to  $[\text{Cu}(4\text{-Etpy})(\text{N}_3)_2]_2$  (4-Etpy = 4-ethylpyridine), a ladder-like chain of weakly interacting end-on azido bridged Cu(II) dimers. In fact, the ladder-like molecular structure of the latter compound is almost identical to 4 other than the differing the organic ligands as well as solid-state packing.<sup>258</sup> All Cu—N bond distances and Cu—N—Cu and N—Cu—N bond angles are comparable to those reported for similar end-on azido bridged Cu(II) complexes.<sup>237,247-249</sup>

#### Structure of $[\text{Cu}_2(\text{terpy})_2-\mu-(\text{N}_3)_4\text{Cu}_2-\mu-(\text{N}_3)_2(\text{N}_3)_2]$

The structure of 5 consists of neutral, ladder-like azido-bridged copper(II) coordination polymers that extend along the crystallographic *b*-axis. The “rungs” consist of centrosymmetric  $\text{Cu}_2(\text{N}_3)_4$  dinuclear units positioned parallel to the crystallographic *a*-axis. Figure 4-6 depicts a portion of a typical ladder. The rung copper ions adopt a distorted square pyramidal geometry. The basal plane is defined by two nitrogen atoms from the double end-on azide bridges (N7 and N7A), a nitrogen atom (N13) from a single end-to-end azide bridge to the adjacent  $[\text{Cu}(\text{terpy})(\text{N}_3)_2]$  groups, and a nitrogen atom (N10) from a monocoordinate azide ligand. The apical site is occupied by the ligated nitrogen atom (N4) from a single end-on azide bridge to the adjacent  $[\text{Cu}(\text{terpy})(\text{N}_3)_2]$  units. An apical elongation is observed since the weak Cu2—N4 contacts (2.37 Å) are significantly longer than the basal bonds. In the basal plane, the Cu2—N bonds to the double end-on azide bridges (1.99 Å and 2.04 Å) are slightly longer than the Cu—N bonds to the single end-to-end azide bridge (1.98 Å) and the monodentate azide ligand Cu—N10 (1.98 Å) bonds. The average values of the N(apical)—Cu—N(basal) angles is 95.1 ° while the *trans*-basal N7A—Cu—N10 and N13—Cu—N7 angles are 177.1 ° and

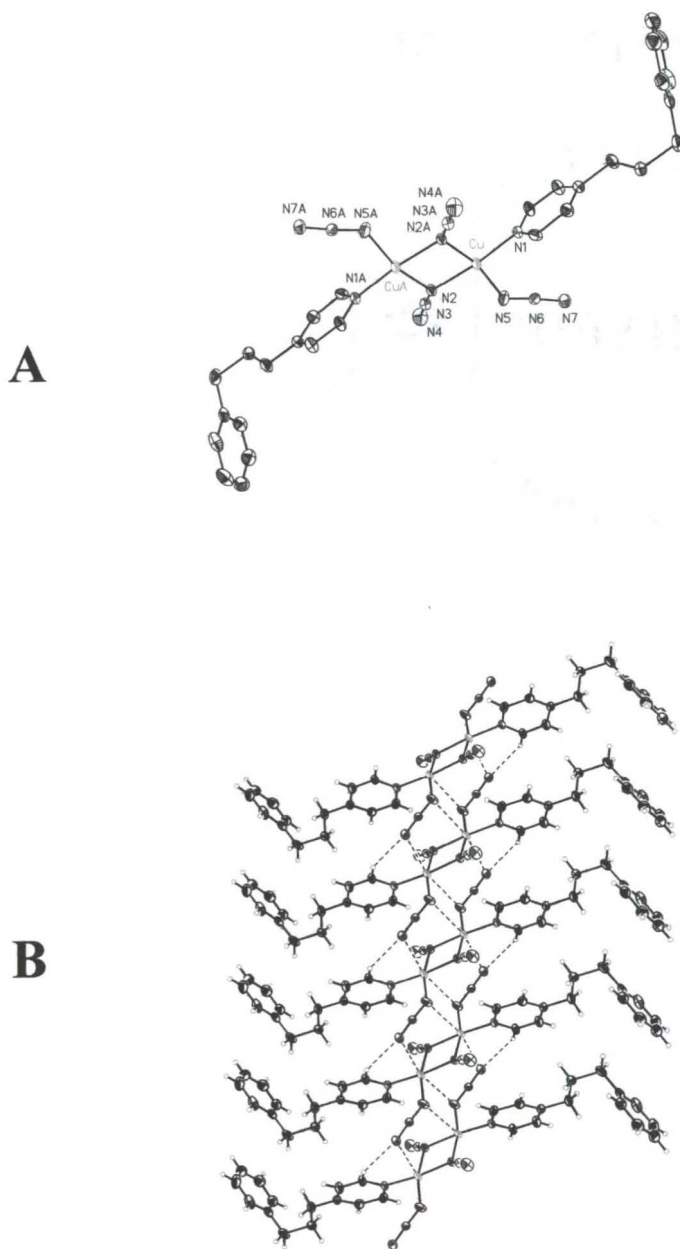


Figure 4-4.  $[\text{Cu}_2(\text{PhPyPy})_2-\mu-(\text{N}_3)_2(\text{N}_3)_2]$ . A) The  $\mu$ -diazo dicopper units. B) A ladder-like stack of dimer. All hydrogen atoms have been omitted from A) for clarity. All non-hydrogen atoms are represented by thermal ellipsoids drawn to encompass 30 % of electron density.

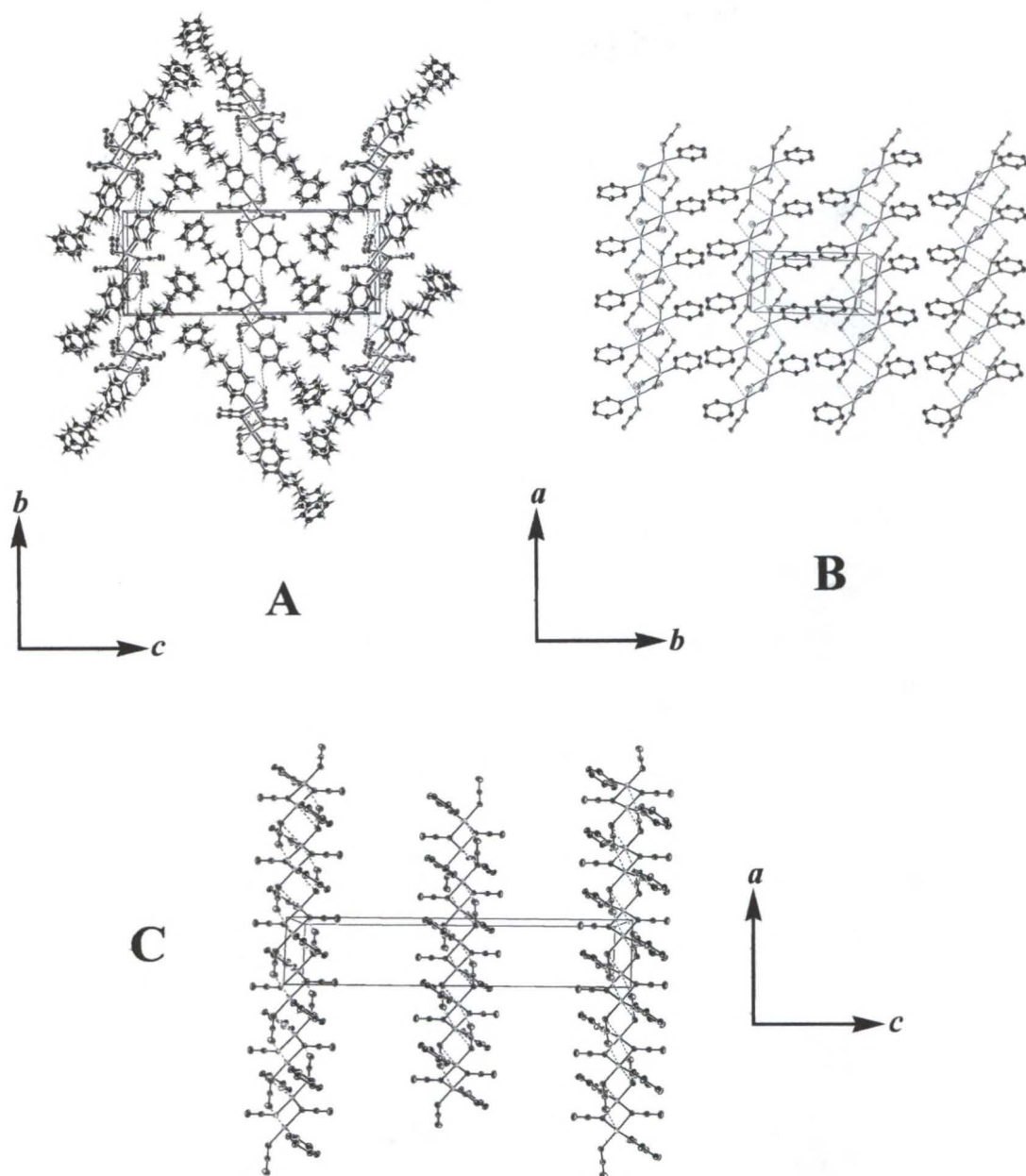


Figure 4-5.  $[\text{Cu}_2(\text{PhPyPy})_2] \cdot \mu\text{-(N}_3)_2(\text{N}_3)_2$ . A) The structure within the crystallographic  $bc$ -plane. B) The structure within the crystallographic  $ab$ -plane. C) The structure within the crystallographic  $ac$ -plane. For clarity, the phenylpropyl fragments and pyridyl hydrogen atoms from the organic ligand have been omitted from B) and the organic ligands have been removed altogether from C).

154.2 °, respectively. The Cu(II) ion is displaced 0.187 Å from mean basal plane Cu2—N7—N10—N13—N16 directed toward the apical ligand. The monocoordinate azide ligand is slightly bent (176.5 °) at the central nitrogen atom.

The Cu(II) ions within the Cu<sub>2</sub>(N<sub>3</sub>)<sub>4</sub> moieties are bridged by the nitrogen atoms (N7 and N7A) of two  $\mu$ -1,1-azido (end-on) ligands. The bridge is slightly asymmetric since the Cu—N7 and Cu—N7A bond distances, 1.99 Å and 2.04 Å respectively, are not quite equal. The bridging azide ligands are nearly linear (178.0 °). The Cu2—N7—Cu2A bridging angle is 103.3 ° and the Cu—Cu distance within the dimeric unit is 3.17 Å. The cyclic Cu<sub>2</sub>(bridging)N<sub>2</sub> units are planar and no folding of the CuN<sub>2</sub> planes about an in-plane axis joining the bridging atoms is observed.

The “legs” of **5** consist of stacks of [Cu(terpy)(N<sub>3</sub>)<sub>2</sub>] monomeric units that extend along the crystallographic *b*-axis. These moieties are not directly connected to each other but coordinated to the Cu<sub>2</sub>(N<sub>3</sub>)<sub>4</sub> dimers. In the [Cu(terpy)(N<sub>3</sub>)<sub>2</sub>] units, the Cu(II) ions adopt a distorted square pyramidal geometry. The rigid nature of the terpy ligand as well as the bridging azide groups causes the deviation from the ideal square pyramidal behavior. The basal plane is defined by three pyridyl nitrogen donors from the terpyridine ligand (N1, N2, and N3) and a nitrogen atom (N4) from a single end-on azide bridge to the rungs. The apical site is occupied by a single end-to-end azide bridge (N15) to the rungs. An axial elongation is observed since the Cu1—N15 bond (2.36 Å) is significantly longer than the basal Cu—N bonds. In the basal plane, the Cu1—N bonds from both the bridging azide ligand and the central pyridyl moiety (1.94 Å) of the terpy are slightly shorter than the bonds to the peripheral pyridyl groups (2.04 Å). The average value of the N(apical)—Cu1—N(basal) angles is 94.4 ° while the *trans*-basal N1—Cu1—

N3 and N2—Cu1—N4 angles are 159.5 ° and 163.2 °, respectively. The Cu(II) ion is displaced 0.13 Å from mean basal plane Cu1—N1—N2—N3—N4 directed toward the apical ligand. Due to the steric influence of nearby azide ions, the pyridyl rings of the terpy ligands are not coplanar, but bowed. Both the single end-on (176.5 °) and single end-to-end (177.1 °) bridging azide ions are slightly bent at the central nitrogen atoms. Furthermore, the terpy ligand is not planar, but slightly bowed. Due to the large distance as well as the steric interference of the terminal azido ligands, no  $\pi$ -stacking interactions between the terpy ligands within the ladders are present.

The Cu(terpy)(N<sub>3</sub>)<sub>2</sub> moieties, the “legs”, are connected to the Cu<sub>2</sub>(N<sub>3</sub>)<sub>4</sub> groups, the “rungs”, by both single end-to-end azido (N13, N14, and N15) and single end-on azido (N4, N5, and N6) bridges. Therefore, **5** can be considered a true coordination polymer ladder because of the strong coordinate covalent bonds between the legs and the rungs as opposed to the a ladder-like structures defined by stacks of weakly interacting oligomers. A single ladder of **5** is shown in Figure 4-6. The single end-on bridge is asymmetric since the Cu1—N4 bond, (1.94 Å), is shorter than the Cu2—N4 bond (2.37 Å). The Cu1—N4—Cu2 bridging angle is 107.1 °. The single end-to-end bridge is asymmetric as well since the Cu1—N15A bond (2.36 Å) is longer than the Cu2B—N13 bond (1.98 Å). The Cu2B—N13—N14 and N14—N15—Cu1 bond angles are 124.2 ° and 114.6 °, respectively. The dihedral angle between the Cu2B—N13—N14—N15 and N15—N14—N15—Cu1 planes is 89.8 °.

The packing diagrams of **5** are shown in Figure 4-7. The ladders pack to form sheets within the crystallographic *ab*-plane. The ladders within a sheet are juxtaposed in registry; adjacent ladders are related by a single translation along the *a*-axis. The sheets

of ladders are layered along the crystallographic *c*-axis. Note that the different orientation of the ladders in adjacent sheets. A ladder in an adjacent sheet is related by both a net glide plane as well as  $\frac{1}{2}$  translation along both the *a*- and *c*-axes. Within the sheets, the terpy ligands between adjacent ladders overlap in an offset parallel fashion with a face-to-face distance of 3.4 Å. This distance is well within the range for significant  $\pi$ -stacking interactions. However, the parallel overlap between the adjacent terpy ligands is hindered due to the steric interference of the terminal azide ligands from the ladder rungs. Weak N—H contacts within and between the sheets of ladders are present. The central nitrogen atoms from the monocoordinate azide ligands that are part of the ladder “rungs” form N—H contacts (2.60 Å) with the hydrogen atoms from the peripheral terpy pyridyl moieties on adjacent ladders within the same sheet. The terminal nitrogen atoms from the double azide bridges that are part of the ladder “rungs” form N—H contacts with the hydrogen atoms from both the central (2.56 Å) and peripheral (2.54 Å) terpy pyridyl moieties on adjacent ladders between the sheets as well.

All Cu—N bond distances and Cu—N—Cu and N—Cu—N bond angles in **5** are comparable to those reported for similar end-on azido bridged Cu(II) complexes.

216,237,247-249,255

#### **Structure of $[\text{Cu}_2(\text{terpy})_2-\mu-(\text{N}_3)_2(\text{N}_3)_2\text{Cu}_3-\mu-(\text{N}_3)_4(\text{N}_3)_2]$**

The structure of **6** consists of neutral, ladder-like stacks of  $[\text{Cu}_5(\text{terpy})_2(\text{N}_3)_{10}]$  pentanuclear units. Each pentamer, one of which is shown in Figure 4-8, possesses  $-1$

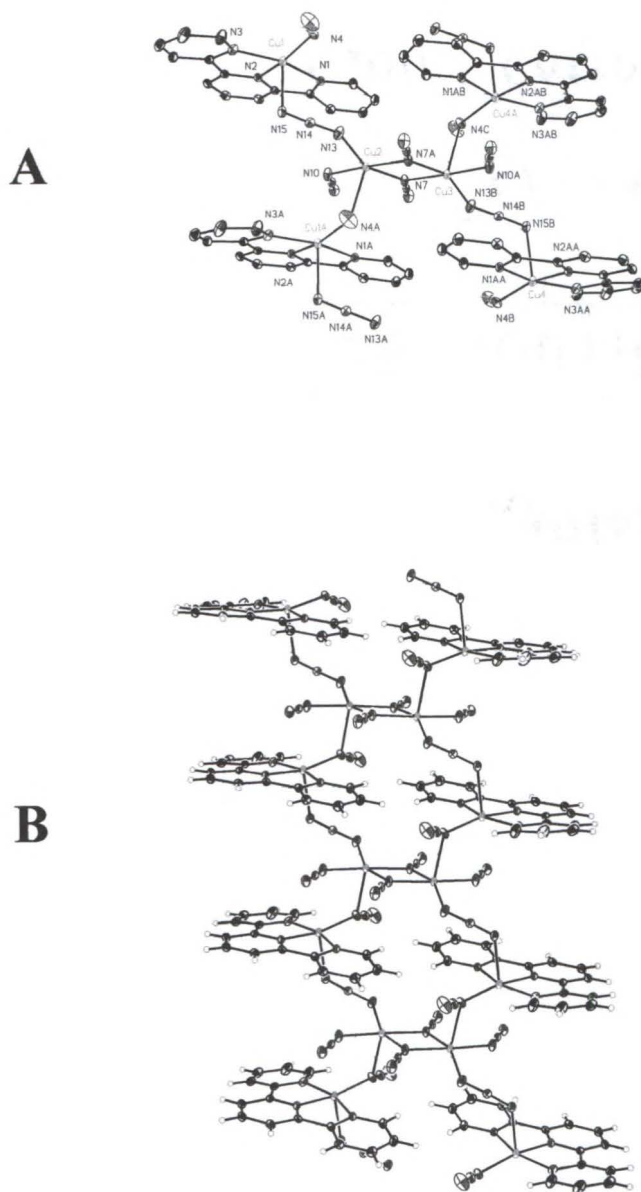


Figure 4-6.  $[\text{Cu}_2(\text{terpy})_2-\mu-(\text{N}_3)_4\text{Cu}_2-\mu-(\text{N}_3)_2(\text{N}_3)_2]$ . A) A fragment of the ladder-like structure. B) A single ladder. All hydrogen atoms have been omitted from A) for clarity. All non-hydrogen atoms are represented by thermal ellipsoids drawn to encompass 30 % of electron density.

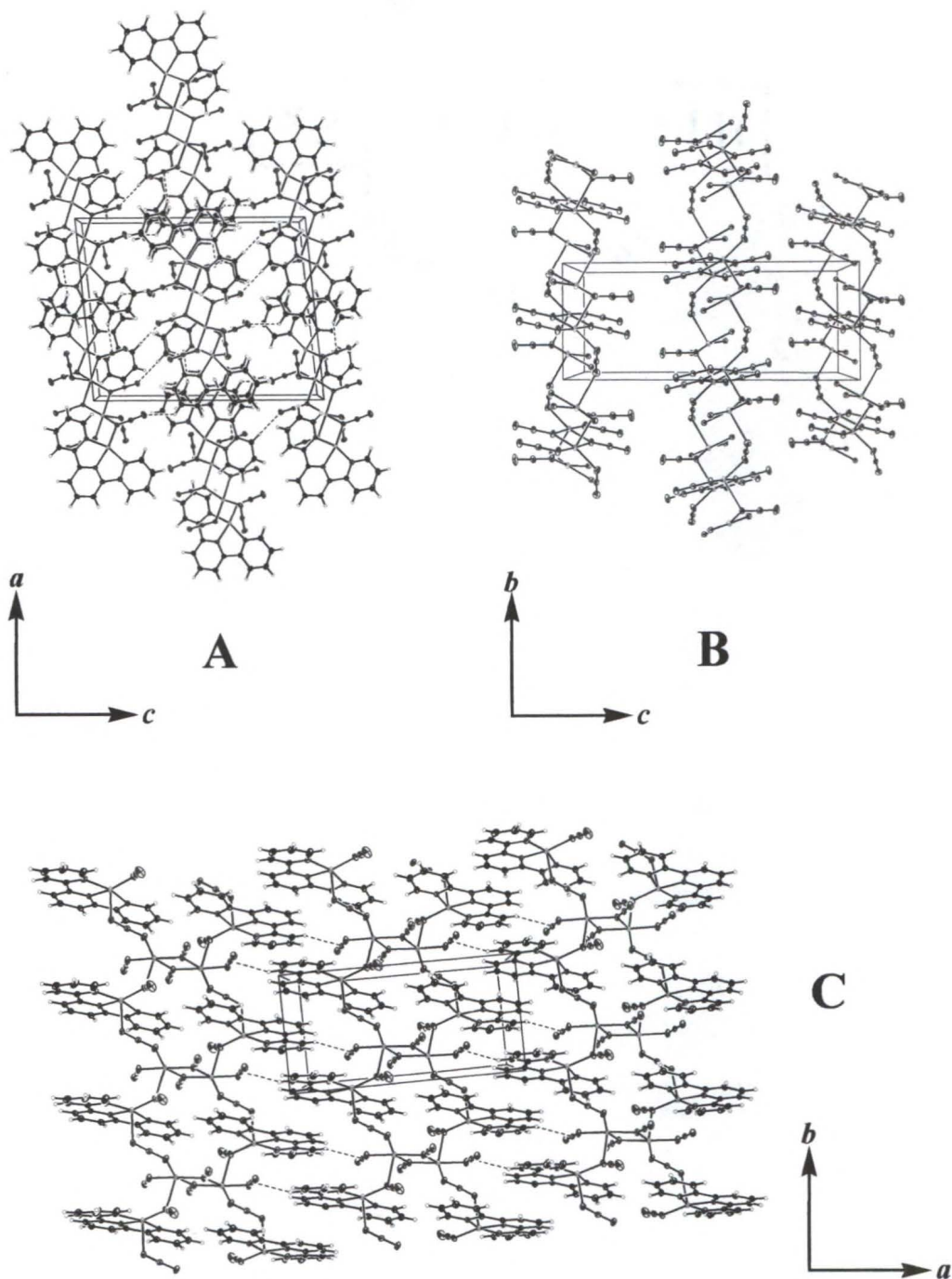


Figure 4-7.  $[\text{Cu}_2(\text{terpy})_2-\mu-(\text{N}_3)_4\text{Cu}_2-\mu-(\text{N}_3)_2(\text{N}_3)_2]$ . A) The structure within the crystallographic  $ac$ -plane. B) The structure within the crystallographic  $bc$ -plane. C) The structure within the crystallographic  $ab$ -plane. For clarity, the terpy ligands have been omitted from B).

crystallographic symmetry. The pentamers are comprised of two terminal  $[\text{Cu}(\text{terpy})(\text{N}_3)_2]$  moieties and a single central  $[\text{Cu}_3(\text{N}_3)_6]$  fragment. In the monomeric  $[\text{Cu}(\text{terpy})(\text{N}_3)_2]$  units, the Cu(II) ions adopt a distorted square pyramidal geometry. The rigid nature of the terpy ligand as well as the bridging azide groups causes the deviation from the ideal square pyramidal behavior. The basal plane is defined by three pyridyl nitrogen donors from the terpyridine ligand (N1, N2, and N3) and a nitrogen atom from a monocoordinate azide ion (N4). The apical site is occupied by a single end-on azide bridging ligand (N7). An axial elongation is observed since the Cu1—N7 bond (2.29 Å) is significantly longer than the basal Cu—N bonds. In the basal plane, the Cu1—N bonds from both the terminal azide ligand and the central pyridyl moiety (1.95 Å) of the terpy are slightly shorter than the bonds to the peripheral pyridyl groups (2.03 Å). The average value of the N(apical)—Cu1—N(basal) angles is 98.0 ° while the *trans*-basal N1—Cu1—N3 and N2—Cu1—N4 angles are 159.7 ° and 150.8 °, respectively. The Cu(II) ion is displaced 0.21 Å from mean basal plane Cu1—N1—N2—N3—N4 directed toward the apical ligand. Due to the steric influence of nearby azide ions, the pyridyl rings of the terpy ligands are not coplanar, but bowed. Both the monocoordinate (174.6 °) and bridging (174.6 °) azide ions are slightly bent at the central nitrogen atoms.

The terminal  $[\text{Cu}(\text{terpy})(\text{N}_3)_2]$  units are connected to the central  $[\text{Cu}_3(\text{N}_3)_6]$  moieties through single end-on azide bridges. The bridge is asymmetric since the Cu1—N7 bond, (2.288 Å), is longer than the Cu2—N7 bond (1.956 Å). The Cu1—N4—Cu2 bridging angle is 117.8 °.

The central  $[\text{Cu}_3(\text{N}_3)_6]$  fragment is itself comprised of two types of metal centers. The two peripheral copper(II) ions (Cu2 and Cu2A) are connected to the central Cu(II)

ions (Cu3) through double end-on azide bridges thus forming two  $\text{Cu}(\mu\text{-N}_3)_2\text{Cu}$  units. The peripheral to central metal (Cu2—Cu3) distance is 3.09 Å while the Cu2—N—Cu3 bridging angle is 101.1°. These bridging azides are nearly linear (179.5°). The  $\text{Cu}(\mu\text{-N}_3)_2\text{Cu}$  units are planar; no folding of the  $\text{CuN}_2$  planes about an in-plane axis joining the two bridging nitrogen atoms (N13 and N16) is observed. The local geometry of the central copper ion is distorted octahedral. The equatorial plane is defined by four nitrogen atoms from the four azide bridges (N13, N16, N13A, and N16A). All equatorial Cu3—N bond distances (1.97 Å to 1.99 Å) are similar. The axial positions are formed by weak Cu3—N contacts (2.65 Å) with the terminal nitrogen atoms of monocoordinate azide ligands from the  $[\text{Cu}(\text{terpy})(\text{N}_3)_2]$  moieties on adjacent pentamers. As a result of Jahn-Teller distortions, the axial Cu3—N bonds are considerably longer than the equatorial bonds. The peripheral copper ions adopt a distorted square pyramidal geometry. The basal plane is defined by two nitrogen atoms from the double end-on azide bridges (N13 and N16) to the central metal center (Cu3), a nitrogen atom (N7) from a single end-on azide bridge to the terminal  $[\text{Cu}(\text{terpy})(\text{N}_3)_2]$  groups, and a nitrogen atom from a monocoordinate azide ligand (N10). The apical site is occupied by the ligated nitrogen atom of the monodentate azide ligand from the  $[\text{Cu}(\text{terpy})(\text{N}_3)_2]$  moiety on an adjacent pentamer. An apical elongation is observed since the weak Cu2—N4 contacts (2.64 Å) are significantly longer than the basal bonds. In the basal plane, the Cu2—N bonds to the double end-on azide bridges are unequal (Cu2—N13 of 2.03 Å and Cu2—N16 of 2.00 Å) but longer than the bonds to the single end-on azide bridge (Cu2—N7 of 1.97 Å) and the monodentate azide ligand Cu—N10 (1.94 Å) bonds. The average values of the N(apical)—Cu—N(basal) angles is 93.4° while the *trans*-basal N10—Cu—N16

and N13—Cu—N7 angles are 167.5 ° and 164.5 °, respectively. The Cu(II) ion is displaced 0.09 Å from mean basal plane Cu2—N7—N10—N13—N16 directed toward the apical ligand. The monocoordinate azide ligand is slightly bent (176.5 °) at the central nitrogen atom.

The pentanuclear units stack atop one another to form ladder-like chains within the [0 -1 0] plane that extend along the crystallographic *a*-axis. A single ladder of **6** is shown in Figure 4-8. Within each ladder, adjacent pentamers are related by a single translation along the *a*-axis and stack in registry along both the *b*- and *c*-axes. The weaker interpentamer bonding consists of double asymmetric end-on and single asymmetric end-to-end azide bridges. The terminal nitrogen atoms from the monocoordinate azide ligands from the [Cu(terpy)(N<sub>3</sub>)<sub>2</sub>] fragments of each pentamer interact with the central Cu3 ions from the [Cu<sub>3</sub>(N<sub>3</sub>)<sub>6</sub>] moieties on adjacent pentamers to form the single end-to-end bridges. The single end-to-end bridge is asymmetric since the Cu1—N4 bond (1.95 Å) is shorter than the Cu3—N6 bond (2.65 Å) on an adjacent pentamer. The Cu3B—N6—N5 and N5—N4—Cu1 bridging angles are 102.4 ° and 131.9 °, respectively, and the dihedral angle between the Cu3B—N6—N5—N4 and N6—N5—N4—Cu1 planes is 111.7 °. The ligated nitrogen atoms from the monodentate azide ligands on both the [Cu(terpy)(N<sub>3</sub>)<sub>2</sub>] and [Cu<sub>3</sub>(N<sub>3</sub>)<sub>6</sub>] fragments interact with the metal centers on adjacent pentamers to form the double end-on azide bridges as well. The double end-on bridge is asymmetric since the Cu1—N4 bond, (1.95 Å), is shorter than the Cu2—N4 bond (2.64 Å) on an adjacent pentamer. The Cu1—N4—Cu2 bridging angle is 102.3 °. The shortest Cu—Cu distance (Cu1—Cu2B) between the pentamers is 3.60 Å. Since the interpentamer bonding is significantly weaker than the intrapentamer

interactions, the molecular structure of **6** is best described as ladder-like stacks of weakly interacting pentamers. Although the terpy's within each ladder stack in an offset parallel fashion,  $\pi$  interactions are negligible due to the large distance ( $\sim 6.5$  Å) and steric interference of bridging azide groups between the organic ligands.

The packing diagrams of **6** are shown in Figure 4-9. The ladders pack to form layered sheets in the solid state. The sheets are contained within the  $[0 -1 1]$  plane. The ladders within a sheet are juxtaposed in registry; adjacent ladders are related by translations along the  $[0 1 -1]$  direction. The sheets, however, do not pack in registry with respect to one another, and adjacent ladders related by single translations along either the crystallographic *b*- or *c*-axes. Weak N—H contacts within and between the sheets of ladders are present. The terminal nitrogen atoms from both the monocoordinate azide ligands from the  $[\text{Cu}(\text{terpy})(\text{N}_3)_2]$  units form twin N—H contacts ( $2.47 - 2.53$  Å) with two hydrogen atoms from two terpy pyridyl moieties on adjacent ladders within the same sheet. The terminal nitrogen atoms of the double azide bridges from the  $[\text{Cu}(\text{terpy})(\text{N}_3)_2]$  units also form twin N—H bonds ( $2.42 - 2.46$  Å) with two hydrogen atoms from two terpy pyridyl moieties on adjacent ladders between the sheets. Due to the lack of any significant parallel face-to-face overlap as well as the steric interference of bridging azide ligands, no  $\pi$ -stacking interactions are observed between the terpy ligands on adjacent ladders within the sheets.

All Cu—N bond distances and Cu—N—Cu and N—Cu—N bond angles in **6** are comparable to those reported for similar end-on azido bridged Cu(II) complexes.

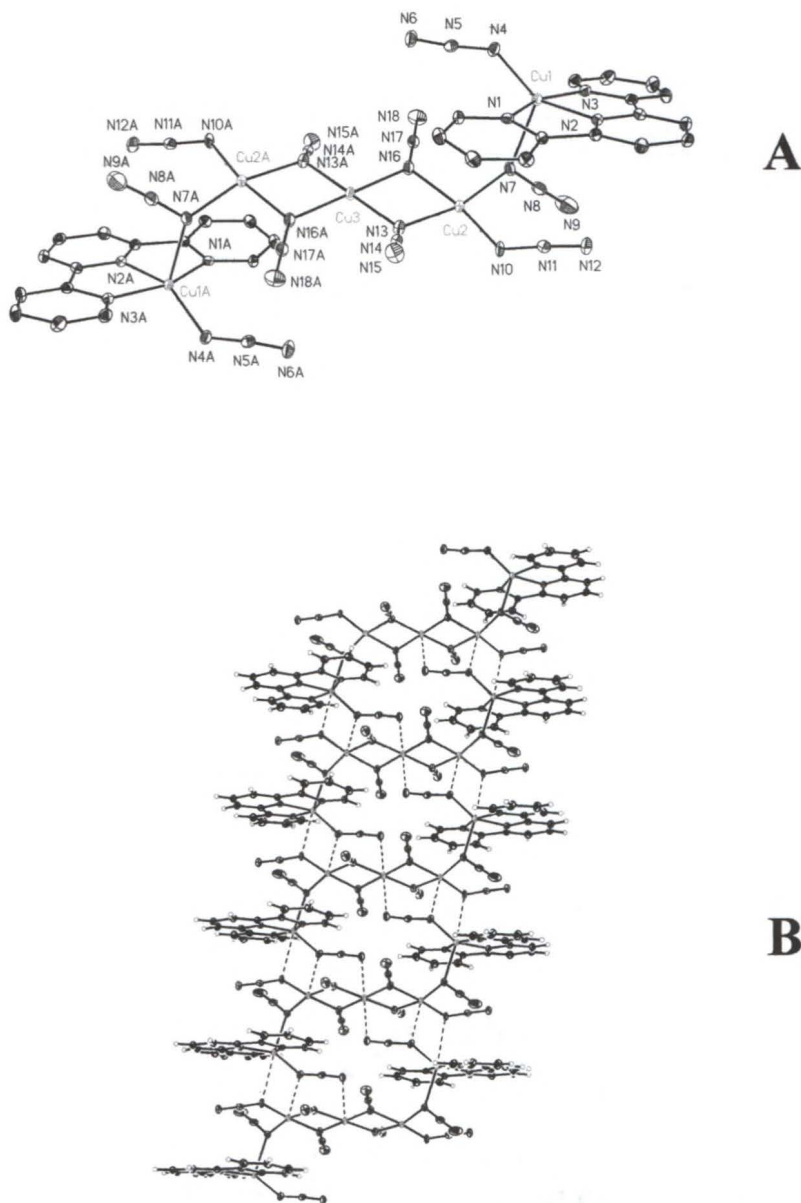


Figure 4-8.  $[\text{Cu}_2(\text{terpy})_2-\mu\text{-(N}_3)_2(\text{N}_3)_2\text{Cu}_3-\mu\text{-(N}_3)_4(\text{N}_3)_2]$ . A) A pentamer. B) A ladder-like stack of pentamers. All hydrogen atoms have been omitted from the A) for clarity. All non-hydrogen atoms are represented by thermal ellipsoids drawn to encompass 30 % of electron density.

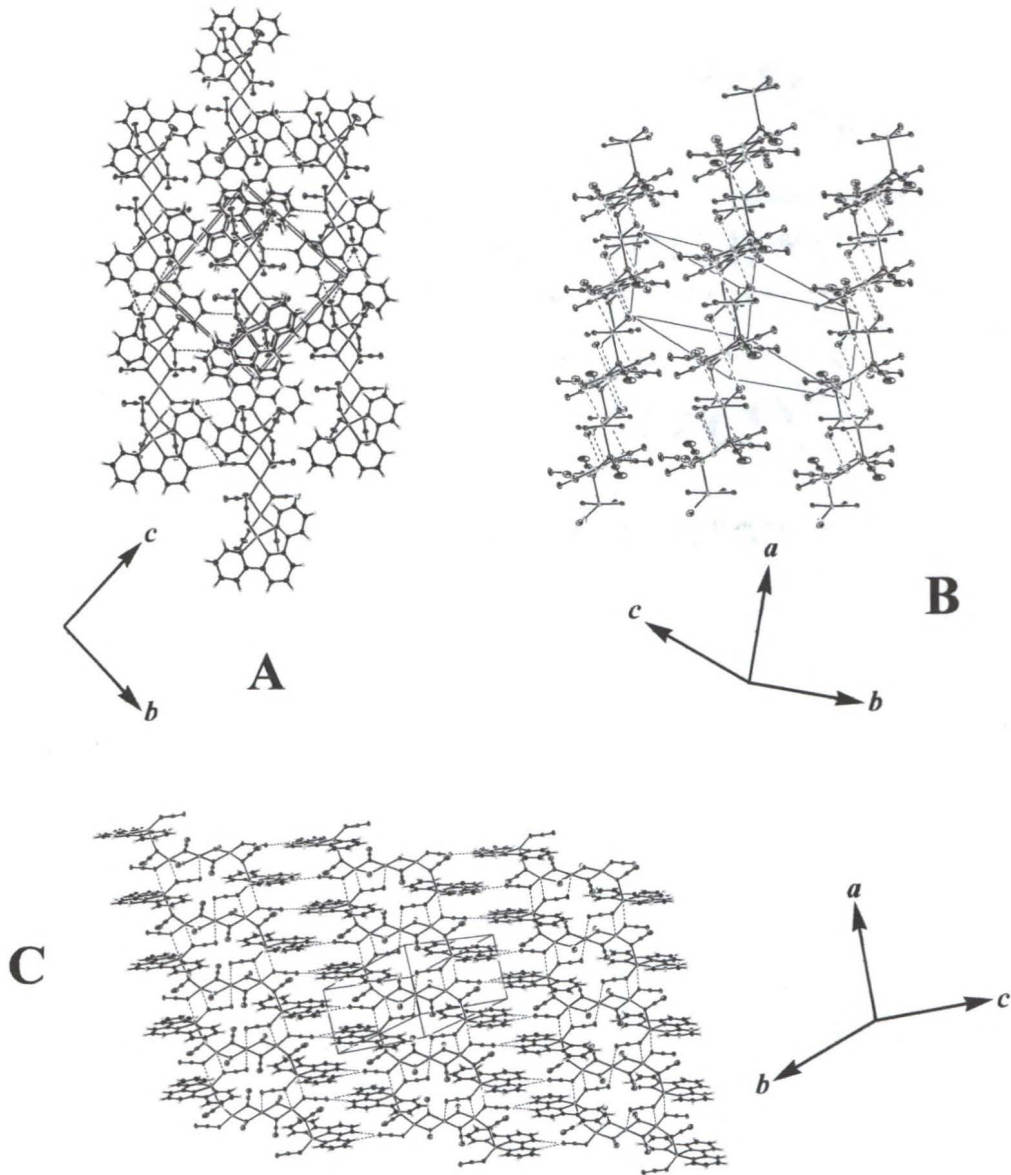


Figure 4-9.  $[\text{Cu}_2(\text{terpy})_2-\mu-(\text{N}_3)_2(\text{N}_3)_2\text{Cu}_3-\mu-(\text{N}_3)_4(\text{N}_3)_2]$ . A) The structure within the crystallographic  $bc$ -plane. B) The structure within the crystallographic  $ab$ -plane. C) The structure along the  $[0\ 1\ -1]$  direction. For clarity, the terpy ligands have been removed from B).

## Electron Paramagnetic Resonance

Selected X-Band EPR spectra of powder samples of **4** over the temperature range 7 K – 300 K are shown in Figure 4-10. The EPR spectrum exhibits a broadened singlet (1441 G peak-to-peak) at room temperature corresponding to an average  $g$ -value of  $g_{\text{avg}} = 2.00$ . The broadened spectra lead to large uncertainty in the measuring the  $g$ -values thus accounting for the rather low calculated value. The normalized, integrated area of each EPR signal was found to increase as the temperature decreases. The spectra do not change significantly upon cooling to 7 K, remaining relatively broad indicating that dipolar effects are important while magnetic exchange interactions are relatively weak. No half-field forbidden transition between  $\Delta M_S = \pm 2$  states were detected over the temperature range further indicating the coupling in **4** are weak.<sup>157</sup>

Selected X-Band EPR spectra of powder samples of **5** over the temperature range 5 K – 300 K are shown in Figure 4-10. Sample **5** exhibits a broad (832 G peak-to-peak) and symmetric X-band EPR signal at room temperature. A weak signal at  $B = 1500$  G, possibly the half-field signal in the  $g = 4$  region corresponding to “forbidden” transitions within the  $\Delta M_S = \pm 2$  states, indicates low-dimensional magnetic exchange interactions between the Cu(II) ions. As the temperature is decreased, the signal in the  $g = 2$  region narrows and the  $g = 4$  peak disappears. This progressive narrowing of the EPR spectra indicates the presence of relatively strong magnetic exchange interactions present within **5**. However, below 50 K, the signal in the  $g = 2$  region evolves into a weak axial spectrum with  $g_{\parallel} = 2.07$  and  $g_{\perp} = 2.23$ . This effect appears to be intrinsic to the sample; the presence of a small quantity of uncoupled, paramagnetic impurity within **5** would not account for the abrupt change in the spectra. The narrowing is likely a thermal effect due

to the onset of strong exchange interactions or a decrease in the relaxation time of the unpaired spins. The  $g$ -values are consistent with the distorted square pyramidal geometry and indicate a basically  $d_x^2-y^2$  ground state for the Cu(II) ions.<sup>157</sup>

Selected X-Band EPR spectra of powder samples of **6** over the temperature range 5 K – 300 K are shown in Figure 4-10. Sample **6** exhibits a broad (832 G peak-to-peak) EPR signal in the  $g_{\text{avg}} = 2.14$  region at room temperature. A weak signal at  $B = 1500$  G may be the half-field signal in the  $g = 4$  region corresponding to “forbidden” transitions within the  $\Delta M_S = \pm 2$  states but disappears at lower temperatures. The integrated area of the peaks increases as the temperature is lowered and a slight, but apparent, narrowing is observed, however, the spectrum does not vary significantly upon cooling indicating the presence of relatively weak magnetic exchange interactions.<sup>157</sup>

### **Magnetic Properties of [Cu<sub>2</sub>(PhPrPy)<sub>2</sub>- $\mu$ -(1,1-N<sub>3</sub>)<sub>2</sub>(N<sub>3</sub>)<sub>2</sub>]**

#### **Magnetic Data**

A plot of the zero-field cooled magnetization (open boxes) and the field-cooled magnetization (open circles) for **4** is shown in Figure 4-11. The two sets of data superimpose one another indicating that **4** does not experience any long-range magnetic order down to 2 K. Plots of both the magnetic susceptibility ( $\chi_M$ ) vs. temperature and the inverse susceptibility vs. temperature per mole of dimer for **4** are shown in Figures 4-11 and 4-12, respectively, as open squares. For **4**, the susceptibility increases steadily as the temperature is lowered and no maximum is observed. The high temperature inverse susceptibility data (from 250 K to 300 K) were fit to a straight line and extrapolated to the  $x$ -axis giving  $T = 17.3$  K suggesting that the dominant magnetic exchange in **4** is ferromagnetic. A plot of the temperature dependence of the product of the susceptibility

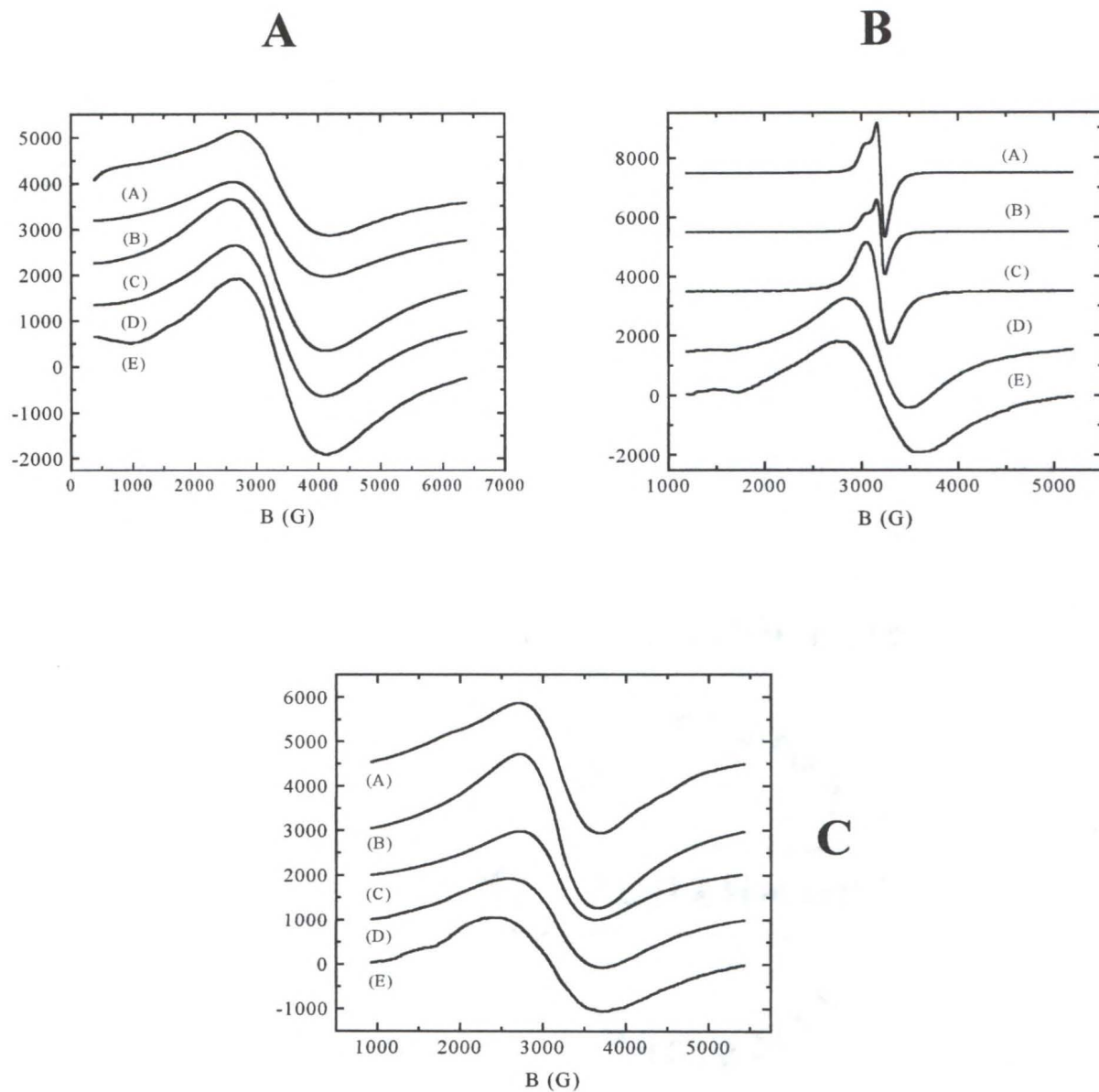


Figure 4-10. X-Band, Variable Temperature ESR Spectra. A) Compound **4** at (A) 7 K, (B) 10 K, (C) 50 K, (D) 150 K, and (E) 298 K. B) Compound **5** at (A) 5 K, (B) 10 K, (C) 50 K, (D) 150 K, and (E) 298 K. C) Compound **6** at (A) 5 K, (B) 10 K, (C) 50 K, (D) 150 K, and (E) 298 K.

and temperature ( $\chi_M T$ ) per mole of dimer is shown in Figure 4-12 as open squares. The  $\chi_M T$  value at room temperature (0.423 emu K mol<sup>-1</sup> of Cu(II) ions) is very close to the expected spin-only value for a collection of non-interacting  $S = \frac{1}{2}$  paramagnetic centers ( $\chi_M T = 0.413$  emu K mol<sup>-1</sup>). As the temperature is lowered, the  $\chi_M T$  value increases until reaching a maximum value of 1.00 emu K mol<sup>-1</sup> at 10 K. The increasing  $\chi_M T$  value with decreasing temperature indicates the presence of a ferromagnetic coupling. Below 10 K however, the  $\chi_M T$  value decreases, quickly approaching zero indicating that an additional weak, antiferromagnetic exchange interaction is also present. The field dependence of the magnetization ( $M_M$ ) per mole of dimer for **4** is shown in Figure 4-13 as open squares. The magnetization initially increases with increasing field, but begins to level out at 20 kG asymptotically approaching a constant value of approximately 11 000 emu G mol<sup>-1</sup>. Below 10 kG, the magnetization varies linearly with the applied field with no apparent change in slope observed.

### Magnetic Model and Fits

Recall the structure of **4** consists of ladder-like chains of azido-bridged Cu(II) dimers. The various types of superexchange pathways between the Cu(II) ions in **4** are schematically depicted in Figure 4-13. The intradimer coupling ( $J$ ) is expected to be the dominant magnetic exchange interaction since the double end-on azide ligands bridge the square pyramidal copper ions through the equatorial coordination sites. The interdimer exchange is expected to be weak due to the long Cu—N contacts associated with the asymmetric azide bridges as well as the end-on and end-to-end azide ligands bridging the axial-equatorial coordination sites of the metal centers. Note that there are two possible interdimer superexchange pathways, through the asymmetric end-to-end bridges ( $J'$ ) and

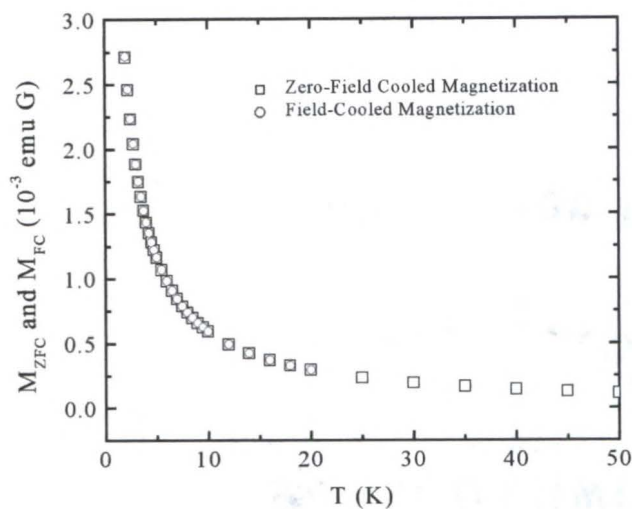
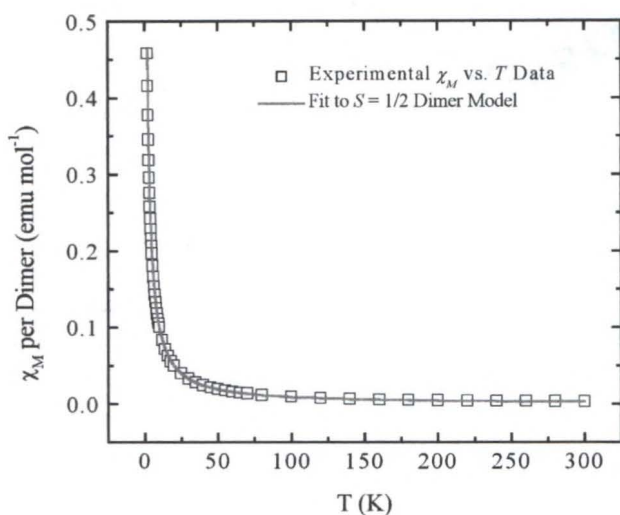
**A****B**

Figure 4-11. Magnetic data for compound **4** at 100 G from 2 K to 300 K. A) Field-cooled ( $M_{FC}$ ) and zero-field cooled ( $M_{ZFC}$ ) magnetization vs. temperature. B) Molar susceptibility,  $\chi_M$ , per dimer. The data have been corrected for background signals arising from the sample container and diamagnetic contributions. The fit of  $\chi$  to the  $S = 1/2$  dimer model from Equations 4-3 to 4-5 is shown by the solid line in B).

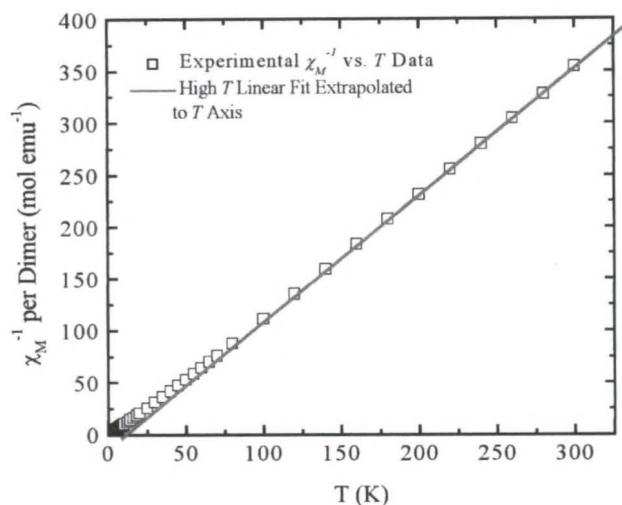
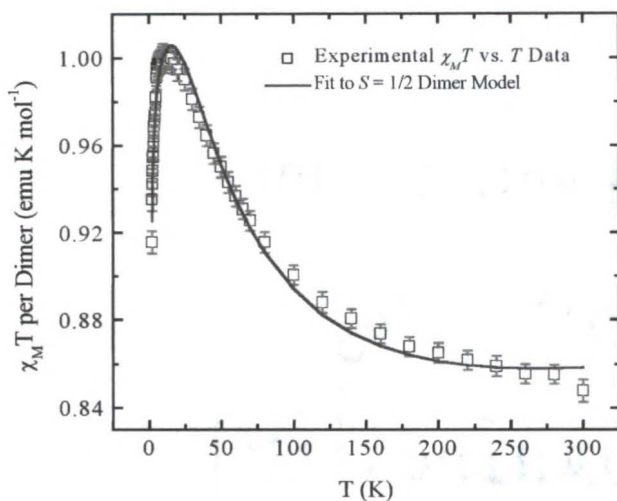
**A****B**

Figure 4-12. Magnetic data for compound **4** at 100 G from 2 K to 300 K. A) Inverse molar susceptibility,  $\chi^{-1}$ , per dimer versus temperature. B) The product of the molar susceptibility and temperature,  $\chi T$ , per dimer at versus temperature. The data have been corrected for background signals arising from the sample container and diamagnetic contributions. A linear fit to the high temperature data in A) is shown by the solid line. The fit of  $\chi T$  to the  $S = 1/2$  dimer model from Equations 4-3 to 4-5 is show by the solid line in B).

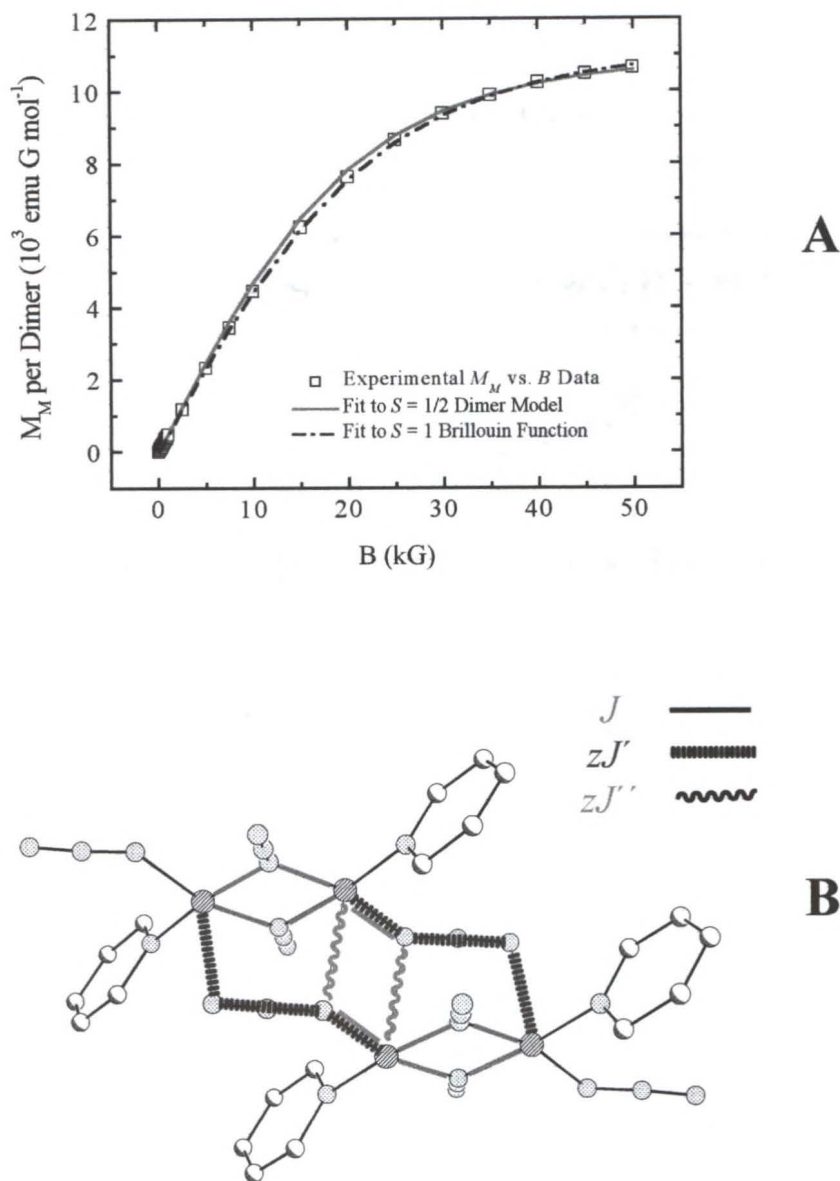


Figure 4-13. A) The molar magnetization ( $M$ ) per dimer at 2 K from 0 to 50 kG for compound 4. The data have been corrected for background signals arising from the sample container. The fit of  $M$  to the  $S = 1/2$  dimer model from Equation 4-2 is shown as the solid line and the fit to the  $S = 1$  Brillouin function is shown as the dotted line. B) A fragment consisting of two dinuclear units of compound 4 depicting the possible superexchange pathways. The copper(II) ions are represented by the shaded circles.

the asymmetric end-on bridges ( $J'$ ). Since the Cu—N contacts associated with the asymmetric end-on bridges (3.14 Å) are significantly longer than the corresponding Cu—N contacts with the asymmetric end-to-end bridges (2.62 Å), only the weak exchange through the latter pathway is considered significant. Any magnetic interactions between the ladder-like chains are assumed to be negligible since only weak N—H(aromatic) contacts and hydrophobic interactions between the organic ligands are observed. Therefore, the magnetic data were analyzed by assuming that **4** consists of isolated chains comprised weakly interacting  $S = \frac{1}{2}$  dimers.

The exchange interactions of a Cu(II) dimer can be described by the spin-Hamiltonian with the corresponding the Zeeman term

$$\hat{H} = -2J(\hat{\mathbf{S}}_1 \cdot \hat{\mathbf{S}}_2) + \mu_B B \cdot (\bar{g}_1 \cdot \hat{\mathbf{S}}_1 + \bar{g}_2 \cdot \hat{\mathbf{S}}_2) \quad (4-1)$$

which assumes isotropic exchange interactions,  $J$ . For simplicity,  $g$ -values are assumed to be isotropic. The weak, interdimer exchange is approximated by a molecular field term ( $\theta$ ) applied to the Hamiltonian. The zero field energy levels of the spin-Hamiltonian are  $E_1 = 0$  ( $S = 0$ ) and  $E_2 = J$  ( $S = 1$ ).<sup>6</sup> The magnetization vs. field is

$$M_M = N_R N_A \mu_B g \frac{\exp \frac{J+2\mu_B g B}{k_B T} - \exp \frac{J}{k_B T}}{\exp \frac{J}{k_B T} + \exp \frac{\mu_B g B}{k_B T} + \exp \frac{J+\mu_B g B}{k_B T} + \exp \frac{J+2\mu_B g B}{k_B T}} + M_0 \quad (4-2)$$

where the parameter  $N_R$  normalizes the number of moles of sample between 0 and 1 and  $M_0$  corrects the zero-field magnetization to 0. The Van Vleck magnetic susceptibility vs. temperature,  $\chi_{\text{Dimer}}$ , is

$$\chi_{\text{Dimer}} = \frac{2N_R N_A \mu_B^2 g^2}{k_B T} \frac{\exp \frac{2J}{k_B T}}{1 + 3 \exp \frac{2J}{k_B T}} + N\alpha \quad (4-3)$$

where  $N\alpha$  is the temperature independent paramagnetism. The mean field corrected susceptibility,  $\chi'$ , is

$$\chi' = \chi_{Dimer} \left( \frac{T}{T - \theta} \right) \quad (4-4)$$

and the total susceptibility,  $\chi$ , corrected for a fraction of uncoupled, monomeric impurity,  $\rho$ , is

$$\chi = \chi'(1 - \rho) + \frac{N_A g^2 \mu_B^2}{2k_B T} \rho + \chi_0 \quad (4-5)$$

The best fit for both the  $\chi$  and  $\chi T$  data of **4** to Equations 4-3 to 4-5 was obtained using non-linear regression analysis with  $N_R$ ,  $g$ ,  $J$ ,  $\rho$ ,  $\theta$ , and  $\chi T_0$  as parameters. The results are shown as the solid lines in Figures 4-11 and 4-12 with  $N_R = 0.943$ ,  $g = 2.09$ ,  $2J = 73.255 \text{ K} \pm 1.921 \text{ K}$ ,  $\theta = -0.206 \text{ K} \pm 0.010 \text{ K}$ ,  $\rho = 0.01$ , and  $\chi T_0 = 1.6 \times 10^{-4} \text{ emu K mol}^{-1}$  and  $\chi_0 = 1.7 \times 10^{-4} \text{ emu mol}^{-1}$ . The impurity fraction was fixed since the fitting procedure consistently produced large, negative values when  $\rho$  was allowed to vary. The fitting ultimately therefore converged giving  $N_R$  and  $\rho$  values that do not correlate. The agreement factor  $R = 3 \times 10^{-5}$  is very small indicating the model fits the data well, where  $R$  is defined as

$$R = \frac{\sum [(\chi_M T)^{obsd} - (\chi_M T)^{calcd}]^2}{\sum [(\chi_M T)^{obsd}]^2} \quad (4-6)$$

The best fit for the magnetization data of **4** to Equation 4-2 was obtained with  $N_R$ ,  $g$ ,  $J$ , and  $M_0$  as parameters. The results are shown as the solid line in Figure 4-13 with  $N_R = 0.94$ ,  $g = 2.09$ ,  $2J = 71.066 \text{ K}$  and  $M_0 = -1.107 \text{ emu G mol}^{-1}$ . Although the agreement factor is large, expected for fits to  $M$  vs.  $B$  data, the  $N_R$ ,  $g$ , and  $J$  values are consistent

with those obtained from the  $\chi T$  data and the fit to the data is relatively good. An additional simulation of the  $S = 1$  Brillouin function, given as

$$M_M = N_R N_A \mu_B g \frac{\exp\left(\frac{2\mu_B g B}{k_B T}\right) - 1}{\exp\left(\frac{2\mu_B g B}{k_B T}\right) + \exp\left(\frac{\mu_B g B}{k_B T}\right) + 1} + M_0 \quad (4-7)$$

is shown in Figure 4-13 as the dashed line, with  $N_R$ ,  $g$ , and  $M_0$ , obtained from the fits to the magnetization data, as fixed parameters.

The average, isotropic  $g$ -value obtained from the bulk magnetic data is consistent with square pyramidal Cu(II) ions. The magnetic data and corresponding fits indicate that the dominant intradimer exchange interaction is ferromagnetic while the interdimer exchange is weak and antiferromagnetic.

### Interpretation of the Magnetic Data

The  $\chi T$  plot in Figure 4-12 depicts the thermal population of the triplet ( $S = 1$ ) ground state at low ( $T = 10$  K) temperature. At high temperature, **4** behaves paramagnetically, *i.e.*, the unpaired spins within each dimer along the ladder-like chains are uncoupled and essentially randomized resulting in a small net magnetic moment. As  $T$  is lowered, the intradimer coupling takes effect, as insufficient thermal energy is now present to populate excited states. An increase in the net magnetic moment is observed due to the onset of the ferromagnetic interactions. At  $T = 10$  K, the triplet ground state is fully populated and **4** now consists of stacks of  $S = 1$  dimers. At even lower temperatures, the weak interdimer coupling takes effect and a sudden drop in the net magnetic moment is observed due to antiferromagnetic coupling of the dimers. The magnetization plot in Figure 4-13 depicts the population of the  $S = 1$  triplet state at high

field. At 2 K, due to the strong ferromagnetic intradimer coupling, **4** consists of  $S = 1$  dimers and thus the magnetization closely follows the  $S = 1$  Brillouin function. In contrast, if the coupling was weak, **4** would be comprised of weakly coupled  $S = \frac{1}{2}$  dimers and the magnetization would be expected to follow the product of two  $S = \frac{1}{2}$  Brillouin functions (not shown in the plot).

### **Rationalizing the Sign and Magnitude of the Coupling Constants**

Recall that the intradimer exchange interactions are mediated by end-on azide ligands bridging the two Cu(II) ions. Both the magnetic data and corresponding fits indicate that the intradimer coupling,  $J$ , is strongly ferromagnetic. The calculated coupling constant is consistent with other similar  $\mu$ -diazido bridged copper(II) complexes.<sup>6,17,237,246-249</sup> The positive sign of the coupling constant is also consistent with the small Cu—N—Cu bridging angle of  $101.9^\circ$ . The large magnitude of the coupling constant is reasonable for the small bridging angle, the short Cu—(bridging)N bonds, the planar Cu—(N)<sub>2</sub>—Cu moiety, and the double end-on azido ligands that bridge equatorial-equatorial coordination sites (both associated with the  $d_x^2-y^2$  orbitals with significant unpaired spin density) on both Cu(II) ions (Figure 4-14).<sup>255</sup>

The interdimer superexchange pathway consists of asymmetric, double end-on and single end-to-end bridging azide ligands. Both the magnetic data and corresponding fits indicate that the interdimer coupling is weakly antiferromagnetic. The small, antiferromagnetic coupling is consistent with asymmetric end-on and end-to-end azide ligands bridging square pyramidal Cu(II) ions in other similar complexes as well.<sup>205,255</sup> The long, weak Cu—N bonds between the dimers are associated with poor orbital overlap between the two exchanging metal centers thus reducing the magnitude of the

exchange interaction. The azide ligands bridging the apical-basal coordination sites of the square pyramidal Cu(II) ions between the dimers also accounts for the small interdimer coupling as well (Figure 4-14). The interdimer exchange is between the axial-equatorial coordination sites of the metal centers between the dimers, in which case the unpaired spins from the metal centers reside in  $d_z^2$  and  $d_x^2-y^2$  atomic orbitals, respectively.<sup>255</sup> Low unpaired electron density is associated with the  $d_z^2$  orbital in octahedral and square pyramidal coordinated Cu(II) ions. There is a good delocalization of the electron density to the bridging azide ligand coordinated to the equatorial Cu(II) ions since the unpaired spin is primarily located in a  $d_x^2-y^2$  orbital but the delocalization to the azide bridge coordinated to the axial Cu(II) ions is poor since the  $d_z^2$  orbital is occupied by paired spins.<sup>6,205,255</sup> As a result, the superexchange pathway via azide ligands bridging axial and equatorial sites between Cu(II) ions is inefficient. Therefore, **4** consists of antiferromagnetic chains of ferromagnetically coupled  $S = \frac{1}{2}$  dimers.

### **Magnetic Properties of $[\text{Cu}_2(\text{terpy})_2-\mu-(\text{N}_3)_4\text{Cu}_2-\mu-(\text{N}_3)_2(\text{N}_3)_2]$**

#### **Magnetic Data**

A plot of the zero-field cooled magnetization (open boxes) and the field-cooled magnetization (open circles) is shown in Figure 4-15. The two sets of data superimpose one another indicating that **5** does not experience any long-range magnetic order down to 2 K. Plots of both the magnetic susceptibility ( $\chi_M$ ) vs. temperature and the inverse susceptibility vs. temperature per mole of tetramer for **5** are shown in Figures 4-15 and 4-16, respectively, as open squares. For **5**, the susceptibility increases steadily as the temperature is lowered and no maximum is observed. The high temperature inverse susceptibility data (from 140 K to 300 K) were fit to a straight line and extrapolated to

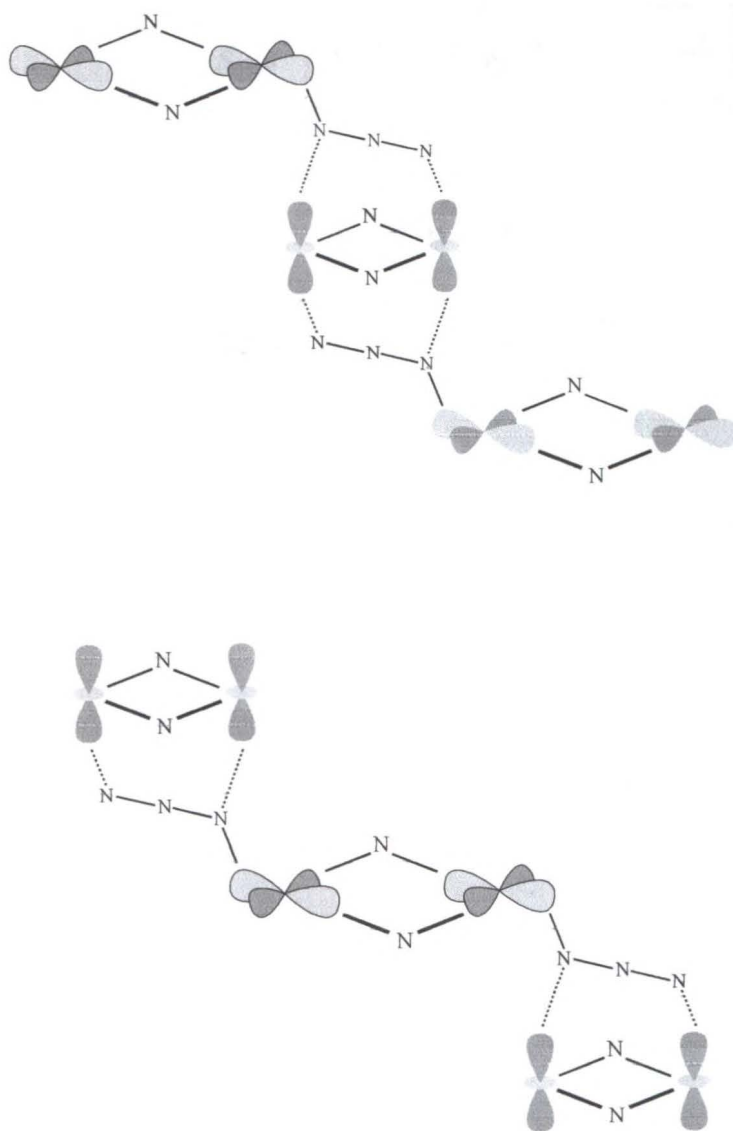


Figure 4-14. The metal  $d$ -orbitals involved in the superexchange interactions present in compound **4**. Within the dimer, the end-on azide ions bridge both equatorial sites of the metal centers and thus a strong intradimer coupling is expected. The long Cu—N contacts between the dimers as well as the axial-equatorial coordination by the azide ligands results in a weak interdimer coupling.

the  $x$ -axis giving  $T = -46.32$  K suggesting that the dominant magnetic exchange in **5** is antiferromagnetic in nature. A plot of the temperature dependence of the product of the susceptibility and temperature ( $\chi_M T$ ) is shown in Figure 4-16 as open squares. The  $\chi_M T$  value at room temperature ( $0.393 \text{ emu K mol}^{-1}$  Cu(II) ions) is very close to the expected spin-only value for a collection of non-interacting  $S = \frac{1}{2}$  paramagnetic centers ( $\chi_M T = 0.413 \text{ emu K mol}^{-1}$ ). As the temperature is lowered to 50 K, the  $\chi_M T$  value decreases until reaching a plateau where the  $\chi_M T$  value ( $0.380 \text{ emu K mol}^{-1}$  Cu(II) ions) remains relatively constant. The decreasing  $\chi_M T$  value with decreasing temperature indicates the presence of an antiferromagnetic coupling. Below 5 K, the  $\chi_M T$  value decreases again approaching zero suggesting that an additional, weak antiferromagnetic exchange is present. The field dependence of the molar magnetization ( $M_M$ ) of **5** is shown in Figure 4-17 as open squares. The magnetization increases with increasing field but begins to level out at 40 kG asymptotically approaching a constant value of approximately  $11\,000 \text{ emu G mol}^{-1}$ . Below 10 kG, the magnetization varies linearly with the applied field with no apparent change in slope observed.

### Magnetic Model and Fits

Recall the structure of **5** consists of ladder-like coordination polymers of azido-bridged Cu(II) ions. The various types of superexchange pathways between the Cu(II) ions in **5** are schematically depicted in Figure 4-18. The rung or intradimer coupling ( $J_{\perp}$ ) within the  $\text{Cu}_2(\text{N}_3)_4$  units is expected to be the dominant magnetic exchange interaction since the double end-on azide ligands bridge the square pyramidal copper ions through the equatorial coordination sites. Two exchange pathways are possible through the legs: the single end-to-end ( $J_{\parallel}^{(1)}$ ) and single end-on ( $J_{\parallel}^{(2)}$ ) bridges between the rungs and the

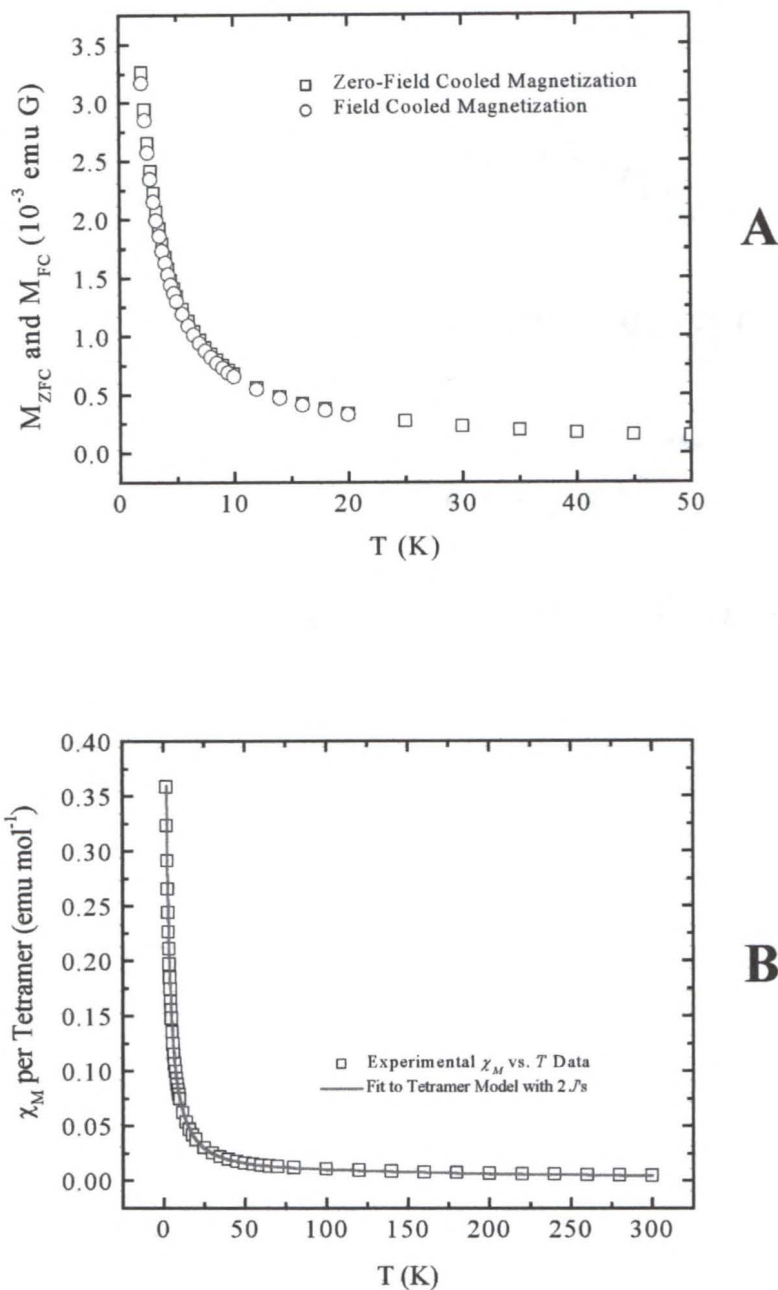


Figure 4-15. Magnetic data for compound **5** at 100 G from 2 K to 300 K. A) Field-cooled ( $M_{FC}$ ) and zero-field cooled ( $M_{ZFC}$ ) magnetization versus temperature. B) Molar susceptibility,  $\chi_M$ , per tetramer. The data have been corrected for background signals arising from the sample container and diamagnetic contributions. The fit of  $\chi$  to the tetramer model with two coupling constants from Equations 4-11 to 4-15 is shown by the solid line in B).

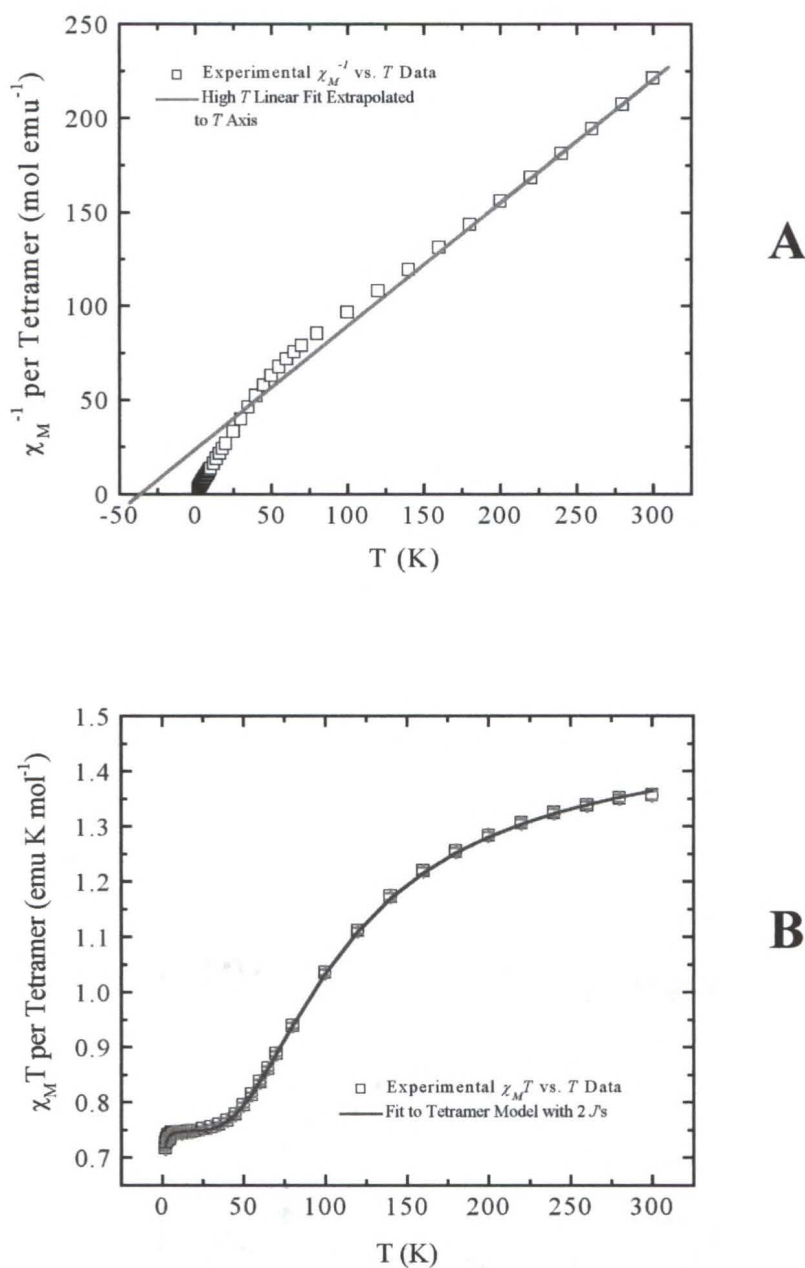


Figure 4-16. Magnetic data for compound **5** at 100 G from 2 K to 300 K. A) Inverse molar susceptibility,  $\chi^{-1}$ , per tetramer versus temperature. B) The product of the molar susceptibility and temperature,  $\chi T$ , per tetramer at versus temperature. The data have been corrected for background signals arising from the sample container and diamagnetic contributions. A linear fit to the high temperature data in A) is shown by the solid line. The fit of  $\chi T$  to the tetramer model with two coupling constants from Equations 4-11 to 4-15 is show by the solid line in B).

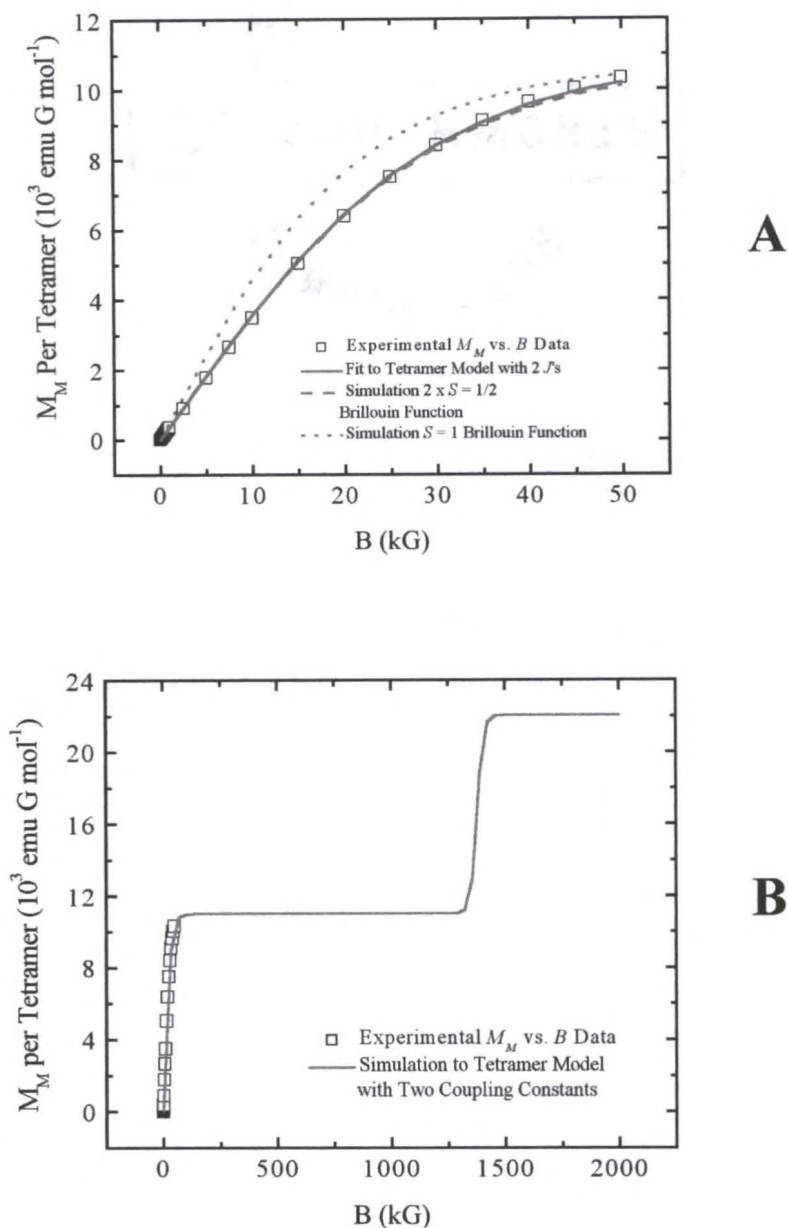


Figure 4-17. Magnetic data for compound **5**. A) The molar magnetization ( $M$ ) per tetramer at 2 K from 0 to 50 kG. The data have been corrected for background signals arising from the sample container. The fit of  $M$  to the tetramer model with two coupling constants is shown as the solid line and the fit to the  $S = 1$  Brillouin function is shown as the dotted line. B) A simulation of the  $M$  data to 2000 kG by the tetramer model. In the simulation, the upper critical field for the first plateau is 68 kG. The critical fields for the second plateau are  $H_{C1} = 1300$  kG and  $H_{C2} = 1460$  kG.

Cu(terpy)(N<sub>3</sub>)<sub>2</sub> units. Due to the long Cu—N contacts associated with the single azide bridges as well as the end-on and end-to-end azide ligands bridging the axial-equatorial coordination sites of the metal centers between the legs and rungs, the exchange is expected to be weak.

A ladder model would best reproduce the magnetic behavior of **5**. Assuming pairwise coupling of the unpaired electrons, the appropriate spin Hamiltonian ladder model, based on the structure from Figure 4-18, for describing the magnetic data is given by:

$$\hat{H} = J_{\perp} \sum_{i=1}^{N/4} \hat{S}_{4i-2} \cdot \hat{S}_{4i-1} + 2\{J_{\parallel}^{(1)} \sum_{i=1}^{N/4} \hat{S}_{4i-2} \cdot \hat{S}_{4i-3}\} + 2\{J_{\parallel}^{(2)} \sum_{i=1}^{N/4} \hat{S}_{4i-2} \cdot \hat{S}_{4i+1}\} + \mu_B \left\{ \sum_{i=1}^{N/4} \hat{S}_{4i-3} \cdot \vec{g}_1 \cdot \vec{B} + \sum_{i=1}^{N/4} \hat{S}_{4i-2} \cdot \vec{g}_2 \cdot \vec{B} \right\} \quad (4-8)$$

which assumes isotropic exchange interactions.<sup>271</sup> The first term in the spin-Hamiltonian represents the nearest neighbor exchange within and between the rungs and the second term is the Zeeman perturbation. The coordination environment of the copper ions within the rungs is distinct from that in the legs so two different *g*-values are needed to account for this difference. However, no attempt to fit the experimental magnetic data based on this Hamiltonian was made due to the complexity of such processes. Furthermore, no explicit expressions for the thermal and field dependence of magnetization and susceptibility for such a Hamiltonian, to our knowledge, exist in the literature. Therefore, modeling the magnetic data according to this Hamiltonian was abandoned.

By making certain assumptions regarding the relative magnitudes of the exchange interactions mediated by the various azide bridges, a linear tetramer model with two

coupling constants was employed to model the magnetic data.<sup>259</sup> The tetramer consists of the central  $\text{Cu}_2(\text{N}_3)_4$  moiety bridged to the two terminal  $\text{Cu}(\text{terpy})(\text{N}_3)_4$  groups via the

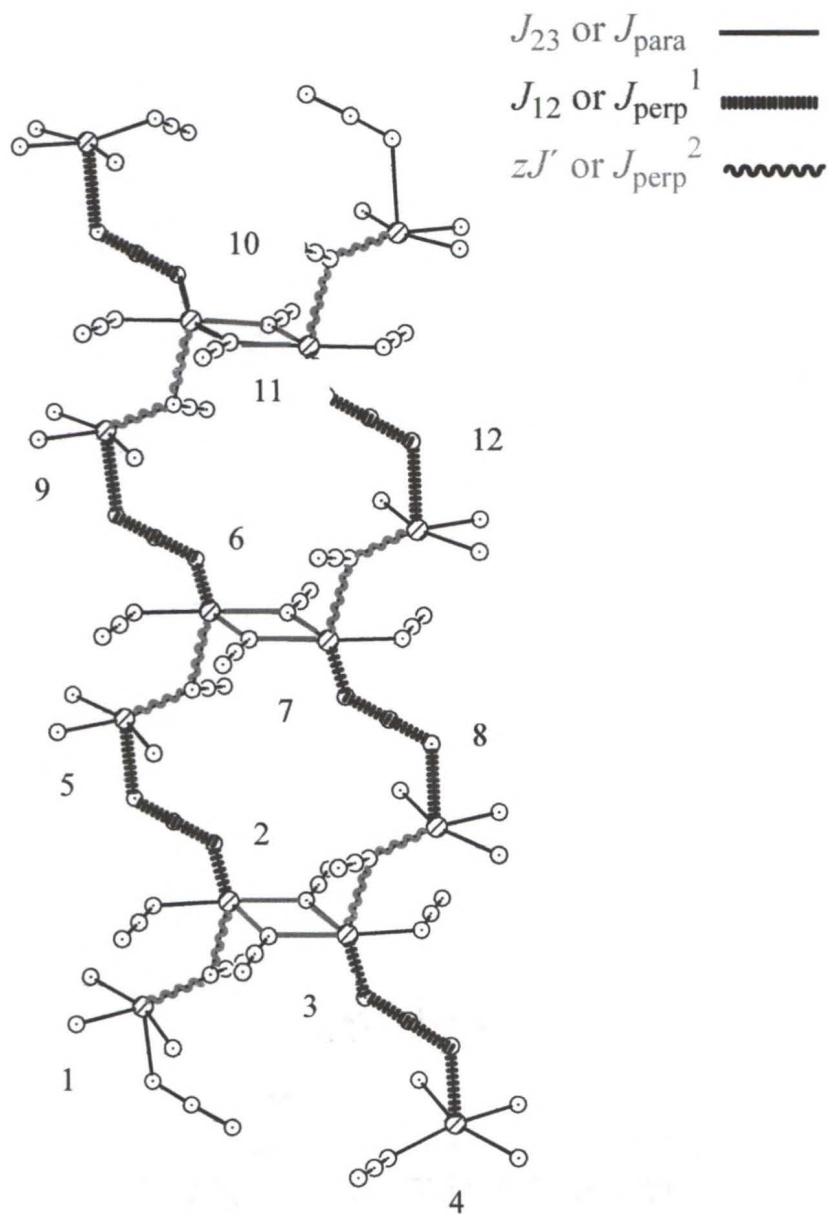


Figure 4-18. A fragment of the ladder-like structure of compound 5 depicting the possible superexchange pathways. The copper(II) ions, shown in the circles enclosed by the vertical lines, are numbered to correspond to Equation 4-8.

single end-to-end azide ligands. Again, the exchange mediated by the single end-to-end azide bridges ( $J_{12}$ ) is expected to be smaller, but not negligible, compared to the exchange mediated by the double end-on bridges ( $J_{23}$ ). However, the intertetramer exchange mediated by the single end-on azide ligands is assumed to be very small, if not negligible in comparison. Despite the short Cu—N bonds, the Cu—N—Cu bridging angle (107.1 °) is very close to the angle of accidental orthogonality (108.5 °), where the ferro- and antiferromagnetic contributions to the total exchange nullify each other. The single end-on azide bridge is the magnetic “weak” link in the ladder. The magnetic data is therefore analyzed assuming **5** consists of weakly interacting tetramers. Interactions between the ladders, such as exchange mediated by the overlapping terpy ligands, have been neglected.

The exchange interactions of a linear, tetranuclear Cu(II) oligomers with two coupling constants can be described by the spin-Hamiltonian

$$\hat{H} = -2J_{12}(\hat{\mathbf{S}}_1 \cdot \hat{\mathbf{S}}_2 + \hat{\mathbf{S}}_3 \cdot \hat{\mathbf{S}}_4) - 2J_{23}(\hat{\mathbf{S}}_2 \cdot \hat{\mathbf{S}}_3) + \mu_B B \cdot (\bar{g}_1 \cdot \hat{\mathbf{S}}_1 + \bar{g}_2 \cdot \hat{\mathbf{S}}_2 + \bar{g}_3 \cdot \hat{\mathbf{S}}_3 + \bar{g}_4 \cdot \hat{\mathbf{S}}_4) \quad (4-9)$$

which assumes an isotropic exchange interactions where  $J_{23}$  describes the intradimer exchange interactions within the  $\text{Cu}_2(\text{N}_3)_4$  groups mediated by the double end-on azide bridges and  $J_{12} = J_{34}$  accounts for the exchange mediated by the single end-to-end azide bridges between the “rungs” and the  $\text{Cu}(\text{terpy})(\text{N}_3)_2$  moieties. For simplicity,  $g$ -values are assumed to be isotropic. The next-nearest neighbor intratetramer couplings, *i.e.*  $J_{13}$ ,  $J_{14}$ , and  $J_{24}$ , have been neglected. The exchange mediated by the single end-on azide bridges between the “rungs” and the terminal  $\text{Cu}(\text{terpy})(\text{N}_3)_2$  units is small and is

approximated by a molecular field term ( $\theta$ ) applied to the Hamiltonian. The zero-field energy levels of the spin-Hamiltonian are<sup>259</sup>

$$\begin{aligned}
 (S=2)E_1 &= -J_{12} - \frac{1}{2}J_{23} \\
 (S=1)E_2 &= J_{12} - \frac{1}{2}J_{23} \\
 (S=1)E_3 &= \frac{1}{2}J_{23} + \sqrt{J_{12}^2 + J_{23}^2} \\
 (S=1)E_4 &= \frac{1}{2}J_{23} - \sqrt{J_{12}^2 + J_{23}^2} \\
 (S=0)E_5 &= J_{12} + \frac{1}{2}J_{23} + \sqrt{4J_{12}^2 - 2J_{12}J_{23} + J_{23}^2} \\
 (S=0)E_6 &= J_{12} + \frac{1}{2}J_{23} - \sqrt{4J_{12}^2 - 2J_{12}J_{23} + J_{23}^2}
 \end{aligned} \tag{4-10}$$

The Van Vleck magnetic susceptibility vs. temperature is

$$\chi_{\text{Tetramer}} = \frac{N_A g^2 \mu_B^2}{k_B T} \frac{10 + \exp\left(\frac{-E_1}{k_B T}\right) + 2 \exp\left(\frac{-E_2}{k_B T}\right) + 2 \exp\left(\frac{-E_3}{k_B T}\right) + 2 \exp\left(\frac{-E_4}{k_B T}\right)}{Z} \tag{4-11}$$

where  $Z$ , the partition function, is

$$5 \exp\left(\frac{-E_1}{k_B T}\right) + 3 \exp\left(\frac{-E_2}{k_B T}\right) + 3 \exp\left(\frac{-E_3}{k_B T}\right) + 3 \exp\left(\frac{-E_4}{k_B T}\right) + 3 \exp\left(\frac{-E_5}{k_B T}\right) + 3 \exp\left(\frac{-E_6}{k_B T}\right) \tag{4-12}$$

and parameters have the usual meaning. The mean field corrected susceptibility is

$$\chi' = \chi_{\text{Tetramer}} \left( \frac{T}{T - \theta} \right) \tag{4-13}$$

and the total susceptibility, corrected for a fraction of uncoupled, monomeric impurity, is

$$\chi = \chi'(1 - \rho) + \frac{N_A g^2 \mu_B^2}{2k_B T} \rho + \chi_0 \tag{4-14}$$

The best fit for both the  $\chi$  and  $\chi T$  data of **5** to Equations 4-10 to 4-14 was obtained using

non-linear regression analysis with  $g$ ,  $J_{12}$ ,  $J_{23}$ ,  $\rho$ ,  $\theta$ , and  $\chi T_0$  or  $\chi_0$  as parameters. The

results of the best fit are shown as the solid lines in Figures 4-15 and 4-16 with  $N_R = 0.952$ ,  $g = 2.05$ ,  $2J_{12} = 10.697 \text{ K} \pm 3.408 \text{ K}$ ,  $2J_{23} = -108.283 \text{ K} \pm 1.188 \text{ K}$ ,  $\theta = 0.174 \pm 0.165 \text{ K}$ ,  $\rho = 3.482 \times 10^{-6}$ ,  $\chi T_0 = -5.550 \times 10^{-6} \text{ emu K mol}^{-1}$  and  $\chi_0 = 6.92 \times 10^{-6} \text{ emu mol}^{-1}$ . A similar fit was also obtained when  $\theta$  is negative. Given the present susceptibility data, little significance should be associated with the result that  $\theta$  is positive since in the absence of extremely low temperature data, the sign cannot be unambiguously determined. Although the agreement factor  $R = 0.329$  is somewhat large, the model fits the data well.

The best fit for **5** to the corresponding field dependent magnetization expression derived from equation 4-9 was obtained with  $N_R$ ,  $g$ ,  $J_{12}$ ,  $J_{23}$ , and  $M_0$  as parameters.<sup>260</sup> The results are shown as the solid line in Figure 4-17 with  $N_R = 0.935$ ,  $g = 2.11$ ,  $2J_{12} = 8.310 \text{ K}$ ,  $2J_{23} = -101.627 \text{ K}$ , and  $M_0 = -1.255 \text{ emu G mol}^{-1}$ . Although the agreement factor is large, expected for fits to  $M$  vs.  $B$  data, the  $N_R$ ,  $g$ , and  $J_{12}$ , and  $J_{23}$  values are consistent with those obtained from the  $\chi T$  data and the fit to the data is relatively good. The magnetization data were also compared to simulations of both the  $S = 1$  Brillouin function and the  $S = \frac{1}{2}$  Brillouin function multiplied by two, shown in Figure 4-17 as the dotted and dashed lines, respectively. The simulations were performed with the fixed parameters,  $N_R$ ,  $g$ , and  $M_0$ , obtained from the fits to the susceptibility data.

The average, isotropic  $g$ -value agrees well with the corresponding average value obtained from room temperature ESR measurements ( $g = 2.12$ ). The data indicate the exchange between the double end-on bridges within the ladder "rungs" is strongly antiferromagnetic, an unexpected result. The exchange between the single end-to-end bridges is weak and ferromagnetic, and the exchange between the single end-on bridges

in very weak. Thus the utilization of the tetramer model to analyze the magnetic data of **5** was justified.

### Interpretation of the Magnetic Data

The  $\chi T(T)$  plot in Figure 4-16 depicts the thermal population of an excited triplet state ( $S = 1$ ) at 10 K, then the  $S = 2$  state at 50 K. Similarly, the  $M(B)$  plot in Figure 4-17 depicts the population of the  $S = 1$  triplet state at 7 K. A simulation of the magnetization high field, up to 2000 kG (Figure 4-17), shows two plateaus indicating the population and saturation of the  $S = 1$  state with an upper critical field of 68 kG followed by the population and saturation of the  $S = 2$  state with a lower critical field of  $H_{C1} = 1300$  kG and an upper critical field of  $H_{C2} = 1460$  kG. The behavior of the variable field magnetization and variable temperature susceptibility can be correlated with Figure 4-19. Figure 4-19 schematically depicts two tetramers of **5** with the signs of the corresponding coupling constants within and between the tetramers, represented by the small arrows, determined from the fitting results obtained above. The schematic shows the changes in the total spin state of each tetramer as a function of increasing temperature and external field strength. At the lowest temperature, a singlet ground state is observed. Each tetramer has no net spin ( $S = 0$ ) and the weak, intertetramer exchange, ( $\theta$ ) is important and couples the tetramers ferromagnetically. However, as explained above, the intertetramer coupling could be antiferromagnetic, but the overall message conveyed by the diagram does not change. As the temperature is raised slightly, the intertetramer coupling is broken, but not the intratetramer exchange interactions, so the total spin of each tetramer is still zero, and a singlet state is still observed. As the temperature is increased to 10 K, the plateau in the  $\chi T$  plot corresponds to an  $S = 1$  excited state. This

can be achieved if the weak, ferromagnetic coupling,  $J_{12}$ , mediated by the single end-on azide bridges within each tetramer is broken and the spins at the ends of the oligomers align parallel with respect to each other. As the temperature is increased above 50 K, the  $\chi T$  product increases again, now approaching an  $S = 2$  excited state. Sufficient thermal energy is available to break the strong, antiferromagnetic coupling,  $J_{23}$ , mediated by the double end-on azide bridges within each tetramer. Now all of the spins per tetramer align in a parallel fashion. A similar effect is observed as an external field is applied to **5**, although no change in the magnetization is observed at low field due to the very weak, intertetramer coupling. From the  $M(B)$  plot in Figure 4-17, between 0 and 50 kG, the data did not fit the  $S = 1$  Brillouin function, but rather the product of two  $S = \frac{1}{2}$  Brillouin functions, indicating that the  $J_{12}$  coupling between the terminal metal centers with the rungs is weak since the first plateau in the magnetization is related to the exchange constant between these two types of magnetic centers.

### **Rationalizing the Sign and Magnitude of the Coupling Constants**

Recall the exchange interactions within the dinuclear  $\text{Cu}_2(\text{N}_3)_4$  moieties are mediated by end-on azide ligands bridging the Cu(II) ions. Both the magnetic data and corresponding fits indicate that the intradimer coupling,  $J_{23}$  is strongly antiferromagnetic. The negative sign of the coupling constant is not consistent with the small Cu—N—Cu bridging angle of  $103.3^\circ$  where a large ferromagnetic coupling is expected. The sign of the coupling constant is also not consistent with other similar  $\mu$ -diazido bridged copper(II) complexes as there appear to be no examples with antiferromagnetic coupling when the bridging angle is less than  $108.5^\circ$ .<sup>6,17,237,246-249</sup> However, the magnitude of the coupling constant is strong due to the short Cu—(bridging)N bonds, the planarity

of the cyclic  $\text{Cu}-(\text{N})_2-\text{Cu}$  moiety, and the double end-on azido ligands that bridge basal-basal coordination sites (both associated with the  $d_{x^2-y^2}$  orbitals with significant unpaired spin density) on both  $\text{Cu}(\text{II})$  ions (Figure 4-20).<sup>255</sup>

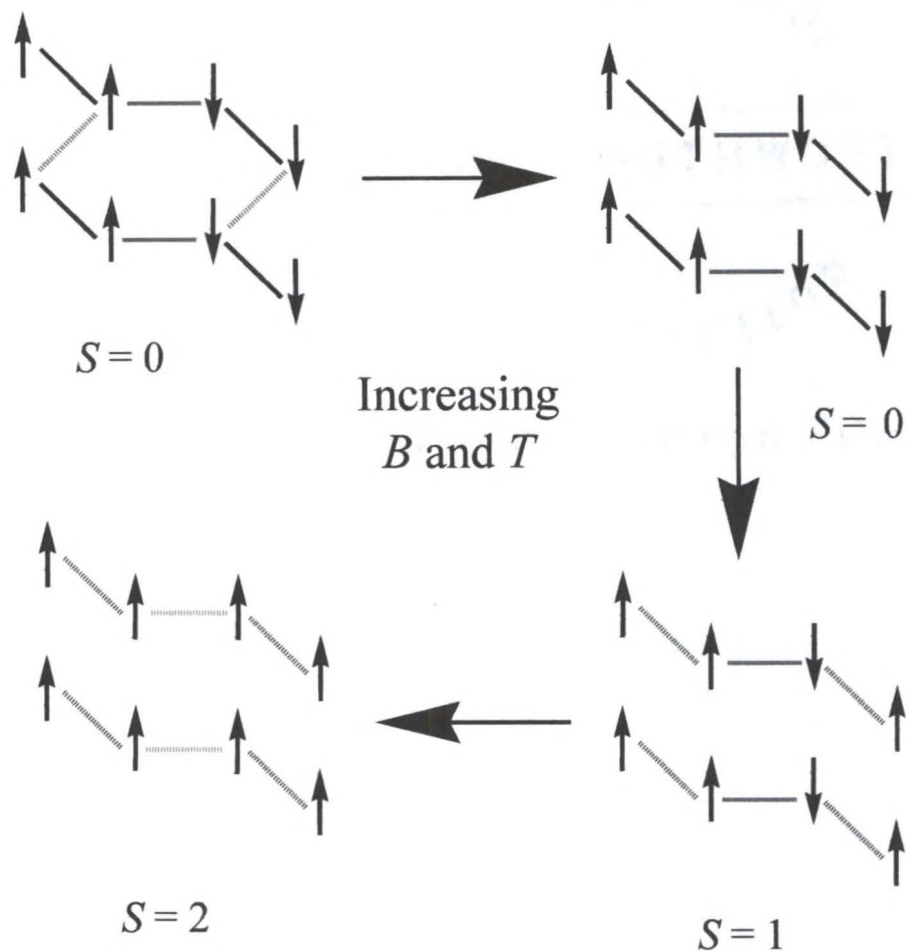


Figure 4-19. The change in the total  $S$  per tetramer as a function of temperature or applied field in compound **5**. The nearest neighbor inter- and intratetramer exchange interactions, represented by the small black arrows, were obtained from best fits to the bulk magnetic susceptibility data.

The reason for this unexpectedly large antiferromagnetic intradimer exchange in **5** is not clear. Perhaps strong bonding interactions to neighboring rungs via the  $\text{Cu}(\text{terpy})(\text{N}_3)_2$  moieties or other electronic factors are reducing the ferromagnetic component to the point that the antiferromagnetic contribution to the total exchange dominates.<sup>21</sup> Although these terminal units are only weakly coupled to the rungs, the presence of the terminal moieties may influence the relative energies of the magnetic orbitals within the dimers. The normally degenerate magnetic orbitals of the dimers must experience a dramatic shifting of the magnetic energy levels producing a large energy gap between the magnetic orbitals. Hence, a singlet ground state is strongly stabilized thus giving rise to the dominant antiferromagnetic coupling. Molecular orbital and singlet-triplet energy gap calculations may be required to confirm or reject this explanation.

The exchange between both the single end-to-end ( $J_{12}$ ) and single end-on ( $\theta$ ) azide bridges in **5** was determined to be small in magnitude. Both types of  $\text{Cu}(\text{II})$  ions exhibit square pyramidal geometry. In the single end-to-end azide bridge, one nitrogen atom is linked to the apical position of the  $\text{Cu}(\text{terpy})(\text{N}_3)_2$  group and the other nitrogen atom from the same bridge is coordinated to the basal sites of neighboring  $\text{Cu}_2(\text{N}_3)_2$  moiety (Figure 4-20). Conversely, in the single end-on azide bridge, the nitrogen atom is linked to both the basal position of the  $\text{Cu}(\text{terpy})(\text{N}_3)_2$  moiety and the apical site of neighboring  $\text{Cu}_2(\text{N}_3)_2$  group (Figure 4-20). When the superexchange interaction is between the apical-basal coordination sites, the coupling is very small in magnitude. For square pyramidal and octahedrally coordinated  $\text{Cu}(\text{II})$  ions, there is a good delocalization of the electron density to the bridging azide ligand coordinated to the basal  $\text{Cu}(\text{II})$  ions

since the unpaired spin density is primarily located in a  $d_{x^2-y^2}$  atomic orbital but the delocalization to the azide bridge from the apical Cu(II) ions is poor since the  $d_z^2$  orbital is occupied by paired spins and thus the unpaired spin density is low.<sup>6,190,255</sup> The longer apical Cu—N distance compared to the analogous equatorial Cu—N distance also results in a weaker exchange interaction as well.

Recall that the coupling through the single end-to-end bridge was ferromagnetic. The small Cu—N—N bridging angles ( $124.2^\circ$  and  $114.6^\circ$ ) tend to favor antiferromagnetic coupling. However, the large Cu—N<sub>3</sub>—Cu torsion angle ( $89.8^\circ$ ), along with the apical-basal bridging mode of the single end-on azide ligand and the square pyramidal geometry of the Cu(II) metal centers may orient the magnetic orbitals in an almost orthogonal fashion to nullify the antiferromagnetic contribution of the total superexchange resulting in a net weak ferromagnetic coupling through the single end-to-end bridges.<sup>255</sup>

For the single end-on bridges, the coupling was found to be very weakly ferromagnetic.<sup>216</sup> As explained above, in the absence of low temperature data, the sign cannot be unambiguously determined. The Cu—N—Cu bridging angle ( $107.1^\circ$ ) is very close to, but slightly lower than, the angle of accidental orthogonality ( $108.5^\circ$ ), where the ferromagnetic and antiferromagnetic contributions cancel out one another and virtually no net exchange interaction is observed. The assignment of the intertetramer coupling to the exchange through the single end-on bridges rather than the single end-to-end bridges is justified. Thus, **5** consists of weakly interacting antiferromagnetically coupled tetramers and the reasoning for analyzing the magnetic data using a tetramer model as opposed to the ladder model is justified.

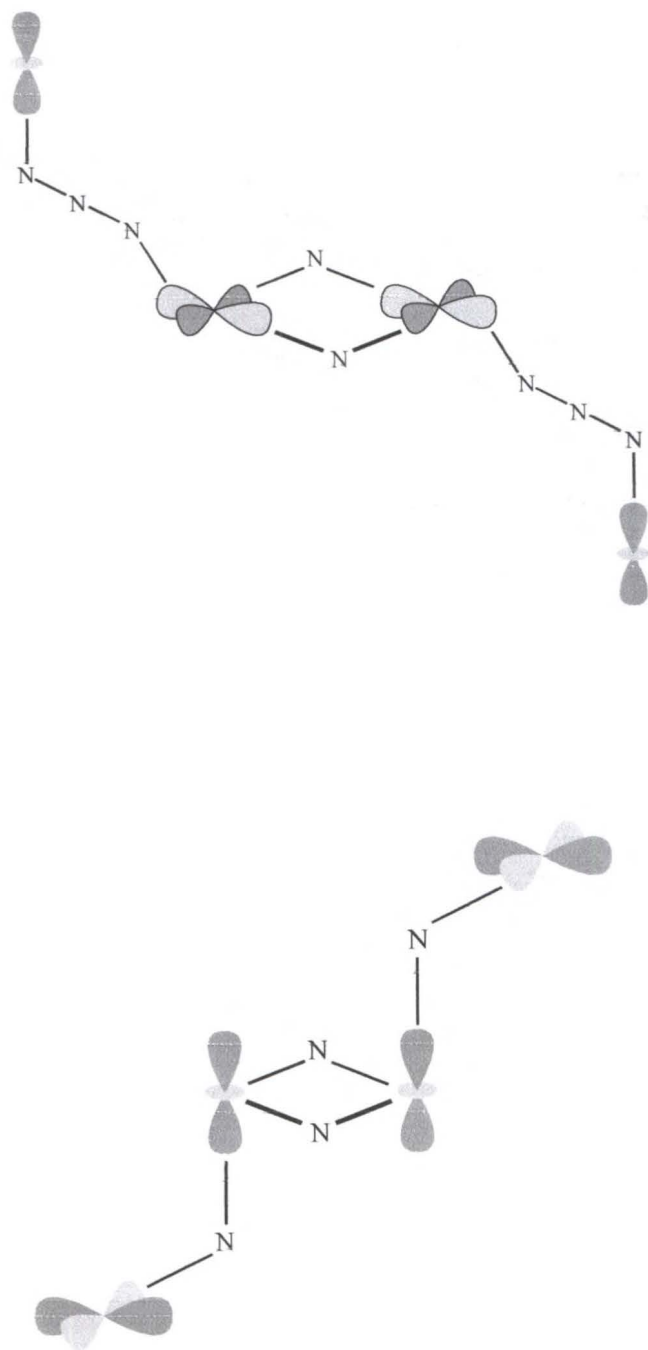


Figure 4-20. The metal  $d$ -orbitals involved in the superexchange interactions present in compound **5**. Within the dinuclear units that comprise the ladder rungs, the end-on azide ions bridge both equatorial sites of the metal centers and thus a strong intradimer coupling is observed. The axial-equatorial coordination by the single end-on and end-to-end azide ligands between the rungs and legs results in a weak coupling.

## Magnetic Properties of $[\text{Cu}_2(\text{terpy})_2-\mu-(\text{N}_3)_2(\text{N}_3)_2\text{Cu}_3-\mu-(\text{N}_3)_4(\text{N}_3)_2]$

### Magnetic Data

A plot of the zero-field cooled magnetization (open boxes) and the field-cooled magnetization (open circles) is shown in Figure 4-21. The two sets of data superimpose one another indicating that **6** does not experience any long-range magnetic order down to 2 K. Plots of both the magnetic susceptibility ( $\chi_M$ ) vs. temperature and the inverse susceptibility vs. temperature for **6** are shown in Figures 4-21 and 4-22, respectively, as open squares. The susceptibility increases steadily as the temperature is lowered and no maximum is observed. The high temperature inverse susceptibility data (from 250 K to 300 K) were fit to a straight line and extrapolated to the  $x$ -axis with  $T = 40.72$  K suggesting that the dominant magnetic exchange in **5** is ferromagnetic in nature. A plot of the temperature dependence of the product of the susceptibility and temperature ( $\chi_M T$ ) is shown in Figure 4-22 as open squares. The  $\chi_M T$  value at room temperature (0.336 emu K mol<sup>-1</sup> Cu(II) ions) is slightly lower than the expected spin-only value for a collection of non-interacting  $S = 1/2$  paramagnetic centers ( $\chi_M T = 0.413$  emu K mol<sup>-1</sup>). As the temperature is lowered, the  $\chi_M T$  value increases until reaching a maximum value of 2.48 emu K mol<sup>-1</sup> at 6.5 K. The increase is not smooth as two changes in slope of the data in this region are observed. The increasing of the  $\chi T$  product with decreasing temperature indicates the presence of a ferromagnetic coupling. Below 6.5 K however, the  $\chi_M T$  value decreases approaching zero suggesting that a weak antiferromagnetic exchange interaction is present as well. Note that although  $\chi^I(T)$  is reported per mole of pentamer,  $\chi(T)$  and  $\chi T(T)$  are given as per mole of trimer; this discrepancy is addressed below. The field dependence of the molar magnetization ( $M_M$ ) per mole of pentamer for **6** is shown in

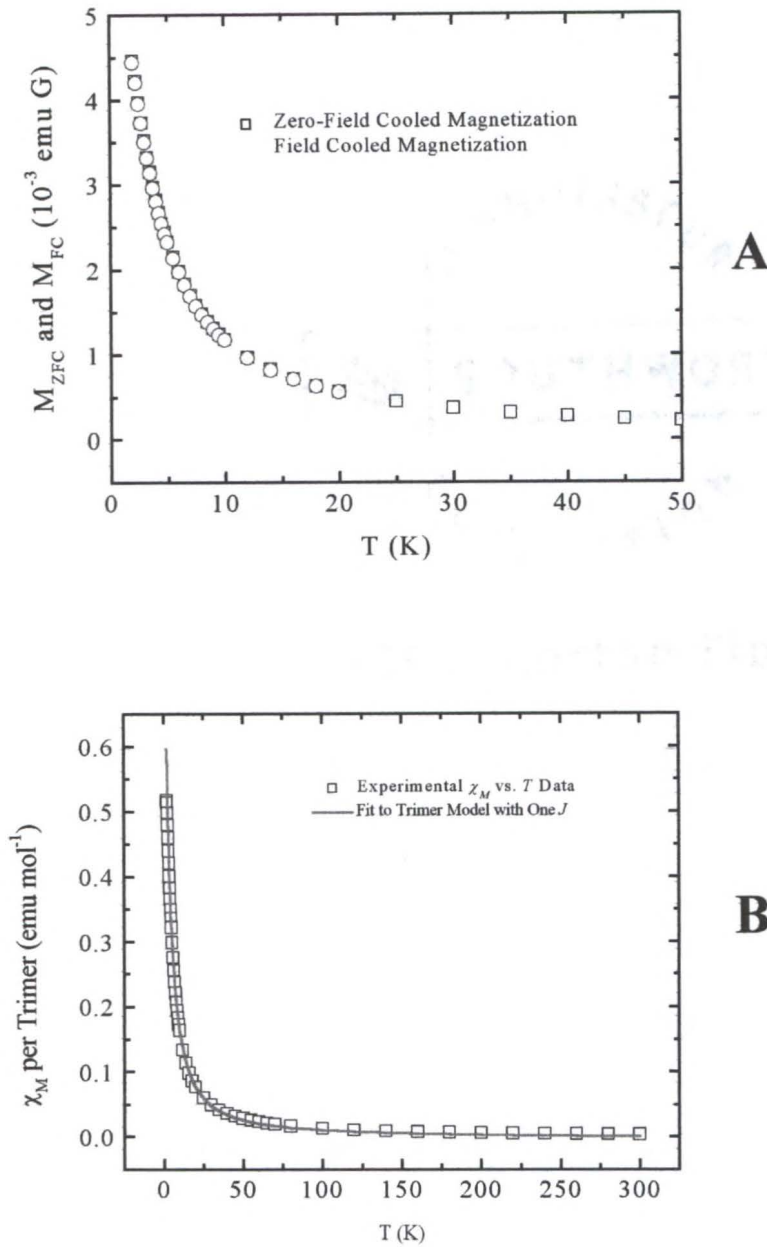


Figure 4-21. Magnetic data for compound **6** at 100 G from 2 K to 300 K. A) Field-cooled ( $M_{FC}$ ) and zero-field cooled ( $M_{ZFC}$ ) magnetization versus temperature. B) Molar susceptibility,  $\chi_M$ , per trimer. The data have been corrected for background signals arising from the sample container and diamagnetic contributions. The fit of  $\chi$  to the uniform  $S = \frac{1}{2}$  trimer model from Equations 4-18 to 4-20 is shown by the solid line in B).

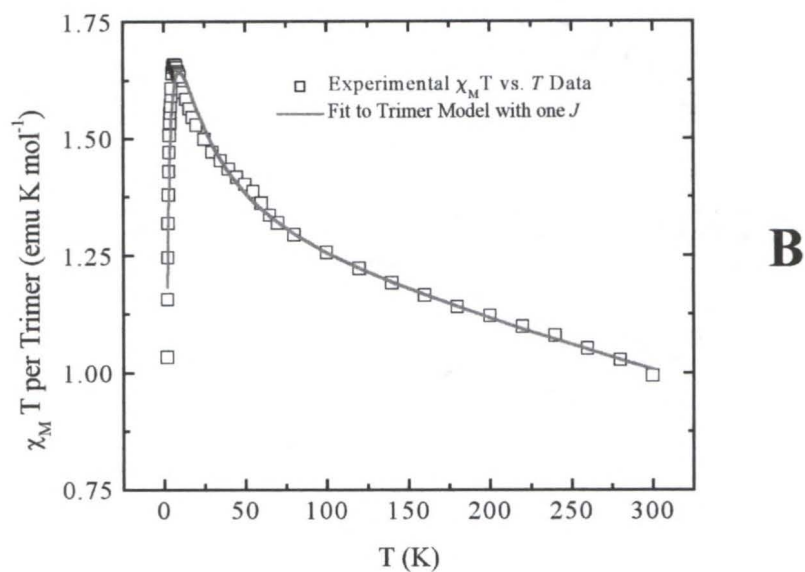
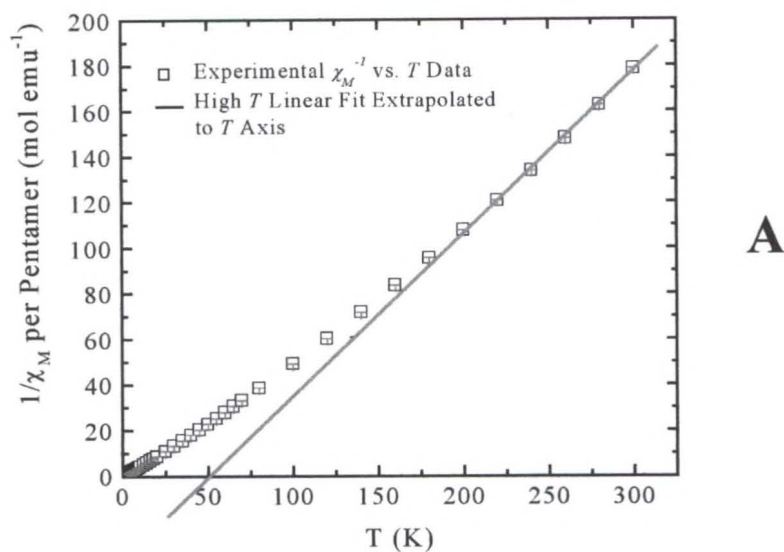


Figure 4-22. Magnetic data for compound **6** at 100 G from 2 K to 300 K. A) Inverse molar susceptibility,  $\chi^{-1}$ , per pentamer versus temperature. B) The product of the molar susceptibility and temperature,  $\chi T$ , per trimer at versus temperature. The data have been corrected for background signals arising from the sample container and diamagnetic contributions. A linear fit to the high temperature data in A) is shown by the solid line. The fit of  $\chi T$  to the uniform  $S = \frac{1}{2}$  trimer model from Equations 4-18 to 4-20 is shown by the solid line in B).

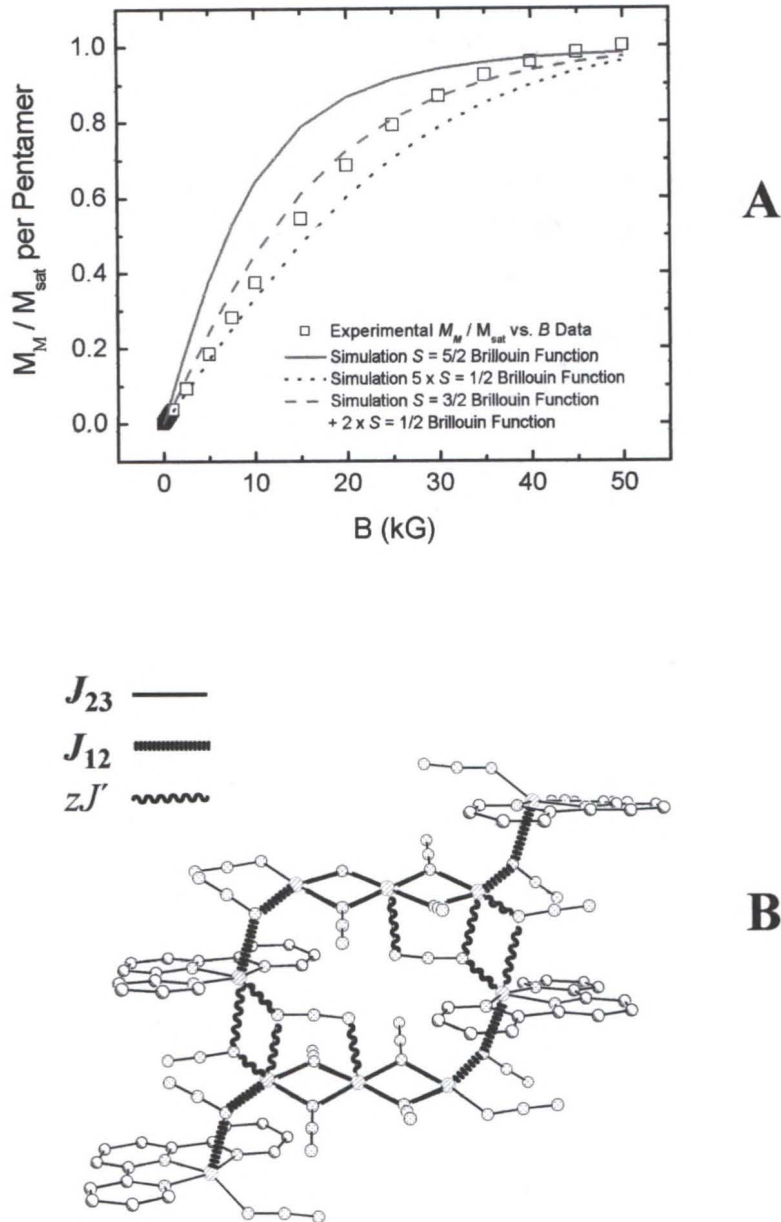


Figure 4-23. A) The molar magnetization ( $M$ ) per trimer at 2 K from 0 to 50 kG for compound **6**, normalized to the saturation magnetization,  $M_{sat}$ . The data have been corrected for background signals arising from the sample container. The simulation of  $M$  to the  $S = 5/2$  Brillouin function,  $5 \times S = 1/2$  Brillouin function, and  $S = 3/2$  Brillouin +  $2 \times S = 1/2$  Brillouin function is shown as the solid line, the dotted line, and the dashed line, respectively. B) A fragment consisting of two pentamers of compound **6** depicting the possible superexchange pathways. The copper(II) ions are shown as the shaded circles.

Figure 4-23 as open squares. The magnetization initially increases with increasing field but begins to level out at 30 kG asymptotically approaching a constant value of approximately  $26\,000 \text{ emu G mol}^{-1}$ . Below 10 kG, the magnetization varies linearly with the applied field with no apparent change in slope observed.

### Magnetic Model and Fits

Recall the structure of **6** consists of ladder-like stacks of azido-bridged Cu(II) pentamers. Three distinct types of exchange pathways can be distinguished, depicted schematically in Figure 4-23. The central trinuclear  $\text{Cu}_3(\text{N}_3)_6$  units of each pentamer are expected to mediate the dominant superexchange interactions ( $J_{23}$ ) in **6** since the double end-on azide ligands bridge the square pyramidal copper ions through the basal coordination sites. However, the coupling ( $J_{12}$ ) between the central  $\text{Cu}_3(\text{N}_3)_6$  trimers to the terminal  $\text{Cu}(\text{terpy})(\text{N}_3)_2$  moieties is expected to be, at best, weak due to the single end-on azide ligands bridging the apical-basal coordination sites of the metal centers. Due to the long Cu—N contacts associated with the asymmetric end-to-end and end-on azide bridges, the corresponding interpentamer exchange ( $J'$ ) is also expected to be weak. Any magnetic interactions between the ladders-like stacks are assumed to be negligible since only weak N—H(aromatic) contacts and hydrophobic interactions are present between the organic ligands.

The spin-Hamiltonian, with the corresponding Zeeman term, that describes the nearest-neighbor exchange within linear, pentanuclear Cu(II) oligomers with two distinct superexchange pathways resembling **6** is

$$\begin{aligned} \hat{H} = & -2J_{12}(\hat{\mathbf{S}}_1 \cdot \hat{\mathbf{S}}_2 + \hat{\mathbf{S}}_4 \cdot \hat{\mathbf{S}}_5) - 2J_{23}(\hat{\mathbf{S}}_2 \cdot \hat{\mathbf{S}}_3 + \hat{\mathbf{S}}_3 \cdot \hat{\mathbf{S}}_4) + \\ & \mu_B B \cdot (\bar{g}_1 \cdot \hat{\mathbf{S}}_1 + \bar{g}_2 \cdot \hat{\mathbf{S}}_2 + \bar{g}_3 \cdot \hat{\mathbf{S}}_3 + \bar{g}_4 \cdot \hat{\mathbf{S}}_4 + \bar{g}_5 \cdot \hat{\mathbf{S}}_5) \end{aligned} \quad (4-15)$$

which assumes an isotropic exchange interactions,  $J_{12}$  and  $J_{23}$ , and neglects the next-nearest neighbor intratrimer coupling between the end atoms, *i.e.*  $J_{13}, J_{14}, J_{25}, J_{36}$ , etc. However, calculating the eigenvalues from Equation 4-16 is not trivial and the resulting analytical expressions for the field dependence of the magnetization and temperature dependence of the susceptibility are rather complex. The exchange between the terminal  $\text{Cu}(\text{terpy})(\text{N}_3)_2$  units and the central  $\text{Cu}_3(\text{N}_3)_6$  trimers, mediated by the single end-on azide bridges, is small compared to the intratrimer coupling. Thus the terminal units are assumed to behave in a paramagnetic fashion since they are magnetically isolated from the central trimers. The susceptibility of these two  $S = 1/2$  uncoupled units was calculated and subtracted from the total susceptibility of **6** to obtain the susceptibility due to the coupled trimers and the interactions between the trimers. Thus,  $J_{12}$  is neglected and **6** is assumed to consist of stacks of weakly interacting trimers.

The exchange interactions of uniform, linear trinuclear  $\text{Cu}(\text{II})$  oligomers can be well described by the spin-Hamiltonian with corresponding including the Zeeman term

$$\hat{H} = -2J(\hat{\mathbf{S}}_1 \cdot \hat{\mathbf{S}}_2 + \hat{\mathbf{S}}_2 \cdot \hat{\mathbf{S}}_3) + \mu_B B \cdot (\bar{g}_1 \hat{\mathbf{S}}_1 + \bar{g}_2 \hat{\mathbf{S}}_2 + \bar{g}_3 \hat{\mathbf{S}}_3) \quad (4-16)$$

which assumes an isotropic exchange interaction,  $J$ , within the central  $\text{Cu}_3(\text{N}_3)_6$  trimers and neglects the next-nearest neighbor intratrimer coupling between the end atoms, *i.e.*  $J_{13}$ . For simplicity,  $g$ -values are assumed to be isotropic. The weak, intertrimer exchange is approximated by a molecular field term ( $\theta$ ) applied to the Hamiltonian. The zero-field energy levels of the spin-Hamiltonian are  $E_1 = 2J$  ( $S = 1/2$ ),  $E_2 = 0$  ( $S = 1/2$ ), and  $E_3 = -J$  ( $S = 3/2$ ).<sup>261</sup> The Van Vleck susceptibility vs. temperature is

$$\chi_{Trimer} = \frac{N_A g^2 \mu_B^2}{k_B T} \frac{1 + \exp\left(\frac{2J}{k_B T}\right) + 10 \exp\left(\frac{3J}{k_B T}\right)}{4 + 4 \exp\left(\frac{2J}{k_B T}\right) + 8 \exp\left(\frac{3J}{k_B T}\right)} + N\alpha \quad (4-17)$$

where the parameters have the usual meaning. The mean field corrected susceptibility is

$$\chi' = \chi_{Trimer} \left( \frac{T}{T - \theta} \right) \quad (4-18)$$

and the total susceptibility, corrected for a fraction of uncoupled, monomeric impurity is

$$\chi = \chi'(1 - \rho) + \frac{N_A g^2 \mu_B^2}{2k_B T} \rho \quad (4-19)$$

The best fit for both the  $\chi$  and  $\chi T$  data of **6** to Equations 4-17 to 4-19 was obtained using non-linear regression analysis with  $g$ ,  $J$ ,  $\rho$ ,  $\theta$ , and  $\chi T_0$  or  $\chi_0$  as parameters. The results are shown as the solid lines in Figures 4-21 and 4-22 with  $N_R = 1.007$ ,  $g = 2.11$ ,  $2J = 14.598 \text{ K} \pm 0.556 \text{ K}$ ,  $\theta = -1.526 \text{ K} \pm 0.034 \text{ K}$ ,  $\rho = 9.33 \times 10^{-3}$ ,  $\chi T_0 = -9.3 \times 10^{-4} \text{ emu K mol}^{-1}$  and  $\chi_0 = 7.7 \times 10^{-4} \text{ emu mol}^{-1}$ . The agreement factor  $R = 1.31 \times 10^{-3}$  is very small indicating the model fits the data well.

Because of the complexity of expressions describing the field dependence of magnetization for a five-spin system, no corresponding fits to the field dependent magnetization data were attempted. However, the data were compared to simulations of the  $S = 5/2$  Brillouin function,  $S = 1/2$  Brillouin function multiplied by five, and the product of the  $S = 3/2$  Brillouin function and two the  $S = 1/2$  Brillouin function, are shown in Figure 4-23 as the solid, dotted, and dashed lines, respectively. The simulations were performed with the fixed parameters,  $N_R$ ,  $g$ , and  $M_0$ , obtained from the fits to the susceptibility data.

The average, isotropic  $g$ -value agrees well with the corresponding average value obtained from room temperature ESR measurements ( $g = 2.14$ ). The magnetic data and corresponding fits indicate that the dominant exchange interaction within the central  $\text{Cu}_3(\text{N}_3)_6$  trimers in **6** is weakly ferromagnetic and the interpentamer coupling is weakly antiferromagnetic. Furthermore, the assumption that **6** consists of weakly interacting trimers by neglecting the weak interpentamer exchange,  $J_{12}$ , between the central  $\text{Cu}_3(\text{N}_3)_6$  trimers and the terminal  $\text{Cu}(\text{terpy})(\text{N}_3)_4$  units, is justified since the corresponding trimer susceptibility expressions fit the magnetic data well.

### Interpretation of the Magnetic Data

The  $\chi T$  plot in Figure 4-22 depicts the thermal population of the  $S = 5/2$  ground state at low temperature ( $T = 6.5$  K). At high temperature, **6** behaves paramagnetically, *i.e.*, the unpaired spins within each pentamer along the ladder-like chains are uncoupled and essentially randomized resulting in a small net magnetic moment. As  $T$  is lowered, the intrapentamer coupling takes effect, as insufficient thermal energy is present to populate excited states. An increase in the  $\chi T$  product is observed due to the onset of the ferromagnetic exchange interactions. Two changes in slope of the data in this region possibly indicate the onset of two distinct coupling constants. At  $T = 6.5$  K, the  $S = 5/2$  ground state (where all five spin vectors per pentamer align in a parallel fashion) is fully populated and **6** consists of stacks of ferromagnetically coupled pentamers. At even lower temperatures, a sudden decrease in the  $\chi T$  product indicates the weak interpentamer interactions take effect. The magnetization data in Figure 4-23 depicts the population of the  $S = 5/2$  state at high field. Since all of the exchange interactions,  $J_{12}$ ,  $J_{23}$ , and  $\theta$ , are relatively weak, **6** resembles a linear array of five weakly interacting  $S = 1/2$

metal centers since the magnetization data follow the  $S = 1/2$  Brillouin function. If both interpentamer coupling constants,  $J_{12}$  and  $J_{23}$ , were strong, the magnetization data would follow the  $S = 5/2$  Brillouin function. If the intratrimer exchange,  $J$ , within central  $\text{Cu}_3(\text{N}_3)_6$  trimers was strong but the exchange,  $J_{12}$ , between the two terminal  $\text{Cu}(\text{terpy})(\text{N}_3)_4$  units was weak, then the magnetization data would be reproduced by the  $S = 3/2$  Brillouin function + the  $S = 1/2$  Brillouin function multiplied by two.

### **Rationalizing the Sign and Magnitude of the Coupling Constants**

Recall the exchange interactions within the trinuclear  $\text{Cu}_3(\text{N}_3)_6$  moieties are mediated by end-on azide ligands bridging the Cu(II) ions. Both the magnetic data and corresponding fits indicate that the intratrimer coupling,  $J$ , is weakly ferromagnetic. The positive sign of the coupling constant is consistent with the small Cu—N—Cu bridging angle of  $101.7^\circ$ . However, the magnitude of the coupling constant is much smaller than expected and is not consistent with other similar  $\mu$ -diazido bridged copper(II) complexes.<sup>6,17,237,246-249</sup> The small bridging angle, short Cu—(bridging)N bonds, the planar Cu—(N)<sub>2</sub>—Cu moiety, and the double end-on azido ligands that bridge basal-basal coordination sites (both associated with the  $d_x^2-y^2$  orbitals with significant unpaired spin density) on both Cu(II) ions (Figure 4-24) suggest that the magnitude of the coupling should be greater.<sup>255</sup>

The reason for this unexpectedly small ferromagnetic exchange is not clear but it does correlate with the unexplained antiferromagnetic intradimer coupling observed in **5**. Perhaps structural-bonding or electronic factors are reducing the ferromagnetic component and thus enhancing the antiferromagnetic contributions to the total exchange within the trinuclear  $\text{Cu}_3(\text{N}_3)_6$  moieties. One possible cause could be the presence of the

monomeric  $\text{Cu}(\text{terpy})(\text{N}_3)_2$  units linked to the ends of the trimers in **6**.<sup>21</sup> Note that similar  $\text{Cu}(\text{terpy})(\text{N}_3)_2$  groups are present in **5** as well. Although these terminal units are essentially magnetically isolated from the coupled central trimers, the presence of the terminal moieties may influence the relative energies of the magnetic orbitals within the trimers. The normally degenerate magnetic orbitals of the trimers could be experiencing an increased energy gap thus reducing the ferromagnetic contribution and increasing the antiferromagnetic effects. In the case of **6**, however, the shifting of energies is not sufficient to stabilize a singlet state, the antiferromagnetic contribution does not dominate, and the net exchange is still, albeit weakly, ferromagnetic. Molecular orbital and singlet-triplet energy gap calculations may be required to confirm or reject this explanation.

Recall that, for the purposes of fitting the magnetic data, the exchange between the single end-on azide bridges,  $J_{12}$ , between the  $\text{Cu}(\text{terpy})(\text{N}_3)_2$  units and the  $\text{Cu}_3(\text{N}_3)_6$  moieties was neglected. Therefore, the sign and magnitude of the coupling constant was not determined. However, based on the structural data, the magnitude of the exchange is expected to be weak. In the single end-on azide bridges, the same nitrogen atom is linked to the basal position of the  $\text{Cu}(\text{terpy})(\text{N}_3)_2$  moiety and to the apical sites of  $\text{Cu}_2(\text{N}_3)_2$  group (Figure 4-24).<sup>6,205,255</sup> There is a good delocalization of the electron density to the bridging azide ligand coordinated to the basal  $\text{Cu}(\text{II})$  ions since the unpaired spin is primarily located in a  $d_{x^2-y^2}$  orbital but the delocalization to the azide bridge coordinated to the apical  $\text{Cu}(\text{II})$  ions is poor since the  $d_z^2$  orbital is occupied by paired spins. The longer apical  $\text{Cu}-\text{N}$  distance compared to the analogous basal  $\text{Cu}-\text{N}$  distance also results in a weaker exchange interaction as well. Computer simulations of  $\chi T$  vs.  $T$  based

with analytical susceptibility expressions derived from Equation (4-16), utilizing the  $J_{23}$  value obtained from the above fits, suggests that  $J_{12}$  is weakly ferromagnetic. The  $\chi T$  vs.  $T$  plot in Figure 4-22 is uniquely reproduced only when both coupling constants are positive and  $J_{23} \gg J_{12}$ . When  $J_{12}$  is negative and small, for example, a broadened maximum in  $\chi T$  at low temperature, rather than the observed sharp peak, results.

Attempts to rationalize the sign were based on similar magnetostructural correlations for single end-to-end bridges. Despite the large Cu—N—Cu bridging angle (117.8 °) that is expected to favor antiferromagnetic coupling, the azide ligands bridging the approximately perpendicular oriented apical-basal coordination sites of the square pyramidal Cu(II) ions between the metal centers may orient the magnetic orbitals an orthogonal or nearly orthogonal fashion to nullify the antiferromagnetic contribution of the total superexchange resulting in a net weak, ferromagnetic coupling.<sup>205,216,255</sup>

The interpentamer superexchange pathway consists of asymmetric, double end-on and single end-to-end bridging azide ligands. Both the magnetic data and corresponding fits indicate that the interpentamer coupling is weakly antiferromagnetic. The negative sign of the interpentamer coupling is consistent with the interdimer exchange observed in **4** since the structural parameters of the asymmetric azide bridges in both samples are similar. The small, antiferromagnetic coupling is also consistent with asymmetric end-on and end-to-end azide ligands bridging square pyramidal Cu(II) ions in other similar complexes as well.<sup>205,255</sup> The long, weak Cu—N bonds creates large distances between the metal centers and thus orbital overlap between the two exchanging metal centers is poor resulting in the small coupling constant. The azide ligands bridging the apical-basal coordination sites of the square pyramidal Cu(II) ions between the pentamers

also accounts for the small interpentamer coupling as well (Figure 4-24).<sup>205,255</sup>

Therefore, **6** consists of antiferromagnetic stacks of pentamers with two paramagnetic  $S = \frac{1}{2}$  sites and ferromagnetically coupled trimers.

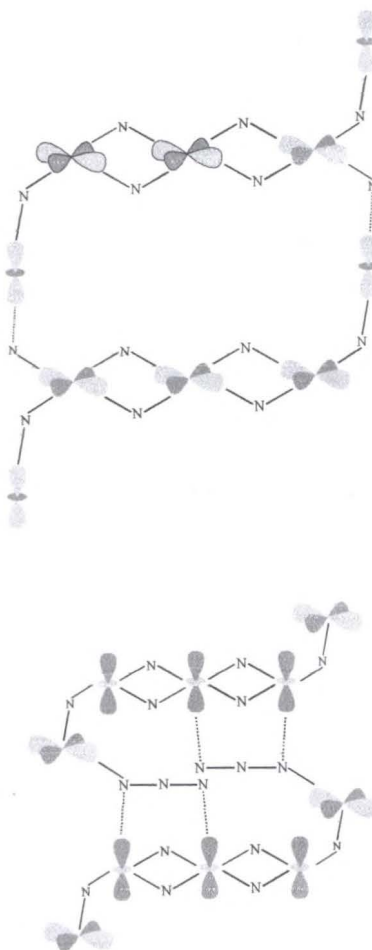


Figure 4-24. The metal *d*-orbitals involved in the superexchange interactions present in compound **6**. Within the central trinuclear units, the end-on azide ions bridge both equatorial sites of the metal centers and thus a strong intratimer coupling is expected. The axial-equatorial coordination by the single end-on azide ligands to the terminal Cu-terpy moieties is expected to provide a poor superexchange pathway resulting in a weak coupling. The long Cu—N contacts between the pentamers as well as the axial-equatorial coordination by the azide ligands results in a weak interpentamer coupling.

## Conclusions

This chapter summarizes the experiments performed in order to investigate the structural and magnetic properties of three azido-bridged copper(II) ladder-like coordination polymers,  $[\text{Cu}_2(\text{PhPyPy})_2-\mu-(\text{N}_3)_2(\text{N}_3)_2]$ , **4**,  $[\text{Cu}_2(\text{terpy})_2-\mu-(\text{N}_3)_4\text{Cu}_2-\mu-(\text{N}_3)_2(\text{N}_3)_2]$ , **5**, and  $[\text{Cu}_2(\text{terpy})_2-\mu-(\text{N}_3)_2(\text{N}_3)_2\text{Cu}_3-\mu-(\text{N}_3)_4(\text{N}_3)_2]$ , **6**. Compound **4** structurally resembles ladder-like chains of weakly interacting end-on azido bridged copper(II) dimers. Magnetically, **4** consists of antiferromagnetic chains of ferromagnetically coupled  $S = \frac{1}{2}$  dimers. Compound **5** consists of ladder-like copper(II) coordination polymers with double and single end-on and single end-on azido bridges. Magnetically, **5** consists of ladder-like stacks of weakly interacting tetramers with a dominant antiferromagnetic exchange, but this coupling cannot be easily rationalized on the basis of present structural-bonding parameters. Compound **6** structurally resembles ladder-like chains of weakly interacting copper(II) pentamers featuring both single and double end-on azide bridges. Magnetically, **6** consists of antiferromagnetic stacks of pentamers with two paramagnetic  $S = \frac{1}{2}$  sites and ferromagnetically coupled trimers.

## CHAPTER 5 CONCLUSIONS

This dissertation describes the synthesis and structural, chemical, and magnetic properties of low-dimensional coordination polymers. The original goal of this project focused on the design, self-assembly, and magnetic properties of molecular coordination polymer ladders. Instead, several new quasi-one-, one/two-, and two-dimensional materials were isolated as a result of serendipity rather than rational design but did not incorporate the desired structural and physical properties of ladder-like systems. Consequently, the work presented here is concerned primarily with the characterization of selected examples of these low-dimensional materials obtained in the course of this graduate research. Chapters 2 and 3 describe the structural, thermal, host-guest, and magnetic properties of a series of two-dimensional, layered, network solids. Chapter 4 details the structural and magnetic properties of a series of ladder-like azido bridged Cu(II) coordination polymers.

The structural, thermal, and magnetic properties of a series of clathrated porous network solids,  $[\text{Ni}(4,4'\text{-bipy})_3(\text{H}_2\text{O})_2](\text{ClO}_4)_2 \cdot 1.4(4,4'\text{-bipy}) \cdot 3(\text{H}_2\text{O})$ , **1**,  $[\text{Co}(4,4'\text{-bipy})_3(\text{H}_2\text{O})_2](\text{ClO}_4)_2 \cdot 1.4(4,4'\text{-bipy}) \cdot 3(\text{H}_2\text{O})$ , **2**, and  $[\text{Cu}(4,4'\text{-bipy})_3(\text{DMSO})_2](\text{ClO}_4)_2 \cdot 2(4,4'\text{-bipy})$  **3**, are in Chapter 2. These materials consist of chains of transition metal ions (Ni(II), Co(II), and Cu(II)) bridged by 4,4'-bipyridine spacer ligands. The chains pack to form two-dimensional, non-interpenetrated sheets with hydrophobic, rectangular cavities within the framework. The

sheets, in turn, pack to form layered, three-dimensional solids with oblique, extended channels containing enclathrated guest molecules and counterions. The guest molecules are easily lost, suggesting that the samples are thermally unstable. The magnetic properties of **1**, **2**, and **3** are similar in the sense that only very weak exchange interactions are present between the metal centers.

The host-guest properties of **1** and **2** are investigated in Chapter 3. Gas chromatography experiments determined that both hosts exchange clathrated bipy molecules with trialkylphosphine oxide probe molecules, TMPO (trimethylphosphine oxide), TEPO (triethylphosphine oxide), and TPPO (tripropylphosphine oxide). While the uptake of TMPO by both **1** and **2** is essentially complete, steric constraints are believed to limit the uptake of TEPO and TPPO by the host. The trialkylphosphine oxides interact with acid sites within the host as determined by  $^{31}\text{P}$  MAS NMR spectroscopy. TMPO interacts with both coordinated water molecules (strong acid sites) and lattice waters (weak acid sites) in compound **1** and coordinates directly to the metal centers in compound **2**. However, TEPO and TPPO seem to attack only the weaker acid sites within the hosts. X-ray diffraction patterns show that the loss of bipy and uptake of the probe causes significant structural rearrangements in **1** and only relatively mild structural changes in **2**. However, the nature of these guest-exchanged products is unknown. These experiments show that solid-state NMR spectroscopy can be used to investigate host-guest interactions.

Finally, the structural and magnetic properties of three azido-bridged copper(II) ladder-like coordination polymers,  $[\text{Cu}_2(\text{PhPyPy})_2-\mu-(\text{N}_3)_2(\text{N}_3)_2]$ , **4**,  $[\text{Cu}_2(\text{terpy})_2-\mu-(\text{N}_3)_4\text{Cu}_2-\mu-(\text{N}_3)_2(\text{N}_3)_2]$ , **5**, and

[Cu<sub>2</sub>(terpy)<sub>2</sub>-μ-(N<sub>3</sub>)<sub>2</sub>(N<sub>3</sub>)<sub>2</sub>Cu<sub>3</sub>-μ-(N<sub>3</sub>)<sub>4</sub>(N<sub>3</sub>)<sub>2</sub>], **6**, are discussed in Chapter 4. Compound **4** structurally resembles ladder-like chains of weakly interacting end-on azido bridged copper(II) dimers. Magnetically, compound **4** consists of antiferromagnetic chains of ferromagnetically coupled  $S = \frac{1}{2}$  dimers. Compound **5** consists of ladder-like copper(II) coordination polymers with double and single end-on azido bridges. Magnetically, compound **5** consists of ladder-like stacks of weakly interacting tetramers with a dominant and unusual antiferromagnetic exchange mediated through end-on azido bridges. Compound **6** structurally resembles ladder-like chains of weakly interacting copper(II) pentamers featuring both single and double end-on azide bridges. Magnetically, compound **6** consists of antiferromagnetic stacks of pentamers with two paramagnetic  $S = \frac{1}{2}$  sites and ferromagnetically coupled trimers.

The study of low-dimensional materials has been a rapidly expanding area of solid-state chemistry. Because of the anisotropic bonding present, these systems often exhibit unique or enhanced chemical and physical properties compared to higher-dimensional systems<sup>4</sup> such as low temperature catalysis,<sup>41-43</sup> inclusion phenomena,<sup>37,44,45</sup> magnetism,<sup>40,46-49</sup> electrical conductivity,<sup>50-52</sup> photochemistry,<sup>53</sup> and second-order nonlinear optical behavior.<sup>54-57</sup> This dissertation describes the chemical (host-guest) properties of selected porous, layered two-dimensional sheets as well as the physical (magnetic) properties of ladder-like coordination polymers. These samples represent new examples of low-dimensional materials and an understanding of their characteristic structural, chemical, and physical properties can better contribute to solid-state chemistry.

## APPENDIX A CRYSTAL STRUCTURES OF SELECTED LOW-DIMENSIONAL SOLIDS

### Comment

A few selected structures, obtained throughout the course of the graduate research, are presented in this appendix. As discussed at the beginning of the introduction, many products were obtained from the various synthetic attempts employed to self-assemble ladder-like coordination polymers that did not meet with success. Since these materials did not quite fit within the context of the preceding chapters, a few are included in this appendix for completeness. Discussed are the structures of  $[\text{Ni}(\text{terpy})(\text{H}_2\text{O})][\text{Ni}(\text{CN})_4]$ , **7**, a one-dimensional linear chain comprised of alternating  $[\text{Ni}(\text{terpy})(\text{H}_2\text{O})]^{2+}$  cations bridged by *trans*- $[\text{Ni}(\text{CN})_4]^{2-}$  anions. Also presented are  $[\text{Zn}(4,4'\text{-bipy})(\text{DMSO})_4]_n(\text{ClO}_4)_{2n}$ , **8**, a linear one-dimensional chain with *trans*-4,4'-bipyridine bridging ligands and  $[\text{Cu}(4,4'\text{-bipy})(\text{DMSO})_4]_n(\text{ClO}_4)_{2n}$ , **9**, a zig-zag chain with *cis*-4,4'-bipyridine bridges. Finally  $[\text{Cd}(4,4'\text{-bipy})_3(\text{H}_2\text{O})_2](\text{ClO}_4)_2 \cdot 2(\text{DMSO})$ , **10**, a layered sheet structure with clathrated hydrophobic pores, similar to structures **1**, **2**, and **3**, is detailed.

### Experimental Section

#### Materials

The starting materials nickel(II) perchlorate hexahydrate (98 %), zinc(II) perchlorate hexahydrate (98 %), copper(II) perchlorate hexahydrate (98 %), and cadmium(II) perchlorate hexahydrate (98 %), 4,4'-bipyridine (98 %) and 2,2':6',2''-

terpyridine (98 %) were purchased from Aldrich Chemical Co. Potassium cyanide (99.9 %), dimethyl sulfoxide (99.9 %), and ammonia (15 M) were purchased from Fisher Scientific. All reagents were used without further purification.

#### **Synthesis of [Ni(terpy)(H<sub>2</sub>O)][Ni(CN)<sub>4</sub>]**

The combination of Ni(ClO<sub>4</sub>)<sub>2</sub>·6H<sub>2</sub>O (366 mg, 1 mmol) with terpy (234 mg, 1 mmol) and KCN (97.5 mg, 1.5 mmol) in water (50 mL) produced a tan precipitate. Addition of NH<sub>3</sub> solution (20 mL, 15 M) followed by 50 mL of 100 % ethanol with stirring dissolved the precipitate resulting in a yellow-colored solution. The reaction mixture was filtered into a 500 mL Erlenmeyer flask, capped with paraffin (punctured with small holes), and set aside for crystallization. Within about four months, small brown blocks appeared in solution. These blocks were determined to be [Ni(terpy)<sub>2</sub>](ClO<sub>4</sub>)<sub>2</sub>·H<sub>2</sub>O, a known monomeric bis(terpy)nickel(II) complex.<sup>262</sup> Small gray needles of **7** were obtained after an additional month of solvent evaporation.

#### **Synthesis of [Zn(4,4'-bipy)(DMSO)<sub>4</sub>]<sub>n</sub>(ClO<sub>4</sub>)<sub>2n</sub>**

A solution containing 741 mg of Zn(ClO<sub>4</sub>)<sub>2</sub>·6 H<sub>2</sub>O (2.0 × 10<sup>-3</sup> mol) dissolved in 10 mL of DMSO was combined with a solution containing 467 mg of 4,4'-bipyridine (4.0 × 10<sup>-3</sup> mol) dissolved in 10 mL of DMSO. The resulting clear mixture, contained within an evaporating dish, produced small plates of **8** within two weeks of solvent evaporation.

#### **Synthesis of [Cu(4,4'-bipy)(DMSO)<sub>4</sub>]<sub>n</sub>(ClO<sub>4</sub>)<sub>2n</sub>**

A solution containing 741 mg of Cu(ClO<sub>4</sub>)<sub>2</sub>·6 H<sub>2</sub>O (2.0 × 10<sup>-3</sup> mol) dissolved in 10 mL of DMSO was combined with a solution containing 311 mg of 4,4'-bipyridine (2.0 × 10<sup>-3</sup> mol) dissolved in 10 mL of DMSO. The resulting light blue colored mixture, contained within an evaporating dish, produced small blue blocks of **9** within two to three weeks of solvent evaporation.

### Synthesis of $[\text{Cd}(4,4'\text{-bipy})_3(\text{H}_2\text{O})_2](\text{ClO}_4)_2 \cdot 2(\text{DMSO})$

A solution containing 741 mg of  $\text{Cd}(\text{ClO}_4)_2 \cdot 6 \text{H}_2\text{O}$  ( $2.0 \times 10^{-3}$  mol) dissolved in 10 mL of DMSO was combined with a solution containing 934 mg of 4,4'-bipyridine ( $6.0 \times 10^{-3}$  mol) dissolved in 10 mL of DMSO. The resulting clear mixture, contained within an evaporating dish, produced large blocks within a month of solvent evaporation.

### X-ray Structure Determination

Gray needles of **7** ( $0.17 \times 0.09 \times 0.09 \text{ mm}^3$ ), clear plates of **8** ( $0.04 \times 0.20 \times 0.23 \text{ mm}^3$ ), blue blocks of **9** ( $0.32 \times 0.19 \times 0.19 \text{ mm}^3$ ), and clear blocks of **10** ( $0.38 \times 0.38 \times 0.38 \text{ mm}^3$ ) were selected for X-ray analysis. Each crystal was mounted on a glass fiber under nitrogen gas. The same data collection was used for each sample. Data were collected at 173 K on a Siemens SMART PLATFORM equipped with a CCD area detector and a graphite monochromator utilizing  $\text{MoK}_\alpha$  radiation ( $\lambda = 0.71073 \text{ \AA}$ ). Cell parameters were refined using 3713 reflections for **7**, 4817 reflections for **8** and **9**, and 8192 reflections for **10**. A hemisphere of data (1381 frames) was collected using the  $\omega$ -scan method ( $0.3^\circ$  frame width). The first 50 frames were re-measured at the end of data collection to monitor instrument and crystal stability (maximum correction of  $I$  was  $< 1\%$ ). Absorption corrections by integration were applied based on measured indexed crystal faces.

All structures were solved by the Direct Methods in *SHELLXTL6* and refined using full-matrix squares.<sup>155</sup> The non-H atoms were treated anisotropically, whereas the hydrogen atoms were calculated in ideal positions by riding on their respective carbon atoms. For **7**, a total of 264 parameters were refined using  $F^2$  in the final cycle using 3713 reflections with  $I > 2\sigma(I)$  to yield  $R_1 = 3.00\%$  and  $wR_2 = 6.75\%$ . For **8**, a total of

363 parameters were refined using  $F^2$  in the final cycle using 6069 reflections with  $I > 2\sigma(I)$  to yield  $R_1 = 2.74\%$  and  $wR_2 = 6.71\%$ . For **9**, a total of 199 parameters were refined using  $F^2$  in the final cycle using 3097 reflections with  $I > 2\sigma(I)$  to yield  $R_1 = 2.90\%$  and  $wR_2 = 6.98\%$ . For **10**, the non-H atoms were treated anisotropically, whereas the hydrogen atoms were calculated in ideal positions by riding on their respective carbon atoms except for the the hydrogen atoms from the two water molecules, which were found from a Difference Fourier map and refined freely. The asymmetric unit consists of  $[\text{Cd}(4,4'\text{-bipy})_3(\text{H}_2\text{O})_2]$  units, two perchlorate anions and two DMSO molecules. A sulfur atom from one of the DMSO molecules was disordered and refined in two parts. Their site occupation factors were dependently refined to 0.85(1) for the major part, and consequently 0.15(1) for the minor part. A total of 540 parameters were refined using  $F^2$  in the final cycle using 8601 reflections with  $I > 2\sigma(I)$  to yield  $R_1 = 3.72\%$  and  $wR_2 = 9.90\%$ .

### Description of the Structures

Crystallographic and structural refinement data for **7** and **8** are listed in Table A-1 and for **9** and **10** in Table A-2. Tables of atomic coordinates and thermal displacement parameters are provided in Appendix B.

#### Structure of $[\text{Ni}(\text{terpy})(\text{H}_2\text{O})][\text{Ni}(\text{CN})_4]$

The structure of **7** consists of infinite, one-dimensional linear chains comprised of alternating  $[\text{Ni}(\text{terpy})(\text{H}_2\text{O})]^{2+}$  cations and  $[\text{Ni}(\text{CN})_4]^{2-}$  anions that extend along the  $[1\ 0\ -1]$  direction. Figure A-1 shows a typical chain fragment. In the  $[\text{Ni}(\text{terpy})(\text{H}_2\text{O})]^{2+}$  cations, the local coordination environment of the metal centers is distorted octahedral. The equatorial plane is defined by three nitrogen atoms (N5, N6, and N7) from the terpy

Table A-1. Summary of Crystallographic Data for Compounds **7** and **8**

Sample	<b>7</b>	<b>8</b>
Empirical Formula	C <sub>19</sub> H <sub>13</sub> N <sub>7</sub> Ni <sub>2</sub> O	C <sub>18</sub> H <sub>32</sub> Cl <sub>2</sub> N <sub>2</sub> O <sub>12</sub> S <sub>4</sub> Zn
Formula Weight	472.78	732.97
Space Group	Monoclinic, Cc	Triclinic, P-1
<i>a</i> , Å	15.5712(8)	8.3491(4)
<i>b</i> , Å	11.5546(6)	9.3154(4)
<i>c</i> , Å	11.2428(6)	19.4783(8)
α, deg	90	86.677(1)
β, deg	97.076(1)	89.337(1)
γ, deg	90	89.421(1)
V, Å <sup>3</sup>	2007.4(2)	1512.2(1)
Z	4	2
T, K	173(2)	173(2)
λ(Mo K <sub>α</sub> ), Å	0.71073	0.71073
ρ <sub>calc</sub> , g cm <sup>-3</sup>	1.564	1.610
μ, mm <sup>-1</sup>	1.900	1.323
R <sub>1</sub> <sup>a</sup> (wR <sub>2</sub> <sup>b</sup> )	0.0300 (0.0675)	0.0274 (0.0671)

$${}^a R_1 = \frac{\sum (\| F_0 | - | F_c \|)}{\sum | F_0 |} \quad {}^b wR_2 = \left[ \frac{\sum [w(F_0^2 - F_c^2)^2]}{\sum [w(F_0^2)]} \right]^{1/2}$$

$$S = \left[ \frac{\sum [w(F_0^2 - F_c^2)]}{(n - p)} \right]^{1/2}$$

$$w = 1/[\sigma^2(F_0^2) + (0.0370 * p)^2 + 0.31 * p], p = [\max(F_0^2, 0) + 2 * F_c^2]/3$$

Table A-2. Summary of Crystallographic Data for Compounds **9** and **10**

Sample	<b>9</b>	<b>10</b>
Empirical Formula	C <sub>18</sub> H <sub>32</sub> Cl <sub>2</sub> CuN <sub>2</sub> O <sub>12</sub> S <sub>4</sub>	C <sub>34</sub> H <sub>40</sub> CdCl <sub>2</sub> N <sub>6</sub> O <sub>12</sub> S <sub>2</sub>
Formula Weight	731.14	972.14
Space Group	Trigonal, P3(2)21	Orthorhombic, Pna2(1)
<i>a</i> , Å	10.6492(5)	23.563(2)
<i>b</i> , Å	10.6492(5)	12.7457(8)
<i>c</i> , Å	23.036(2)	13.6674(8)
α, deg	90	90
β, deg	90	90
γ, deg	120	90
V, Å <sup>3</sup>	2262.4(2)	4104.7(4)
Z	3	4
T, K	173(2)	173(2)
λ(Mo K <sub>α</sub> ), Å	0.71073	0.71073
ρ <sub>calc</sub> , g cm <sup>-3</sup>	1.610	1.573
μ, mm <sup>-1</sup>	1.236	0.831
R <sub>1</sub> <sup>a</sup> (wR <sub>2</sub> <sup>b</sup> )	0.0290 (0.0698)	0.0372 (0.0990)

$${}^a R_1 = \frac{\sum (|| F_0 | - | F_c ||)}{\sum | F_0 |} \quad {}^b wR_2 = \left[ \frac{\sum [w(F_0^2 - F_c^2)^2]}{\sum [w(F_0^2)^2]} \right]^{1/2}$$

$$S = \left[ \frac{\sum [w(F_0^2 - F_c^2)^2]}{(n - p)} \right]^{1/2}$$

$$w = 1/[\sigma^2(F_0^2) + (0.0370 * p)^2 + 0.31 * p], p = [\max(F_0^2, 0) + 2 * F_c^2] / 3$$

ligand and one oxygen atom (O1) from the aqua ligand. The Ni2—N5 and Ni2—N7 bonds (2.11 Å – 2.13 Å) from the peripheral pyridyl moieties of the terpy ligands are longer than the Ni2—N6 bond (2.01 Å) from the central pyridyl group and the Ni2—O1 bond (2.06 Å). The axial coordination sites are filled by the nitrogen atoms from the bridging cyano groups from adjacent  $[\text{Ni}(\text{CN})_4]^{2-}$  anions. Since the axial Ni2—N2 and Ni2—N4 bonds (2.08 Å – 2.09 Å) are of comparable length to the Ni2—O1 bond and Ni2—N6 bond to the central pyridyl moiety of the terpy, the axis of elongation is N7—Ni2—N5 from the peripheral pyridyl nitrogen donors of the terpy. The deviation of Ni2 from ideal octahedral geometry is partly due to the geometric requirements of the sterically bulky terpy ligands. The Ni—O (water) and Ni—N (terpy) bond angles and distances agree with those for other similar Ni-terpy complexes.<sup>263-265</sup>

In the planar  $[\text{Ni}(\text{CN})_4]^{2-}$  anions, the bridging cyano ligands are positioned *trans* to one another. The mean deviation of the Ni(II) ions from the least squares plane, Ni1—C1—C2—C3—C4, is 0.0037 Å. The Ni—C1 and Ni—C4 bonds (1.85 Å) from one pair of terminal and bridging cyano groups are shorter than the other Ni—C2 and Ni—C3 pair (1.89 Å) while, in contrast, the C1—N1 and C4—N4 bonds (1.17 Å) are longer than the C2—N2 and C3—N3 bonds (1.12 Å). Interactions with nearby terpy ligands force the anion to twist, thereby relieving the repulsion felt between the terpy and the terminal cyano groups. This twist forces angles Ni2—N2—C2 of 172.2 ° and Ni1—C2—N2 of 176.2 ° to deviate significantly from the ideal geometry. This repulsion can also be seen in the opening of angle C1—Ni1—C2 to 91.1 °. The Ni—C and C—N bond distances, from both the bridging and terminal cyano groups, in the  $[\text{Ni}(\text{CN})_4]^{2-}$  group are typical of those found in other similar trans-bridging tetracyanonickelate chains.<sup>266,267</sup>

A single chain of **7** is shown in Figure A-1. Within the chains, the distance between two octahedral Ni(II) ions is 10.149 Å while the distance between octahedral and planar metal centers is 5.075 Å. Note the regular alternation in regards to the relative positions of both the  $[\text{Ni}(\text{CN})_4]^{2-}$  groups and terpy ligands along the chain. Adjacent  $[\text{Ni}(\text{CN})_4]^{2-}$  groups are oriented nearly perpendicular (86.3 °) with respect to one another. The terpy ligands alternate along the chains in an antiparallel fashion with respect to one another.

The packing diagrams of **7** are shown in Figure A-2. Adjacent chains are related by  $\frac{1}{2}$  translation along the crystallographic *a*-, *b*-, and *c*-axes. In the solid, the chains pack to maximize both  $\pi$ -stacking and hydrogen bonding interactions between the chains. The offset  $\pi$ -stacking interactions originate from the overlap of terpy ligands between neighboring chains with a face-to-face distance of  $\sim 3.5$  Å. The protons from the aqua ligands form twin hydrogen bonds (1.88 Å – 1.90 Å) with the terminal nitrogen atoms from monocoordinate cyano group on two adjacent chains.

Ordoenac, *et al.* has published a review of detailing the synthesis, crystal structures, and magnetic properties of one-dimensional tetracyanonickelate complexes.<sup>268</sup>

### Structure of $[\text{Zn}(4,4'\text{-bipy})(\text{DMSO})_4]_n(\text{ClO}_4)_{2n}$

The structure of **8** consists of cationic one-dimensional  $[\text{Zn}(4,4'\text{-bipy})(\text{DMSO})_4]^{2+}$  chains and  $\text{ClO}_4^-$  anions. The local coordination environment surrounding a typical Zn(II) ion is depicted in Figure A-3. The metal center is six-coordinate and the coordination sphere consists of two pyridyl nitrogen donors from two 4,4'-bipyridine

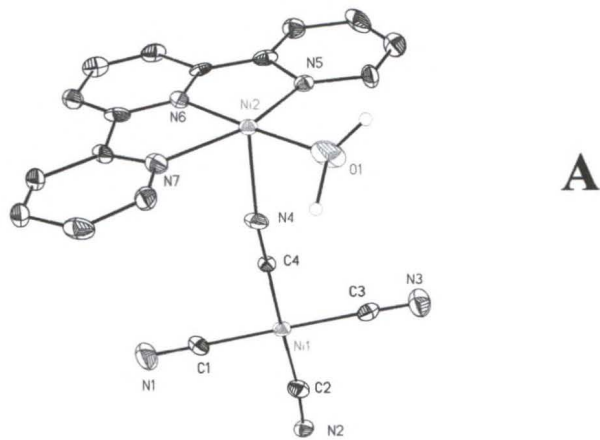
**A****B**

Figure A-1.  $[\text{Ni}(\text{terpy})(\text{H}_2\text{O})][\text{Ni}(\text{CN})_4]$ . A) A typical chain fragment. B) A one-dimensional linear chain. All aromatic hydrogen atoms have been omitted from the top figure for clarity. All non-hydrogen atoms are represented by thermal ellipsoids drawn to encompass 30 % of electron density.

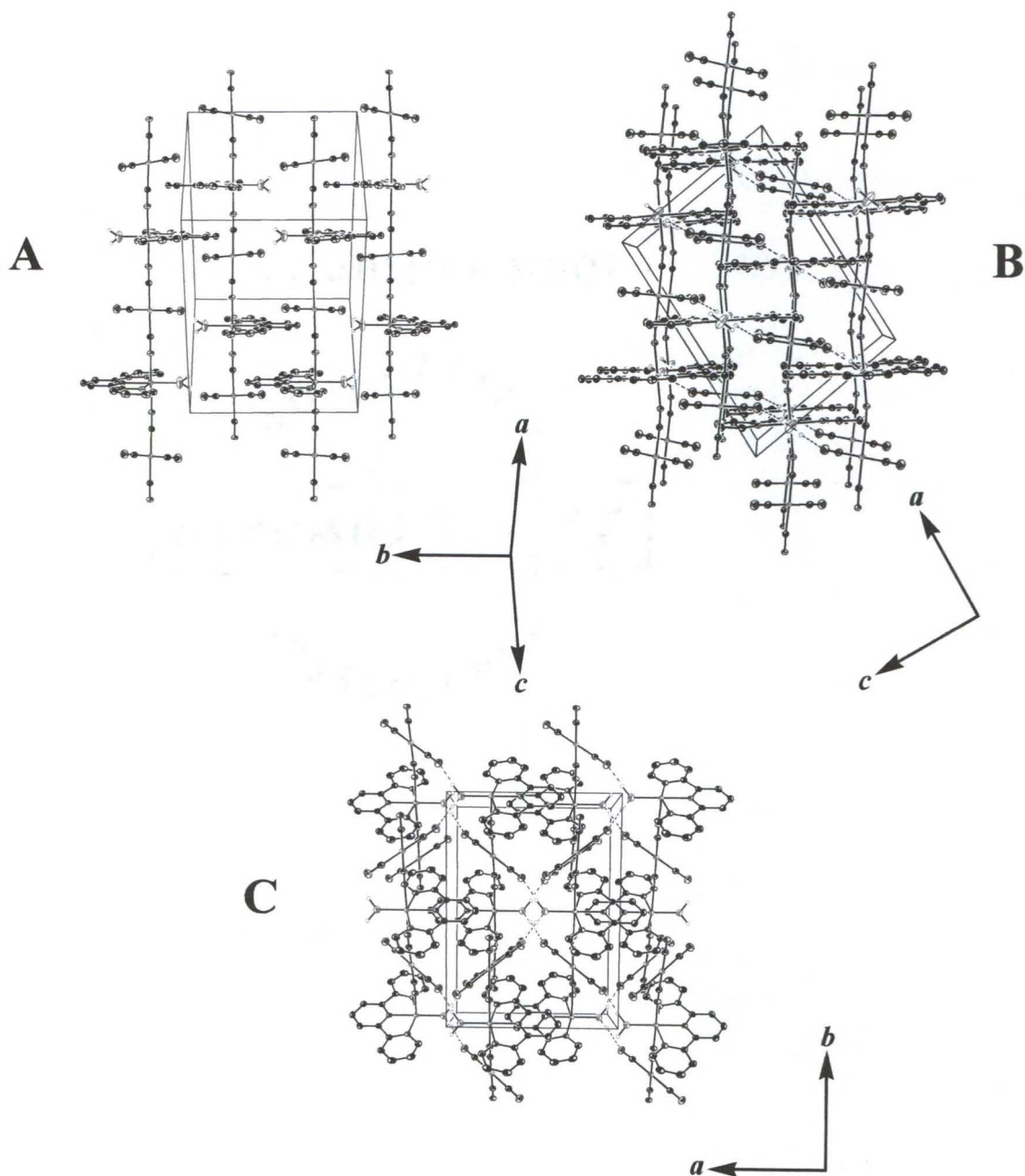


Figure A-2.  $[\text{Ni}(\text{terpy})(\text{H}_2\text{O})][\text{Ni}(\text{CN})_4]$ . A) The structure of **7** along the  $[1\ 0\ -1]$  direction. B) The structure within the crystallographic  $ac$ -plane. C) The structure within the crystallographic  $ab$ -plane. For clarity, the aromatic hydrogen atoms have been omitted.

ligands and four oxygen atoms from ligated DMSO molecules. The Zn—O1, Zn—O1A, Zn—N1, and Zn—N1A bond distances are all similar (2.13 Å) but slightly shorter than the Zn—O2 and Zn—O2A bonds (2.15 Å). The local coordination geometry of ZnN<sub>2</sub>O<sub>4</sub> adopts an axially elongated octahedral geometry with two pyridyl nitrogen atoms (Zn1 and Zn1A) and two DMSO oxygen atoms (O1 and O1A) occupying the equatorial positions while the remaining two DMSO oxygen atoms (O2 and O2A) fill the axial sites. The bipy ligands are coordinated to *trans* to one another other. The pyridyl rings the bipy ligands are not coplanar but twisted along the central C—C bond at an angle of 38.0° with respect to each another. All Zn—O and Zn—N bond angles and distances are consistent with those reported for other similar Zn-bipy complexes.<sup>133,269</sup>

The molecular structure of **8** consists of infinite, one-dimensional chains that extend along the [1 -1 1] direction. The *trans*-coordination of the bridging bipy ligands results in a linear configuration of the chains, shown in Figure A-3. The distance between any two adjacent Zn(II) ions within a chain is 11.32 Å. Packing diagrams of **8** are shown in Figures A-4. In the solid, adjacent chains are related by a single translation along the *a*-axis and ½ of a “step” along both *b* and *c*. The methyl groups from the DMSO ligands on adjacent chains interact with each other in a side-by-side fashion. The perchlorate counterions reside in the void spaces present between the chains in close proximity to methyl groups of the DMSO ligands. However, no S—O contacts between the perchlorate oxygen atoms and the DMSO sulfur atoms are observed.

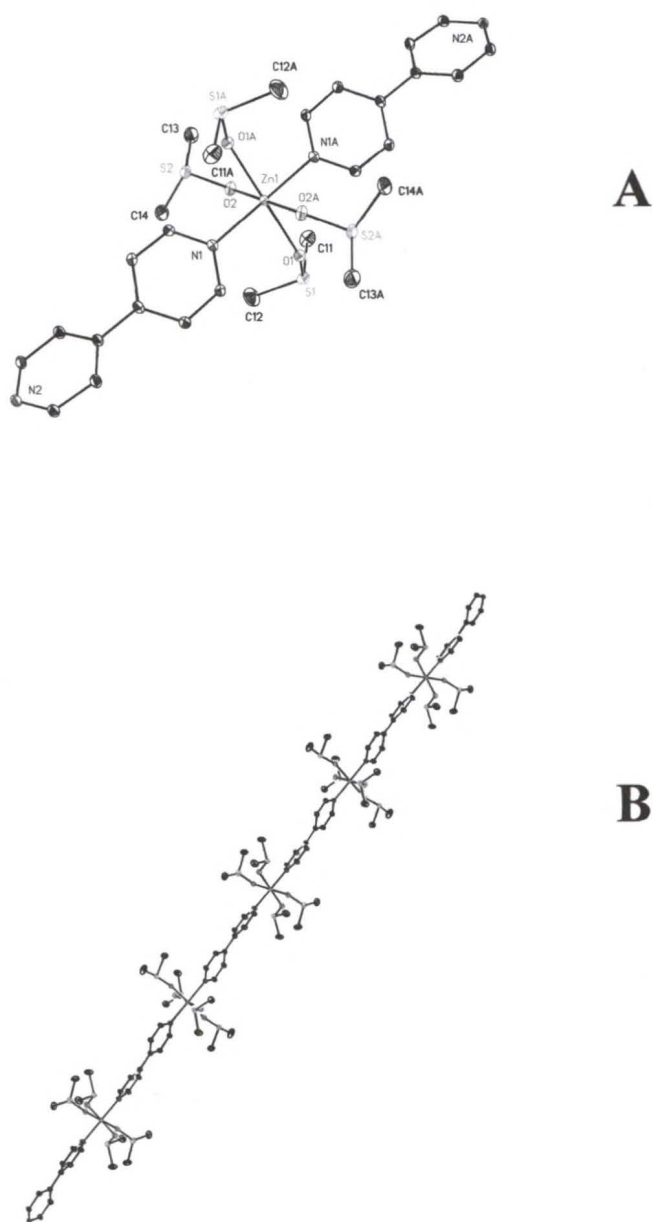


Figure A-3.  $[\text{Zn}(4,4'\text{-bipy})(\text{DMSO})_4]_n(\text{ClO}_4)_{2n}$ . A) A typical chain fragment. B) A one-dimensional linear chain. All hydrogen atoms have been omitted from both figures for clarity. All non-hydrogen atoms are represented by thermal ellipsoids drawn to encompass 30 % of electron density.

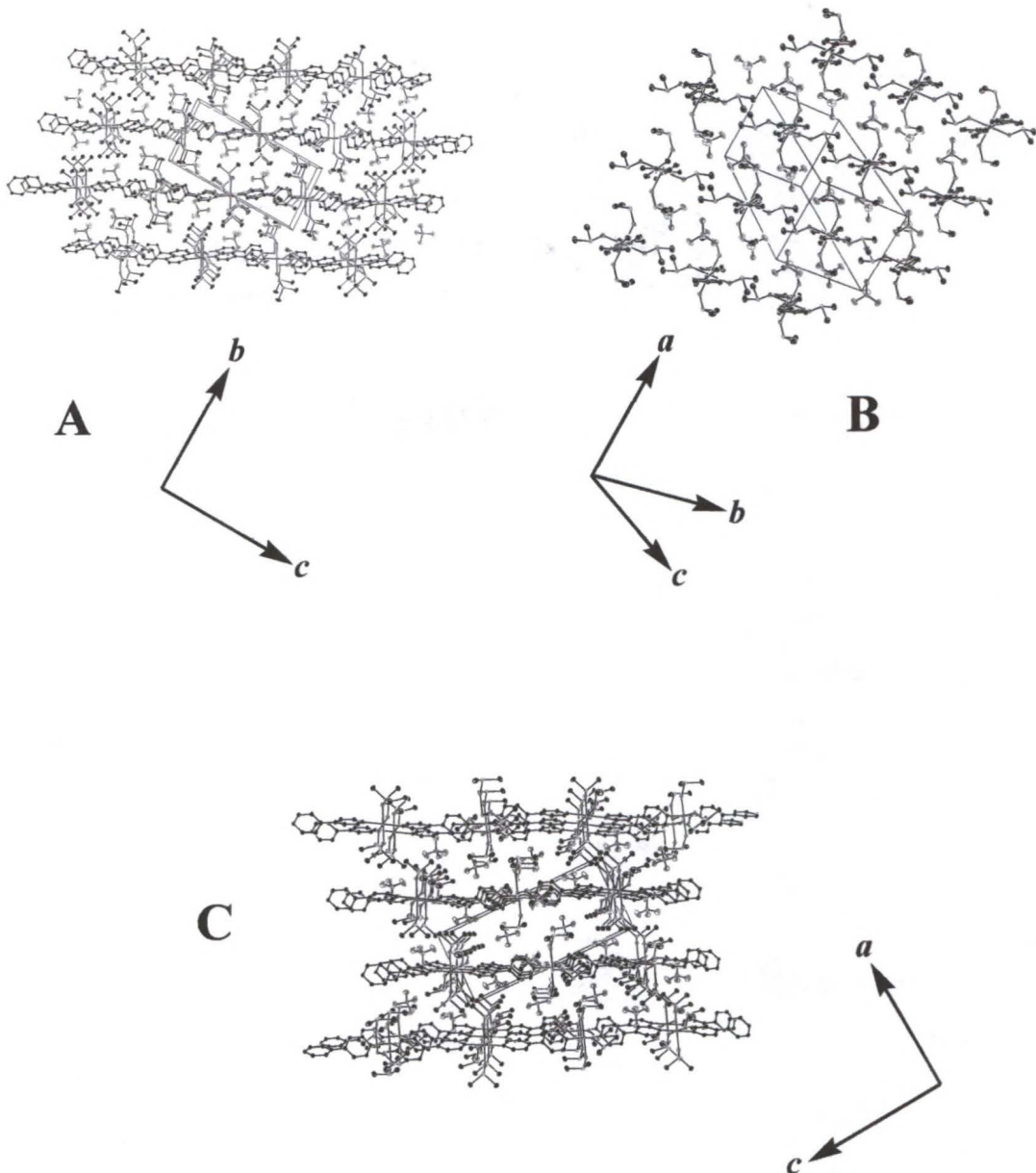


Figure A-4.  $[\text{Zn}(4,4'\text{-bipy})(\text{DMSO})_4]_n(\text{ClO}_4)_{2n}$ . A) The structure within the crystallographic  $bc$ -plane. B) The structure along the  $[1 -1 1]$  direction. C) The structure within the crystallographic  $ac$ -plane. For clarity, the hydrogen atoms have been omitted.

### Structure of $[\text{Cu}(4,4'\text{-bipy})(\text{DMSO})_4]_n(\text{ClO}_4)_{2n}$

The structure of **9** consists of cationic one-dimensional  $[\text{Cu}(4,4'\text{-bipy})(\text{DMSO})_4]^{2+}$  chains and  $\text{ClO}_4^-$  anions. The local coordination environment surrounding a typical Cu(II) ion is depicted in Figure A-5. The metal center is six-coordinate and the coordination sphere consists of two pyridyl nitrogen donors from two 4,4'-bipyridine ligands and four oxygen atoms from ligated DMSO molecules. The Cu—O2, Cu—O2A, Cu—N1, and Cu—N1A bond distances are all similar (2.01 Å) but shorter than the Cu—O1 and Cu—O1A bonds (2.30 Å). The  $\text{CuN}_2\text{O}_4$  unit therefore adopts an axially elongated geometry with two pyridyl nitrogen atoms (N1 and N1A) and two DMSO oxygen atoms (O2 and O2A) occupying the equatorial positions while the remaining two DMSO oxygen atoms (O1 and O1A) fill the axial sites. Not only are the bipy ligands coordinated *cis* to one another but are positioned at nearly right angles with respect to one another as well (90.9 °). The pyridyl rings of the bipy ligands are not coplanar but twisted along the central C—C bond at an angle of 17.1 ° with respect to each other. All Cu—O and Cu—N bond angles and distances are consistent with those reported for other similar Cu-bipy complexes.<sup>92,69,104</sup>

The molecular structure of **9** consists of infinite, one-dimensional chains that extend along the crystallographic *c*-axis. The *cis*-coordination of the bipy ligands that bridge the metal centers results in a zig-zag configuration of the chains, shown in Figure A-5. The distance between any two adjacent Cu(II) ions within a chain is approximately *c*/2 units. Packing diagrams of **9** are shown in Figures A-6. In the solid, adjacent chains are related by single translations along both the *a*- and *b*-axes. The chains pack in registry with respect to one another along both the *a*- and *b*-axes. The methyl groups

from the DMSO ligands on adjacent chains interact with each other in a side-by-side fashion. The perchlorate counterions reside in the void spaces present between the chains in close proximity to the methyl groups of the DMSO ligands. The oxygen atoms of the perchlorate anions interact with the sulfur atoms from the DMSO ligands with S—Cl contacts of 3.22 Å.

### Structure of $[\text{Cd}(4,4'\text{-bipy})_3(\text{H}_2\text{O})_2](\text{ClO}_4)_2 \cdot 2(\text{DMSO})$

The structure of **10** consists of one-dimensional cationic  $[\text{Cd}(4,4'\text{-bipy})_3(\text{H}_2\text{O})_2]^{2+}$  chains that pack to form layered sheets in the solid. The local coordination environment surrounding a typical Cd(II) ion is depicted in Figure A-7. The metal center is six-coordinate and the coordination sphere consists of four pyridyl nitrogen donors, one from four 4,4'-bipyridine ligands and two oxygen atoms from aqua ligands. The four nitrogen atoms define the equatorial plane and the oxygen atoms occupy the axial sites. Both Cd—O bond distances are unequal (Cd—O1 = 2.30 Å and Cd—O2 = 2.32 Å) and one Cd—(bridging)N bond (Cd—N2' = 2.38 Å) is longer than the other three Cd—N bonds (Cd—N1, Cd—N2, and Cd—N3 = 2.34 Å). Since the Cd—O bonds are shorter than the Cd—N bonds, the  $\text{CdN}_4\text{O}_2$  unit adopts an axially compressed geometry with the compression axis O2—Cd—O1 from the aqua ligands. All Cu—O and Cu—N bond angles and distances are consistent with those reported for other similar Cu-bipy complexes.<sup>44,133</sup>

Two of the bipy ligands, coordinated *trans* with respect to one another, bridge the Cd(II) ions to form infinite one-dimensional linear chains that extend along the crystallographic *a*-axis. A single chain is depicted in Figure A-7. The Cd—Cd distance

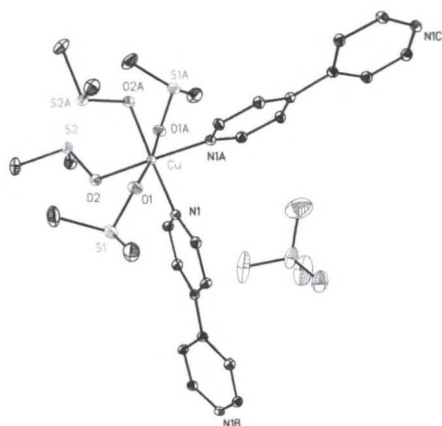
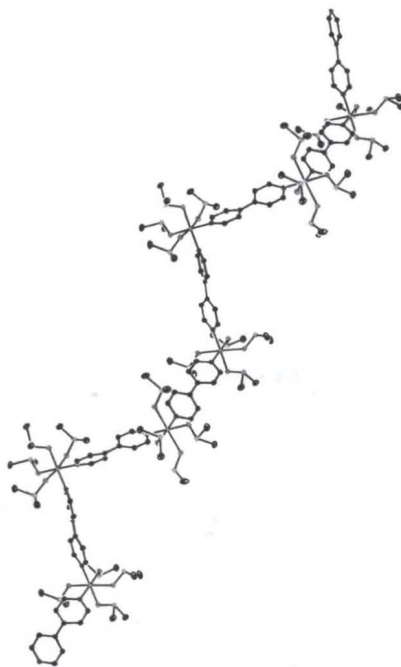
**A****B**

Figure A-5.  $[\text{Cu}(4,4'\text{-bipy})(\text{DMSO})_4]_n(\text{ClO}_4)_{2n}$ . A) A typical chain fragment. B) A one-dimensional zig-zag chain. All hydrogen atoms have been omitted for clarity. All non-hydrogen atoms are represented by thermal ellipsoids drawn to encompass 30% of electron density.

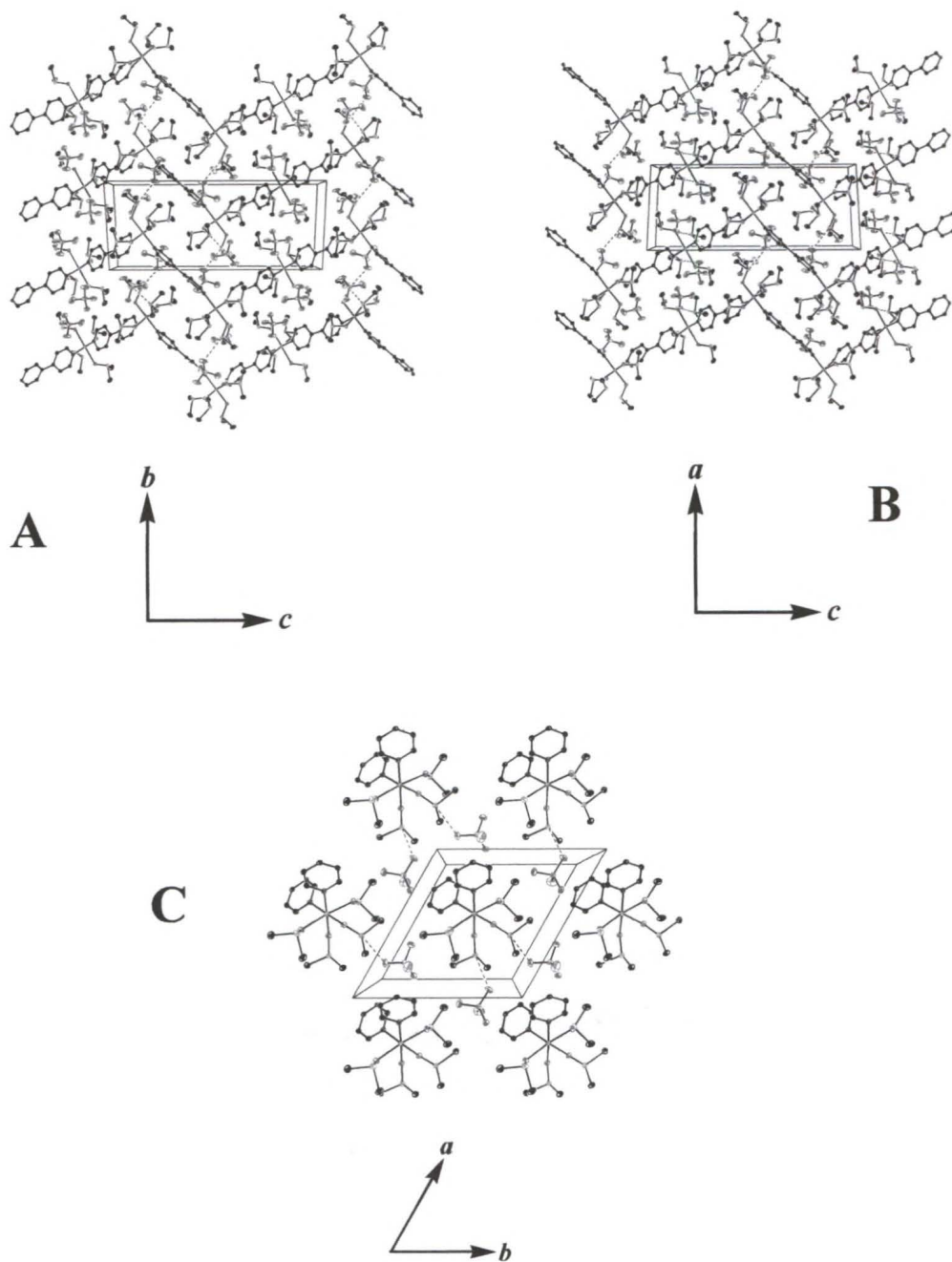


Figure A-6.  $[\text{Cu}(4,4'\text{-bipy})(\text{DMSO})_4]_n(\text{ClO}_4)_{2n}$ . A) The structure within the crystallographic  $bc$ -plane. B) The structure within the crystallographic  $ac$ -plane. C) The structure within the crystallographic  $ab$ -plane. For clarity, the hydrogen atoms have been omitted.

along a chain is  $a/2$  units (11.78 Å). From each bridging bipy ligand, the pyridyl rings are not coplanar but twisted along the central C—C bond at an angle of 45.1 ° with respect to each other. The metal:bipy stoichiometry in **10** is 1:3 since the bipy ligands perpendicular to the chains are monocoordinate. A twist angle of 29.4 ° is observed along the central C—C bond between the pyridyl ligands in these monodentate bipy's as well. The plane defined by Cd(II) and the four pyridyl nitrogen atoms (Cd—N1—N2—N2'—N3) is not coplanar with analogous adjacent planes along the chains but twisted 42.8 ° with respect to one another. Thus the monocoordinate bipy ligands are not aligned in registry but twisted in an alternating criss-cross fashion along the chains, as depicted by a top view perspective of a chain fragment in Figure A-7.

The Cd-bipy chains are juxtaposed in a side-by-side fashion to form two-dimensional sheets within the crystallographic  $ab$ -plane. A typical sheet is shown in Figure A-8. Within each sheet, the chain are spaced  $b$  units apart. In addition to packing forces, the sheets are sustained through a combination of hydrogen bonding interactions between the protons of the coordinated water molecules with the terminal nitrogen atoms from the monodentate bipy ligands on adjacent chains (N—H contacts 2.81 Å), and offset  $\pi$ -stacking between the monocoordinate bipy ligands on adjacent chains. The face-to-face distance between these overlapping bipy groups from adjacent chains is about 3.7 Å. The characteristic packing motif of the Cd-bipy chains produces hydrophobic, rectangular cavities within the sheets. Each cavity is defined by four cadmium ions at the corners and along the sides by the faces of two bridging bipy's along the chains and the edges of four bipy's perpendicular to the chains. The dimensions of the rectangles are  $a/2 \times b$  and, if the Van der Waals radii of the carbon atoms from the bipy ligands are

approximated as 1.7 Å, the effective size of the cavities is approximately 10.1 Å x 11.0 Å.

As shown in Figure A-8, the sheets pack along the crystallographic *c*-axis to form a layered solid-state structure. Note the criss cross arrangement of the bipy pairs perpendicular to the chains extending along the *a*-axis. The sheets are not packed in registry but related by  $\frac{1}{4}$  translation along the *a*-axis and  $\frac{1}{2}$  translation along both the *b*- and *c*-axes. This packing motif aligns the hydrophobic cavities within the sheets to form oblique channels that extend along the [4 2 2] direction throughout the solid. The void space within the hydrophobic pores and between the sheets is not empty but occupied by guest molecules and counterions acting to prevent self-inclusion from neighboring sheets. Specifically, two perchlorate anions and two DMSO molecules occupy each rectangular portion of a channel. Each face of the sheet is associated with one perchlorate and one DMSO per Cd(II) ion in the vicinity of the hydrophobic cavities. The perchlorate counterions are positioned near the center of the cavity while the DMSO molecules are positioned near the corners. One DMSO guest is disordered about the S atom. The oxygen atoms of each DMSO guest forms hydrogen bonds with nearby protons from the aqua ligands (1.6 Å – 1.9 Å), not interacting with the bipy nitrogens, and the hydrogen atoms with neighboring monocoordinate bipy ligands (2.4 Å – 2.5 Å). The oxygen atoms from each perchlorate interact with the hydrogen atoms from nearby bridging and monocoordinate bipy ligands (2.4 Å – 2.5 Å) and hydrogen atoms from neighboring DMSO ligands (2.3 Å).

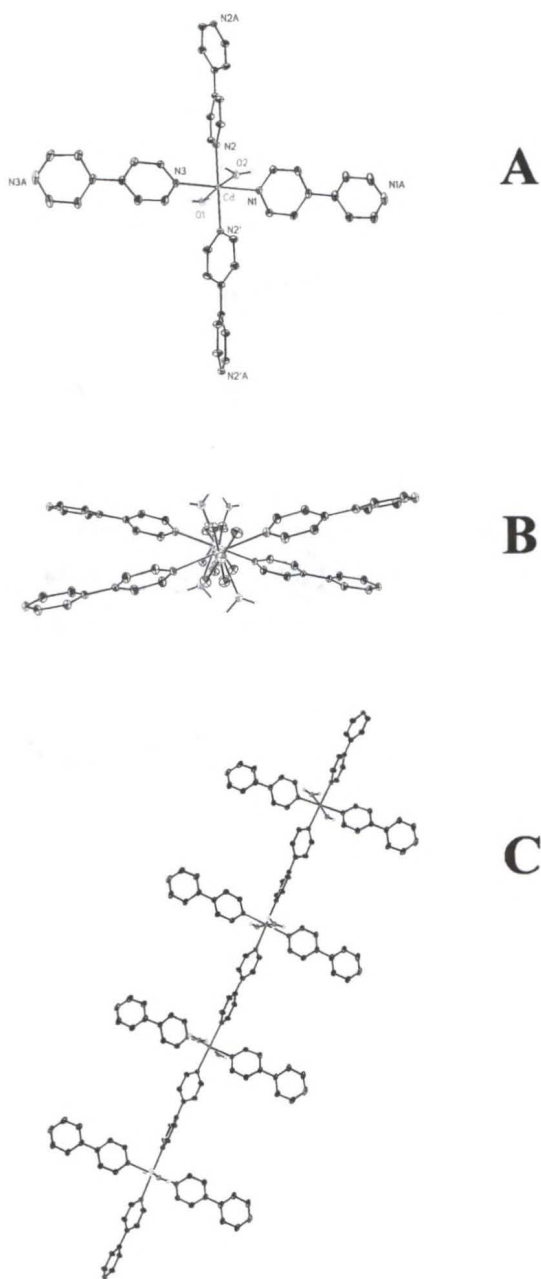


Figure A-7.  $[\text{Cd}(4,4'\text{-bipy})_3(\text{H}_2\text{O})_2](\text{ClO}_4)_2 \cdot 2(\text{DMSO})$ . A) The local coordination sphere of Cd(II). B) A one-dimensional zig-zag chain viewed from the top. C) A chain viewed from the side. All hydrogen atoms except the aqua protons have been omitted from the both figures for clarity. All non-hydrogen atoms are represented by thermal ellipsoids drawn to encompass 30 % of electron density.

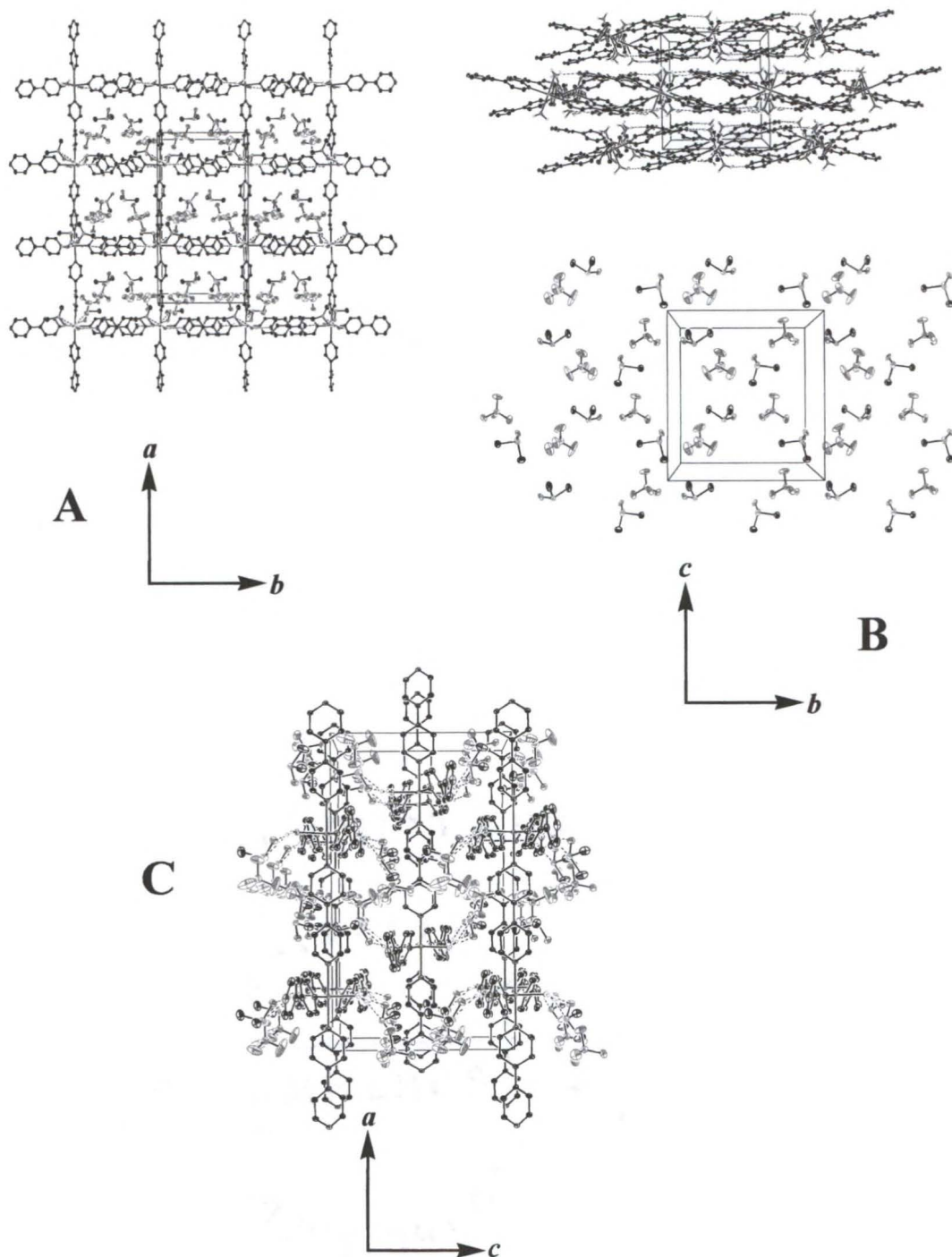


Figure A-8.  $[\text{Cd}(4,4'\text{-bipy})_3(\text{H}_2\text{O})_2](\text{ClO}_4)_2 \cdot 2(\text{DMSO})$ . The structure within the crystallographic  $ab$ -plane. B) The structure within the crystallographic  $bc$ -plane, with the guests shown separately. C) The structure within the crystallographic  $ac$ -plane. For clarity, the hydrogen atoms except for water protons have been omitted.

APPENDIX B  
TABLES OF ATOMIC COORDINATES AND BOND ANGLES AND DISTANCES

Table B-1. Atomic coordinates ( $\times 10^4$ ) and equivalent isotropic displacement parameters ( $\text{\AA}^2 \times 10^3$ ) for compound **1**.  $U_{eq}$  is defined as one third of the trace of the orthogonalized  $U_{ij}$  tensor.

Atom	$x$	$y$	$z$	$U_{eq}$
Ni	0	4210(1)	7500	21(1)
O1	-1071(2)	4207(2)	7113(1)	27(1)
N11	0	2345(3)	7500	26(1)
N11'	0	-3877(3)	7500	23(1)
C11	636(2)	1733(3)	7426(2)	33(1)
C12	659(2)	528(3)	7423(2)	36(1)
C13	0	-107(4)	7500	31(1)
C14	0	-1411(4)	7500	28(1)
C15	643(2)	-2054(3)	7670(2)	31(1)
C16	620(2)	-3258(3)	7664(2)	29(1)
N21	-448(2)	4164(2)	8285(1)	24(1)
N21'	-1216(2)	4755(3)	11094(1)	41(1)
C21	-146(2)	3430(3)	8665(2)	30(1)
C22	-320(2)	3463(3)	9207(2)	32(1)
C23	-831(2)	4295(3)	9385(1)	26(1)
C24	-1165(2)	5023(4)	8987(2)	35(1)
C25	-960(2)	4929(3)	8450(2)	31(1)
C26	-985(2)	4432(3)	9975(1)	29(1)
C27	-652(2)	3705(4)	10374(2)	36(1)
C28	-774(2)	3906(4)	10921(2)	38(1)
C29	-1559(3)	5424(5)	10709(2)	53(1)
C30	-1457(3)	5302(5)	10154(2)	45(1)
N31	-2649(6)	3081(9)	8550(4)	41(2)
N31'	-2541(6)	2261(11)	11421(4)	48(2)

Table B-1. Continued

Atom	<i>x</i>	<i>y</i>	<i>z</i>	<i>U</i> <sub>eq</sub>
C31	-2255(7)	2137(11)	8769(5)	38(3)
C32	-2230(7)	1928(10)	9328(5)	40(3)
C33	-2570(6)	2690(9)	9691(4)	25(2)
C34	-2952(7)	3620(13)	9448(5)	43(4)
C35	-2977(6)	3760(11)	8918(4)	42(3)
C36	-2568(7)	2561(11)	10289(5)	42(3)
C37	-2119(10)	1666(16)	10544(7)	66(6)
C38	-2151(10)	1554(16)	11158(7)	73(5)
C39	-2938(11)	3048(15)	11165(7)	77(6)
C40	-2968(9)	3203(12)	10611(6)	57(4)
Cl1	-1640(5)	7980(8)	8699(4)	92(3)
O11	-1890(15)	7709(17)	9214(8)	123(10)
O12	-1718(10)	9273(15)	8635(8)	80(5)
O13	-2110(20)	7530(40)	8387(12)	210(20)
O14	-768(10)	7752(14)	8811(10)	81(6)
Cl2	-807(13)	8933(17)	9188(7)	125(5)
Cl3	-1262(6)	8528(7)	8884(3)	86(2)
O31	-390(30)	8390(30)	8814(13)	220(20)
O32	-1350(60)	8570(90)	9445(15)	520(80)
O33	-1180(20)	9650(20)	8953(18)	203(19)
O34	-1934(19)	7360(20)	8257(9)	131(13)
Cl4	-323(9)	9430(14)	9215(5)	105(4)
N41	1201(10)	11160(18)	9041(8)	120(8)
C41	1382(11)	11340(18)	9594(8)	110(9)
C42	918(15)	10880(20)	9984(6)	124(11)
C43	272(14)	10240(20)	9820(8)	890(190)
C44	90(11)	10060(20)	9267(9)	100(8)
C45	555(11)	10520(17)	8877(6)	91(7)
O2	-2469(19)	3870(20)	7553(15)	73(9)
O2'	-2401(11)	3780(20)	7508(7)	110(9)
O3	-2677(19)	6120(30)	8024(14)	148(10)

Table B-2. Atomic coordinates ( $\times 10^4$ ) and equivalent isotropic displacement parameters ( $\text{\AA}^2 \times 10^3$ ) for compound **2**.  $U_{eq}$  is defined as one third of the trace of the orthogonalized  $U_{ij}$  tensor.

Atom	<i>x</i>	<i>y</i>	<i>z</i>	$U_{eq}$
Co	0	4224(1)	7500	22(1)
O1	-1068(2)	4244(2)	7125(1)	28(1)
N11	0	2331(3)	7500	28(1)
N11'	0	-3838(3)	7500	24(1)
C11	635(2)	1727(3)	7420(2)	34(1)
C12	658(2)	529(3)	7416(2)	38(1)
C13	0	-99(4)	7500	33(1)
C14	0	-1394(4)	7500	30(1)
C15	645(2)	-2022(3)	7658(2)	33(1)
C16	623(2)	-3223(3)	7652(1)	29(1)
N21	-461(2)	4164(2)	8303(1)	24(1)
N21'	-1217(2)	4766(3)	11106(1)	41(1)
C21	-160(2)	3439(3)	8679(2)	32(1)
C22	-332(2)	3476(3)	9223(1)	33(1)
C23	-835(2)	4303(3)	9403(1)	27(1)
C24	-1169(2)	5022(4)	9009(2)	36(1)
C25	-968(2)	4926(4)	8473(2)	34(1)
C26	-989(2)	4438(3)	9991(1)	28(1)
C27	-651(2)	3723(3)	10385(2)	37(1)
C28	-776(3)	3929(4)	10932(2)	39(1)
C29	-1560(3)	5432(5)	10725(2)	57(1)
C30	-1463(3)	5305(5)	10171(2)	48(1)
N31	-2633(6)	3059(9)	8558(4)	44(2)
N31'	-2575(6)	2283(10)	11416(4)	47(2)
C31	-2250(7)	2104(10)	8776(4)	39(2)
C32	-2233(6)	1897(8)	9333(4)	38(2)
C33	-2577(5)	2693(9)	9688(3)	25(2)
C34	-2926(6)	3632(12)	9445(5)	45(3)
C35	-2930(7)	3747(12)	8911(5)	49(3)

Table B-2. Continued

Atom	<i>x</i>	<i>y</i>	<i>z</i>	<i>U</i> <sub>eq</sub>
C36	-2576(6)	2557(10)	10285(4)	37(3)
C37	-2103(8)	1721(15)	10545(6)	61(4)
C38	-2147(10)	1610(16)	11148(7)	73(5)
C39	-2994(10)	3053(13)	11162(6)	72(4)
C40	-3011(8)	3193(11)	10596(5)	58(3)
Cl1	-1616(3)	8005(5)	8717(2)	88(2)
O11	-1949(8)	7641(12)	9210(5)	98(4)
O12	-1697(8)	9217(10)	8637(6)	88(4)
O13	-1952(9)	7453(17)	8269(5)	95(5)
O14	-789(7)	7766(10)	8781(7)	78(4)
Cl2	-829(13)	8874(15)	9178(7)	118(5)
O21	-270(40)	8460(50)	8831(15)	210(30)
O22	-1240(50)	8960(100)	9491(16)	360(70)
O23	-1080(20)	9690(20)	9001(18)	140(15)
O24	-170(30)	8800(30)	9646(13)	163(19)
Cl3	-1216(9)	8585(10)	8957(7)	103(3)
Cl4	-343(10)	9341(14)	9176(5)	114(4)
N41	1241(8)	11180(13)	9013(6)	121(6)
C41	1414(8)	11350(14)	9564(6)	124(8)
C42	945(9)	10887(15)	9949(5)	120(8)
C43	304(8)	10255(14)	9784(5)	109(6)
C44	131(7)	10086(13)	9233(6)	95(5)
C45	600(9)	10548(14)	8848(4)	114(7)
O2	-2404(12)	3910(60)	7570(20)	81(7)
O2'	-2427(18)	3690(90)	7490(30)	86(11)
O3	-2703(16)	6130(30)	8026(11)	125(8)
O3'	-2250(20)	7200(30)	8357(15)	121(13)

Table B-3. Atomic coordinates ( $\times 10^4$ ) and equivalent isotropic displacement parameters ( $\text{\AA}^2 \times 10^3$ ) for compound **3**.  $U_{eq}$  is defined as one third of the trace of the orthogonalized  $U_{ij}$  tensor.

Atom	$x$	$y$	$z$	$U_{eq}$
Cu	1845(1)	5923(1)	2992(1)	21(1)
S1	3582(1)	6193(1)	2464(1)	33(1)
C1	4075(4)	7430(6)	2715(2)	72(2)
C2	4237(3)	5081(6)	2527(3)	61(2)
S2	58(1)	6173(1)	3442(1)	28(1)
S2'	-51(6)	5567(9)	2961(4)	45(3)
C3	-464(3)	4871(5)	3456(3)	53(2)
C4	-585(3)	7070(6)	3072(3)	61(2)
O1	3075(2)	5913(3)	2867(1)	33(1)
O2	618(2)	5907(3)	3089(1)	38(1)
N1	1840(2)	7753(2)	3001(2)	20(1)
N1'	1860(3)	14083(2)	3005(2)	22(1)
N2	1588(2)	5906(3)	2209(1)	24(1)
N2'	780(2)	5868(4)	-565(2)	36(1)
N3	2116(2)	5935(3)	3777(1)	22(1)
N3'	3049(3)	5757(4)	6516(2)	44(1)
C11	2404(2)	8365(4)	3213(2)	25(1)
C12	2428(2)	9600(4)	3223(2)	24(1)
C13	1844(3)	10250(2)	3024(2)	20(1)
C14	1262(2)	9624(4)	2818(2)	23(1)
C15	1281(2)	8376(4)	2804(2)	23(1)
C16	1853(3)	11582(2)	3021(2)	20(1)
C17	1387(2)	12234(4)	3296(2)	25(1)
C18	1410(2)	13473(4)	3284(2)	25(1)
C19	2306(2)	13451(4)	2734(2)	26(1)
C20	2332(2)	12213(4)	2741(2)	25(1)
C21	1879(2)	6696(4)	1895(2)	27(1)
C22	1733(2)	6718(4)	1357(2)	30(1)
C23	1280(2)	5888(4)	1116(2)	25(1)

Table B-3. Continued

Atom	<i>x</i>	<i>y</i>	<i>z</i>	<i>U</i> <sub>eq</sub>
C24	982(3)	5069(4)	1436(2)	33(1)
C25	1149(3)	5108(4)	1975(2)	32(1)
C26	1109(3)	5889(4)	536(2)	27(1)
C27	1486(2)	6558(4)	204(2)	34(1)
C28	1309(3)	6522(4)	-337(2)	37(1)
C29	422(3)	5218(5)	-242(2)	38(1)
C30	558(3)	5204(4)	298(2)	34(1)
C31	2676(2)	5308(4)	3980(2)	25(1)
C32	2880(2)	5290(4)	4510(2)	28(1)
C33	2509(2)	5926(3)	4859(2)	23(1)
C34	1932(2)	6590(4)	4642(2)	26(1)
C35	1755(2)	6571(4)	4111(2)	25(1)
C36	2697(2)	5876(4)	5431(2)	26(1)
C37	3056(3)	4901(4)	5657(2)	31(1)
C38	3214(3)	4889(5)	6199(2)	39(1)
C39	2721(3)	6699(5)	6297(2)	45(1)
C40	2526(3)	6805(4)	5762(2)	35(1)
N4	40(2)	2178(5)	6813(2)	49(1)
N4'	-1176(3)	2717(5)	4107(2)	62(2)
C41	225(4)	1445(6)	6458(2)	64(2)
C42	2(4)	1496(6)	5922(2)	61(2)
C43	-452(3)	2386(5)	5742(2)	41(1)
C44	-650(3)	3181(7)	6117(2)	67(2)
C45	-384(3)	3039(7)	6631(2)	69(2)
C46	-707(3)	2499(5)	5179(2)	44(1)
C47	-401(3)	1830(6)	4791(2)	55(1)
C48	-660(4)	2006(6)	4278(2)	63(2)
C49	-1472(3)	3337(6)	4479(2)	59(2)
C50	-1253(3)	3263(5)	5006(2)	49(1)
N5	263(3)	-2253(6)	6719(2)	68(2)
N5'	1040(7)	-175(11)	4267(5)	63(3)

Table B-3. Continued.

Atom	<i>x</i>	<i>y</i>	<i>z</i>	<i>U</i> <sub>eq</sub>
N5''	296(8)	-482(14)	4023(6)	66(4)
C51	-206(3)	-2415(5)	6318(2)	57(1)
C52	-113(3)	-2100(5)	5820(2)	51(1)
C53	508(3)	-1560(5)	5693(2)	46(1)
C54	1023(4)	-1422(6)	6117(2)	63(1)
C55	865(4)	-1788(6)	6613(3)	68(2)
C56	728(5)	-1145(7)	5201(3)	36(2)
C57	327(5)	-1444(8)	4739(4)	48(2)
C58	497(7)	-969(11)	4274(5)	60(3)
C59	1425(5)	63(8)	4654(4)	51(2)
C60	1301(5)	-392(8)	5148(4)	47(2)
C56'	384(7)	-1182(9)	5092(4)	35(2)
C57'	-206(8)	-1384(12)	4749(5)	54(3)
C58'	-222(9)	-1036(14)	4222(6)	69(4)
C59'	828(14)	-400(20)	4276(8)	63(6)
C60'	964(7)	-613(12)	4868(5)	50(3)
Cl1	-2149(2)	-4676(2)	6638(1)	41(1)
O11	-1880(3)	-3501(5)	6564(3)	62(2)
O12	-1712(10)	-5445(17)	7006(9)	182(10)
O13	-2839(4)	-4567(7)	6819(3)	60(2)
O14	-2202(4)	-5305(6)	6150(2)	70(2)
Cl2	-1794(6)	-4586(6)	6838(2)	66(2)
O21	-1679(13)	-5310(20)	7039(7)	51(4)
O22	-2650(19)	-4920(30)	6800(14)	116(12)
O23	-1880(20)	-3660(30)	7112(15)	186(13)
O24	-1546(18)	-4550(30)	6327(13)	165(11)
Cl3	-1562(3)	-2906(5)	4436(2)	47(1)
O31	-1748(12)	-2457(16)	4896(5)	92(7)
O32	-2048(11)	-3575(17)	4123(7)	138(7)
O33	-1298(6)	-1987(9)	4135(4)	80(4)
O34	-1033(6)	-3696(12)	4653(7)	93(4)

Table B-3. Continued

Atom	<i>x</i>	<i>y</i>	<i>z</i>	<i>U</i> <sub>eq</sub>
C14	-1834(4)	-3239(5)	4414(2)	45(1)
O41	-2438(5)	-4018(10)	4386(4)	73(3)
O42	-1929(8)	-2424(10)	3996(4)	91(5)
O43	-1934(10)	-2597(18)	4860(7)	97(7)
O44	-1241(7)	-3935(9)	4321(6)	78(4)

Table B-4. Atomic coordinates ( $\times 10^4$ ) and equivalent isotropic displacement parameters ( $\text{\AA}^2 \times 10^3$ ) for compound 4.  $U_{eq}$  is defined as one third of the trace of the orthogonalized  $U_{ij}$  tensor.

Atom	$x$	$y$	$z$	$U_{eq}$
Cu	7896(1)	6007(1)	45(1)	34(1)
N1	6698(3)	7368(2)	-391(1)	35(1)
N2	9489(3)	4598(2)	422(1)	30(1)
N3	9590(3)	4524(2)	869(1)	35(1)
N4	9643(5)	4436(2)	1286(1)	60(1)
N5	5113(4)	6119(2)	514(1)	48(1)
N6	3307(3)	6785(2)	484(1)	31(1)
N7	1475(4)	7389(2)	467(1)	48(1)
C1	5310(30)	7176(14)	-772(7)	44(4)
C2	4485(16)	8226(7)	-1068(3)	39(2)
C3	4967(12)	9424(5)	-919(3)	34(1)
C4	6390(17)	9570(7)	-486(3)	44(2)
C5	7240(20)	8587(10)	-224(3)	36(2)
C1'	5490(30)	7070(20)	-852(9)	37(3)
C2'	4511(19)	7828(9)	-1197(4)	36(2)
C3'	4985(12)	9079(8)	-1134(3)	33(1)
C4'	6330(20)	9429(8)	-704(4)	42(2)
C5'	7080(40)	8505(17)	-376(4)	49(3)
C6	4038(9)	10564(4)	-1207(2)	45(1)
C7	1965(8)	10328(5)	-1600(2)	43(1)
C6'	4070(10)	9992(5)	-1525(2)	42(2)
C7'	2139(14)	10914(8)	-1344(3)	59(2)
C8	987(5)	11616(3)	-1803(1)	62(1)
C9	3019(4)	12330(2)	-2066(1)	44(1)
C10	3887(5)	11945(2)	-2520(1)	50(1)
C11	5797(5)	12570(3)	-2758(1)	61(1)
C12	6878(6)	13601(3)	-2552(1)	67(1)
C13	6061(7)	14015(3)	-2104(1)	75(1)
C14	4146(6)	13378(3)	-1861(1)	62(1)

Table B-5. Bond lengths [ $\text{\AA}$ ] and angles [ $^\circ$ ] for compound 4.

Bond	Distance /Angle
Cu-N5	1.9568(18)
Cu-N1	1.9747(17)
Cu-N2#1	1.9934(16)
Cu-N2	1.9968(15)
N1-C5'	1.243(18)
N1-C1	1.258(18)
N1-C5	1.416(10)
N1-C1'	1.42(2)
N2-N3	1.212(2)
N2-Cu#1	1.9934(16)
N3-N4	1.134(2)
N5-N6	1.184(2)
N6-N7	1.155(2)
C1-C2	1.447(16)
C2-C3	1.374(7)
C3-C4	1.378(7)
C3-C6	1.526(7)
C4-C5	1.343(15)
C1'-C2'	1.33(2)
C2'-C3'	1.382(9)
C3'-C4'	1.394(9)
C3'-C6'	1.514(8)
C4'-C5'	1.38(2)
C6-C7	1.515(7)
C7-C8	1.574(5)
C6'-C7'	1.506(9)
C7'-C8	1.561(7)
C8-C9	1.504(4)
C9-C14	1.382(4)
C9-C10	1.385(3)
C11-C12	1.359(4)

Table B-5. Continued

Bond	Distance /Angle
C10-C11	1.377(4)
C13-C14	1.391(5)
C12-C13	1.372(5)
N5-Cu-N1	96.60(7)
N5-Cu-N2#1	164.38(8)
N1-Cu-N2#1	94.20(7)
N5-Cu-N2	91.20(7)
N1-Cu-N2	172.19(7)
N2#1-Cu-N2	78.08(7)
C5'-N1-C1	106.1(9)
C5'-N1-C5	16.8(7)
C1-N1-C5	121.2(8)
C5'-N1-C1'	108.7(10)
C1-N1-C1'	9.0(18)
C5-N1-C1'	124.8(9)
C5'-N1-Cu	131.7(6)
C1-N1-Cu	122.1(7)
C5-N1-Cu	116.3(4)
C1'-N1-Cu	118.8(9)
N3-N2-Cu#1	126.92(13)
N3-N2-Cu	124.37(14)
Cu#1-N2-Cu	101.92(7)
N4-N3-N2	178.5(2)
N6-N5-Cu	126.36(15)
N7-N6-N5	176.4(2)
N1-C1-C2	118.7(12)
C3-C2-C1	121.6(9)
C2-C3-C4	116.5(6)
C2-C3-C6	123.7(6)
C4-C3-C6	119.8(6)
C5-C4-C3	121.3(7)

Table B-5. Continued

Bond	Distance /Angle
C4-C5-N1	120.3(7)
C2'-C1'-N1	129.0(19)
C1'-C2'-C3'	116.7(12)
C2'-C3'-C6'	119.8(7)
C4'-C3'-C6'	123.4(7)
C5'-C4'-C3'	117.9(9)
N1-C5'-C4'	130.3(9)
C7-C6-C3	115.6(4)
C6-C7-C8	108.3(4)
C7'-C6'-C3'	113.6(5)
C6'-C7'-C8	107.8(6)
C9-C8-C7'	111.4(3)
C9-C8-C7	113.1(2)
C7'-C8-C7	34.9(3)
C14-C9-C10	117.2(2)
C14-C9-C8	121.7(3)
C10-C9-C8	121.1(2)
C11-C10-C9	121.8(2)
C12-C11-C10	120.3(3)
C11-C12-C13	119.6(3)
C12-C13-C14	120.1(3)
C9-C14-C13	121.0(3)

Symmetry transformations used to generate equivalent atoms:

#1 -x+2,-y+1,-z

Table B-6. Atomic coordinates ( $\times 10^4$ ) and equivalent isotropic displacement parameters ( $\text{\AA}^2 \times 10^3$ ) for compound **5**.  $U_{eq}$  is defined as one third of the trace of the orthogonalized  $U_{ij}$  tensor.

Atom	$x$	$y$	$z$	$U_{eq}$
Cu1	12615(1)	12105(1)	-367(1)	19(1)
Cu2	10997(1)	15636(1)	-182(1)	18(1)
N1	12092(2)	10955(4)	516(1)	19(1)
N2	13741(2)	11852(4)	288(1)	18(1)
N3	13563(2)	13029(4)	-1027(1)	24(1)
C1	11213(2)	10406(5)	555(2)	23(1)
C2	10943(2)	9465(5)	1154(2)	27(1)
C3	11596(2)	9101(5)	1736(2)	27(1)
C4	12510(2)	9688(5)	1706(2)	23(1)
C5	12732(2)	10600(4)	1088(2)	18(1)
C6	13684(2)	11212(4)	965(2)	18(1)
C7	14470(2)	11134(5)	1461(2)	22(1)
C8	15312(2)	11678(5)	1226(2)	24(1)
C9	15369(2)	12292(5)	517(2)	23(1)
C10	14550(2)	12387(4)	55(2)	18(1)
C11	14445(2)	12977(4)	-716(2)	20(1)
C12	15199(2)	13365(5)	-1113(2)	26(1)
C13	15035(3)	13752(5)	-1846(2)	32(1)
C14	14133(3)	13767(6)	-2166(2)	40(1)
C15	13414(3)	13433(6)	-1742(2)	35(1)
N4	11421(2)	12944(4)	-827(1)	25(1)
N5	11165(2)	12931(4)	-1464(2)	26(1)
N6	10873(3)	12928(7)	-2065(2)	56(1)
N7	10345(2)	14590(4)	628(1)	22(1)
N8	10585(2)	14218(4)	1262(1)	20(1)
N9	10788(2)	13836(5)	1855(2)	35(1)
N10	12285(2)	15744(5)	281(2)	29(1)
N11	12507(2)	15360(4)	907(1)	21(1)
N12	12765(2)	15001(5)	1499(2)	31(1)

Table B-6. Continued

Atom	<i>x</i>	<i>y</i>	<i>z</i>	<i>U</i> <sub>eq</sub>
N13	11207(2)	17508(4)	-938(2)	31(1)
N14	11908(2)	18360(4)	-960(1)	21(1)
N15	12574(2)	19240(4)	-1004(2)	28(1)

Table B-7. Bond lengths [ $\text{\AA}$ ] and angles [ $^\circ$ ] for compound **5**.

Bond	Distance /Angle
Cu1-N2	1.940(2)
Cu1-N4	1.943(3)
Cu1-N3	2.035(3)
Cu1-N1	2.037(3)
Cu1-N15#1	2.358(3)
Cu2-N10	1.975(3)
Cu2-N13	1.977(3)
Cu2-N7	1.992(3)
Cu2-N7#2	2.040(3)
Cu2-N4	2.374(3)
N1-C1	1.341(4)
N1-C5	1.358(4)
N2-C6	1.342(4)
N2-C10	1.343(4)
N3-C11	1.348(4)
N3-C15	1.348(4)
C1-C2	1.383(5)
C2-C3	1.383(5)
C3-C4	1.395(5)
C4-C5	1.380(4)
C5-C6	1.485(4)
C6-C7	1.388(4)
C7-C8	1.390(5)
C8-C9	1.390(5)
C9-C10	1.393(4)
C10-C11	1.477(4)
C11-C12	1.402(4)
C12-C13	1.379(5)
C13-C14	1.380(5)
C14-C15	1.384(5)
N4-N5	1.197(4)

Table B-7. Continued

Bond	Distance /Angle
N5-N6	1.147(4)
N7-N8	1.217(4)
N7-Cu2#2	2.040(3)
N8-N9	1.137(4)
N10-N11	1.200(4)
N11-N12	1.149(4)
N13-N14	1.188(4)
N14-N15	1.161(4)
N15-Cu1#3	2.358(3)
N2-Cu1-N4	163.23(11)
N2-Cu1-N3	80.00(11)
N4-Cu1-N3	105.28(11)
N2-Cu1-N1	79.67(10)
N4-Cu1-N1	95.05(11)
N3-Cu1-N1	159.47(11)
N2-Cu1-N15#1	101.95(10)
N4-Cu1-N15#1	94.19(11)
N3-Cu1-N15#1	88.18(11)
N1-Cu1-N15#1	93.20(10)
N10-Cu2-N13	94.22(12)
N10-Cu2-N7	100.87(11)
N13-Cu2-N7	154.23(13)
N10-Cu2-N7#2	177.09(11)
N13-Cu2-N7#2	88.65(11)
N7-Cu2-N7#2	76.61(11)
N10-Cu2-N4	88.16(11)
N13-Cu2-N4	97.41(12)
N7-Cu2-N4	103.79(11)
N7#2-Cu2-N4	91.02(10)
C1-N1-C5	118.8(3)
C1-N1-Cu1	126.3(2)

Table B-7. Continued

Bond	Distance /Angle
C5-N1-Cu1	114.69(19)
C6-N2-C10	122.1(3)
C6-N2-Cu1	119.1(2)
C10-N2-Cu1	118.7(2)
C11-N3-C15	118.5(3)
C11-N3-Cu1	113.8(2)
C15-N3-Cu1	127.1(2)
N1-C1-C2	122.1(3)
C1-C2-C3	119.1(3)
C2-C3-C4	119.3(3)
C5-C4-C3	118.4(3)
N1-C5-C4	122.2(3)
N1-C5-C6	113.5(3)
C4-C5-C6	124.2(3)
N2-C6-C7	120.3(3)
N2-C6-C5	112.8(3)
C7-C6-C5	126.9(3)
C6-C7-C8	118.1(3)
C9-C8-C7	121.2(3)
C8-C9-C10	117.7(3)
N2-C10-C9	120.5(3)
N2-C10-C11	112.4(3)
C9-C10-C11	127.1(3)
N3-C11-C12	121.8(3)
N3-C11-C10	114.8(3)
C12-C11-C10	123.3(3)
C13-C12-C11	119.1(3)
C12-C13-C14	119.0(3)
C13-C14-C15	119.4(3)
N3-C15-C14	122.2(3)
N5-N4-Cu1	127.0(2)

Table B-7. Continued

Bond	Distance /Angle
N5-N4-Cu2	115.3(2)
Cu1-N4-Cu2	107.11(12)
N6-N5-N4	176.5(4)
N8-N7-Cu2	133.8(2)
N8-N7-Cu2#2	122.7(2)
Cu2-N7-Cu2#2	103.39(11)
N9-N8-N7	178.0(3)
N11-N10-Cu2	123.9(2)
N12-N11-N10	176.5(3)
N14-N13-Cu2	124.2(2)
N15-N14-N13	177.1(3)
N14-N15-Cu1#3	114.5(2)

Symmetry transformations used to generate equivalent atoms:

#1  $x, y-1, z$  #2  $-x+2, -y+3, -z$  #3  $x, y+1, z$

Table B-8. Atomic coordinates ( $\times 10^4$ ) and equivalent isotropic displacement parameters ( $\text{\AA}^2 \times 10^3$ ) for compound **6**.  $U_{eq}$  is defined as one third of the trace of the orthogonalized  $U_{ij}$  tensor.

Atom	$x$	$y$	$z$	$U_{eq}$
Cu1	-1356(1)	2807(1)	7795(1)	19(1)
Cu2	4031(1)	3351(1)	6766(1)	21(1)
Cu3	5000	5000	5000	20(1)
N1	91(5)	2147(3)	6368(2)	19(1)
N2	-1149(5)	1305(3)	8176(3)	18(1)
N3	-2633(5)	2919(3)	9365(3)	20(1)
N4	-2961(6)	4103(3)	7435(3)	25(1)
N5	-2540(5)	4750(3)	6756(3)	23(1)
N6	-2302(6)	5387(3)	6112(3)	34(1)
N7	1720(5)	3318(3)	8011(3)	24(1)
N8	2076(6)	3111(4)	8865(3)	36(1)
N9	2329(7)	2908(6)	9673(4)	80(2)
N10	5307(6)	1890(3)	6814(3)	33(1)
N11	4623(5)	1215(3)	7402(3)	25(1)
N12	4059(6)	531(3)	7943(3)	38(1)
N13	5784(6)	3491(3)	5280(3)	23(1)
N14	6346(5)	2775(3)	4639(3)	23(1)
N15	6869(6)	2102(3)	4042(3)	38(1)
N16	3067(6)	4836(3)	6392(3)	25(1)
N17	1796(6)	5496(3)	6950(3)	24(1)
N18	594(6)	6111(4)	7466(3)	39(1)
C1	720(6)	2662(4)	5471(3)	21(1)
C2	1847(7)	2131(4)	4555(3)	26(1)
C3	2383(7)	1048(4)	4581(3)	25(1)
C4	1716(6)	512(4)	5509(3)	24(1)
C5	542(6)	1073(3)	6390(3)	19(1)
C6	-319(6)	585(3)	7419(3)	19(1)
C7	-333(7)	-496(4)	7636(3)	24(1)
C8	-1218(6)	-795(4)	8652(3)	25(1)

Table B-8. Continued

Atom	<i>x</i>	<i>y</i>	<i>z</i>	<i>U</i> <sub>eq</sub>
C9	-2085(6)	-33(4)	9421(3)	24(1)
C10	-2022(6)	1030(4)	9151(3)	21(1)
C11	-2812(6)	1968(4)	9859(3)	20(1)
C12	-3623(7)	1921(4)	10932(3)	29(1)
C13	-4213(7)	2849(4)	11505(3)	32(1)
C14	-3975(7)	3816(4)	11008(3)	30(1)
C15	-3166(6)	3816(4)	9923(3)	24(1)

Table B-9. Bond lengths [ $\text{\AA}$ ] and angles [ $^\circ$ ] for compound **6**.

Bond	Distance /Angle
Cu1-N4	1.950(4)
Cu1-N2	1.951(4)
Cu1-N3	2.032(3)
Cu1-N1	2.034(3)
Cu1-N7	2.288(3)
Cu2-N10	1.941(4)
Cu2-N7	1.956(3)
Cu2-N16	1.996(4)
Cu2-N13	2.033(3)
Cu3-N13	1.966(4)
Cu3-N13#1	1.966(4)
Cu3-N16#1	1.987(3)
Cu3-N16	1.987(3)
N1-C1	1.334(5)
N1-C5	1.356(5)
N2-C10	1.330(5)
N2-C6	1.333(5)
N3-C15	1.329(5)
N3-C11	1.359(5)
N4-N5	1.203(5)
N5-N6	1.151(5)
N7-N8	1.214(5)
N8-N9	1.130(5)
N10-N11	1.196(5)
N11-N12	1.148(5)
N13-N14	1.213(5)
N14-N15	1.133(5)
N16-N17	1.225(5)
N17-N18	1.144(5)
C1-C2	1.392(6)
C1-H1A	0.9500

Table B-9. Continued

Bond	Distance /Angle
C2-C3	1.374(6)
C2-H2A	0.9500
C3-C4	1.385(6)
C3-H3A	0.9500
C4-C5	1.383(6)
C4-H4A	0.9500
C5-C6	1.486(5)
C6-C7	1.392(6)
C7-C8	1.386(6)
C7-H7A	0.9500
C8-C9	1.381(6)
C8-H8A	0.9500
C9-C10	1.386(6)
C9-H9A	0.9500
C10-C11	1.486(6)
C11-C12	1.384(5)
C12-C13	1.372(6)
C12-H12A	0.9500
C13-C14	1.383(6)
C13-H13A	0.9500
C14-C15	1.396(6)
C14-H14A	0.9500
C15-H15A	0.9500
N4-Cu1-N2	150.78(15)
N4-Cu1-N3	95.54(14)
N2-Cu1-N3	79.45(14)
N4-Cu1-N1	103.01(14)
N2-Cu1-N1	80.32(14)
N3-Cu1-N1	159.69(15)
N4-Cu1-N7	105.46(15)
N2-Cu1-N7	103.43(14)

Table B-9. Continued

Bond	Distance /Angle
N3-Cu1-N7	91.27(13)
N1-Cu1-N7	91.69(13)
N10-Cu2-N7	97.93(16)
N10-Cu2-N16	167.54(15)
N7-Cu2-N16	93.83(15)
N10-Cu2-N13	90.18(15)
N7-Cu2-N13	164.50(15)
N16-Cu2-N13	77.43(14)
N13-Cu3-N13#1	180.000(1)
N13-Cu3-N16#1	100.78(15)
N13#1-Cu3-N16#1	79.22(15)
N13-Cu3-N16	79.22(15)
N13#1-Cu3-N16	100.78(15)
N16#1-Cu3-N16	180.000(1)
C1-N1-C5	119.4(3)
C1-N1-Cu1	126.9(3)
C5-N1-Cu1	113.6(3)
C10-N2-C6	122.1(4)
C10-N2-Cu1	119.2(3)
C6-N2-Cu1	118.3(3)
C15-N3-C11	119.7(3)
C15-N3-Cu1	125.7(3)
C11-N3-Cu1	114.5(3)
N5-N4-Cu1	131.9(3)
N6-N5-N4	174.6(4)
N8-N7-Cu2	120.4(3)
N8-N7-Cu1	114.4(3)
Cu2-N7-Cu1	117.84(16)
N9-N8-N7	177.3(5)
N11-N10-Cu2	126.4(3)
N12-N11-N10	176.5(5)

Table B-9. Continued

Bond	Distance /Angle
N14-N13-Cu3	126.8(3)
N14-N13-Cu2	125.1(3)
Cu3-N13-Cu2	101.14(16)
N15-N14-N13	179.7(5)
N17-N16-Cu3	130.1(3)
N17-N16-Cu2	127.6(3)
Cu3-N16-Cu2	101.68(16)
N18-N17-N16	179.4(5)
N1-C1-C2	121.9(4)
N1-C1-H1A	119.0
C2-C1-H1A	119.0
C3-C2-C1	119.1(4)
C3-C2-H2A	120.5
C1-C2-H2A	120.5
C2-C3-C4	118.9(4)
C2-C3-H3A	120.5
C4-C3-H3A	120.5
C5-C4-C3	119.7(4)
C5-C4-H4A	120.1
C3-C4-H4A	120.1
N1-C5-C4	120.9(4)
N1-C5-C6	114.4(3)
C4-C5-C6	124.7(4)
N2-C6-C7	120.1(4)
N2-C6-C5	112.9(4)
C7-C6-C5	127.0(4)
C8-C7-C6	118.4(4)
C8-C7-H7A	120.8
C6-C7-H7A	120.8
C9-C8-C7	120.4(4)
C9-C8-H8A	119.8

Table B-9. Continued

Bond	Distance /Angle
C7-C8-H8A	119.8
C8-C9-C10	118.3(4)
C8-C9-H9A	120.8
C10-C9-H9A	120.8
N2-C10-C9	120.7(4)
N2-C10-C11	112.4(4)
C9-C10-C11	127.0(4)
N3-C11-C12	120.9(4)
N3-C11-C10	114.0(3)
C12-C11-C10	125.1(4)
C13-C12-C11	119.4(4)
C13-C12-H12A	120.3
C11-C12-H12A	120.3
C12-C13-C14	119.8(4)
C12-C13-H13A	120.1
C14-C13-H13A	120.1
C13-C14-C15	118.3(4)
C13-C14-H14A	120.8
C15-C14-H14A	120.8
N3-C15-C14	121.9(4)
N3-C15-H15A	119.1
C14-C15-H15A	119.1

Symmetry transformations used to generate equivalent atoms:

#1  $-x+1, -y+1, -z+1$

Table B-10. Atomic coordinates ( $\times 10^4$ ) and equivalent isotropic displacement parameters ( $\text{\AA}^2 \times 10^3$ ) for compound 7.  $U_{eq}$  is defined as one third of the trace of the orthogonalized  $U_{ij}$  tensor.

Atom	$x$	$y$	$z$	$U_{eq}$
Ni1	2102(3)	2497(1)	1094(3)	24(1)
C1	2733(6)	1395(9)	2016(9)	32(2)
C2	2936(8)	2450(9)	9(12)	38(3)
C3	1467(6)	3607(9)	112(9)	32(2)
C4	1258(6)	2542(7)	2113(9)	19(2)
N1	3132(7)	704(9)	2607(9)	60(3)
N2	3507(7)	2471(6)	-505(8)	28(2)
N3	1104(6)	4278(9)	-448(8)	50(3)
N4	731(7)	2586(7)	2773(8)	33(2)
Ni2	-395(3)	2538(1)	3596(3)	22(1)
O1	-439(7)	4322(3)	3532(13)	76(1)
N5	-1161(5)	2151(7)	1937(6)	24(2)
N6	-403(7)	801(2)	3595(10)	24(1)
N7	390(6)	2165(9)	5221(7)	30(2)
C5	-1543(6)	2942(10)	1131(8)	38(3)
C6	-2076(9)	2553(10)	127(10)	40(3)
C7	-2246(7)	1468(11)	-21(9)	51(3)
C8	-1847(6)	616(11)	760(8)	37(2)
C9	-1314(6)	957(8)	1764(9)	30(2)
C10	-868(5)	253(8)	2649(7)	21(2)
C11	-861(6)	-1008(9)	2683(9)	35(2)
C12	-406(10)	-1567(3)	3547(14)	38(1)
C13	86(6)	-929(10)	4528(8)	32(2)
C14	57(5)	208(10)	4448(8)	33(2)
C15	535(6)	1064(9)	5410(7)	25(2)
C16	1101(6)	598(11)	6373(8)	37(2)
C17	1488(7)	1344(9)	7212(9)	35(2)
C18	1337(8)	2572(10)	7031(10)	42(3)
C19	770(6)	2880(10)	6024(8)	33(2)

Table B-11 Atomic coordinates ( $\times 10^4$ ) and equivalent isotropic displacement parameters ( $\text{\AA}^2 \times 10^3$ ) for compound **8**.  $U_{eq}$  is defined as one third of the trace of the orthogonalized  $U_{ij}$  tensor.

Atom	$x$	$y$	$z$	$U_{eq}$
Zn1	0	0	5000	19(1)
Zn2	5000	5000	0	17(1)
S1	-3616(1)	-507(1)	4249(1)	30(1)
S2	1849(1)	-2671(1)	4249(1)	25(1)
S3	6697(1)	7394(1)	838(1)	26(1)
S4	7942(1)	2890(1)	591(1)	24(1)
O1	-2389(2)	280(1)	4645(1)	25(1)
O2	330(2)	-2040(1)	4554(1)	27(1)
O3	5203(2)	6977(1)	457(1)	23(1)
O4	7270(2)	4371(1)	387(1)	26(1)
N1	865(2)	1156(2)	4099(1)	22(1)
N2	3805(2)	4137(2)	907(1)	19(1)
C1	2323(2)	849(2)	3843(1)	24(1)
C2	2909(2)	1459(2)	3232(1)	25(1)
C3	1976(2)	2453(2)	2850(1)	21(1)
C4	490(2)	2820(2)	3127(1)	23(1)
C5	-18(2)	2148(2)	3743(1)	23(1)
C6	2566(2)	3055(2)	2175(1)	20(1)
C7	3426(2)	2178(2)	1742(1)	23(1)
C8	3999(2)	2751(2)	1120(1)	22(1)
C9	2946(2)	4975(2)	1315(1)	21(1)
C10	2298(2)	4477(2)	1942(1)	22(1)
C11	-3620(3)	-2316(2)	4594(1)	42(1)
C12	-2741(3)	-795(3)	3427(1)	54(1)
C13	1959(3)	-4482(2)	4577(1)	45(1)
C14	1357(3)	-2991(3)	3386(1)	46(1)
C15	6439(4)	9276(2)	909(2)	62(1)
C16	6347(3)	6847(3)	1717(1)	44(1)
C17	9901(2)	2856(2)	225(1)	37(1)

Table B-11. Continued

Atom	<i>x</i>	<i>y</i>	<i>z</i>	<i>U</i> <sub>eq</sub>
C18	8465(3)	2970(3)	1468(1)	45(1)
C11	10998(1)	8872(1)	1614(1)	38(1)
O5	11073(4)	9581(2)	952(1)	95(1)
O6	10123(3)	9732(2)	2070(1)	78(1)
O7	10251(2)	7502(2)	1577(1)	54(1)
O8	12578(2)	8652(2)	1880(1)	58(1)
Cl2	6159(1)	14432(1)	3407(1)	36(1)
O9	5785(3)	13667(3)	4038(1)	78(1)
O10	6277(2)	13464(2)	2870(1)	70(1)
O11	4931(2)	15480(3)	3262(1)	72(1)
O12	7650(2)	15143(2)	3475(1)	63(1)

Table B-12. Atomic coordinates ( $\times 10^4$ ) and equivalent isotropic displacement parameters ( $\text{\AA}^2 \times 10^3$ ) for compound **9**.  $U_{eq}$  is defined as one third of the trace of the orthogonalized  $U_{ij}$  tensor.

Atom	$x$	$y$	$z$	$U_{eq}$
Cu	4310(1)	4310(1)	5000	17(1)
S1	5759(1)	3350(1)	6143(1)	29(1)
S2	5984(1)	7555(1)	5279(1)	24(1)
O1	5521(2)	3337(2)	5496(1)	27(1)
O2	5145(2)	6023(2)	5539(1)	24(1)
N1	2571(2)	3398(2)	5526(1)	19(1)
C1	2175(2)	2118(2)	5781(1)	21(1)
C2	1163(2)	1560(2)	6223(1)	21(1)
C3	516(2)	2338(2)	6418(1)	18(1)
C4	864(2)	3618(2)	6125(1)	20(1)
C5	1890(2)	4118(2)	5686(1)	20(1)
C6	7598(3)	4702(3)	6264(1)	50(1)
C7	5907(4)	1785(3)	6283(1)	45(1)
C8	4849(3)	8323(3)	5384(1)	34(1)
C9	7325(3)	8570(3)	5814(1)	39(1)
O3	1154(3)	-3266(2)	5675(1)	50(1)
Cl	1398(1)	-1865(1)	5523(1)	40(1)
O4	102(3)	-1815(4)	5576(2)	77(1)
O5	2548(6)	-801(6)	5876(3)	68(2)
O6	1859(4)	-1602(5)	4924(2)	86(1)
Cl'	1165(9)	-1867(8)	5764(4)	41(2)
O4'	930(30)	-1390(30)	5204(10)	66(6)
O5'	2310(60)	-800(60)	5950(20)	59(11)
O6'	180(20)	-1960(20)	6123(8)	51(5)

Table B-13. Atomic coordinates ( $\times 10^4$ ) and equivalent isotropic displacement parameters ( $\text{\AA}^2 \times 10^3$ ) for compound **10**.  $U(\text{eq})$  is defined as one third of the trace of the orthogonalized  $U_{ij}$  tensor.

Atom	$x$	$y$	$z$	$U_{\text{eq}}$
Cd	3237(1)	7487(1)	-719(1)	20(1)
O1	3202(1)	8129(3)	869(2)	27(1)
O2	3202(1)	6812(2)	-2281(2)	27(1)
N1	3275(1)	5772(2)	-96(3)	26(1)
N2	4228(1)	7546(2)	-728(7)	24(1)
N3	3207(1)	9194(2)	-1346(3)	24(1)
N4	3264(2)	335(3)	987(3)	47(1)
N5	7229(1)	7572(2)	-715(5)	23(1)
N6	3115(2)	14620(3)	-2463(3)	43(1)
C1	2835(2)	5331(3)	365(3)	30(1)
C2	2821(2)	4281(3)	635(3)	32(1)
C3	3291(2)	3645(3)	420(3)	28(1)
C4	3745(2)	4108(3)	-26(3)	30(1)
C5	3730(2)	5163(3)	-275(3)	31(1)
C6	3278(2)	2498(3)	647(5)	34(2)
C7	2768(2)	1950(3)	638(3)	36(1)
C8	2787(2)	867(4)	821(4)	43(1)
C9	3746(2)	871(3)	1000(3)	45(1)
C10	3774(2)	1950(3)	831(3)	37(1)
C11	4524(2)	7738(3)	82(3)	28(1)
C12	5111(2)	7748(3)	116(3)	27(1)
C13	5410(1)	7564(3)	-753(6)	22(1)
C14	5106(2)	7403(3)	-1595(3)	28(1)
C15	4519(2)	7381(3)	-1564(3)	28(1)
C16	6041(1)	7578(3)	-757(5)	23(1)
C17	6339(2)	7047(3)	-11(3)	30(1)
C18	6926(2)	7064(3)	-23(3)	29(1)
C19	6936(2)	8070(3)	-1414(3)	29(1)
C20	6348(2)	8096(3)	-1452(3)	29(1)

Table B-13. Continued

Atom	<i>x</i>	<i>y</i>	<i>z</i>	<i>U</i> <sub>eq</sub>
C21	3659(2)	9820(3)	-1247(3)	27(1)
C22	3660(2)	10868(3)	-1507(3)	31(1)
C23	3165(2)	11318(3)	-1876(3)	25(1)
C24	2701(2)	10668(3)	-2009(3)	32(1)
C25	2739(2)	9621(3)	-1743(3)	31(1)
C26	3150(2)	12453(3)	-2106(5)	29(1)
C27	2637(2)	13012(3)	-2042(3)	36(1)
C28	2646(2)	14090(3)	-2217(4)	41(1)
C29	3589(2)	14075(3)	-2546(3)	42(1)
C30	3630(2)	13003(3)	-2378(3)	36(1)
Cl1	358(1)	646(1)	731(1)	57(1)
Cl2	4831(1)	9548(1)	2718(1)	48(1)
O10	138(5)	756(8)	1621(6)	208(5)
O11	198(3)	-191(6)	252(8)	195(5)
O12	103(3)	1546(6)	237(7)	146(3)
O13	938(2)	809(4)	697(5)	102(2)
O20	4936(2)	10514(3)	2197(4)	86(1)
O21	4952(2)	9666(5)	3722(3)	85(2)
O22	5196(2)	8769(3)	2319(3)	73(1)
O23	4253(2)	9235(4)	2568(4)	82(2)
S1	4028(1)	6041(1)	2120(1)	38(1)
S1'	3958(4)	6384(7)	2831(7)	50(3)
S2	3934(1)	8500(1)	-4177(1)	52(1)
O30	3536(1)	6740(2)	2290(3)	45(1)
O40	3405(2)	8286(3)	-3613(3)	48(1)
C31	3898(3)	4890(4)	2804(5)	64(2)
C32	4608(3)	6480(4)	2793(6)	79(2)
C41	3951(3)	9897(4)	-4358(5)	62(2)
C42	3761(3)	8154(6)	-5374(5)	78(2)

## LIST OF REFERENCES

- (1) Hatfield, W. M.; Estes, W. E.; Marsh, W. E.; Pickens, M. W.; Harr, L. W. T.; Weller, R. R. In *Extended Linear Chain Compounds*; Miller, J. S., Ed.; Plenum Press: New York, 1983; pp 43-142.
- (2) de Jongh, L. J. *Magnetic Properties of Layered Transition Metal Compounds*; Kluwer Academic Publishers: Dordrecht, 1990.
- (3) Rouxel, J. *Acc. Chem. Res.* **1992**, *25*, 328.
- (4) Ward, B. H. *Electronic and Magnetic Phenomena of Inorganic and Organic Low-Dimensional Solids*. University of Florida, 1997.
- (5) Carlin, R. L. *Magnetochemistry*; 1st ed.; Springer-Verlag: Berlin, 1986.
- (6) Kahn, O. *Molecular Magnetism*; VCH: New York, 1993.
- (7) a) Kahn, O.; Galy, J.; Journaux, J.; Jaud, J.; Morgenstern-Badarau, I. *J. Am. Chem. Soc.* **1982**, *104*, 2165-2176. b) Miller, J. S.; Epstein, A. J. *MRS Bulletin* **2000**, *11*, 21-28.
- (8) Coronado, E.; Tsukerblat, B. S.; Gorges, R., Eds.; *Molecular Magnetism: From Molecular Assemblies to the Devices*; Kluwer Academic Publishers: Boston, 1996; Vol. 321.
- (9) a) Fanucci, G. E. *Metal Phosphonate Solids and Langmuir-Blodgett Films: Structural and Physical Characterization*. University of Florida, 1999. b) Boersma, F.; de Jonge, W. J. M.; Kopinga, K. *Phys. Rev. B* **1981**, *23*, 186-197.
- (10) Jezowska-Trezbiatowska, B.; Wojciechowski, W. *Theory of Bridge Bonding and the Structure of Binuclear Coordination Compounds*; 1st ed.; Marcel Dekker: New York, 1971; Vol. 6.
- (11) Palacio, E., Ed.; *Molecular Magnetism: From Molecular Assemblies to the Devices*; Kluwer Academic Publishers: Boston, 1996; Vol. 321.
- (12) de Jongh, L. J.; Miedema, A. R. *Adv. Phys.* **1974**, *24*, 1-260.
- (13) Onsager, L. *Phys. Rev.* **1944**, *65*, 117-149.

- (14) Pokrovsky, V. L.; Uimin, G. V., Eds.; *Magnetic Properties of Layered Transition Metal Compounds*; Kluwer Academic Publishers: Dordrecht, 1990, pp 53-103.
- (15) Block, F. *Z. Phys.* **1930**, *61*, 206.
- (16) Boersma, F. L.; de Jongh, W. J. L. *Phys. Rev. B* **1981**, *23*, 186-214.
- (17) Bencini, A.; Gatteschi, D. *Inorg. Chim. Acta.* **1978**, *31*, 11-18.
- (18) Crawford, V. H.; Richardson, H. W.; Wasson, J. R.; Hodgson, D. J.; Hatfield, W. E. *Inorg. Chem.* **1976**, *15*, 2107-2110.
- (19) Jeter, D. Y.; Lewis, D. L.; Hempel, J. C.; Hodgson, D. J.; Hatfield, W. E. *Inorg. Chem.* **1972**, *11*, 1958-1960.
- (20) Willet, R. D.; Gatteschi, D.; Kahn, O. *Magneto-Structural Correlations in Exchanged Coupled Systems*; Reidel Publishing Company: Dordrecht, 1985.
- (21) Hay, P. J.; Thibeault, J. C.; Hoffmann, R. *J. Am. Chem. Soc.* **1975**, *97*, 4884-4899.
- (22) Michalowicz, A.; Girerd, J. J.; Goulon, J. *Inorg. Chem.* **1979**, *18*, 3004.
- (23) Girerd, J. J.; Kahn, O.; Verdaguer, M. *Inorg. Chem.* **1980**, *19*, 274.
- (24) Meyer, A.; Gleizes, A.; Girerd, J. J.; Verdaguer, M.; Kahn, O. *Inorg. Chem.* **1982**, *21*, 1729.
- (25) Bonner, J. C.; Fisher, M. E. *Phys. Rev. A* **1964**, *135*, 640.
- (26) Orbach, R. L. *Phys. Rev.* **1958**, *112*, 309.
- (27) Baker, G. A.; Rushbrooke, G. S.; Gilbert, H. E. *Phys. Rev.* **1964**, *135*, A1272.
- (28) Diederix, K. M.; Blote, H. W. J.; Bray, J. W.; Jacobs, I. S. *J. Appl. Phys.* **1979**, *50*, 1810.
- (29) Bonner, J. C.; Friedberg, S. A.; Kobayashi, H.; Meier, D. L.; Blote, H. W. J. *Phys. Rev.* **1983**, *B27*, 248.
- (30) Roberts, S. A.; Bloomquist, D. R.; Willet, R. D.; Dodgen, H. W. *J. Am. Chem. Soc.* **1981**, *103*, 2603.
- (31) Harr, L. W. T.; Hatfield, W. E. *Inorg. Chem.* **1985**, *24*, 1022.
- (32) Hong, C. S.; Do, Y. *Angew. Chem. Int. Ed.* **1999**, *38*, 193.
- (33) Rovira, C. *Structure and Bonding* **2001**, *100*, 163-187.

- (34) Rovira, C. *Chem. Eur. J.* **2000**, *6*, 1723.
- (35) Dagotto, E.; Rice, T. M. *Science* **1996**, *271*, 618-623.
- (36) Azuma, M.; Hiroi, Z.; Takano, M.; Ishida, K.; Kitaoka, Y. *Phys. Rev. Lett.* **1994**, *73*, 3463.
- (37) Yaghi, O.; Li, H.; Davis, C.; Richardson, D.; Groy, T. L. *Acc. Chem. Res.* **1998**, *32*, 474-484.
- (38) Maekawa, S. *Science* **1996**, *273*, 1515.
- (39) Zaworotko, M. J. *Chem. Commun.* **2001**, 1-9.
- (40) Lu, J. Y.; Lawandy, M. A.; Li, J.; Yuen, T.; Lin, C. L. *Inorg. Chem.* **1999**, *38*, 2695-2704.
- (41) Carlucci, L.; Ciani, G.; Prosperio, D. M.; Sironi, A. *J. Am. Chem. Soc.* **1995**, *117*, 4562.
- (42) Hoskins, B. F.; Robson, R. *J. Am. Chem. Soc.* **1990**, *112*, 1546-1554.
- (43) Robson, R.; Abrahams, B. F.; Batten, S. R.; Gable, R. W.; Hoskins, B. F.; Liu, J. *Supramolecular Architecture*; American Chemical Society: Washington D. C., 1995.
- (44) Fujita, M.; Kwon, Y. J.; Washizu, S.; Ogura, K. *Inorg. Chem.* **1994**, *116*, 1151-1152.
- (45) Yaghi, O. M.; Li, G.; Li, H. *Nature* **1995**, *378*, 703-706.
- (46) Inoue, M.; Kubo, M. *Coord. Chem. Rev.* **1976**, *21*, 1.
- (47) Kawata, S.; Kitagawa, S.; Kondo, M.; Furuchi, I.; Munakata, M. *Angew. Chem. Int. Ed. Engl.* **1994**, *33*, 1759-1761.
- (48) Entley, W. R.; Girolami, G. S. *Inorg. Chem.* **1994**, *33*, 5165.
- (49) Manson, J. L.; Campana, C.; Miller, J. S. *Chem. Commun.* **1998**, 251.
- (50) Manavalan, R.; Patal, M. M. *J. Makromol. Sci. Chem.* **1983**, *A19*, 951.
- (51) Kobel, W.; Hanack, M. *Inorg. Chem.* **1986**, *25*, 103.
- (52) Sinzger, K.; Hunig, S.; Jopp, M.; Bauer, D.; Bietsch, W.; Schutz, J. U. v.; Wolf, H. C.; Kremer, H. C.; Metzenthin, T.; Bau, R.; Khan, S. I.; Lindbaum, A.; Langauer, C. L.; Tillmanns, E. *J. Am. Chem. Soc.* **1993**, *115*, 7696.

- (53) Masciocchi, N.; Cairati, D.; Carlucci, L.; Mezza, G.; Ciani, G.; Sireni, A. *J. Chem. Soc., Dalton Trans.* **1996**, 2739.
- (54) Evans, O. R.; Xiong, R. G.; Wang, Z.; Wong, G. K.; Lin, W. *Angew. Chem. Int. Ed. Engl.* **1999**, 38, 536.
- (55) Janiak, C.; Scharmann, T. G.; Albrecht, P.; Marlow, F.; MacDonald, R. *J. Am. Chem. Soc.* **1996**, 118, 6307.
- (56) Lin, O.; Evans, O. R.; Xiong, R. G.; Wang, Z. *J. Am. Chem. Soc.* **1998**, 120, 13272.
- (57) Zhang, H.; Wang, X.; Teo, B. K. *J. Am. Chem. Soc.* **1996**, 118.
- (58) Lehn, J. M. *Supramolecular Chemistry: Concepts and Perspectives*; VCH: Weinheim, 1995.
- (59) Ward, M. D.; Fagan, P. J.; Calabrese, J. C.; Johnson, D. C. *J. Am. Chem. Soc.* **1989**, 111, 1719-1732.
- (60) Fagan, P.; Ward, M. D. *Sci. Am.* **1992**, 7, 48.
- (61) Garcia-Tellado, F.; Geib, S. J.; Goswami, S.; Hamilton, A. D. *J. Am. Chem. Soc.* **1991**, 113, 9265-9269.
- (62) Russell, V. A.; Evans, C. C.; Li, W.; Ward, M. D. *Science* **1997**, 273, 575-579.
- (63) Aakeroy, C. B.; Seddon, K. R. *Chem. Soc. Rev.* **1993**, 397-407.
- (64) Groeneman, R. H.; MacGillivray, L. H.; Atwood, J. L. *Inorg. Chem.* **1999**, 38, 208-209.
- (65) Melendez, R. E.; Sharma, C. V. K.; Zaworotko, M. J.; Bauer, C.; Rogers, R. D. *Angew. Chem. Int. Ed. Engl.* **1996**, 32, 2213-2215.
- (66) Lehn, J. M. *Angew. Chem. Int. Ed. Engl.* **1998**, 27, 89.
- (67) Hunter, C. A. *Chem. Rev.* **1994**, 101-109.
- (68) Desiraju, G. R.; Gavezzotti, A. *J. Chem. Soc., Chem. Commun.* **1989**, 621.
- (69) Hagrman, D.; Hammond, R. P.; Haushalter, R.; Zubieta, J. *Chem. Mater.* **1998**, 10, 2091-2100.
- (70) Power, K. N.; Hennigar, T. L.; Zaworotko, M. J. *New. J. Chem.* **1998**, 177-181.
- (71) Haynes, J. S.; Retting, S. J.; Sams, J. R.; Thompson, R. C.; Trotter, J. *Can. J. Chem.* **1987**, 65, 420.

- (72) Real, J. A.; DeMunno, G.; Munoz, M. C.; Julve, M. *Inorg. Chem.* **1991**, *30*, 2701.
- (73) Robinson, F.; Zaworotko, M. J. *J. Chem. Soc., Chem. Commun.* **1995**, 2413-2414.
- (74) Gable, R. W.; Hoskins, B. F.; Robson, R. *J. Chem. Soc., Chem Commun.* **1990**, 1677.
- (75) Hagrman, D.; Zubieta, C.; Rose, D. J.; Zubieta, J.; Haushalter, R. C. *Angew. Chem. Int. Ed. Engl.* **1997**, *36*, 873-876.
- (76) Kondo, M.; Yoshitomi, T.; Seki, K.; Matsuzaka, H.; Kitagawa, S. *Angew. Chem. Int. Ed. Engl.* **1997**, *36*, 1725-1727.
- (77) Yaghi, O. M.; Li, G. *Angew. Chem. Int. Ed. Engl.* **1995**, *34*, 207-209.
- (78) Lu, J.; Crisci, G.; Niu, T.; Jacobson, A. J. *Inorg. Chem.* **1997**, *36*, 5140.
- (79) Yaghi, O. M.; Li, H. *J. Am. Chem. Soc.* **1995**, *117*, 10401-10402.
- (80) Carlucci, L.; Ciani, G.; Proserpio, D. M. *New. J. Chem.* **1998**, *1998*, 1319.
- (81) Blake, A. J.; Champness, N. R.; Chung, S. S. M.; Li, W. S.; Schoder, M. *Chem. Commun.* **1997**, 1675-1676.
- (82) Abrahams, B. F.; Batten, S. R.; Hamit, H.; Hoskins, B. F.; Robson, R. *Angew. Chem. Int. Ed. Engl.* **1996**, *35*, 1690-1692.
- (83) Batten, S. R.; Hoskins, B. F.; Robison, R. *Angew. Chem. Int. Ed. Engl.* **1995**, *34*, 820-822.
- (84) Batten, S. R.; Hoskins, B. F.; Robson, R. *J. Am. Chem. Soc.* **1995**, *117*, 5385-5386.
- (85) Abrahams, B. F.; Batten, S. R.; Hamit, H.; Hoskins, B. F.; Robson, R. *Chem. Commun.* **1996**, 1313-1314.
- (86) Gardner, G. B.; Venkataraman, D.; Moore, J. S.; Lee, S. *Nature* **1995**, *374*, 792-795.
- (87) Yaghi, O. M.; Davis, C. E.; Li, G.; Li, H. *J. Am. Chem. Soc.* **1997**, *119*, 2861-2868.
- (88) Fujita, M.; Kwon, Y. J.; Sasaki, Y. O.; Yamaguchi, K.; Ogura, K. *J. Am. Chem. Soc.* **1995**, *117*, 7287.
- (89) Wang, Z.; Xiong, R. G.; Foxman, B. M.; Wilson, S. R.; Lin, W. *Inorg. Chem.* **1999**, *38*, 1523-1528.
- (90) Mayr, A.; Mao, L. F. *Inorg. Chem.* **1998**, *37*, 5776-5780.

- (91) Tabellion, F. M.; Seidel, S. R.; Arif, A. M.; Stang, P. J. *Angew. Chem. Int. Ed.* **2001**, *40*, 1529-1532.
- (92) Blake, A. J.; Hill, S. J.; Hubberstey, P.; Li, W. S. *J. Chem. Soc., Dalton Trans.* **1997**, 913-914.
- (93) Venkataraman, D.; Gardiner, G. B.; Lee, S.; Moore, J. S. *J. Am. Chem. Soc.* **1995**, *117*, 11600-11601.
- (94) Hennigar, T. L.; MacQuarrie, D. C.; Losier, P.; Rogers, R. D.; Zaworotko, M. J. *Angew. Chem. Int. Ed. Engl.* **1997**, *36*, 972.
- (95) Lu, J.; Paliwala, T.; Lim, S. C.; Yu, C.; Niu, T.; Jacobson, A. J. *Inorg. Chem.* **1997**, *36*, 923.
- (96) Lu, J.; Yu, C.; Niu, T.; Paliwala, T.; Crisci, G.; Somosa, F.; Jacobson, A. J. *Inorg. Chem.* **1998**, *37*, 4637-4640.
- (97) Shen, H.; Liao, D.; Jiang, Z.; Yan, S.; Sun, B.; Wang, G.; Yao, X.; Wang, H. *Polyhedron* **1998**, *17*, 1953-1957.
- (98) Xiong, R. G.; Liu, C. M.; You, X. Z. *Polyhedron* **1997**, *16*, 2667-2671.
- (99) Chen, C.; Xu, D.; Xu, Y.; Cheng, C. *Acta. Cryst. Sect. C* **1992**, *C48*, 1231.
- (100) Abrahams, B. F.; Hoskins, B. F.; Winter, G. *Aust. J. Chem.* **1990**, *43*, 1759.
- (101) Hagrman, D.; Zubieta, C.; Rose, D. J.; Zubieta, J.; Haushalter, R. C. *Angew. Chem. Int. Ed. Engl.* **1997**, *36*, 8.
- (102) Lopez, S.; Keller, S. W. *Inorg. Chem.* **1999**, 1999.
- (103) Chen, X. M.; Tong, M. L.; Luo, Y. J.; Chen, Z. N. *Aust. J. Chem.* **1996**, *49*, 835.
- (104) Tong, M. L.; Chen, X. L.; Yu, X. L.; Mak, T. C. W. *J. Chem. Soc., Dalton Trans.* **1998**, 5-6.
- (105) Biradha, K.; Domasevitch, K. V.; Moulton, B.; Seward, C.; Zaworotko, M. J. *Chem. Commun.* **1999**, 1327-1328.
- (106) Hayashi, M.; Miyamoto, Y.; Inoue, T.; Oguni, N. *J. Chem. Soc., Chem. Commun.* **1992**, 1752.
- (107) MacGillivray, L. R.; Subramanian, S.; Zaworotko, M. J. *J. Chem. Soc., Chem. Commun* **1994**, 1325-1326.
- (108) Carlucci, L.; Giani, G.; Proserpio, D. M.; Sironi, A. *J. Chem. Soc., Chem. Commun.* **1994**, 2755-2756.

- (109) Losier, P.; Zaworotko, M. J. *Angew. Chem. Int. Ed. Engl.* **1996**, *35*, 2779-2782.
- (110) Yaghi, O. M.; Li, H. *J. Am. Chem. Soc.* **1996**, *118*, 295-296.
- (111) Blake, A. J.; Champness, N. R.; Khlobystov, A.; Lemenovskii, D. A.; Li, W. S.; Schoder, M. *Chem. Commun.* **1997**.
- (112) Withersby, M. A.; Blake, A. J.; Champness, N. R.; Cooke, P. A.; Hubberstey, P.; Schroder, M. *New. J. Chem.* **1999**, *23*, 573.
- (113) Gudbjartson, H.; Biradha, K.; Poirier, K. M.; Zaworotko, M. J. *J. Am. Chem. Soc.* **1999**, *121*, 2599-2600.
- (114) Yaghi, O. M.; Li, H.; Groy, T. L. *Inorg. Chem.* **1997**, *36*, 4292-4293.
- (115) Domasevitch, K. V.; Enright, G. D.; Moulton, B.; Zaworotko, M. J. *Journal of Solid State Chemistry* **2000**, *152*, 280-285.
- (116) Soma, T.; Yuge, H.; Iwamoto, T. *Angew. Chem. Int. Ed. Engl.* **1994**, *33*, 1655.
- (117) Subramanian, S.; Zaworotko, M. J. *Angew. Chem. Int. Ed. Engl.* **1995**, *34*, 2127-2129.
- (118) Buser, H. J.; Schwarzenback, D.; Petter, W. *Inorg. Chem.* **1977**, *16*, 2704.
- (119) Abrahams, B. F.; Hardie, M. J.; Hoskins, B. F.; Robson, R.; Sutherland, E. E. *J. Chem. Soc., Chem. Commun.* **1994**, 1049.
- (120) Halasyamani, P.; Heier, K. R.; Willis, M. J.; Stern, C. L.; Poppelmeier, K. R. *Z. Anorg. Allg. Chem.* **1996**, *622*, 479.
- (121) Darriet, J.; Haddad, M. S.; Duesler, E. N.; Hendrickson, D. N. *Inorg. Chem.* **1979**, *18*, 2679.
- (122) Otieno, T.; Rettig, S. J.; Thompson, R. C.; Trotter, J. *Inorg. Chem.* **1993**, *32*, 4384.
- (123) Otieno, T.; Rettig, S. J.; Thompson, R. C.; Trotter, J. *Inorg. Chem.* **1993**, *32*, 1607.
- (124) Kitagawa, S.; Kawata, S.; Kondo, M.; Nozaka, Y.; Munakata, M. *Bull. Chem. Soc. Jpn.* **1993**, *66*, 3387.
- (125) Carlucci, L.; Ciani, G.; Proserpio, D. M.; Sironi, A. *Inorg. Chem.* **1995**, *34*, 5698.
- (126) Carlucci, L.; Ciani, G.; Proserpio, D. M.; Sironi, A. *Angew. Chem. Int. Ed. Engl.* **1995**, *34*, 1895.
- (127) Lu, J.; Harrison, W. T. A.; Jacobson, A. J. *Angew. Chem. Int. Ed. Engl.* **1995**, *34*, 2557-2559.

- (128) Venkataraman, D.; Lee, S.; Moore, J. S.; Zhang, P.; Hirsch, K. A.; Gardner, G. B.; Covey, A. C.; Prentice, C. L. *Chem. Mater.* **1996**, *8*, 2030-2040.
- (129) Dyer, A. *An Introduction to Zeolite Molecular Sieves*; Wiley: Chichester, 1988.
- (130) Yaghi, O. M.; Sun, Z.; Richardson, D. A.; Groy, T. L. *J. Am. Chem. Soc.* **1994**, *116*, 807-808.
- (131) Park, K. M.; Iwamoto, T. *J. Chem. Soc., Chem. Commun.* **1992**, 72-74.
- (132) Kim, J.; Whang, D.; Lee, J. I.; Kim, K. *J. Chem. Soc., Chem. Commun.* **1993**, 1400-1402.
- (133) Tong, M. L.; Ye, B. H.; Cai, J. W.; Chen, X. M.; Ng, S. W. *Inorg. Chem.* **1998**, *37*, 2645-2650.
- (134) Michaelides, A.; Kiritsis, V.; Skoulika, S.; Aubry, A. *Angew. Chem. Int. Ed. Engl.* **1993**, *32*, 1495-1497.
- (135) Munukata, M.; Ning, G. L.; Kuroda-Sowa, T.; Maekawa, M.; Suenaga, Y.; Horino, T. *Inorg. Chem.* **1998**, *37*, 5651-5656.
- (136) Powell, H. M.; Wetters, B. D. P. *Chem. Ind.* **1955**, 256-7.
- (137) Allison, S. A.; Barrer, R. M. *J. Chem. Soc. A* **1967**, 1717-1723.
- (138) MacNicol, D. D. *Inclusion Compounds*; Academic Press: London, 1984; Vol. 2.
- (139) MacAdie, H. G. *Can. J. Chem.* **1962**, *40*, 2195-2203.
- (140) Knight, H. B.; Witnauer, L. P.; Coleman, J. E.; Noble, W. R. J.; Swern, D. *Anal. Chem.* **1952**, *24*, 1331-1334.
- (141) Wang, X.; Simard, M.; Wuest, J. D. *J. Am. Chem. Soc.* **1994**, *116*, 12119-12120.
- (142) Endo, K.; Sawaki, T.; Koyanagi, M.; Kobayashi, K.; Masuda, H.; Aoyama, Y. *J. Am. Chem. Soc.* **1995**, *117*, 8341-8352.
- (143) Zaworotko, M. J. *Chem. Soc. Rev.* **1994**, 283.
- (144) Kondo, M.; Shimamura, M.; Noro, S. I.; Minakoshi, S.; Asami, A.; Seki, K.; Kitagawa, S. *Chem. Mater.* **2000**, *12*, 1288-1299.
- (145) Kondo, M.; Okubo, T.; Asami, A.; Noro, S.; Kitagawa, S.; Ishii, T.; Matsuzaka, M.; Seki, K. *Angew. Chem. Int. Ed. Engl.* **1999**, *38*, 140-143.
- (146) Li, H.; Eddaoudi, M.; O'Keeffe, M.; Yaghi, O. M. *Nature* **1999**, *402*, 276-279.

- (147) Pan, L.; Ching, N.; Huang, X.; Li, J. *Inorg. Chem.* **2000**, *39*, 5333-5340.
- (148) Hillier, A. C.; Ward, M. D. *Science* **1994**, *263*, 1261.
- (149) Russel, V. A.; Etter, M. C.; Ward, M. D. *J. Am. Chem. Soc.* **1994**, *116*, 1941.
- (150) Chen, X. M.; Tong, M. L.; Luo, Y. J.; Chen, Z. N. *Aust. J. Chem.* **1996**, *49*, 835.
- (151) MacGillivray, L. R.; Groeneman, R. H.; Atwood, J. L. *J. Am. Chem. Soc.* **1998**, *120*, 2676-2677.
- (152) Decurtins, S.; Schmalle, H. W.; Pellaux, R.; Schneuwly, P.; Hauser, A. *Inorg. Chem.* **1996**, *35*, 1451-1460.
- (153) Kiritsis, V.; Michaelides, A.; Skoulika, S.; Golhen, S.; Ouahab, L. *Inorg. Chem.* **1998**, *37*, 3407-3410.
- (154) McCleverty, J. A.; Ward, M. D. *Acc. Chem. Res.* **1998**, *31*, 842-851.
- (155) Sheldrick, G. M. ; 6 ed.; Bruker-AXS: Madison, Wisconsin, USA, 2000.
- (156) Woodward, J. D.; Backov, R.; Abboud, K. A.; Talham, D. R. Unpublished Results. **1998**.
- (157) Abragam, A.; Bleaney, B. *Electron Paramagnetic Resonance of Transition Ions*; Oxford University Press: London, 1970.
- (158) Papanicolaou, N.; Spathis, P. N. *Physical Review B* **1995**, *52*, 16001-16011.
- (159) Orendac, M.; Orendacova, A.; Cernak, J.; Feher, A.; Signore, P. J. C.; Meisel, M. W.; Merah, S.; Verdager, M. *Physical Review B* **1995**, *52*, 3435-3440.
- (160) Orendac, M.; Zvyagin, S.; Orendacova, A.; Sieling, M.; Luthi, B.; Feher, A.; Meisel, M. W. *Physical Review B* **1999**, *60*, 4170-4175.
- (161) Orendac, M.; Cizmar, E.; Orendac, M.; Cernak, J.; Feher, A.; Meisel, M. W.; Abboud, K. A.; Zvyagin, S.; Sieling, M.; Rieth, T.; Luthi, B. *Phys. Rev. B* **2000**, *61*, 3323.
- (162) Haddad, M. S.; Hendrickson, D. N.; Cannady, J. P.; Drago, R. S.; Bieksza, D. S. *J. Am. Chem. Soc.* **1979**, *101*, 898.
- (163) Julve, M.; Verdauger, M.; Faus, J.; Tinti, F.; Moratal, J.; Monge, A.; Guitierrez-Puebla, E. *Inorg. Chem.* **1987**, *26*, 3520.
- (164) Li, M. X.; Xie, G. Y.; Gu, Y. D. *Polyhedron* **1995**, *14*, 1235-1239.
- (165) Osegovic, J. *The Prospect of Using Triethylphosphine Oxide to Observe Intercalation Compounds*. 1999; pp 1-4.

- (166) Baltusis, L.; Frye, J. S.; Maciel, G. E. *J. Am. Chem. Soc.* **1987**, *109*, 40-46.
- (167) Biaglo, A. I.; Gorte, R. J.; Kokotailo, G. T.; White, D. *Journal of Catalysis* **1994**, *148*.
- (168) Biaglow, A. I.; Gorte, R. J.; White, D. *Journal of Catalysis* **1994**, *150*, 221-224.
- (169) Biaglow, A. I.; Sepa, J.; Gorte, R. J.; White, D. *Journal of Catalysis* **1995**, *151*, 373-384.
- (170) Fletcher, W. P.; Gilbert, C. S.; Biaglow, A. I. *Catalysis Letters* **1997**, *47*.
- (171) Farcasiu, D.; Ghenciu, A. *J. Org. Chem.* **1991**, *56*, 6050.
- (172) Farcasiu, D.; Ghenciu, A. *Journal of Catalysis* **1992**, *134*, 126.
- (173) Farcasiu, D.; Ghenciu, A. *J. Am. Chem. Soc.* **1993**, *115*, 10901.
- (174) Xu, T.; Munson, E. J.; Haw, J. F. *J. Am. Chem. Soc.* **1994**, *116*, 1962.
- (175) Joerg, S. D. *Extensions of the Electrostatic-Covalent and Unified Solvation Models*. University of Florida, 1998.
- (176) Ripmeester, J. A. *J. Am. Chem. Soc.* **1983**, *105*, 2925-2927.
- (177) Maciel, G. E.; Haw, J. F.; Chuang, I. S.; Hawkins, B. L.; Early, T. E.; McKay, D. R.; Petrakis, L. *J. Am. Chem. Soc.* **1983**, *105*, 5529-5535.
- (178) Haw, J. F.; Chuang, I. S.; Hawkins, B. L.; Maciel, G. E. *J. Am. Chem. Soc.* **1983**, *105*, 7206-7207.
- (179) Majors, P. D.; Ellis, P. D. *J. Am. Chem. Soc.* **1987**, *109*, 1648-1653.
- (180) Xu, T.; Kob, N.; Drago, R. S.; Nicholas, J. B.; Haw, J. F. *J. Am. Chem. Soc.* **1997**, *119*, 12231-12239.
- (181) Rakiewicz, E. F.; Peters, A. W.; Wormsbecher, R. F.; Sutovich, K. J.; Mueller, K. T. *J. Phys. Chem. B* **1998**, *102*, 2890-2896.
- (182) Zalewski, D. J.; Chu, P. J.; Tutunjian, P. N.; Lunsford, J. H. *Langmuir* **1989**, *5*, 1026-1030.
- (183) Osegovic, J. P.; Drago, R. S. *Journal of Catalysis* **1999**, *182*, 1-4.
- (184) Majors, P. D.; Raidy, T. E.; Ellis, P. D.; Inners, R. R. *J. Am. Chem. Soc.* **1986**, *108*, 8123-8129.

- (185) Sutovich, K. J.; Peters, A. W.; Rakiewicz, E. F.; Wormsbecher, R. F.; Mattingly, S. M.; Mueller, K. T. *Journal of Catalysis* **1999**, *182*, 155-158.
- (186) Osegovic, J. *New Methods for Characterizing Solid Acidity*. University of Florida, 1999.
- (187) Lunsford, J. H.; Rothwell, W. P.; Shen, W. X. *J. Am. Chem. Soc.* **1985**, *107*, 1540-1547.
- (188) Baltusis, L.; Frye, J. S.; Maciel, G. S. *J. Am. Chem. Soc.* **1986**, *108*, 7119-7120.
- (189) Sheng, T. C.; Gay, I. D. *Journal of Catalysis* **1994**, *145*.
- (190) Sang, H.; Chu, H. Y.; Lunsford, J. H. *Catalysis Letters* **1994**, *26*.
- (191) Kolling, O. W. *Transactions of the Kansas Academy of Science* **1984**, *84*, 115-118.
- (192) Riddle, F. L.; Fowkes, F. M. *Polymer Preprints* **1988**, *29*, 188-189.
- (193) Lunsford, J. H.; Tutunjian, P. N.; Chu, P. J.; Zalewski, D. J. *J. Phys. Chem.* **1989**, *93*.
- (194) Rothwell, W. P.; Shen, W. X.; Lunsford, J. H. *J. Am. Chem. Soc.* **1983**, *106*, 2452.
- (195) Lunsford, J. *Top. Catal.* **1997**, *4*, 91-98.
- (196) Meyer, U.; Gutmann, V.; Gerger, W. *Monatsh. Chem.* **1975**, *106*.
- (197) Riddle, F. L.; Fowkes, F. M. *J. Am. Chem. Soc.* **1990**, *112*, 3259-3264.
- (198) Pearson, R. M. *Journal of Catalysis* **1971**, *23*, 288.
- (199) Bertini, I. *NMR of Paramagnetic Molecules in Biological Systems*; Benjamin/Cummings Publishing Company: Menlo Park, California, 1986.
- (200) Rojo, T.; Larramendi, J. I. R.; Duran, I.; Mesa, J. L.; Via, J.; Arriortua, M. I. *Polyhedron* **1990**, *9*, 2693.
- (201) Goher, M. A. S.; Wang, R. J.; Mark, T. C. W. *Polyhedron* **1992**, *11*, 829.
- (202) Real, J. A.; Ruiz, R.; Faus, J.; Lloret, F.; Julve, M.; Jounaux, Y.; Philoche-Levisalles, M.; Bois, C. *J. Chem. Soc., Dalton Trans* **1994**, 3769.
- (203) Mautner, F. A.; Goher, M. A. S. *Polyhedron* **1996**, *15*, 1133.
- (204) Drew, M. G. B.; Nelson, J.; Esho, F.; McKee, V.; Nelson, S. M. *J. Chem. Soc., Dalton Trans.* **1982**, 1837.

- (205) Sikorav, S.; Bkouche-Waksman, I.; Kahn, O. *Inorg. Chem.* **1984**, *23*, 490-495.
- (206) Goher, M. A. S.; Mak, T. C. W. *Inorg. Chim. Acta* **1984**, *89*, 119.
- (207) Baily, N. A.; Fennon, D. E.; Mclean, C. R. *Inorg. Chim. Acta* **1991**, *179*, 1.
- (208) Mautner, F. A.; Goher, M. A. S. *Polyhedron* **1993**, *12*, 2823-2829.
- (209) Goher, M. A. S.; Al-Salem, N. A.; Mautner, F. A. *Polyhedron* **1996**, *15*, 4513.
- (210) Felthouse, T. R.; Hendrickson, D. N. *Inorg. Chem.* **1978**, *17*, 444.
- (211) Bkouche-Waksman, I.; Siorav, S.; Khan, O. *J. Cryst. Spectrosc. Res.* **1983**, *13*, 303.
- (212) Angus, Y.; Louis, R.; Gisselbrecht, J. P.; Weiss, R. *J. Am. Chem. Soc.* **1984**, *106*, 93.
- (213) Bkouche-Waksman, I.; Boillot, M. L.; Khan, O.; Sikorav, S. *Inorg. Chem.* **1984**, *23*, 4454.
- (214) McKee, V.; Dagdigian, J. V.; Bau, R.; Reed, C. A. *J. Am. Chem. Soc.* **1981**, *103*, 7000.
- (215) Sorrell, T. N.; O'Connor, C. J.; Huchinson, J. P.; Zubieta, J. *J. Am. Chem. Soc.* **1985**, *107*, 4199.
- (216) Mukherjee, P. S.; Maji, T. K.; Mostafa, G.; Mallah, T.; Chaudhuri, N. R. *Inorg. Chem.* **2000**, *39*, 5147-5150.
- (217) Mukherjee, P. S.; Dalai, S.; Mostafa, G.; Lu, T. H.; Rentschler, E.; Chaudhuri, N. R. *New J. Chem.* **2001**, *25*, 1203.
- (218) Ribas, J.; Monfort, M.; Diaz, C.; Bastos, C.; Solans, X. *Inorg. Chem.* **1993**, *32*, 3557.
- (219) Ribas, J.; Monfort, M.; Costa, R.; Solans, X. *Inorg. Chem.* **1993**, *32*, 695.
- (220) Escuer, A.; Vicente, R.; Ribas, J.; Fallah, M. S. E.; Solans, X.; Font-Bardia, M. *Inorg. Chem.* **1994**, *33*, 1842.
- (221) Vicente, R.; Escuer, A.; Ribas, J.; Fallah, M. S. E.; Solans, X.; Font-Bardia, M. *Inorg. Chem.* **1995**, *34*, 1278.
- (222) Ribas, J.; Monfort, M.; Ghosh, B. K.; Cortes, R.; Solans, X.; Font-Bardia, M. *Inorg. Chem.* **1996**, *35*, 864.
- (223) Monfort, M.; Ribas, J.; Solans, X. *J. Chem. Soc., Chem. Commun* **1993**, 350.

- (224) Monfort, M.; Resino, I.; Ribas, J.; Stoeckli-Evans, H. *Angew. Chem. Int. Ed.* **2000**, *39*.
- (225) Mautner, F. A.; Cortes, R.; Lezema, L.; Rojo, T. *Angew. Chem. Int. Ed. Engl.* **1996**, *35*, 96.
- (226) Goher, M. A. S.; Mak, T. C. W. *Inorg. Chim. Acta* **1984**, *85*, 117.
- (227) Mak, T. C. W.; Goher, M. A. S.; Mautner, F. A. *Inorg. Chim. Acta* **1986**, *115*, 17.
- (228) Goher, M. A. S.; Mautner, F. A. *Naturforsch* **1991**, *46(b)*, 687.
- (229) Goher, M. A. S.; Mautner, F. A.; Al-Salem, N. A. *Polyhedron* **1997**, *16*, 2239.
- (230) Halcrow, M. C.; Sun, J. S.; Huffman, J. C.; Christou, G. *Inorg. Chem.* **1995**, *34*, 4167.
- (231) Maji, T. K.; Mukherjee, P. S.; Koner, S.; Mostafa, G.; Tuchagues, J. P.; Chaudhuri, N. R. *Inorg. Chim. Acta* **2001**, *314*, 111-116.
- (232) Goher, M. A. S.; Mak, T. C. W. *Inorg. Chim. Acta* **1985**, *99*, 223.
- (233) Munno, G. D.; Real, J. A.; Julve, M.; Munoz, C. M. *Inorg. Chim. Acta* **1993**, *211*, 227.
- (234) Goher, M. A. S.; Wang, R. J.; Mak, T. C. W. *J. Mol. Struct.* **1991**, *243*, 179.
- (235) Escuer, A.; Font-Bardia, M.; Penalba, E.; Solans, X.; Vicente, R. *Polyhedron* **1998**, *18*, 211.
- (236) Thompson, L. K.; Tandon, S. S.; Lloret, F.; Cano, J.; Julve, M. *Inorg. Chem.* **1997**, *36*, 3301-3306.
- (237) Chaudhuri, P.; Guttman, M.; Ventur, D.; Weighardt, K.; Nuber, B.; Weiss, J. J. *Chem. Soc., Chem. Commun* **1985**.
- (238) Tandon, S. S.; Thompson, L. K.; Manuel, M. E.; Bridson, J. N. *Inorg. Chem.* **1994**, *33*, 5555-5570.
- (239) Mak, T. C. W.; Goher, M. A. S. *Inorg. Chim. Acta* **1986**, *115*, 17.
- (240) Escuer, A.; Vicente, R.; Ribas, J. *J. Magn. Magn. Mater.* **1992**, *110*, 181.
- (241) Arriortua, M. I.; Cortes, A. R.; Lezema, L.; Rojo, T.; Solans, X. *Inorg. Chim. Acta* **1990**, *174*, 263.
- (242) Cortes, R.; Lezama, L.; Pizarro, J. L.; Arriortua, M. I.; Solans, X.; Rojo, T. *Angew. Chem. Int. Ed. Engl.* **1994**, *33*, 2488-2489.

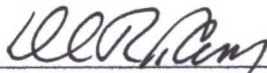
- (243) Ribas, J.; Monfort, M.; Solans, X.; Drillon, M. *Inorg. Chem.* **1994**, *33*, 742.
- (244) Tandon, S. S.; Thompson, L. K.; Miller, D. O. *Chem. Commun.* **1995**, 1907.
- (245) Mautner, F. A.; Goher, M. A. S. *Polyhedron* **1992**, *11*, 2537.
- (246) Kahn, O. *Inorg. Chim. Acta.* **1982**, *62*, 3-14.
- (247) Cortes, R.; Pizarro, J. L.; Lezama, L.; Arriortua, M. I.; Rojo, T. *Inorg. Chem.* **1994**, *33*, 2697.
- (248) Han, S.; Manson, J. L.; Kim, J.; Miller, J. S. *Inorg. Chem.* **2000**, *39*, 4189.
- (249) Barandika, M. G.; Cortes, R.; Lezama, L.; Urriaga, M. K.; Arriortua, M. I.; Rojo, T. *J. Chem. Soc., Dalton Trans.* **1999**, 2971.
- (250) Comarmond, J.; Plumere, P.; Lehn, J. M.; Angus, Y.; Louis, R.; Weiss, R.; Khan, O.; Morgesten-Badarau, I. *J. Am. Chem. Soc.* **1982**, *104*, 6330.
- (251) Kahn, O.; Sikorav, S.; Gouteron, J.; Jeannin, S.; Jeannin, Y. *Inorg. Chem.* **1983**, *22*, 2877-2883.
- (252) Pierpont, C. G.; Hendrickson, D. N.; Duggan, D. M.; Wagner, F.; Barefield, E. K. *Inorg. Chem.* **1975**, *14*, 604-610.
- (253) Escuer, A.; Vicente, R.; Ribas, J.; Fallah, M. S. E.; Solans, X. *Inorg. Chem.* **1993**, *32*, 1033.
- (254) Angus, Y.; Louis, R.; Weiss, R. *J. Am. Chem. Soc.* **1979**, *101*, 3381.
- (255) Mukherjee, P. S.; Maji, T. K.; Escuer, A.; Vincente, R.; Ribas, J.; Rosair, G.; Mautner, F. A.; Chadhuri, N. R. *Eur. J. Inorg. Chem.* **2002**, 943-949.
- (256) Thompson, L. K.; Tandon, S. S. *Inorg. Chem.* **1995**, *34*, 2356-2366.
- (257) Wyatt, J. F.; Hillier, I. H.; Saunders, V. R.; Connor, J. A.; Barber, M. *J. Chem. Phys.* **1971**, *54*, 5311.
- (258) Goher, M. A. S.; Escuer, A.; Mautner, F. A.; Al-Salem, N. A. *Polyhedron* **2001**, *20*, 2971-2977.
- (259) Rubenacker, G. V.; Drumheller, J. E.; Emerson, K.; Willett, R. D. *Journal of Magnetism and Magnetic Materials* **1986**, *54-57*, 1483-1484.
- (260) Woodward, J. D.; Backov, R.; Meisel, M. W.; Talham, D. R. Unpublished Results. **2000**.

- (261) Grigereit, T. E.; Ramakrishna, B. L.; Place, H.; Willett, R. D.; Pellacani, G. C.; Manfredini, T.; Menabue, L.; Bonamartini-Corradi, A.; Battaglia, L. P. *Inorg. Chem.* **1984**, *26*, 2235-2243.
- (262) Baker, A. T.; Craig, D. C.; Rae, A. D. *Aust. J. Chem.* **1995**, *48*, 1373-1378.
- (263) Cortes, R.; Arriortua, M. I.; Rojo, T.; Solans, X.; Beltran, D. *Polyhedron* **1986**, *5*, 1987-1990.
- (264) Cortes, R.; Arriortua, M. I.; Rojo, T.; Solans, X.; Miravittles, C.; Beltran, D. *Acta Cryst.* **1985**, *C41*, 1733-1736.
- (265) Iwamoto, T.; Miyoshi, T.; Sasaki, Y. *Acta Cryst.* **1974**, *B30*, 292-295.
- (266) Cernak, J.; Chomic, J.; Domiano, P.; Ori, O.; Andreett, G. D. *Acta Cryst.* **1991**, *C46*, 2103-2107.
- (267) Yuge, H.; Iwamoto, T. *J. Chem. Soc., Dalton Trans.* **1994**, 1237-1242.
- (268) Cernak, J.; Orendac, M.; Potocnak, I.; Chomic, J.; Orendacova, A.; Skorsepa, J.; Feher, A. *Coordination Chemistry Reviews* **2002**, *224*, 51-66.
- (269) Sen, S.; Mitra, S.; Kundu, P.; Saha, M. K.; Kruger, C.; Bruckmann, J. *Polyhedron* **1997**, *16*, 2475-2481.
- (270) Hay, P. J.; Thibeault, J. C.; Hoffmann, R. *J. Am. Chem. Soc.* **1975**, *97*, 4884-4899.
- (271) Watson, B. C. *Quantum Transitions in Antiferromagnets and Liquid Helium-3*. University of Florida, 2000.

## BIOGRAPHICAL SKETCH

Jonathan David Woodward was born in Birmingham, Alabama on April 22, 1974. He has lived in Birmingham for most of his life where, in 1992, he graduated from Pelham High School, Pelham, Alabama. In 1996, he graduated cum laude from the University of Montevallo, Montevallo, Alabama, with a Bachelor of Science in Chemistry. It wasn't until late in his junior year of college that he realized that he wanted to go to graduate school and that a career in medicine was really feasible. Later that same year, he began graduate school at the University of Florida (Gainesville, Florida) to work toward a Ph.D. in Chemistry under the supervision of Dr. Daniel R. Talham. Despite living in Gainesville for the better part of 5 years, he still remains a "gator-hater." Upon completing his doctorate, Jonathan's immediate plans include a postdoctoral fellowship at the University of Tennessee. Eventually he plans to pursue an industrial research career.

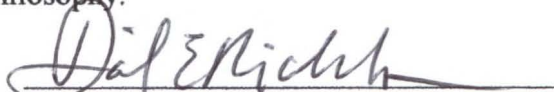
I certify that I have read this study and that in my opinion it conforms to acceptable standards of scholarly presentation and is fully adequate, in scope and quality, as a dissertation for the degree of Doctor of Philosophy.



---

Daniel R. Talham, Chair  
Professor of Chemistry

I certify that I have read this study and that in my opinion it conforms to acceptable standards of scholarly presentation and is fully adequate, in scope and quality, as a dissertation for the degree of Doctor of Philosophy.



---

David E. Richardson  
Professor of Chemistry

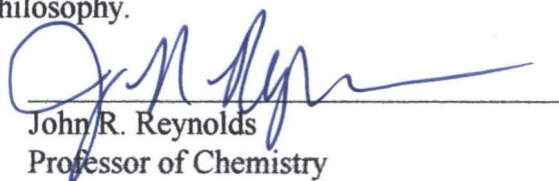
I certify that I have read this study and that in my opinion it conforms to acceptable standards of scholarly presentation and is fully adequate, in scope and quality, as a dissertation for the degree of Doctor of Philosophy.



---

Gus J. Palenik  
Professor of Chemistry

I certify that I have read this study and that in my opinion it conforms to acceptable standards of scholarly presentation and is fully adequate, in scope and quality, as a dissertation for the degree of Doctor of Philosophy.



---

John R. Reynolds  
Professor of Chemistry

I certify that I have read this study and that in my opinion it conforms to acceptable standards of scholarly presentation and is fully adequate, in scope and quality, as a dissertation for the degree of Doctor of Philosophy.



---

Mark W. Meisel  
Professor of Physics